

論文 / 著書情報
Article / Book Information

題目(和文)	高速な時間領域境界要素法及びその非線形超音波シミュレーションへの適用
Title(English)	Fast time-domain boundary element method and its application to nonlinear ultrasonic simulation
著者(和文)	丸山泰蔵
Author(English)	Taizo Maruyama
出典(和文)	学位:博士(工学), 学位授与機関:東京工業大学, 報告番号:甲第10240号, 授与年月日:2016年3月26日, 学位の種別:課程博士, 審査員:廣瀬 壮一,天谷 賢治,三上 貴正,アニール ワイジェ,中村 隆志,斎藤 隆泰
Citation(English)	Degree:Doctor (Engineering), Conferring organization: Tokyo Institute of Technology, Report number:甲第10240号, Conferred date:2016/3/26, Degree Type:Course doctor, Examiner:,,,,,
学位種別(和文)	博士論文
Type(English)	Doctoral Thesis

FAST TIME-DOMAIN BOUNDARY ELEMENT METHOD AND ITS APPLICATION TO
NONLINEAR ULTRASONIC SIMULATION

by

Taizo Maruyama

Master of Engineering
Tokyo Institute of Technology, 2013

Bachelor of Engineering
Tokyo Institute of Technology, 2011

Submitted in Partial Fulfillment of the
Requirements for the Degree of Doctor of Engineering in the
Department of Mechanical and Environmental Informatics
Graduate School of Information Science and Engineering
Tokyo Institute of Technology
2016

Academic Supervisor and Chief of Committee: Professor Sohichi Hirose

Committee Members:

Professor Kenji Amaya
Associate Professor Anil C. Wijeyewickrema
Associate Professor Takahiro Saitoh
Associate Professor Takamasa Mikami
Lecturer Takashi Nakamura

Acknowledgments

I would like to express my gratitude to Professor Sohichi Hirose for his excellent support and providing me the precious study opportunity as a doctoral student in his laboratory. His shrewd advice and enthusiastic direction always helped me to conduct this research. I especially would like to express my deepest appreciation to Associate Professor Takahiro Saitoh of Gunma University for his guidance, encouragement, and discussion. He was an Assistant Professor of Tokyo Institute of Technology until March 2012. I have been really helped by him since I was an undergraduate student.

I would like to thank to Associate Professor Kazuyuki Nakahata of Ehime University for his advice and many discussion. I would like to express my gratitude to Professor Terumi Touhei of Tokyo University of Science for his advice and many discussion. His advice was pertinent and helped my research. I would like to thank to Professor Naoshi Nishimura of Kyoto University for his advice and many discussion about a boundary element method and its acceleration. I would also thank to Lecturer Hitoshi Yoshikawa of Kyoto University for many discussion about a time-domain boundary element method at conferences.

I am grateful to Professor Toshihiko Sugiura of Keio University for his useful advice about non-linear ultrasonic generation phenomena. I wish to thank committee members of my doctoral research, Professor Kenji Amaya, Associate Professor Anil C. Wijeyewickrema, Associate Professor Takamasa Mikami, and Lecturer Takashi Nakamura, for their enthusiastic discussion and useful advice.

I would also like to thank to members of Hirose laboratory for their encouragement and many discussion. Especially, I could learn a lot from Assistant Professor Akira Furukawa's sincere attitude toward his education and research. Also, I thank to Tinh Q. Bui of Postdoctoral Fellowship for Research Abroad for his advice and many discussion. Thank to him, my English skill became much better than before.

I am also very grateful to Japan Society for the Promotion of Science for making my doctoral study possible by the financial support.

Finally, I would like to express my gratitude to my parents for their understanding, support, and encouragement although I quitted the high school on account of personal reasons. They have always supported my life.

Department of Mechanical and Environmental Informatics,
Graduate School of Information Science and Engineering,
Tokyo Institute of Technology, Japan.

Abstract

The nonlinear ultrasonic testing (NLUT) based on the contact acoustic nonlinearity (CAN) has attracted notice recently because it is expected to be a new technique for detection of closed cracks, which cannot be detected by using the conventional linear ultrasonic testing. In the NLUT, the nonlinear ultrasonic waves which consist of higher- and sub-harmonic waves generated from the defects are evaluated, and the location and size of the defect are predicted by analyzing the frequency characteristic of them.

The higher-harmonic generation due to the CAN was advocated over three decades ago. Thereafter, this phenomenon has been vigorously investigated, and its mechanism has been clearly understood from theoretical and experimental points of view. However, when the higher-harmonic generation is caused owing to an interface crack, the contribution of material difference has not been investigated sufficiently. Moreover, the mechanism of sub-harmonic generation has not been understood from a theoretical point of view yet although its generation has confirmed in the measurement. Therefore, further theoretical and/or numerical approaches are demanded in order to utilize this nonlinear phenomenon for the nondestructive evaluation (NDE).

In general, the higher-harmonic waves are generated by many causes such as transducer, couplant, and material nonlinearity. On the other hand, it is considered that the sub-harmonic waves are generated only by crack faces with contact in this situation. Thus, if the sub-harmonic waves can be used for the NDE, the more precise detection and size measurement of closed cracks are expected.

At this stage, there are a few numerical approaches for sub-harmonic generation, and these simulations have been succeeded only in the case of very thin debonding plate. However, the sub-harmonic generation has also been observed for different situations in the realistic measurement. Therefore, the author conducts numerical simulation of the sub-harmonic generation due to cracks in an unbounded elastic solid and a surface breaking crack in an elastic half-space in order to investigate the causes.

The time-domain boundary element method (TD-BEM) is considered as an appropriate numerical method for this simulation because the (semi-)infinite domain is dealt with in this study, and the nonlinear boundary conditions on crack faces can be treated exactly. In order to investigate stable sub-harmonic waves due to the CAN, a long-time transient analysis for the nonlinear boundary problem has to be carried out. The computational cost of numerical simulation becomes large (especially for three-dimensional (3-D) problems).

In this dissertation, a convolution quadrature time-domain boundary element method (CQ-BEM), which is known as the one of stable and accurate TD-BEMs, is accelerated using a fast multipole

method (FMM) and a rapid convolution algorithm for solving large-scale wave problems. The author has applied the proposed fast CQ-BEM to the numerical simulation of NLUT due to the CAN.

First, the higher-harmonic generation due to an interface crack is investigated by using the developed 3-D TD-BEM. Second, many 2-D numerical simulations are conducted for the sub-harmonic generation due to cracks in an unbounded infinite elastic solid and a surface breaking crack in an elastic half-space. Finally, some 3-D numerical simulations of the sub-harmonic generation are carried out for cracks in an unbounded infinite elastic solid, and the author investigates the dimensional effects, i.e. difference from 2-D results. Through obtained numerical results, the causes and characteristics of the nonlinear ultrasonic generation phenomenon are discussed.

Contents

Acknowledgments	iii
Abstract	v
List of figures	xix
List of Tables	xxi
List of Main Symbols	xxiii
1. Introduction	1
1.1. Background of study	1
1.2. Previous researches of nonlinear ultrasonic testing	2
1.3. Time-domain boundary element method (TD-BEM)	4
1.4. Organization of dissertation	5
2. Convolution Quadrature Time-domain Boundary Element Method (CQ-BEM)	7
2.1. Convolution quadrature method (CQM)	7
2.1.1. Linear multistep-based CQM	7
2.1.2. Implicit Runge-Kutta (IRK)-based CQM	9
2.1.3. Behavior of Laplace parameter	12
2.2. CQ-BEM for 3-D acoustic wave problems	13
2.2.1. Formulation of boundary integral equation (BIE)	13
2.2.2. Discretization of BIE	14
2.3. Numerical results	15
2.4. Concluding remarks	18
3. Acceleration of CQ-BEM	19
3.1. Fast multipole accelerated CQ-BEM (CQ-FMBEM)	19
3.1.1. Time-marching process	19
3.1.2. Fast multipole method (FMM)	20
3.1.3. Some numerical techniques for efficient CQ-FMBEM	24
3.1.4. Computational complexity	27
3.1.5. Numerical results	28

3.1.6.	CQ-FMBEM for 3-D elastic wave problems	30
3.1.7.	CQ-FMBEM for 3-D coupled acoustic-elastic wave problems	38
3.2.	Acceleration for number of time steps	45
3.2.1.	New time-marching process of CQ-FMBEM	45
3.2.2.	Truncation condition for M2L using arrival time of influence waves	48
3.2.3.	Numerical results	48
3.3.	Concluding remarks	50
4.	3-D Simulation of Higher-harmonic Waves Due to an Interface Crack of Bi-material	53
4.1.	Problem statement and BIE	53
4.2.	Discretization of BIE and contact boundary conditions	55
4.2.1.	Nonlinear interface conditions	55
4.2.2.	Modification of BIE	57
4.3.	Numerical procedure for nonlinear analysis	58
4.4.	Numerical results	59
4.4.1.	Accuracy verification	60
4.4.2.	Nonlinear ultrasonic simulation	61
4.5.	Concluding remarks	73
5.	2-D Simulation of Nonlinear Ultrasonic Waves Due to Interior and Surface Breaking Cracks	77
5.1.	Problem statement and BIE	77
5.1.1.	Scattering problem by cracks in infinite domain	77
5.1.2.	Scattering problem by surface breaking cracks in half-space	79
5.2.	Regularization of BIE	81
5.3.	Discretization of BIE	82
5.3.1.	Scattering problem by cracks in infinite domain	83
5.3.2.	Scattering problem by surface breaking cracks in half-space	85
5.4.	Nonlinear boundary conditions and numerical procedure	86
5.5.	Numerical results	87
5.5.1.	Linear problem	87
5.5.2.	Higher-harmonic simulation	88
5.5.3.	Simulation of sub-harmonic waves due to interior cracks	92
5.5.4.	Simulation of sub-harmonic waves due to a surface breaking crack	112
5.6.	Concluding remarks	115
6.	3-D Simulation of Nonlinear Ultrasonic Waves Due to Interior Cracks	121
6.1.	Problem statement and BIE	121
6.2.	Regularization of BIE	122
6.3.	Discretization of BIE	124

6.4. Numerical integration over element surfaces	127
6.5. Application of FMM	127
6.6. Nonlinear boundary conditions and numerical procedure	129
6.7. Numerical results	131
6.7.1. Linear problem	131
6.7.2. Higher-harmonic simulation	134
6.7.3. Sub-harmonic simulation	137
6.8. Concluding remarks	146
7. Final Remarks	149
A. Translation Operators and Recursions	153
B. Far-field Approximation of Scattered Waves	155
B.1. Inclusions and cracks in 2-D and 3-D	155
B.2. Interface cracks between two semi-infinite elastic solids in 3-D	157
B.3. Surface breaking cracks in 2-D elastic half-space	158
C. Free-field for two-layered elastic solid	161
Bibliography	164

List of Figures

2.1. (a) Overall picture and (b) enlarged view around the origin of Laplace parameters s required for CQMs with RK_m and BDF_k using computational parameters in Table 2.1.	12
2.2. Analysis model for acoustic wave scattering by an obstacle in a 3-D infinite domain.	13
2.3. Acoustic wave scattering by a rigid sphere subjected to an incident plane wave. . .	16
2.4. Time variations of p/p_0 obtained by using BDF1 at point X in Fig. 2.3.	16
2.5. Time variations of p/p_0 obtained by using BDF2 at point X in Fig. 2.3.	16
2.6. Time variations of p/p_0 obtained by using RK2 at point X in Fig. 2.3.	17
2.7. Time variations of p/p_0 obtained by using RK3 at point X in Fig. 2.3.	17
3.1. Translation theorems (M2M, M2L, and L2L).	24
3.2. Scaling for M2M moment translated from C_ℓ to $C_{2\ell}$ using half diagonal length of cube cell.	25
3.3. Distance between two cells in M2L translation.	27
3.4. Time variations of p/p_0 obtained by CQ-BEM and CQ-FMBEM using RK3 at point X in Fig. 2.3 when $c_f \Delta t/a = 0.069$	28
3.5. Absolute errors between p/p_0 obtained by CQ-BEM and CQ-FMBEM, which are shown in Fig. 3.4.	28
3.6. Computational time comparison between CQ-BEM and CQ-FMBEM using RK3 for 3-D acoustic wave problem.	29
3.7. Required memory comparison between CQ-BEM and CQ-FMBEM using RK3 for 3-D acoustic wave problem.	29
3.8. Analysis model for elastic wave scattering by an obstacle in a 3-D infinite domain .	30
3.9. Elastic wave scattering by a spherical cavity subjected to an incident plane wave. .	34
3.10. Time variations of u_1^{sc}/u_0 obtained by using BDF2 at point X in Fig. 3.9 when $M_e = 9280$	35
3.11. Time variations of u_1^{sc}/u_0 obtained by using RK2 at point X in Fig. 3.9 when $M_e = 9280$	35
3.12. Time variations of u_1^{sc}/u_0 obtained by using RK3 at point X in Fig. 3.9 when $M_e = 9280$	36
3.13. Time variations of u_1^{sc}/u_0 obtained by using RK3 at point X in Fig. 3.9 when $c_T \Delta t/a = 0.06$	36

List of Figures

3.14. Computational time comparison between CQ-BEM and CQ-FMBEM using BDF2 and RK3 for 3-D elastic wave problem.	37
3.15. Required memory comparison between CQ-BEM and CQ-FMBEM using BDF2 and RK3 for 3-D elastic wave problem.	37
3.16. Analysis model 3-D for coupled acoustic-elastic wave problems	39
3.17. Relative errors for calculating convolution integral (3.73) vs. time increments using IRK-based CQM with RK2 and RK3.	42
3.18. Elastic wave scattering by a spherical obstacle subjected to an incident plane wave.	42
3.19. Time variations of far-field backscattered amplitude $\Omega_L/(au_0)$ for various obstacles subjected to an incident plane P wave.	43
3.20. Time variations of far-field forward-scattered amplitude $\Omega_L/(au_0)$ for various obstacles subjected to an incident plane P wave.	43
3.21. Time variations of far-field backscattered amplitude $\Omega_{TV}/(au_0)$ for various obstacles subjected to an incident plane SV wave.	44
3.22. Time variations of far-field forward-scattered amplitude $\Omega_{TV}/(au_0)$ for various obstacles subjected to an incident plane SV wave.	44
3.23. (a) Coefficient matrix structure for time and (b) calculation order of sub-matrix in the rapid convolution algorithm [31].	46
3.24. Time variations of p/p_0 obtained by conventional and new CQ-FMBEMs using RK3 at point X in Fig. 2.3 when $c_f \Delta t/a = 0.069$	49
3.25. Absolute errors between p/p_0 obtained by conventional and new CQ-FMBEMs, which are plotted in Fig. 3.24.	49
3.26. Computational time comparison between conventional and new CQ-FMBEMs using RK3 for 3-D acoustic wave problem varying the number of elements M_e	50
3.27. Computational time comparison between conventional and new CQ-FMBEMs using RK3 for 3-D acoustic wave problem varying the number of time steps N	50
3.28. Ratio of M2L truncation for each sub-matrix in triangular Toeplitz system using (a) only conventional truncation condition (3.33) and (b) both conventional and new ones when $N = 128$ and $M_e = 3176$	51
4.1. Analysis model for wave scattering by a debonding area on bi-material interface in 3-D.	54
4.2. Contact phases on debonding area S_d	56
4.3. Flowchart of numerical procedure for nonlinear analysis.	58
4.4. Local coordinate system for stopping condition of relatively tangential movement.	60
4.5. An incident plane wave scattering by a penny-shaped interface crack with radius a	60
4.6. Vertical COD on S_d at each several time steps $c_T t/a$ when a penny-shaped crack is subjected to normal incidence of P wave.	61
4.7. Time variations of vertical displacement at the center point of a penny-shaped crack subjected to an incident plane P wave when $k_T a = 2.0$ and $\sigma^{st}/\sigma_0 = 0$	63

4.8. Time variations of vertical displacement at the center point of a penny-shaped crack subjected to an incident plane P wave when $k_T a = 5.2$ and $\sigma^{st}/\sigma_0 = 0$	63
4.9. Normalized frequency spectrum of far-field amplitude of backscattered P wave $\Omega_L/(au_0)$ when $k_T a = 2.0$ and $\sigma^{st}/\sigma_0 = 0$	64
4.10. Normalized frequency spectrum of far-field amplitude of backscattered P wave $\Omega_L/(au_0)$ when $k_T a = 5.2$ and $\sigma^{st}/\sigma_0 = 0$	64
4.11. Time variations of vertical COD at the center point of a penny-shaped crack subjected to an incident plane P wave varying σ^{st}/σ_0 when $k_T a = 2.0$	65
4.12. Time variations of vertical COD at the center point of a penny-shaped crack subjected to an incident plane P wave varying σ^{st}/σ_0 when $k_T a = 5.2$	65
4.13. Normalized Fourier amplitude of $\Omega_L/(au_0)$ corresponding to 2nd and 3rd higher-harmonic components, $A_{2\omega}/A_{2\omega}^0$ and $A_{3\omega}/A_{3\omega}^0$, in backscattered P waves varying σ^{st}/σ_0 when $k_T a = 2.0$	66
4.14. Normalized Fourier amplitude of $\Omega_L/(au_0)$ corresponding to 2nd and 3rd higher-harmonic components, $A_{2\omega}/A_{2\omega}^0$ and $A_{3\omega}/A_{3\omega}^0$, in backscattered P waves varying σ^{st}/σ_0 when $k_T a = 5.2$	66
4.15. Time variations of horizontal COD at the center of a penny-shaped crack subjected to an incidence plane SV wave varying σ^{st}/σ_0 when $k_T a = 2.0$	67
4.16. Normalized Fourier amplitude corresponding to 3rd higher-harmonic component $A_{3\omega}/A_{3\omega}^0$ in far-field backscattered SV waves varying σ^{st}/σ_0 when $k_T a = 2.0$. . .	67
4.17. Normalized frequency spectrum of far-field amplitude of backscattered SV wave $\Omega_{TV}/(au_0)$ when $k_T a = 2.0$ and $\sigma^{st}/\sigma_0 = 0.6$	67
4.18. Time variations of far-field amplitude of backscattered P wave $\Omega_L/(au_0)$ varying θ^{in} when $k_T a = 2.0$ and $\sigma^{st}/\sigma_0 = 0.0$	68
4.19. Normalized frequency spectra of far-field amplitude of backscattered P wave $\Omega_L/(au_0)$ varying θ^{in} when $k_T a = 2.0$ and $\sigma^{st}/\sigma_0 = 0.0$	68
4.20. Time variations of far-field amplitude of backscattered P wave $\Omega_L/(au_0)$ varying θ^{in} when $k_T a = 5.2$ and $\sigma^{st}/\sigma_0 = 0.0$	69
4.21. Normalized frequency spectra of far-field amplitude of backscattered P wave $\Omega_L/(au_0)$ varying θ^{in} when $k_T a = 5.2$ and $\sigma^{st}/\sigma_0 = 0.0$	69
4.22. Absolute values of reflection and transmission coefficients for displacement when a semi-infinite and flat interface between steel and aluminum is subjected to an incident plane P wave with incident angle θ^{in}	69
4.23. Time variations of vertical displacement on the center point of a penny-shaped interface crack subjected to an incident plane P wave when $k_T^I a = 2.0$ and $\sigma^{st}/\sigma_0 = 0$	70
4.24. Time variations of vertical displacement on the center point of a penny-shaped interface crack subjected to an incident plane P wave when $k_T^I a = 5.2$ and $\sigma^{st}/\sigma_0 = 0$	70
4.25. Normalized frequency spectrum of far-field amplitude of backscattered P wave $\Omega_L/(au_0)$ when $k_T^I a = 2.0$ and $\sigma^{st}/\sigma_0 = 0$	71

List of Figures

4.26. Normalized frequency spectrum of far-field amplitude of backscattered P wave $\Omega_L/(au_0)$ when $k_T^I a = 5.2$ and $\sigma^{st}/\sigma_0 = 0$	71
4.27. Time variations of vertical COD at the center point of a penny-shaped interface crack subjected to an incident plane P wave varying σ^{st}/σ_0 when $k_T^I a = 2.0$	72
4.28. Time variations of vertical COD at the center point of a penny-shaped interface crack subjected to an incident plane P wave varying σ^{st}/σ_0 when $k_T^I a = 5.2$	72
4.29. Normalized Fourier amplitude of $\Omega_L/(au_0)$ corresponding to 2nd and 3rd higher-harmonic components, $A_{2\omega}/A_{2\omega}^0$ and $A_{3\omega}/A_{3\omega}^0$, in backscattered P waves varying σ^{st}/σ_0 when $k_T^I a = 2.0$	73
4.30. Normalized Fourier amplitude of $\Omega_L/(au_0)$ corresponding to 2nd and 3rd higher-harmonic components, $A_{2\omega}/A_{2\omega}^0$ and $A_{3\omega}/A_{3\omega}^0$, in backscattered P waves varying σ^{st}/σ_0 when $k_T^I a = 5.2$	73
4.31. Time variations of horizontal COD at the center of a penny-shaped interface crack subjected to an incidence plane SV wave varying σ^{st}/σ_0 when $k_T^I a = 2.0$	74
4.32. Normalized Fourier amplitude corresponding to 3rd higher-harmonic component $A_{3\omega}/A_{3\omega}^0$ in far-field backscattered SV waves varying σ^{st}/σ_0 when $k_T^I a = 2.0$	74
4.33. Normalized frequency spectrum of far-field amplitude of backscattered SV wave $\Omega_{TV}/(au_0)$ when $k_T^I a = 2.0$ and $\sigma^{st}/\sigma_0 = 0.4$	74
4.34. Time variations of far-field amplitude of backscattered P wave $\Omega_L/(au_0)$ varying θ^{in} when $k_T^I a = 2.0$ and $\sigma^{st}/\sigma_0 = 0.0$	75
4.35. Normalized frequency spectra of far-field amplitude of backscattered P wave $\Omega_L/(au_0)$ varying θ^{in} when $k_T^I a = 2.0$ and $\sigma^{st}/\sigma_0 = 0.0$	75
4.36. Time variations of far-field amplitude of backscattered P wave $\Omega_L/(au_0)$ varying θ^{in} when $k_T^I a = 5.2$ and $\sigma^{st}/\sigma_0 = 0.0$	76
4.37. Normalized frequency spectra of far-field amplitude of backscattered P wave $\Omega_L/(au_0)$ varying θ^{in} when $k_T^I a = 5.2$ and $\sigma^{st}/\sigma_0 = 0.0$	76
5.1. Analysis model for elastic wave scattering by a crack in a 2-D infinite domain.	78
5.2. Analysis model for wave scattering by a surface breaking crack in a 2-D elastic half-space.	79
5.3. Spatial shape functions with respect to displacement and traction for a crack in an infinite domain.	82
5.4. (a) Double node model and (b) triple node model for connection point between surface breaking crack and free-surface.	85
5.5. A straight-line crack subjected to an incident plane wave.	87
5.6. Time variations of dynamic SIF of mode I when $\theta^{in} = 30^\circ$	88
5.7. Time variations of (a) COD at the center point of a crack and (b) far-field amplitude of backscattered P wave when a straight-line crack is subjected to an incident plane P wave. (c) is normalized frequency spectrum of far-field amplitude.	90

5.8. Time variations of (a) tangential traction at the center point of a crack and (b) far-field amplitude of backscattered S wave when a straight-line crack is subjected to an incident plane S wave, and $\sigma^{\text{st}}/\sigma_0 = 1.0$. (c) is normalized frequency spectrum of far-field amplitude.	91
5.9. Fourier amplitude corresponding to 2nd higher-harmonic wave normalized by the one when $u_g/u_0 = \sigma^{\text{st}}/\sigma_0 = 0.0$ for (a) various $k_T a$ and u_g/u_0 , and (b) various $k_T a$ and $\sigma^{\text{st}}/\sigma_0$	92
5.10. Time variations of far-field amplitude of backscattered P wave when $k_T a = 5.0$. . .	92
5.11. Elastic wave scattering by (a) a half-sine-shaped crack and (b) two straight-line cracks arranged in parallel.	93
5.12. Fourier amplitude ratio of sub-harmonic frequency to fundamental one for various wavenumber $k_T a$, pre-opening displacement u_g/u_0 , and incident angles θ^{in} when a half-sine-shaped crack is subjected to an incident plane P wave with $n^{\text{in}} = 30$ ($h/a = 0.0$).	94
5.13. Fourier amplitude ratio of sub-harmonic frequency to fundamental one for various wavenumber $k_T a$, pre-opening displacement u_g/u_0 , and incident angles θ^{in} when a half-sine-shaped crack is subjected to an incident plane P wave with $n^{\text{in}} = 30$ ($h/a = 0.5$).	95
5.14. Fourier amplitude ratio of sub-harmonic frequency to fundamental one for various wavenumber $k_T a$, pre-opening displacement u_g/u_0 , and incident angles θ^{in} when a half-sine-shaped crack is subjected to an incident plane P wave with $n^{\text{in}} = 30$ ($h/a = 1.0$).	96
5.15. Fourier amplitude ratio of sub-harmonic frequency to fundamental one for various wavenumber $k_T a$, pre-opening displacement u_g/u_0 , and incident angles θ^{in} when a half-sine-shaped crack is subjected to an incident plane P wave with $n^{\text{in}} = 30$ ($h/a = 1.5$).	97
5.16. Fourier amplitude ratio of sub-harmonic frequency to fundamental one for various wavenumber $k_T a$, pre-opening displacement u_g/u_0 , and incident angles θ^{in} when a half-sine-shaped crack is subjected to an incident plane P wave with $n^{\text{in}} = 30$ ($h/a = 2.0$).	98
5.17. (a) Time variation and (b) normalized frequency spectrum of far-field amplitude of backscattered P wave when a curved crack is subjected to an incident plane P wave ($k_T a = 1.2$, $u_g/u_0 = 2.0$, $h/a = 2.0$, and $\theta^{\text{in}} = 60^\circ$).	99
5.18. (a) Time variation and (b) normalized frequency spectrum of far-field amplitude of backscattered P wave when a curved crack is subjected to an incident plane P wave ($k_T a = 2.5$, $u_g/u_0 = 0.0$, $h/a = 2.0$, and $\theta^{\text{in}} = 60^\circ$).	100
5.19. Fourier amplitude ratio of sub-harmonic frequency to fundamental one for various pre-opening displacement u_g/u_0 when $k_T a = 1.2$, $h/a = 2.0$, and $\theta^{\text{in}} = 60^\circ$	100
5.20. Displacement fields around a curved crack from $f^{\text{int}} = 20.0$ to 22.0 when $h/a = 2.0$, $\theta^{\text{in}} = 60^\circ$, $k_T a = 1.2$, and $u_g/u_0 = 2.0$	101

List of Figures

5.21. Histories of displacement at points (a) C1 and C2, and (b) C3 and C4 in the lower right of Fig. 5.20 from $f^{\text{int}} = 20.0$ to 22.0 when $h/a = 2.0$, $\theta^{\text{in}} = 60^\circ$, $k_T a = 1.2$, and $u_g/u_0 = 2.0$	102
5.22. Histories of displacement at points C1–C4 in the lower right of Fig. 5.20 from $f^{\text{int}} = 20.0$ to 21.0 when $h/a = 2.0$, $\theta^{\text{in}} = 60^\circ$, $k_T a = 1.2$, and (a) $u_g/u_0 = 0.5$ and (b) $u_g/u_0 = 3.0$	102
5.23. Fourier amplitude ratio of sub-harmonic frequency to fundamental one for various wavenumber $k_T a$, pre-opening displacement u_g/u_0 , and incident angles θ^{in} when two straight-line cracks arranged in parallel are subjected to an incident plane P wave with $n^{\text{in}} = 30$ ($h/a = 0.5$).	104
5.24. Fourier amplitude ratio of sub-harmonic frequency to fundamental one for various wavenumber $k_T a$, pre-opening displacement u_g/u_0 , and incident angles θ^{in} when two straight-line cracks arranged in parallel are subjected to an incident plane P wave with $n^{\text{in}} = 30$ ($h/a = 1.0$).	105
5.25. Fourier amplitude ratio of sub-harmonic frequency to fundamental one for various wavenumber $k_T a$, pre-opening displacement u_g/u_0 , and incident angles θ^{in} when two straight-line cracks arranged in parallel are subjected to an incident plane P wave with $n^{\text{in}} = 30$ ($h/a = 1.5$).	106
5.26. (a) Time variation and (b) normalized frequency spectrum of far-field amplitude of backscattered P wave when two straight-line cracks arranged in parallel are subjected to an incident plane P wave ($k_T a = 2.5$, $u_g/u_0 = 2.0$, $h/a = 0.5$, and $\theta^{\text{in}} = 0^\circ$).	107
5.27. Fourier amplitude ratio of sub-harmonic frequency to fundamental one for various pre-opening displacement u_g/u_0 when $k_T a = 2.5$, $h/a = 0.5$, and $\theta^{\text{in}} = 0^\circ$	107
5.28. Displacement fields around two cracks arranged in parallel from $f^{\text{int}} = 20.0$ to 22.0 when $h/a = 0.5$, $\theta^{\text{in}} = 0^\circ$, $k_T a = 2.5$, and $u_g/u_0 = 2.0$	108
5.29. Histories of displacement at points (a) D1 and D2, and (b) D3 and D4 in the lower right of Fig. 5.28 from $f^{\text{int}} = 20.0$ to 22.0 when $h/a = 0.5$, $\theta^{\text{in}} = 0^\circ$, $k_T a = 2.5$, and $u_g/u_0 = 2.0$	109
5.30. Histories of displacement at points D1–D4 in the lower right of Fig. 5.28 from $f^{\text{int}} = 20.0$ to 21.0 when $h/a = 0.5$, $\theta^{\text{in}} = 0^\circ$, $k_T a = 2.5$, and (a) $u_g/u_0 = 1.0$ and (b) $u_g/u_0 = 3.0$	109
5.31. Frequency responses for the model in Fig. 5.11(a) using the frequency-domain BEM and assuming that crack faces are always separated. The norm $ [\mathbf{u}] /u_0$ at point A in Fig. 5.11(a) for various θ^{in} and $k_T a$ is plotted when (a) $h/a = 0.0$, (b) 0.5, (c) 1.0, (d) 1.5, and (e) 2.0.	110
5.32. Frequency responses for the model in Fig. 5.11(b) using the frequency-domain BEM and assuming that crack faces are always separated. The norm $ [\mathbf{u}] /u_0$ at point B in Fig. 5.11(b) for various θ^{in} and $k_T a$ is plotted when (a) $h/a = 0.5$, (b) 1.0, and (c) 1.5.	111

5.33. Elastic wave scattering by a surface breaking crack in an elastic half-space.	112
5.34. Fourier amplitude ratio of sub-harmonic frequency to fundamental one for various wavenumber $k_T a$, pre-opening displacement u_g/u_0 , and incident angles θ^{in} when a surface breaking crack is subjected to an incident plane P wave with $n^{\text{in}} = 15$ ($\theta_c = 0^\circ$).	113
5.35. Fourier amplitude ratio of sub-harmonic frequency to fundamental one for various wavenumber $k_T a$, pre-opening displacement u_g/u_0 , and incident angles θ^{in} when a surface breaking crack is subjected to an incident plane P wave with $n^{\text{in}} = 15$ ($\theta_c = 15^\circ$).	114
5.36. Fourier amplitude ratio of sub-harmonic frequency to fundamental one for various wavenumber $k_T a$, pre-opening displacement u_g/u_0 , and incident angles θ^{in} when a surface breaking crack is subjected to an incident plane P wave with $n^{\text{in}} = 15$ ($\theta_c = 30^\circ$).	115
5.37. Fourier amplitude ratio of sub-harmonic frequency to fundamental one for various wavenumber $k_T a$, pre-opening displacement u_g/u_0 , and incident angles θ^{in} when a surface breaking crack is subjected to an incident plane P wave with $n^{\text{in}} = 15$ ($\theta_c = 45^\circ$).	116
5.38. (a) Time variation and (b) normalized frequency spectrum of far-field amplitude of backscattered P wave when a surface breaking crack is subjected to an incident plane P wave ($k_T a = 3.7$, $u_g/u_0 = 0.0$, $\theta_c = 45^\circ$, and $\theta^{\text{in}} = 75^\circ$).	117
5.39. Fourier amplitude ratio of sub-harmonic frequency to fundamental one for various pre-opening displacement u_g/u_0 when $k_T a = 3.7$, $\theta_c = 45^\circ$, and $\theta^{\text{in}} = 75^\circ$	117
5.40. Displacement fields around a surface breaking crack from $f^{\text{int}} t = 10.0$ to 12.0 when $\theta_c = 45^\circ$, $\theta^{\text{in}} = 75^\circ$, $k_T a = 3.7$, and $u_g/u_0 = 0.0$	118
5.41. History of displacement at point E in the lower right of Fig. 5.40 from $f^{\text{int}} t = 10.0$ to 12.0 when $\theta_c = 45^\circ$, $\theta^{\text{in}} = 75^\circ$, $k_T a = 3.7$, and $u_g/u_0 = 0.0$	119
5.42. Frequency responses for the model in Fig. 5.33 using the frequency-domain BEM and assuming that crack faces are always separated. The norm $\ [\mathbf{u}]\ /u_0$ at the origin O in Fig. 5.33 for various θ^{in} and $k_T a$ is plotted when (a) $\theta_c = 0^\circ$, (b) 15° , (c) 30° , and (d) 45°	119
6.1. Analysis model for elastic wave scattering by a crack in a 3-D infinite domain.	122
6.2. Two types of triangular tip element for crack front.	124
6.3. Schematic of element subdivision and coordinate transformation for case 1 tip element in Fig. 6.2.	126
6.4. Schematic of potential calculation to ensure (a) Eq. (6.27) and (b) Eq. (6.28).	130
6.5. A penny-shaped crack with radius a subjected to an incident plane P wave.	131
6.6. Mesh structure of a penny-shaped crack when $M_e = 656$ and $M_d = 361$	131

List of Figures

6.7. (a) Vertical COD at each several time-steps and (b) time variations of normalized dynamic SIF when a penny-shaped crack is subjected to normal incidence of plane P wave.	132
6.8. Computational time of CQ-FMBEM using RK3 for 3-D crack problems varying the number of elements M_e when $N = 128$	133
6.9. Computational time of CQ-FMBEM using RK3 for 3-D crack problems varying the number of time steps N when $M_e = 1464$	133
6.10. Time variations of (a) COD at the center point of a crack and (b) far-field amplitude of backscattered P wave when a penny-shaped crack is subjected to an incident plane P wave. (c) is normalized frequency spectrum of far-field amplitude.	135
6.11. Time variations of (a) tangential traction at the center point of a crack and (b) far-field amplitude of backscattered SV wave when a penny-shaped crack is subjected to an incident plane SV wave, and $\sigma^{st}/\sigma_0 = 1.0$. (c) is normalized frequency spectrum of far-field amplitude.	136
6.12. Elastic wave scattering by (a) a saddle-shaped crack and (b) two penny-shaped cracks arranged in parallel.	137
6.13. Frequency responses for the model in Fig. 6.12(a) using the frequency-domain BEM and assuming that crack faces are always separated. The norm $ [\mathbf{u}] /u_0$ at point F in Fig. 6.12(a) for various θ^{in} and $k_T a$ is plotted when (a) $w/a = 1.0$ and (b) 2.0.	138
6.14. Fourier amplitude ratio of sub-harmonic frequency to fundamental one for various pre-opening displacement u_g/u_0 when a saddle-shaped crack is subjected to an incident plane P wave ($w/a = 1.0$, $\theta^{in} = 60^\circ$, and $n^{in} = 15$).	139
6.15. Fourier amplitude ratio of sub-harmonic frequency to fundamental one for various pre-opening displacement u_g/u_0 when a saddle-shaped crack is subjected to an incident plane P wave ($k_T a = 2.8$, $w/a = 1.0$, $\theta^{in} = 60^\circ$, and $n^{in} = 15$).	140
6.16. (a) Time variation and (b) normalized frequency spectrum of far-field amplitude of backscattered P wave when a saddle-shaped crack is subjected to an incident plane P wave ($k_T a = 2.8$, $u_g/u_0 = 3.4$, $w/a = 1.0$, $\theta^{in} = 60^\circ$, and $n^{in} = 15$).	140
6.17. Fourier amplitude ratio of sub-harmonic frequency to fundamental one for various pre-opening displacement u_g/u_0 when a saddle-shaped crack is subjected to an incident plane P wave ($w/a = 2.0$, $\theta^{in} = 60^\circ$, and $n^{in} = 15$).	141
6.18. (a) Time variation and (b) normalized frequency spectrum of far-field amplitude of backscattered P wave when a saddle-shaped crack is subjected to an incident plane P wave ($k_T a = 1.4$, $u_g/u_0 = 2.6$, $w/a = 2.0$, $\theta^{in} = 60^\circ$, and $n^{in} = 15$).	142
6.19. (a) Time variation and (b) normalized frequency spectrum of far-field amplitude of backscattered P wave when a saddle-shaped crack is subjected to an incident plane P wave ($k_T a = 1.4$, $u_g/u_0 = 2.6$, $w/a = 2.0$, $\theta^{in} = 60^\circ$, and $n^{in} = 30$).	143

6.20. Frequency responses for the model in Fig. 6.12(b) using the frequency-domain BEM and assuming that crack faces are always separated. The norm $ [\mathbf{u}] /u_0$ at point G in Fig. 6.12(b) for various h/a and $k_T a$ is plotted when $\theta^{\text{in}} = 0^\circ$	143
6.21. Fourier amplitude ratio of sub-harmonic frequency to fundamental one for various pre-opening displacement u_g/u_0 when two penny-shaped cracks arranged in parallel are subjected to an incident plane P wave ($h/a = 0.5$, $\theta^{\text{in}} = 0^\circ$, and $n^{\text{in}} = 15$).	144
6.22. (a) Time variation and (b) normalized frequency spectrum of far-field amplitude of backscattered P wave when two penny-shaped cracks arranged in parallel are subjected to an incident plane P wave ($k_T a = 3.0$, $u_g/u_0 = 3.2$, $h/a = 0.5$, $\theta^{\text{in}} = 0^\circ$, and $n^{\text{in}} = 15$).	145
6.23. (a) Time variation and (b) normalized frequency spectrum of far-field amplitude of backscattered P wave when two penny-shaped cracks arranged in parallel are subjected to an incident plane P wave ($k_T a = 3.0$, $u_g/u_0 = 3.2$, $h/a = 0.5$, $\theta^{\text{in}} = 0^\circ$, and $n^{\text{in}} = 30$).	146
6.24. Fourier amplitude ratio of sub-harmonic frequency to fundamental one for various pre-opening displacement u_g/u_0 when two penny-shaped cracks arranged in parallel are subjected to an incident plane P wave ($h/a = 1.0$, $\theta^{\text{in}} = 0^\circ$, and $n^{\text{in}} = 15$).	147
B.1. Interface crack of two-layered elastic solid.	157
B.2. Surface breaking crack in elastic half-space.	158
C.1. Reflection and transmission of the incident plane wave on the interface between two elastic solids.	162
C.2. (a) Real parts and (b) imaginary parts of reflection and transmission coefficients of P wave incidence for various incident angles θ^{in}	163
C.3. (a) Real parts and (b) imaginary parts of reflection and transmission coefficients of SV wave incidence for various incident angles θ^{in}	163

List of Tables

2.1. Computational parameters used for calculating Laplace parameters s in Fig. 2.1. . .	12
3.1. Computational time and required memory of CQ-FMBEM when $N = 128$ and $M_e = 5048$	38
3.2. Material constants for base material and inclusions.	43
3.3. Computational time (sec).	45
4.1. Material constants for steel and aluminum.	62
4.2. Friction coefficients for steel-steel and steel-aluminum interfaces.	62
6.1. Relation between coordinate systems (d_1, d_2) and (d_1^*, d_2^*) for sub-elements E_1, E_2 , and E_3 in Fig. 6.3.	126

List of Main Symbols

Material propaties:

C : Elastic modulus tensor

λ : First Lamé constant

μ : Second Lamé constant

ρ : Density

c_f : wave velocity in fluid

c_L : P wave velocity

c_T : S wave velocity

μ_s : Static friction coefficient

μ_d : Dynamic friction coefficient

Geometry:

\mathbf{x} : Field point

\mathbf{y} : Source point

r : Distance between \mathbf{x} and \mathbf{y}

θ : *Zenith* angle

ϕ : *Azimuthal* angle

\mathbf{n} : Unit normal vector

\mathbf{s} : Unit tangential vector

$\mathbf{x}_0, \mathbf{x}_1$: Local expansion point

$\mathbf{y}_0, \mathbf{y}_1$: Multipole point

Wave problems:

t : Time

f : Frequency

ω : Circular frequency

k_L : Wavenumber of P wave

k_T : Wavenumber of S wave

θ^{in} : Incident angle

Fundamental solutions:

$G(\mathbf{x}, \mathbf{y}, t)$: Fundamental solution of pressure for acoustic wave problem

$H(\mathbf{x}, \mathbf{y}, t)$: Normal derivative of $G(\mathbf{x}, \mathbf{y}, t)$ with respect to \mathbf{y}

$U(\mathbf{x}, \mathbf{y}, t)$: Fundamental solution of displacement for elastic wave problem

$T(\mathbf{x}, \mathbf{y}, t)$: Fundamental solution of traction for elastic wave problem

List of Tables

$\mathbf{W}(\mathbf{x}, \mathbf{y}, t)$: Hypersingular kernel for elastic wave problem

$(\hat{\cdot})$: Laplace-domain function

Numerical simulations:

Δt : Time increment

s : Laplace parameter

N : Number of time steps

M_e : Number of elements

a : Representative length

u_g : Pre-opening displacement of crack

σ^{st} : Compressive static stress over crack

Physical quantities:

p : Pressure

\mathbf{u} : Displacement

$[u]$: Crack opening displacement

\mathbf{t} : Traction force

$\boldsymbol{\sigma}$: Stress

Functions:

$\delta(x)$: Dirac delta distribution

$H(x)$: Heaviside function

$Y_n^m(\hat{\mathbf{x}})$: Spherical harmonics

$P_n^m(x)$: Associated Legendre function

$i_n(z)$: Modified spherical Bessel function of the first kind

$k_n(z)$: Modified spherical Bessel function of the second kind

Special items:

δ_{ij} : Kronecker delta

e_{ijk} : Component of 3-D permutation tensor

e_{ij} : Component of 2-D permutation tensor

Chapter 1

Introduction

1.1. Background of study

The nondestructive evaluation (NDE) of existing structures such as nuclear plants, bridges, and tunnels is important to detect flaws at an early stage and to prevent accidents. The inspection of welded joints is also important to raise its quality in manufacturing. Therefore, it is considered that cost reduction and safe management can be attained by effective utilization of the nondestructive testing (NDT). Among many techniques of NDE, the ultrasonic testing (UT) and radiographic testing (RT) are often used for the flaw detection on the inside of material. The UT has some advantages in its portability and safety compared with the RT, and it is therefore considered as appropriate for the inspection of infrastructures.

However, it is difficult to detect closed cracks, which are flaws at an early stage, using the conventional and linear UT (LUT) that is based on mismatch of acoustic impedance between base material and flaws. This is because an incident wave is hardly scattered on contacting crack faces, and adequate scattered waves cannot be received in the LUT. On the other hand, a nonlinear UT (NLUT) based on the contact acoustic nonlinearity (CAN) has attracted notice as a new technique for detection of closed cracks recently [89]. This method is based on the nonlinear ultrasonic waves which are very sensitive to degradation of material properties at the early stage of damage. The nonlinear ultrasonic waves, which consist of higher- and sub-harmonic waves, are considered as generated by the CAN. The higher- and sub-harmonic wave components correspond to the integer times and integer division of the center frequency of incident wave, respectively.

There are two different mechanisms of higher-harmonic generation, and they have been mostly understood from theoretical and experimental points of view. The first is a non-symmetrical stress-strain diagram under perpendicular vibration to a discontinuous interface such as a closed crack. Thereby, the stiffness crossing the discontinuous interface for compression is harder than that for tension. The clapping motion of crack faces is then caused, and it excites higher-harmonic waves of both odd and even orders. The second is energy dissipation because of the interface roughness. The friction force is generated under some compressive stress, and an incident wave is distorted in a symmetrical way. It is known that odd order higher-harmonic waves are generated by this dynamic friction phenomenon.

1. Introduction

In the NLUT, an incident wave with large amplitude is used for the inspection of closed cracks. Then, the incident wave makes crack faces vibrate with contacting each other, and this vibration causes the clapping motion and dynamic friction on the crack faces. Consequently, the transmitted wave through closed cracks contains the nonlinear ultrasonic wave components. Therefore, it is considered as possible to detect the location of the closed crack and measure its size via the spectrum analysis of received waves.

However, at this stage, the generation mechanism of sub-harmonic wave in the NLUT has not been understood clearly unlike the one of higher-harmonic wave. On the other hand, the excitation of sub-harmonic waves have been observed in the measurement [86]. In order to reveal the generation mechanism of sub-harmonic waves, further theoretical and/or numerical approaches are implemented in this study. In general, the higher-harmonic waves are generated by many causes except flaws such as transducer, and couplant. On the other hand, it is considered that the sub-harmonic waves are generated only by flaws in the NLUT. Thus, if the sub-harmonic waves can be used for the NDE, the more precise detection and size measurement of closed cracks are expected.

Taking into account the numerical approaches for the NLUT, there are two requirements. The first is to accurately calculate physical quantities on the crack faces such as displacement and stress because they significantly effect on the states of crack faces such as contact and non-contact. In addition, appropriate treatment of boundary conditions on crack faces is also important for accuracy. On the other hands, nonlinear boundary value problems have to be solved, and the generation mechanism of sub-harmonic waves is unknown. Hence, we need to conduct many numerical simulations for various parameters. From the above, the second requirement is a fast solver of time-dependent partial differential equations (PDEs), especially for three-dimensional (3-D) problems.

Considering the first requirement, the boundary element method (BEM) is desirable because it can exactly deal with the nonlinear boundary conditions on crack faces, and accuracy of physical quantities on boundaries is much better than the finite element method (FEM) and finite difference method (FDM). To numerically solve the time-dependent problems with nonlinear boundary conditions, a time-domain BEM (TD-BEM) is utilized in this study. The acceleration of TD-BEM must be considered for 3-D problems owing to the second requirement. Therefore, we propose a new fast TD-BEM for the nonlinear ultrasonic simulation and implement many numerical simulations in order to investigate the phenomena of nonlinear ultrasonic generation due to closed cracks.

1.2. Previous researches of nonlinear ultrasonic testing

The generation of higher-harmonic waves due to CAN was advocated over thirty years ago [15], and many experimental and theoretical approaches have been carried out to investigate its mechanism and characteristic. For instances of experimental approach, 2nd and 3rd higher-harmonic wave components in the reflected P waves from a contact surface between two solid blocks have been investigated by Severin and Solodov [81]. The effects of CAN on surface Rayleigh waves have also been investigated by Solodov *et al.* [85]. Moreover, some flaw detection techniques based on the NLUT have been developed recently. For instance, 2nd higher-harmonic waves have been used for

the synthetic aperture focusing technique (SAFT) [66].

On the other hands, the generation of sub-harmonic waves due to CAN has been first observed by Solodov and Vu [86]. At that time, it was considered that the sub-harmonic wave is generated just before the chaotic vibration and an unstable phenomenon. However, comparatively stable sub-harmonic waves have been observed by Yamanaka *et al.* [98] in the ultrasonic measurement for a surface breaking crack, and the depth measurement technique of a surface breaking crack has been developed by Ohara *et al.* [65]. Moreover, Hayashi and Biwa [34] have shown that stable sub-harmonic waves are generated in the case that a thin layer exists between two solid blocks through experiment and 1-D numerical simulation. However, the generation mechanism of sub-harmonic waves has not been understood clearly in all cases of above. It is difficult to intuitively comprehend the generation mechanism of sub-harmonic wave unlike that of higher-harmonic wave.

As previous theoretical and numerical approaches, the 1-D numerical simulation modeling the clapping motion on the discontinuous interface has been first implemented by Richardson [70]. Thereafter, some numerical simulations have been implemented in 2-D and 3-D modeling the clapping motion and dynamic friction on the crack faces. For instance, 2-D numerical simulations have been conducted by the TD-BEM [56, 39]. They have used the Coulomb friction law with constant static and dynamic friction coefficients. Their methods have been extended to the debonding area on the interface of bi-material in 2-D [77]. Also, the 3-D axisymmetric problem, i.e. a penny-shaped crack subjected to normal incidence of P wave, has been solved numerically [38]. However, these numerical approaches using TD-BEM have not succeeded in the simulation of sub-harmonic generation yet. On the other hand, the 2-D antiplane simulation of FEM for the discontinuous interface with dynamic friction conditions has been implemented by Meziane *et al.* [59]. The 2-D FDM simulation for cracks only with clapping motion has also been conducted by Kimoto and Ichikawa [42]. Some 3-D sub-harmonic simulations have been conducted for delamination of thin materials using the FDM [79] and FEM [20]. However, they have presented the sub-harmonic generation only in the case that the thickness of delaminated layer is much smaller than its diameter and specifically less than $1/20$.

From the above, it is necessary to investigate the physical phenomenon of sub-harmonic generation due to cracks. There also remains implementation of the 3-D nonlinear ultrasonic simulation for a debonding area on the interface of bi-material. Therefore, we investigate the characteristic of higher-harmonic generation in the case that a debonding area is subjected to an incident wave by means of the 3-D TD-BEM. Subsequently, 2-D simulations of sub-harmonic generation by cracks in an infinite domain and a surface breaking crack in a half-space are implemented in order to investigate its causes. Finally, sub-harmonic simulations due to cracks in a 3-D infinite domain are carried out, and obtained results are compared between 2-D and 3-D.

1.3. Time-domain boundary element method (TD-BEM)

In this section, we explain the TD-BEM, which is utilized for transient elastic wave scattering problems for the nonlinear ultrasonic simulation in this study. In general, the BEM is widely used for transient analyses of wave propagation in fluid and solid media [13, 25]. The transient elastic wave problems have been investigated by many authors based on different methods, for instance, the frequency- [63] or Laplace-domain BEM [49] with the construction of time-domain results by inverse Fourier or Laplace transform, respectively. However, the indirect methods cannot solve nonlinear boundary value problems such as the nonlinear ultrasonic simulation. Therefore, for such problems, the direct TD-BEM is clearly preferred [35, 36].

In general, it is well known that the conventional TD-BEM in which a collocation method is used for the time discretization, causes numerical instability for small time step size in time-marching process. This issue has been overcome by the Galerkin discretization of both space and time integrals in boundary integral equations (BIEs) [29, 30]. However, it is difficult to solve wave propagation problems for dispersive media such as viscoelastic and poroelastic ones because explicit time-domain fundamental solutions for those complex problems are not available. On the other hand, the convolution quadrature method (CQM) which was pioneered by Lubich [46, 47], has been developed as a technique to approximate convolution integrals in the past two decades. The application of the CQM to a TD-BEM (CQ-BEM) is suitable for transient analysis of wave propagation problems [82]. By using the CQM for discretizing the convolution integrals in boundary integral equations, the accuracy and numerical stability of the time-marching process are substantially improved. The CQ-BEM requires the Laplace-domain fundamental solutions. Therefore, as a result, the dispersion issues encountered in viscoelastic and poroelastic problems can be overcome straightforwardly [75, 78, 83]. Recently, several studies have shown that the CQ-BEM using an implicit Runge-Kutta (IRK) scheme performs better accuracy than that using a linear multistep method [48, 7]. In addition, the stability and error analysis of the IRK-based CQM were conducted by Calvo *et al.* [16] and Banjai *et al.* [5, 6] based on analytical and numerical approaches. The error and behavior of influence functions for heat and wave problems using the IRK-based CQM were also analyzed by Monegato *et al.* [60].

Although the CQ-BEM is powerful, there remains limitations in solving large-scale problems because of low computational efficiency for matrix-vector products of the retarded potentials. The computation of influence functions in the CQ-BEM framework generally requires a great deal of computational time and memory resource compared to that of the conventional TD-BEM. The IRK-based CQ-BEM also requires much computational cost. To overcome these disadvantages and to solve large-scale problems, the CQ-BEM accelerated by the fast multipole method (FMM) [72, 26] (CQ-FMBEM) has been developed [75, 76]. The FMM has been developed as a technique to reduce the computational time and memory usage for solving large-scale problems. The BEM based on FMM (FMBEM) has been developed for wave propagation problems in frequency-domain [62]. The conventional TD-BEM has also been accelerated by Takahashi *et al.* [91, 92] based on the plane wave time-domain (PWTD) algorithm [24]. In addition, the \mathcal{H} -matrix and adaptive cross

approximation (ACA) [9, 10], which is an efficient method for matrix-vector product calculation, has been employed for the acceleration of the CQ-BEM [58].

However, the computational cost for a number of time steps is expensive even if the FMM or \mathcal{H} -matrix is applied to matrix-vector products with respect to space. Banjai and Kachanovska have applied the rapid algorithm of convolution integral [31] and \mathcal{H} -matrix to the CQ-BEM for the 3-D wave equation and shown computational efficiency [8]. However, their method requires comparatively much memory although it is order of $O(NM_e \log M_e)$, where N and M_e are the numbers of time steps and elements, respectively. Moreover, no 3-D elastodynamic formulation for CQ-FMBEM has been proposed yet [18]. Therefore, we propose a new IRK-based CQ-FMBEM for 3-D elastodynamics which is accelerated for number of time steps using the rapid convolution algorithm with the fast Fourier transform (FFT), in order to utilize it for the nonlinear ultrasonic simulation.

1.4. Organization of dissertation

This dissertation consists of seven chapters, and these outlines except this one are shown as follows:

Chapter 2 The formulations of linear multistep- and IRK-based CQMs are briefly presented.

Then, we discuss the expected accuracy in the TD-BEM using each CQMs by comparing the arguments of Laplace-domain fundamental solutions. We also present the application of IRK-based CQM to TD-BEM for 3-D acoustic wave problems and implement some numerical simulations. The accuracy is discussed through numerical results obtained by CQ-BEMs.

Chapter 3 We explain the acceleration techniques of the CQ-BEM for 3-D acoustic and elastic wave problems. First, the IRK-based CQ-BEM for 3-D acoustic wave problems is accelerated by the FMM with respect to spatial components. Second, the CQ-FMBEM is extended to 3-D elastic wave and coupled acoustic-elastic wave problems, and some numerical simulations are implemented. Finally, the CQ-FMBEM is accelerated with respect to the number of time steps using the rapid convolution algorithm, and we demonstrate the computational efficiency of the new CQ-FMBEM from numerical results.

Chapter 4 We implement the 3-D numerical simulation of higher-harmonic generation due to an interface crack between two semi-infinite elastic solids. In this simulation, the collocation method and piecewise constant approximation are used for the spatial discretization. The higher-harmonic generation by a penny-shaped interface crack subjected to an incident plane wave is simulated varying the pre-compressive stress over the crack faces. Then, the scattered waves are evaluated by means of the far-field approximation, and their frequency spectra are investigated.

Chapter 5 The 2-D simulations of sub-harmonic generation due to cracks in an infinite domain and a surface breaking crack in an elastic half-space are carried out. We use the Galerkin method for the spatial discretization in the sub-harmonic simulation because we deal with

1. Introduction

cracks of complex shape or arrangement. No acceleration technique is utilized for the 2-D CQ-BEM because the computational cost of the simulations presented in this chapter is not very expensive.

Chapter 6 We extend the 2-D numerical method for cracks with nonlinear boundary conditions in an infinite elastic solid presented in Chapter 5 to the 3-D and implement some numerical simulations. For the 3-D sub-harmonic simulation, we use the new CQ-FMBEM in order to conduct many simulations with a long analysis time. We conduct some sub-harmonic simulations with similar models to the 2-D ones and compare the obtained results between 2-D and 3-D.

Chapter 7 In this chapter, we state conclusions.

Chapter 2

Convolution Quadrature Time-domain Boundary Element Method (CQ-BEM)

In this chapter, we present the CQM formulation and its application to a TD-BEM. Then, 3-D acoustic wave problems are numerically solved for comparison of accuracy between the linear multistep- and IRK-based CQ-BEMs.

2.1. Convolution quadrature method (CQM)

We briefly explain the formulations of the linear multistep- and IRK-based CQMs, which are discretization methods of convolution integrals. The linear multistep-based CQM was pioneered by Lubich [46, 47], and then, the IRK-based one has been developed by Lubich and Ostermann [48]. The Laplace transform of a kernel function is used in both CQMs.

2.1.1. Linear multistep-based CQM

First, the formulation of linear multistep-based CQM is explained. The convolution integral with respect to time t ,

$$u(t) = (k * g)(t) \equiv \int_0^t k(t - \tau)g(\tau)d\tau \quad 0 \leq t, \quad (2.1)$$

is approximated by the linear multistep-based CQM. In the CQM, $\hat{k}(s)$, which is the Laplace transform of kernel function $k(t)$, is used for the computation of quadrature weight, where s is the Laplace parameter. We define the notations with respect to the Laplace transform and its inverse as follows:

$$\hat{k}(s) = \mathcal{L}[k(t)] \equiv \int_0^\infty k(t)e^{-st}dt, \quad (2.2)$$

$$k(t) = \mathcal{L}^{-1}[\hat{k}(s)] \equiv \lim_{R \rightarrow \infty} \frac{1}{2\pi i} \int_{h-iR}^{h+iR} \hat{k}(s)e^{st}ds, \quad (2.3)$$

2. Convolution Quadrature Time-domain Boundary Element Method (CQ-BEM)

where i is the imaginary unit. In Eq. (2.3), h is a real number and $h > 0$. Substituting Eq. (2.3) into Eq. (2.1) yields

$$u(t) = \lim_{R \rightarrow \infty} \frac{1}{2\pi i} \int_{h-iR}^{h+iR} \hat{k}(s) y_s(t) ds, \quad (2.4)$$

where y_s is given by $y_s(t) = \int_0^t e^{s(t-\tau)} g(\tau) d\tau$ and the solution of the following initial value problem:

$$\frac{\partial y(t)}{\partial t} = sy(t) + g(t), \quad y(0) = 0. \quad (2.5)$$

Note that the difference between the linear multistep-based CQM and IRK-based one is each approximation scheme of Eq. (2.5). The second order backward differentiation formula (BDF2), which is one of the A -stable linear multistep methods [32], is often used for this approximation in the linear multistep-based CQM. The A -stable scheme should be taken to compute convolution integrals stably, and there is no A -stable linear multistep method with k -th order ($k > 2$) according to the second Dahlquist barrier [32].

According to [46, 47], Eq. (2.4) can be approximated as follows:

$$u_n = \Delta t \sum_{j=0}^n \omega_{n-j} g_j \quad (n = 0, \dots, N-1), \quad (2.6)$$

where $u_n \simeq u(n\Delta t)$, $g_n \simeq g(n\Delta t)$, and Δt is the time increment. In addition, N is the number of total time steps. Taking into account generating polynomials with variable ζ , the quadrature weight ω_n in Eq. (2.6) can be written as follows:

$$\Delta t \sum_{n=0}^{\infty} \omega_n \zeta^n = \mathcal{L}^{-1} \left[\hat{k}(s) \left(\frac{\gamma(\zeta)}{\Delta t} - s \right)^{-1} \right], \quad (2.7)$$

where γ is the quotient of the generating polynomial. If we use the k -th order BDF, γ is given as follows:

$$\gamma(\zeta) = \sum_{i=1}^k \frac{(1-\zeta)^i}{i}. \quad (2.8)$$

The inverse Laplace transform in Eq. (2.7) is evaluated by the residue theorem. Then, the quadrature weight ω_n can be described in the Cauchy integral form and approximated by using a trapezoidal rule with the number of steps L as follows:

$$\Delta t \omega_n = \frac{1}{2\pi i} \int_{|\zeta|=\mathcal{R}} \left[\hat{k} \left(\frac{\gamma(\zeta)}{\Delta t} \right) \right] \zeta^{-n-1} d\zeta \simeq \tilde{\mathcal{F}}_{ln}^{-1} \left[\hat{k} \left(\frac{\gamma(\zeta_l)}{\Delta t} \right) \right], \quad (2.9)$$

where the operator $\tilde{\mathcal{F}}_{ln}^{-1}$ indicates the inverse discrete Fourier transform for the CQM. The corre-

sponding forward transform $\tilde{\mathcal{F}}_{nl}$ and it are defined by

$$\tilde{\mathcal{F}}_{nl}[h_n] \equiv \mathcal{R}^l \sum_{n=0}^{N-1} h_n e^{\frac{2\pi i n l}{N}}, \quad (2.10)$$

$$\tilde{\mathcal{F}}_{ln}^{-1}[h_l] \equiv \frac{\mathcal{R}^{-n}}{L} \sum_{l=0}^{L-1} h_l e^{-\frac{2\pi i n l}{L}}. \quad (2.11)$$

In Eq. (2.9), $\zeta_l = \mathcal{R} e^{2\pi i l/L}$, and \mathcal{R} is the radius of contour integral. If we select L as $L = N$, Eqs. (2.10) and (2.11) can be evaluated by using the FFT with $O(L \log L)$ computational complexity. A specific integral path \mathcal{R} has to be selected for Eq. (2.9) and is calculated by $\mathcal{R}^L = \sqrt{\epsilon}$ with an error of magnitude $O(\sqrt{\epsilon})$, where ϵ is the error parameter of the numerical calculation of Eq. (2.9).

2.1.2. Implicit Runge-Kutta (IRK)-based CQM

Second, the formulation of the IRK-based CQM is shown. As mentioned in later, note that the IRK-based CQM involves matrix form of the quadrature weight instead of ω_n . A detailed explanation of both explicit and implicit RK methods can be found in [33].

The RK method is applied to the following initial value problem:

$$\frac{\partial y(t)}{\partial t} = f(t, y), \quad y(0) = 0. \quad (2.12)$$

Eq. (2.12) is approximated by the recursions with $y_n \simeq y(n\Delta t)$ as follows:

$$Y_{ni} = y_n + \Delta t \sum_{j=1}^m a_{ij} f((n + c_j)\Delta t, Y_{nj}) \quad (i = 1, \dots, m), \quad (2.13)$$

$$y_{n+1} = y_n + \Delta t \sum_{j=1}^m b_j f((n + c_j)\Delta t, Y_{nj}), \quad (2.14)$$

where a_{ij} , b_i , and c_i are Butcher's parameters and frequently described in the Butcher table with the stage number of RK method m as follows:

$$\left. \begin{array}{c|c} \mathbf{c} & \mathbf{A} \\ \hline & \mathbf{b}^T \end{array} \right\}, \quad \left\{ \begin{array}{l} \mathbf{A} = (a_{ij}) \quad (1 \leq i, j \leq m), \\ \mathbf{b} = (b_1, \dots, b_m)^T, \\ \mathbf{c} = (c_1, \dots, c_m)^T. \end{array} \right. \quad (2.15)$$

The approximations in Eqs. (2.13) and (2.14) are implicit when all of the upper right components of matrix \mathbf{A} are not equal to zero.

2. Convolution Quadrature Time-domain Boundary Element Method (CQ-BEM)

In this study, the Radau IIA method [33], which is one of the A -stable IRK methods with $(2m - 1)$ -th order, is used for the CQM formulation. The coefficient parameters a_{ij} , b_i , and c_i satisfy the following conditions:

$$0 < c_1 < \dots < c_m = 1, \quad b_i = a_{mi} \quad (i = 1, \dots, m). \quad (2.16)$$

Some other specific coefficients pertaining to the Radau IIA method can also be found in [33].

In order to discretize the convolution integral in Eq. (2.1), the following vectors with m components are defined as

$$U_n = (u((n + c_j)\Delta t))_{j=1}^m, \quad G_n = (g((n + c_j)\Delta t))_{j=1}^m,$$

and the generating functions $U(\zeta)$ and $G(\zeta)$ are also defined as follows:

$$U(\zeta) = \sum_{\zeta=0}^{\infty} U_n \zeta^n, \quad G(\zeta) = \sum_{\zeta=0}^{\infty} G_n \zeta^n.$$

Considering the approximation of Eq. (2.5) using the Radau IIA method and using these generating functions, Eq. (2.1) can be approximated as

$$U(\zeta) = \mathcal{L}^{-1} \left[\hat{k}(s) (\mathbf{D}(\zeta, s))^{-1} \right] G(\zeta). \quad (2.17)$$

In Eq. (2.17), $m \times m$ matrix $\mathbf{D}(\zeta, s)$ is defined by

$$\mathbf{D}(\zeta, s) = \frac{\Upsilon(\zeta)}{\Delta t} - sI, \quad (2.18)$$

$$\Upsilon(\zeta) = \left(\mathbf{1} \mathbf{b}^T \frac{\zeta}{1 - \zeta} + \mathbf{A} \right)^{-1}, \quad (2.19)$$

where I is the identity matrix, and $\mathbf{1} = (1, \dots, 1)^T$. From Eq. (2.18), $\mathbf{D}(\zeta, s)$ corresponds to the characteristic equation of $\Upsilon(\zeta)/\Delta t$. If this characteristic equation does not have any multiple roots, $(\mathbf{D}(\zeta, s))^{-1}$ has first-order poles at $s = \lambda_\beta$ ($\beta = 1, \dots, m$), where λ_β are the eigenvalues of $\Upsilon(\zeta)/\Delta t$. Therefore, the inverse Laplace transform in Eq. (2.17) can be evaluated by means of the residue theorem as follows:

$$U(\zeta) = \left[\sum_{\beta=1}^m \hat{k}(\lambda_\beta) \mathbf{E}_\beta(\zeta) \right] G(\zeta), \quad (2.20)$$

$$\mathbf{E}_\beta(\zeta) = \lim_{s \rightarrow \lambda_\beta} (\lambda_\beta - s) (\mathbf{D}(\zeta, s))^{-1} = \frac{\text{adj}(\mathbf{D}(\zeta, \lambda_\beta))}{\prod_{j=1, j \neq \beta}^m (\lambda_j - \lambda_\beta)}, \quad (2.21)$$

where $\text{adj}(\cdot)$ indicates the adjugate matrix. The modification in Eq. (2.21) can be attained by considering that $|\mathbf{D}(\zeta, s)| = \prod_{j=1}^m (\lambda_j - s)$ owing to the matrix diagonalization. Defining the n -th

step quadrature weight matrix W_n as

$$\sum_{n=0}^{\infty} W_n \zeta^n = \sum_{\beta=1}^m \hat{k}(\lambda_\beta) \mathbf{E}_\beta(\zeta), \quad (2.22)$$

the following discretized convolution formula can be obtained from Eq. (2.20) by means of the Cauchy product.

$$U_n \simeq \sum_{k=0}^n W_{n-k} G_k. \quad (2.23)$$

The quadrature weight matrix W_n can be expressed by the Cauchy integral form and approximated by using a trapezoidal rule with the number of steps L as follows:

$$W_n = \frac{1}{2\pi i} \int_{|\zeta|=\mathcal{R}} \left[\sum_{\beta=1}^m \hat{k}(\lambda_\beta) \mathbf{E}_\beta(\zeta) \right] \zeta^{-n-1} d\zeta \simeq \tilde{\mathcal{F}}_{ln}^{-1} \left[\sum_{\beta=1}^m \hat{k}(\lambda_\beta^l) \mathbf{E}_\beta(\zeta_l) \right], \quad (2.24)$$

where λ_β^l are the eigenvalues of $\Upsilon(\zeta_l)/\Delta t$. A specific integral path \mathcal{R} must be selected for Eq. (2.24) and is calculated by $\mathcal{R}^L = \sqrt{\epsilon}$ with an error of magnitude $O(\sqrt{\epsilon})$, where ϵ is the error parameter of the numerical calculation of Eq. (2.24). As presented in [4], \mathcal{R} must also be selected to avoid the issue that the characteristic equation of $\Upsilon(\zeta_l)/\Delta t$ has multiple roots.

The computational manner of λ_β^l is presented here. For $m = 2$, it is easy to exactly determine λ_β^l using the quadratic formula as follows:

$$\lambda_1^l = \frac{1}{\Delta t} \left(2 + \zeta_l + \sqrt{\zeta_l^2 + 10\zeta_l - 2} \right), \quad \lambda_2^l = \frac{1}{\Delta t} \left(2 + \zeta_l - \sqrt{\zeta_l^2 + 10\zeta_l - 2} \right).$$

Therefore, \mathcal{R} must be selected to avoid $\zeta_l^2 + 10\zeta_l - 2 = 0$ (multiple roots) for $m = 2$ as presented in [4]. Similarly, the determination of λ_β^l for $m = 3$ and 4 can be implemented by using the corresponding formulas. However, from a numerical point of view, some rounding errors are introduced when $m \geq 3$ (especially for large m). Therefore, an iterative decomposition must be used to calculate λ_β^l in order to avoid this issue. In this study, the QR algorithm is used for the evaluation of λ_β^l because $\Upsilon(\zeta_l)/\Delta t$ usually becomes an asymmetric complex matrix.

The derivation of IRK-based CQM formulation presented in this paper is a little different from [4, 7], and they have decomposed the quadrature weight matrix after evaluation of the inverse Laplace transform. In this study, we evaluate the inverse Laplace transform after the decomposition of the matrix $\mathbf{D}(\zeta, s)$. The presented derivation is valid if $\hat{k}(s)$ is an analytic function for $\Re[s] > 0$ and the characteristic equation of $\Upsilon(\zeta)/\Delta t$ does not have any multiple roots, where $\Re[z]$ denotes the real part of complex value z . The resulting quadrature weight W_n is identical to the one in [4, 7].

2. Convolution Quadrature Time-domain Boundary Element Method (CQ-BEM)

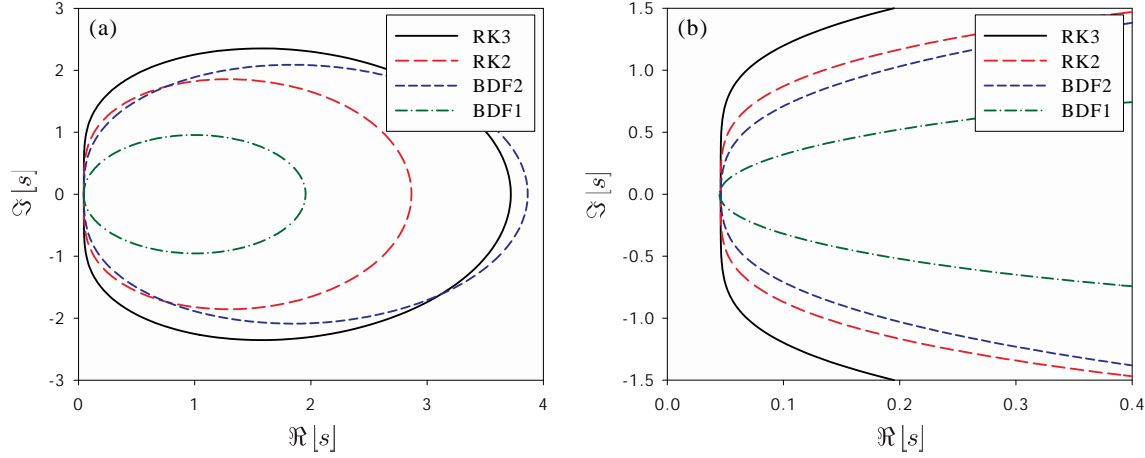


Figure 2.1.: (a) Overall picture and (b) enlarged view around the origin of Laplace parameters s required for CQMs with RK_m and BDF_k using computational parameters in Table 2.1.

Table 2.1.: Computational parameters used for calculating Laplace parameters s in Fig. 2.1.

	RK3	RK2	BDF2	BDF1
L	100	150	300	300
Δt	3.0	2.0	1.0	1.0
\mathcal{R}	0.871	0.933	0.955	0.955

2.1.3. Behavior of Laplace parameter

The arguments of Laplace-domain kernel $\gamma(\zeta_l)/\Delta t$ and λ_β^l correspond to the Laplace parameter s in the linear multistep- and IRK-based CQMs, respectively. Their behavior significantly effects on the accuracy because they correspond to the circular frequencies in frequency-domain. In addition, considering the conjugate features of $\gamma(\zeta_l)/\Delta t$ and λ_β^l , we can reduce the computation number of quadrature weights in the CQM formulation to about half. Hereinafter, BDF_k and RK_m indicate the k th order BDF- and the m -stage IRK-based CQM or CQ-BEM, respectively.

Laplace parameters s which are required for the various CQMs are shown in Fig. 2.1 when $\epsilon = 10^{-12}$ and computational parameters in Table 2.1 are used. $\Re[z]$ and $\Im[z]$ indicate the real and imaginary parts of z , respectively. As we can see from Fig. 2.1 (a), some s are complex conjugate of others. Specifically, $\gamma(\zeta_{L-l}) = \overline{\gamma(\zeta_l)}$ and $\lambda_\beta^{L-l} = \overline{\lambda_\beta^l}$ for $l = 1, \dots, L/2 - 1$, where $\overline{(\cdot)}$ indicates complex conjugate. Therefore, we need to compute $\gamma(\zeta_l)/\Delta t$ or λ_β^l only for $l = 0, \dots, L/2$.

The behavior of s around the imaginary axis is important for the construction of time-domain original kernel $k(t)$ with high frequency components because $\Im[s]$ and $\Re[s]$ correspond to the circular frequency and attenuation, respectively. As shown in Fig. 2.1 (b), higher frequency components near the imaginary axis are contained in RK3 and RK2 than in BDF2 and BDF1. This comparison is conducted under the same division number 300 for the same time range $[0, 300]$ as shown in Table 2.1. Therefore, it is expected that the performance of IRK-based CQM is better in accuracy

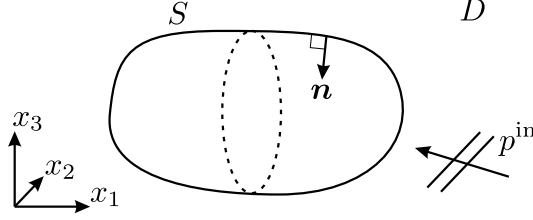


Figure 2.2.: Analysis model for acoustic wave scattering by an obstacle in a 3-D infinite domain.

for high frequency components than that of linear multistep-based one. Hereinafter, ϵ is taken to be $\epsilon = 10^{-12}$ for all numerical simulations.

2.2. CQ-BEM for 3-D acoustic wave problems

The application of the IRK-based CQM to the TD-BEM for 3-D acoustic wave problems is presented. The IRK-based CQ-BEM has been developed by Maruyama *et al.* [51] and Banjai *et al.* [7]. The detailed formulation of the linear multistep-based CQ-BEM can be found in the reference papers [75, 58], and it is omitted here.

2.2.1. Formulation of boundary integral equation (BIE)

Let S be a closed boundary with unit normal vector \mathbf{n} in \mathbb{R}^3 as depicted in Fig. 2.2. D is an exterior domain, which can be considered as an incompressible and non-viscous fluid. The pressure p satisfies the following wave equation:

$$c_f^2 \nabla^2 p(\mathbf{x}, t) - \ddot{p}(\mathbf{x}, t) = 0 \quad \mathbf{x} \in D, \quad (2.25)$$

where c_f is the velocity of wave propagation in D , and $(\dot{})$ indicates the partial differentiation with respect to time t . We assume the following initial condition:

$$p^{\text{sc}}(\mathbf{x}, 0) = \dot{p}^{\text{sc}}(\mathbf{x}, 0) \quad \mathbf{x} \in D, \quad (2.26)$$

where the superscript "sc" indicates the scattered wave. Considering the Sommerfeld radiation condition for scattered waves and initial condition (2.26), the time-domain BIE for pressure p is formulated by means of the usual manner as follows:

$$\begin{aligned} C(\mathbf{x})p(\mathbf{x}, t) = & p^{\text{in}}(\mathbf{x}, t) + \int_0^t \int_S G(\mathbf{x}, \mathbf{y}, t - \tau) q(\mathbf{y}, \tau) dS_y d\tau \\ & - \int_0^t \text{p.v.} \int_S H(\mathbf{x}, \mathbf{y}, t - \tau) p(\mathbf{y}, \tau) dS_y d\tau \quad \mathbf{x} \in S, \end{aligned} \quad (2.27)$$

where the superscript "in" indicates the incident wave, $C(\mathbf{x})$ is the free term [14] depending on the boundary shape at \mathbf{x} , and q is the normal derivative of p . G is the fundamental solution of pressure

2. Convolution Quadrature Time-domain Boundary Element Method (CQ-BEM)

for 3-D acoustic wave problems in time-domain, and H is its normal derivative. In addition, the symbol p.v. indicates the Cauchy principal integral.

2.2.2. Discretization of BIE

The discretization of BIE (2.27) using the IRK-based CQM is presented. The collocation method and piecewise constant approximation are utilized for spatial discretization. If the m -stage Radau IIA method is used and the boundary S is divided into M_e boundary elements, the discretized BIE at n -th and i -th sub-step in time is written as follows:

$$\frac{1}{2}p_{\gamma}^{i;n} = p_{\gamma}^{\text{in};i;n} + \sum_{k=0}^n \sum_{\alpha=1}^{M_e} \sum_{j=1}^m \left[\mathcal{G}_{\gamma\alpha}^{ij;n-k} q_{\alpha}^{j;k} - \mathcal{H}_{\gamma\alpha}^{ij;n-k} p_{\alpha}^{j;k} \right] \quad (i = 1, \dots, m), \quad (n = 0, \dots, N-1), \quad (2.28)$$

where

$$u_{\gamma}^{i;n} = u(\mathbf{x}_{\gamma}, (n + c_i)\Delta t) \quad (u = p, q, \text{ or } p^{\text{in}}),$$

α and γ indicate the indices of a boundary element, and \mathbf{x}_{γ} denotes the collocation point of γ -th element. The collocation point is selected as the barycenter of element. In addition, $\mathcal{G}_{\gamma\alpha}^{ij;\kappa}$ and $\mathcal{H}_{\gamma\alpha}^{ij;\kappa}$ are the influence functions defined by

$$\mathcal{G}_{\gamma\alpha}^{ij;\kappa} = \tilde{\mathcal{F}}_{l\kappa}^{-1} \left[\sum_{\beta=1}^m \left(\mathbf{E}_{\beta}(\zeta_l) \right)_{ij} \int_{S_{\alpha}} \hat{G}(\mathbf{x}_{\gamma}, \mathbf{y}, \lambda_{\beta}^l) dS_y \right], \quad (2.29)$$

$$\mathcal{H}_{\gamma\alpha}^{ij;\kappa} = \tilde{\mathcal{F}}_{l\kappa}^{-1} \left[\sum_{\beta=1}^m \left(\mathbf{E}_{\beta}(\zeta_l) \right)_{ij} \text{p.v.} \int_{S_{\alpha}} \hat{H}(\mathbf{x}_{\gamma}, \mathbf{y}, \lambda_{\beta}^l) dS_y \right], \quad (2.30)$$

where S_{α} is the surface of α -th element. In Eqs. (2.29) and (2.30), \hat{G} and \hat{H} are the Laplace-domain fundamental solutions for pressure and its normal derivative, respectively, and given as follows:

$$\hat{G}(\mathbf{x}, \mathbf{y}, s) = \frac{e^{-s_f r}}{4\pi r}, \quad (2.31)$$

$$\hat{H}(\mathbf{x}, \mathbf{y}, s) = \mathbf{n}(\mathbf{y}) \cdot \nabla_{\mathbf{y}} \hat{G}(\mathbf{x}, \mathbf{y}, s), \quad (2.32)$$

where $r = |\mathbf{y} - \mathbf{x}|$, $\nabla_{\mathbf{y}} = (\partial/\partial y_1, \partial/\partial y_2, \partial/\partial y_3)$, and $s_f = s/c_f$. Note that the integral kernels \hat{G} and \hat{H} in Eqs. (2.29) and (2.30) do not depend on time t . Rearranging Eq. (2.28) according to the time step, the following expression is obtained:

$$\begin{aligned}
& \sum_{\alpha=1}^{M_e} \sum_{j=1}^m \left[\left(\frac{1}{2} \delta_{\gamma\alpha} \delta_{ij} + \mathcal{H}_{\gamma\alpha}^{ij;0} \right) p_{\alpha}^{j;n} - \mathcal{G}_{\gamma\alpha}^{ij;0} q_{\alpha}^{j;n} \right] \\
& = p_{\gamma}^{\text{in};i;n} - \sum_{k=0}^{n-1} \sum_{\alpha=1}^{M_e} \sum_{j=1}^m \left[\mathcal{H}_{\gamma\alpha}^{ij;n-k} p_{\alpha}^{j;k} - \mathcal{G}_{\gamma\alpha}^{ij;n-k} q_{\alpha}^{j;k} \right], \quad (2.33)
\end{aligned}$$

where δ_{ij} is the Kronecker delta.

For the n -th time step, all of the quantities on the right-hand side of Eq. (2.33) are known. Therefore, the unknown values p and q at the n -th time step can be obtained by solving Eq. (2.33). In Eq. (2.33), the total number of unknowns is mM_eN . Therefore, the computational time is proportional to $O(m^2N^2M_e^2)$ order without any acceleration techniques even if we use an iterative solver, such as the Krylov subspace method [95].

2.3. Numerical results

For numerical examples, a scattering problem as depicted in Fig. 2.3 is numerically solved to compare the accuracy between the linear multistep- and IRK-based CQ-BEMs. An incident plane wave is scattered by a rigid sphere with radius a , and the pressure fields at the point X in Fig. 2.3 are investigated using different time increments. The boundary condition on S is given by $q = 0$ here. The following plane wave with amplitude p_0 propagating in x_1 -direction is used as an incident plane wave.

$$\begin{cases} p^{\text{in}}(\mathbf{x}, t) = p_0 (1 - \cos 2\pi \Lambda_f) H(\Lambda_f) H(1 - \Lambda_f), \\ \Lambda_f = \frac{c_f t - (x_1 + a)}{\lambda_f^{\text{in}}}, \end{cases} \quad (2.34a)$$

$$\Lambda_f = \frac{c_f t - (x_1 + a)}{\lambda_f^{\text{in}}}, \quad (2.34b)$$

where λ_f^{in} is the wavelength corresponding to the center frequency of the incident wave, and $H(\cdot)$ is the Heaviside function. The surface of a sphere is discretized into $M_e = 3176$ flatly triangular boundary elements, and λ_f^{in} is given by $\lambda_f^{\text{in}}/a = 1.0$. This problem has been analytically solved in the frequency-domain by Pao and Mow [67]. Therefore, the transient solutions, which are hereinafter called the "reference solutions", can be constructed by using the inverse Fourier transform of the frequency-domain analytical solutions.

The time variations of pressure p/p_0 at point X in Fig. 2.3 obtained by BDF1, BDF2, RK2, and RK3 are shown for different time increments in Figs. 2.4, 2.5, 2.6, and 2.7, respectively. As seen in Fig. 2.4, the BDF1 cannot yield accurate results even if the smallest time increment $c_f \Delta t/a = 0.0087$ is used. In particular, the amplitude of p/p_0 at $c_f t/a = 1$ to 2 is different from the reference solutions, and large oscillation at $c_f t/a = 4$ to 8 is observed. In additions, the oscillation at $c_f t/a = 4$ to 8 is hardly improved with decreasing time increments. Consequently, it is considered as difficult to compute p/p_0 accurately using the BDF1.

As seen in Fig. 2.5, the BDF2 with the smallest time increment $c_f \Delta t/a = 0.0087$, can yield good

2. Convolution Quadrature Time-domain Boundary Element Method (CQ-BEM)

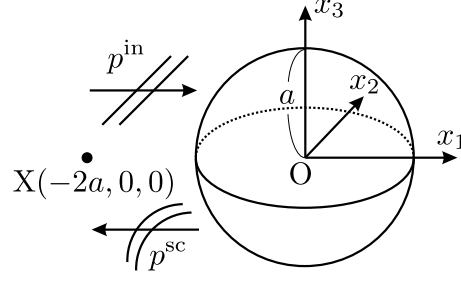


Figure 2.3.: Acoustic wave scattering by a rigid sphere subjected to an incident plane wave.

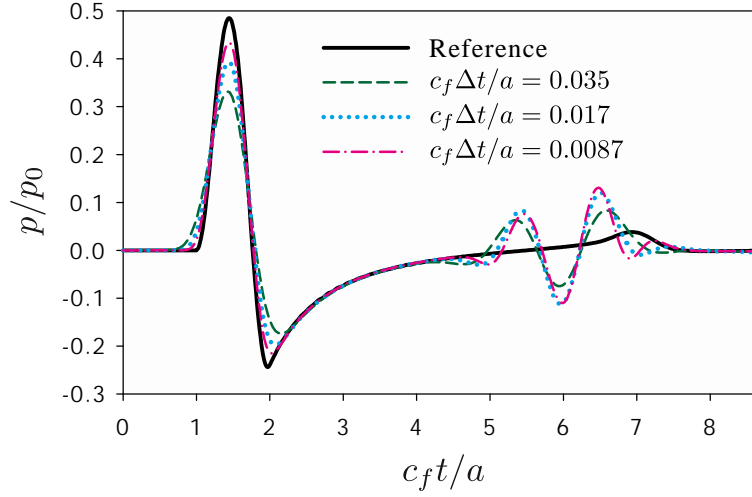


Figure 2.4.: Time variations of p/p_0 obtained by using BDF1 at point X in Fig. 2.3.

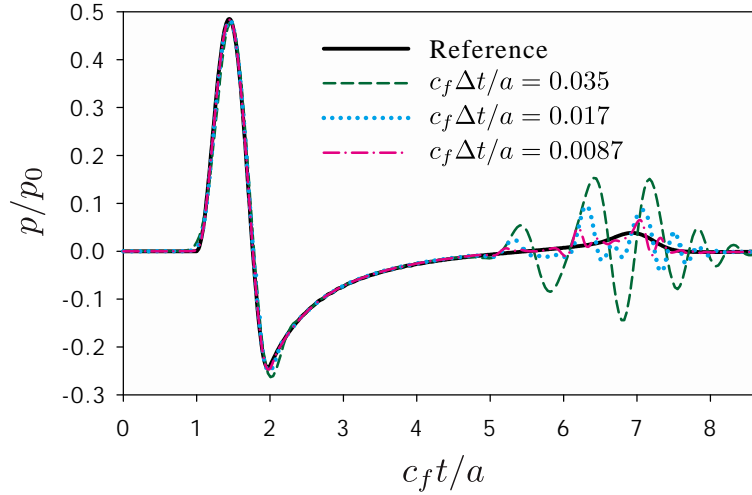
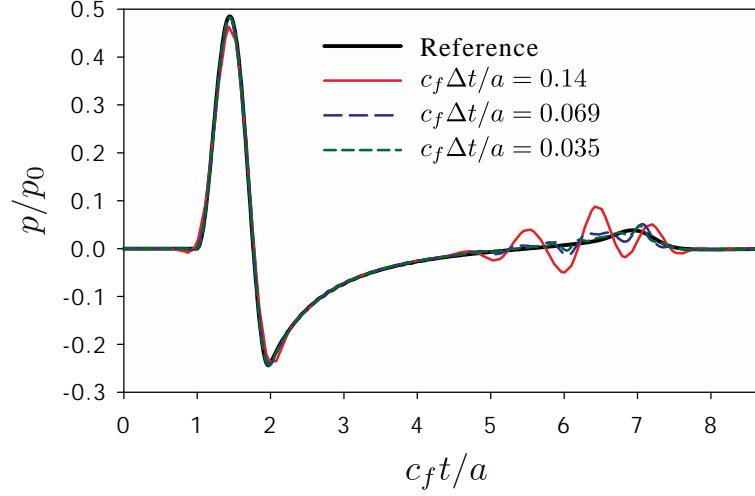
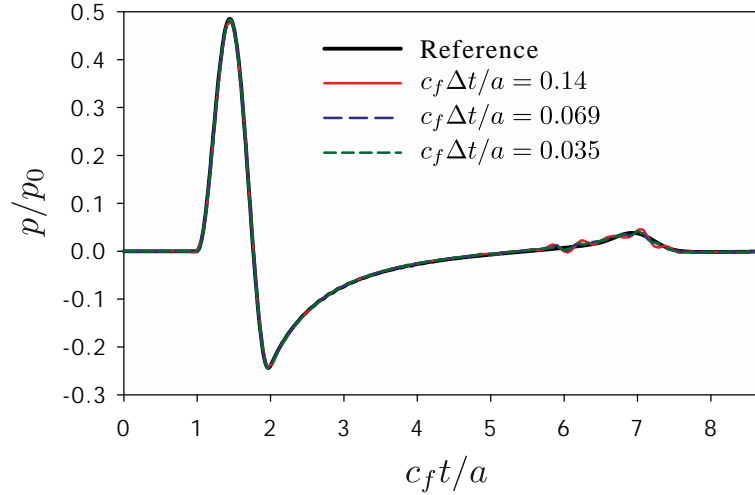


Figure 2.5.: Time variations of p/p_0 obtained by using BDF2 at point X in Fig. 2.3.

results at the time up to $c_f t/a = 5$. However, p/p_0 is not accurate compared with the reference solutions after $c_f t/a = 5$, and fluctuations can be seen clearly. In particular, larger time increments,

Figure 2.6.: Time variations of p/p_0 obtained by using RK2 at point X in Fig. 2.3.Figure 2.7.: Time variations of p/p_0 obtained by using RK3 at point X in Fig. 2.3.

e.g., $c_T \Delta t/a = 0.035$ or 0.017 , give less accurate results. As a result, a small time increment is required for accurate computation of p/p_0 for the time range between $c_f t/a = 5$ to 8 .

As shown in Figs. 2.6 and 2.7, much more accurate results can be obtained by the RK2 and RK3 for the cases of $c_f \Delta t/a = 0.035$ than the BDF2. The fluctuations of p/p_0 increase with increasing time increments. p/p_0 calculated by the RK2 and RK3 using $c_f \Delta t/a = 0.035$ seem to be sufficiently accurate. From the above, the selection of time increments is important, and it has a strong influence on the scattered waves obtained by the CQ-BEM. Therefore, an adequately small time increment must be chosen to obtain sufficiently accurate results for practical engineering applications.

2.4. Concluding remarks

- In Chapter 2, we have explained both linear multistep- and IRK-based CQMs and successfully applied them to the TD-BEM for 3-D acoustic wave problems. To simplify and focus on the time discretization, the collocation method and piecewise constant approximation have been used for the spatial discretization.
- It was confirmed that there is large difference in the behavior of Laplace parameters s among schemes which are used for CQM formulations. This difference, especially behavior near the imaginary axis, is greatly concerned with the available range of circular frequencies. It seems that the single-step methods, such as RK methods have some advantages in the calculation of high frequency components. This is because the influence functions for wave problems contain very rapid fluctuation.
- The BDF1 cannot yield accurate solutions even if the small time increment is used, and better numerical solutions have been obtained by the BDF2 with the small time increment. However, the performance of IRK-based CQ-BEM is much better in accuracy than that of linear multistep-based one when the same number of discretization points are used for the same time range.
- The computational complexity and required memory of IRK-based CQ-BEM without any acceleration techniques are $O(m^2 N^2 M_e^2)$ even if an iterative solver is used.

Chapter 3

Acceleration of CQ-BEM

It is difficult to solve large-scale problems using the CQ-BEM without any acceleration techniques because its computational and memory complexities are $O(m^2 M_e^2 N^2)$ as shown in the previous chapter. Therefore, we present some acceleration techniques for the CQ-BEM in this chapter. First, application of the FMM [72, 26] to the CQ-BEM is explained. Then, the formulations of CQ-FMBEM for 3-D acoustic wave, elastic wave, and their coupling problems, which have been developed by Maruyama *et al.* [52, 53], are shown. Finally, we apply the rapid convolution algorithm using FFT [31] to the CQ-FMBEM for 3-D acoustic wave problems and demonstrate the computational complexity of our proposed method through some numerical results.

3.1. Fast multipole accelerated CQ-BEM (CQ-FMBEM)

The FMM is applied to the IRK-based CQ-BEM to achieve stable, accurate, and efficient calculation for large-scale wave propagation problems. In what follows, we present the time-marching process of the IRK-based CQ-FMBEM, the multipole and local expansions, and translation theorems. In addition, scaling and truncation techniques for the IRK-based CQ-FMBEM are introduced in order to enhance the stability and efficiency of the proposed method.

3.1.1. Time-marching process

Application of the FMM to the IRK-based CQ-BEM complicates the time-marching process because the influence functions defined in Eqs. (2.29) and (2.30) include the inverse discrete Fourier transforms in Eq. (2.11). The time-marching process for the terms including $\mathcal{G}_{\gamma\alpha}^{ij;\kappa}$ in the right-hand side of Eq. (2.33) is explained as an example. The retarded potential vector with mM_e components \mathbf{R}^n is defined by

$$(\mathbf{R}^n)_{m(\gamma-1)+i} = \sum_{k=0}^{n-1} \sum_{\alpha=1}^{M_e} \sum_{j=1}^m \mathcal{G}_{\gamma\alpha}^{ij;n-k} q_{\alpha}^{j;k} = \left(\sum_{k=0}^{n-1} \mathbf{G}^{n-k} \mathbf{q}^k \right)_{m(\gamma-1)+i}. \quad (3.1)$$

The multiplication of $mM_e \times mM_e$ matrix and mM_e dimensional vector is written by $\mathbf{G}^{n-k} \mathbf{t}^k$ here. To evaluate \mathbf{R}_{γ}^n using the FMM, the inverse discrete Fourier transform and the summations in Eqs.

3. Acceleration of CQ-BEM

(2.29) and (2.33) are rearranged as follows:

$$\begin{aligned} (\mathbf{G}^\kappa \mathbf{q}^k)_{m(\gamma-1)+i} &= \sum_{\alpha=1}^{M_e} \sum_{j=1}^m \tilde{\mathcal{F}}_{l\kappa}^{-1} \left[\sum_{\beta=1}^m (\mathbf{E}_\beta(\zeta_l))_{ij} \int_{S_\alpha} \hat{G}(\mathbf{x}_\gamma, \mathbf{y}, \lambda_\beta^l) dS_y \right] q_\alpha^{j;k} \\ &= \tilde{\mathcal{F}}_{l\kappa}^{-1} \left[\sum_{\beta=1}^m \left\{ \sum_{\alpha=1}^{M_e} \hat{G}_{\gamma\alpha}^{\beta;l} q_\alpha^{i;k;\beta;l} \right\} \right], \end{aligned} \quad (3.2)$$

where

$$\hat{G}_{\gamma\alpha}^{\beta;l} = \int_{S_\alpha} \hat{G}(\mathbf{x}_\gamma, \mathbf{y}, \lambda_\beta^l) dS_y, \quad q_\alpha^{i;k;\beta;l} = \sum_{j=1}^m (\mathbf{E}_\beta(\zeta_l))_{ij} q_\alpha^{j;k}.$$

The term inside braces $\{ \}$ in Eq. (3.2) is first calculated for all of γ , β , i , and l via the FMM. Then, taking the summation with respect to β and evaluating the inverse discrete Fourier transform, $\mathbf{G}^\kappa \mathbf{q}^k$ for all κ ($\kappa = 0, \dots, N-1$) are obtained. Finally, the corresponding retarded potential vector $\mathbf{R}^{k+\kappa}$ is updated. This calculation can be expressed in the following matrix form:

$$\begin{Bmatrix} \mathbf{R}^1 \\ \mathbf{R}^2 \\ \mathbf{R}^3 \\ \vdots \\ \mathbf{R}^{N-1} \end{Bmatrix} = \begin{bmatrix} \mathbf{G}^1 & & & & \\ \mathbf{G}^2 & \mathbf{G}^1 & & & 0 \\ \mathbf{G}^3 & \mathbf{G}^2 & \mathbf{G}^1 & & \\ \vdots & & & \ddots & \\ \mathbf{G}^{N-1} & \dots & & & \mathbf{G}^1 \end{bmatrix} \begin{Bmatrix} \mathbf{q}^0 \\ \mathbf{q}^1 \\ \mathbf{q}^2 \\ \vdots \\ \mathbf{q}^{N-2} \end{Bmatrix}. \quad (3.3)$$

Once a set of the boundary values \mathbf{q}^k at k -th step is obtained by solving Eq. (2.33), $\mathbf{G}^\kappa \mathbf{q}^k$ for all κ can be calculated. Then, the resulting vectors are added into \mathbf{R}^n for the rest time steps ($n = k+1, \dots, N-1$) as $\mathbf{R}^n + \mathbf{G}^{n-k} \mathbf{q}^k \Rightarrow \mathbf{R}^n$. If this procedure is conducted at each time step, \mathbf{R}^n is updated for the next time step calculation. Note that Cauchy data $q_\alpha^{j;k}$ are treated in time-domain although the FMM is implemented in Laplace-domain. In this algorithm, the FMM is implemented for $l = 0, \dots, L/2$ at each time step owing to the following relation:

$$\sum_{\beta=1}^m \left\{ \sum_{\alpha=1}^{M_e} \hat{G}_{\gamma\alpha}^{\beta;L-l} q_\alpha^{i;k;\beta;L-l} \right\} = \overline{\sum_{\beta=1}^m \left\{ \sum_{\alpha=1}^{M_e} \hat{G}_{\gamma\alpha}^{\beta;l} q_\alpha^{i;k;\beta;l} \right\}} \quad (l = 1, \dots, L/2 - 1).$$

The terms including $\mathcal{H}_{\gamma\alpha}^{ij;\kappa}$ in Eq. (2.33) can be evaluated as well as $\mathcal{G}_{\gamma\alpha}^{ij;\kappa}$.

3.1.2. Fast multipole method (FMM)

In Eq. (3.2), the FMM is implemented for the Laplace-domain fundamental solutions. The multipole and local expansions for Laplace-domain fundamental solutions can be derived as well as those in frequency-domain [23]. The FMM formulation based on Wigner 3- j symbol [57] with $O(N_t^3)$ arithmetic complexity [28] is used in this study, where N_t is the truncation number of infinite sum-

mations in multipole and local expansions.

Multipole and local expansions

The expansions of fundamental solution of modified Helmholtz equation corresponding to some wave velocities are required for the derivation of multipole and local expansions for elastic wave problems in Section 3.1.6. Therefore, the expansions of \hat{G}^φ , which is the fundamental solution of the modified Helmholtz equation with wave velocity c_φ , are shown here. Note that \hat{G} in Eq. (2.31) is $\hat{G} = \hat{G}^f$. According to [23], the expansions of \hat{G}^φ are given by

$$\hat{G}^\varphi(\mathbf{x}, \mathbf{y}, s) = \sum_{a=0}^{\infty} \sum_{b=-a}^a \frac{s_\varphi(2a+1)}{4\pi} \times \begin{cases} \bar{F}_{a,b}^\varphi(\mathbf{y} - \mathbf{y}_0) O_{a,b}^\varphi(\mathbf{x} - \mathbf{y}_0) & \text{for } |\mathbf{y} - \mathbf{y}_0| \leq |\mathbf{x} - \mathbf{y}_0|, \\ \bar{O}_{a,b}^\varphi(\mathbf{y} - \mathbf{x}_0) F_{a,b}^\varphi(\mathbf{x} - \mathbf{x}_0) & \text{for } |\mathbf{y} - \mathbf{x}_0| > |\mathbf{x} - \mathbf{x}_0|, \end{cases} \quad (3.4a)$$

where $s_\varphi = s/c_\varphi$, and $F_{a,b}^\varphi(\mathbf{x})$, $\bar{F}_{a,b}^\varphi(\mathbf{x})$, $O_{a,b}^\varphi(\mathbf{x})$, and $\bar{O}_{a,b}^\varphi(\mathbf{x})$ are defined by

$$F_{a,b}^\varphi(\mathbf{x}) = i_a(s_\varphi|\mathbf{x}|)Y_a^b(\hat{\mathbf{x}}), \quad \bar{F}_{a,b}^\varphi(\mathbf{x}) = i_a(s_\varphi|\mathbf{x}|)\overline{Y_a^b(\hat{\mathbf{x}})}, \quad (3.5)$$

$$O_{a,b}^\varphi(\mathbf{x}) = k_a(s_\varphi|\mathbf{x}|)Y_a^b(\hat{\mathbf{x}}), \quad \bar{O}_{a,b}^\varphi(\mathbf{x}) = k_a(s_\varphi|\mathbf{x}|)\overline{Y_a^b(\hat{\mathbf{x}})}. \quad (3.6)$$

In Eqs. (3.5) and (3.6), $\hat{\mathbf{x}} = \mathbf{x}/|\mathbf{x}|$, and i_a and k_a are the modified spherical Bessel functions of the first and second kinds, respectively. Y_a^b are the spherical harmonics which are defined by

$$Y_a^b(\hat{\mathbf{x}}) = \sqrt{\frac{(a-b)!}{(a+b)!}} P_a^b(\cos \theta) e^{ib\phi}, \quad (3.7)$$

where θ and ϕ are the *zenith* and *azimuthal* angles of $\hat{\mathbf{x}}$ in the spherical coordinate system, respectively, and P_a^b is the associated Legendre function.

In order to derive the multipole and local expansions, $G_{\gamma\alpha}^{i;k;\beta;l}$ and $H_{\gamma\alpha}^{i;k;\beta;l}$ are defined by

$$G_{\gamma\alpha}^{i;k;\beta;l} = \left[\int_{S_\alpha} \hat{G}^\varphi(\mathbf{x}_\gamma, \mathbf{y}, \lambda_\beta^l) dS_y \right] \mathbf{q}_\alpha^{i;k;\beta;l}, \quad (3.8)$$

$$H_{\gamma\alpha}^{i;k;\beta;l} = \left[\int_{S_\alpha} \hat{H}^\varphi(\mathbf{x}_\gamma, \mathbf{y}, \lambda_\beta^l) dS_y \right] \mathbf{p}_\alpha^{i;k;\beta;l}, \quad (3.9)$$

where \hat{H}^φ is the normal derivative of \hat{G}^φ , and

$$\mathbf{p}_\alpha^{i;k;\beta;l} = \sum_{j=1}^m \left(\mathbf{E}_\beta(\zeta_l) \right)_{ij} p_\alpha^{j;k}.$$

In Eq. (3.9), the symbol p.v. is omitted because γ (field point) is never equal to α (source point) in an FMM far-field calculation. Substituting Eq. (3.4a) into Eqs. (3.8) and (3.9) yields the following

3. Acceleration of CQ-BEM

multipole expansions:

$$\mathbf{G}_{\gamma\alpha}^{i;k;\beta;l} = \sum_{a=0}^{\infty} \sum_{b=-a}^a \frac{s_{\varphi}(2a+1)}{4\pi} \left[\mathbf{O}_{a,b}^{\varphi}(\mathbf{x}_{\gamma} - \mathbf{y}_0) M_{a,b;\alpha}^{G;i;k;\beta;l}(\mathbf{y}_0) \right]_{s=\lambda_{\beta}^l}, \quad (3.10)$$

$$\mathbf{H}_{\gamma\alpha}^{i;k;\beta;l} = \sum_{a=0}^{\infty} \sum_{b=-a}^a \frac{s_{\varphi}(2a+1)}{4\pi} \left[\mathbf{O}_{a,b}^{\varphi}(\mathbf{x}_{\gamma} - \mathbf{y}_0) M_{a,b;\alpha}^{H;i;k;\beta;l}(\mathbf{y}_0) \right]_{s=\lambda_{\beta}^l}, \quad (3.11)$$

where $M_{a,b;\alpha}^{G;i;k;\beta;l}$ and $M_{a,b;\alpha}^{H;i;k;\beta;l}$ are the multipole moments with respect to \hat{G}^{φ} and \hat{H}^{φ} , respectively. The infinite summations in Eqs. (3.10) and (3.11) are truncated by N_t terms in the numerical simulation. The explicit expressions of the multipole moments in Eqs. (3.10) and (3.11) are written as follows:

$$M_{a,b;\alpha}^{G;i;k;\beta;l}(\mathbf{y}_0) = \mathbf{q}_{\alpha}^{i;k;\beta;l} \int_{S_{\alpha}} \bar{F}_{a,b}^{\varphi}(\mathbf{y} - \mathbf{y}_0) dS_y, \quad (3.12)$$

$$M_{a,b;\alpha}^{H;i;k;\beta;l}(\mathbf{y}_0) = \mathbf{p}_{\alpha}^{i;k;\beta;l} \int_{S_{\alpha}} \mathbf{n}(\mathbf{y}) \cdot \nabla_y \bar{F}_{a,b}^{\varphi}(\mathbf{y} - \mathbf{y}_0) dS_y. \quad (3.13)$$

Note that all multipole moments can be evaluated independently on a field point \mathbf{x}_{γ} .

The local expansions for $\mathbf{G}_{\gamma\alpha}^{i;k;\beta;l}$ and $\mathbf{H}_{\gamma\alpha}^{i;k;\beta;l}$ are obtained by substituting Eq. (3.4b) into Eqs. (3.8) and (3.9) as follows:

$$\mathbf{G}_{\gamma\alpha}^{i;k;\beta;l} = \sum_{a=0}^{\infty} \sum_{b=-a}^a \frac{s_{\varphi}(2a+1)}{4\pi} \left[\mathbf{F}_{a,b}^{\varphi}(\mathbf{x}_{\gamma} - \mathbf{x}_0) L_{a,b;\alpha}^{G;i;k;\beta;l}(\mathbf{x}_0) \right]_{s=\lambda_{\beta}^l}, \quad (3.14)$$

$$\mathbf{H}_{\gamma\alpha}^{i;k;\beta;l} = \sum_{a=0}^{\infty} \sum_{b=-a}^a \frac{s_{\varphi}(2a+1)}{4\pi} \left[\mathbf{F}_{a,b}^{\varphi}(\mathbf{x}_{\gamma} - \mathbf{x}_0) L_{a,b;\alpha}^{H;i;k;\beta;l}(\mathbf{x}_0) \right]_{s=\lambda_{\beta}^l}, \quad (3.15)$$

where $L_{a,b;\alpha}^{G;i;k;\beta;l}$ and $L_{a,b;\alpha}^{H;i;k;\beta;l}$ are the coefficients of local expansion. The coefficients of local expansion can be obtained by replacing $\bar{F}_{a,b}^{\varphi}(\mathbf{y} - \mathbf{y}_0)$ by $\bar{O}_{a,b}^{\varphi}(\mathbf{y} - \mathbf{x}_0)$ in Eqs. (3.12) and (3.13) as follows:

$$L_{a,b;\alpha}^{G;i;k;\beta;l}(\mathbf{x}_0) = \mathbf{q}_{\alpha}^{i;k;\beta;l} \int_{S_{\alpha}} \bar{O}_{a,b}^{\varphi}(\mathbf{y} - \mathbf{x}_0) dS_y, \quad (3.16)$$

$$L_{a,b;\alpha}^{H;i;k;\beta;l}(\mathbf{x}_0) = \mathbf{p}_{\alpha}^{i;k;\beta;l} \int_{S_{\alpha}} \mathbf{n}(\mathbf{y}) \cdot \nabla_y \bar{O}_{a,b}^{\varphi}(\mathbf{y} - \mathbf{x}_0) dS_y. \quad (3.17)$$

Translation theorems (M2M, M2L, and L2L)

In the FMM algorithm, multipole expansion to multipole expansion (M2M), multipole expansion to local expansion (M2L), and local expansion to local expansion (L2L), are required [62]. These three translation theorems for \hat{G}^{φ} are described by the following equations for the schematic depicted in Fig. 3.1:

$$\text{M2M : } M_{a,b;\alpha}^{G;i;k;\beta;l}(\mathbf{y}_1) = \sum_{c=0}^{\infty} \sum_{d=-c}^c (\text{M|M})_{a,c}^{b,d}(\mathbf{y}_0 \rightarrow \mathbf{y}_1; s_{\varphi}) M_{c,d;\alpha}^{G;i;k;\beta;l}(\mathbf{y}_0), \quad (3.18)$$

$$\text{M2L : } L_{a,b;\alpha}^{G;i;k;\beta;l}(\mathbf{x}_1) = \sum_{c=0}^{\infty} \sum_{d=-c}^c (\text{M|L})_{a,c}^{b,d}(\mathbf{y}_1 \rightarrow \mathbf{x}_1; s_{\varphi}) M_{c,d;\alpha}^{G;i;k;\beta;l}(\mathbf{y}_1), \quad (3.19)$$

$$\text{L2L : } L_{a,b;\alpha}^{G;i;k;\beta;l}(\mathbf{x}_0) = \sum_{c=0}^{\infty} \sum_{d=-c}^c (\text{L|L})_{a,c}^{b,d}(\mathbf{x}_1 \rightarrow \mathbf{x}_0; s_{\varphi}) L_{c,d;\alpha}^{G;i;k;\beta;l}(\mathbf{x}_1). \quad (3.20)$$

If $M_{a,b;\alpha}^{G;i;k;\beta;l}$ and $L_{a,b;\alpha}^{G;i;k;\beta;l}$ in Eqs. (3.18)–(3.20) are replaced with $M_{a,b;\alpha}^{H;i;k;\beta;l}$ and $L_{a,b;\alpha}^{H;i;k;\beta;l}$, respectively, the translation formulas for \hat{H}^{φ} are derived. In Eqs. (3.18)–(3.20), $(\text{E|F})_{a,c}^{b,d}$ ($\text{E}, \text{F} = \text{M}$ or L) are the translation operators including Wigner 3- j symbol. The operator $(\text{E|F})_{a,c}^{b,d}$ can be calculated recursively in $O(N_t^4)$ arithmetic complexity [28]. Eqs. (3.18)–(3.20) can be recast using the orthogonalization of spherical harmonics in $O(N_t^3)$ arithmetic complexity:

$$\left\{ \begin{array}{l} \tilde{M}_{a,d;\alpha}^{G;i;k;\beta;l}(\mathbf{y}_0) = \sum_{b=-a}^a M_{a,b;\alpha}^{G;i;k;\beta;l}(\mathbf{y}_0) D_{db}^a(\mathbf{R}^T), \end{array} \right. \quad (3.21a)$$

$$\left\{ \begin{array}{l} \tilde{M}_{c,d;\alpha}^{G;i;k;\beta;l}(\mathbf{y}_1) = \sum_{a=|d|}^{\infty} (\text{M|M})_{c,a}^d(\mathbf{y}_0 \rightarrow \mathbf{y}_1; s_{\varphi}) \tilde{M}_{a,d;\alpha}^{G;i;k;\beta;l}(\mathbf{y}_0), \end{array} \right. \quad (3.21b)$$

$$\left\{ \begin{array}{l} M_{c,b;\alpha}^{G;i;k;\beta;l}(\mathbf{y}_1) = \sum_{d=-c}^c \tilde{M}_{c,d;\alpha}^{G;i;k;\beta;l}(\mathbf{y}_1) D_{bd}^c(\mathbf{R}), \end{array} \right. \quad (3.21c)$$

$$\left\{ \begin{array}{l} \tilde{M}_{a,d;\alpha}^{G;i;k;\beta;l}(\mathbf{y}_1) = \sum_{b=-a}^a M_{a,b;\alpha}^{G;i;k;\beta;l}(\mathbf{y}_1) D_{db}^a(\mathbf{R}^T), \end{array} \right. \quad (3.22a)$$

$$\left\{ \begin{array}{l} \tilde{L}_{c,d;\alpha}^{G;i;k;\beta;l}(\mathbf{x}_1) = \sum_{a=|d|}^{\infty} (\text{M|L})_{c,a}^d(\mathbf{y}_1 \rightarrow \mathbf{x}_1; s_{\varphi}) \tilde{M}_{a,d;\alpha}^{G;i;k;\beta;l}(\mathbf{y}_1), \end{array} \right. \quad (3.22b)$$

$$\left\{ \begin{array}{l} L_{c,b;\alpha}^{G;i;k;\beta;l}(\mathbf{x}_1) = \sum_{d=-c}^c \tilde{L}_{c,d;\alpha}^{G;i;k;\beta;l}(\mathbf{x}_1) D_{bd}^c(\mathbf{R}), \end{array} \right. \quad (3.22c)$$

$$\left\{ \begin{array}{l} \tilde{L}_{a,d;\alpha}^{G;i;k;\beta;l}(\mathbf{x}_1) = \sum_{b=-a}^a L_{a,b;\alpha}^{G;i;k;\beta;l}(\mathbf{x}_1) D_{db}^a(\mathbf{R}^T), \end{array} \right. \quad (3.23a)$$

$$\left\{ \begin{array}{l} \tilde{L}_{c,d;\alpha}^{G;i;k;\beta;l}(\mathbf{x}_0) = \sum_{a=|d|}^{\infty} (\text{L|L})_{c,a}^d(\mathbf{x}_1 \rightarrow \mathbf{x}_0; s_{\varphi}) \tilde{L}_{a,d;\alpha}^{G;i;k;\beta;l}(\mathbf{x}_1), \end{array} \right. \quad (3.23b)$$

$$\left\{ \begin{array}{l} L_{c,b;\alpha}^{G;i;k;\beta;l}(\mathbf{x}_0) = \sum_{d=-c}^c \tilde{L}_{c,d;\alpha}^{G;i;k;\beta;l}(\mathbf{x}_0) D_{bd}^c(\mathbf{R}), \end{array} \right. \quad (3.23c)$$

where $D_{bd}^a(\mathbf{R})$ are the rotation matrices of spherical harmonics and can be calculated recursively in $O(N_t^3)$ computational complexity [19]. In Eqs. (3.21)–(3.23), $(\text{E|F})_{a,c}^b = (\text{E|F})_{a,c}^{b,b}$, and the

3. Acceleration of CQ-BEM

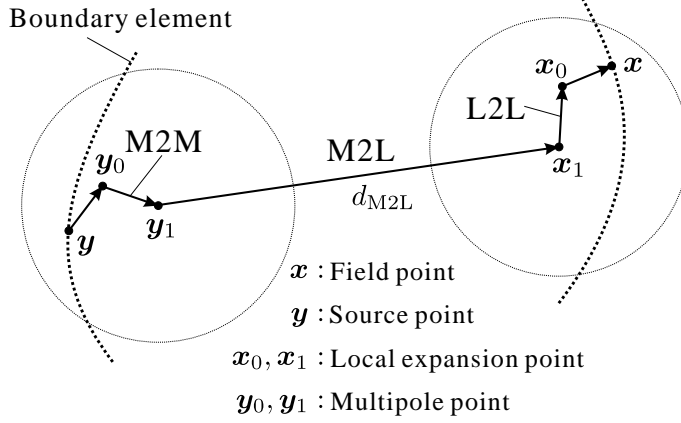


Figure 3.1.: Translation theorems (M2M, M2L, and L2L).

rotation matrices of vector \mathbf{R} are defined by

$$\begin{cases} (\mathbf{y}_0 - \mathbf{y}_1) \cdot \mathbf{R} = |\mathbf{y}_0 - \mathbf{y}_1| \mathbf{e}_3 & \text{in Eq. (3.21),} \\ (\mathbf{x}_1 - \mathbf{y}_1) \cdot \mathbf{R} = |\mathbf{x}_1 - \mathbf{y}_1| \mathbf{e}_3 & \text{in Eq. (3.22),} \\ (\mathbf{x}_0 - \mathbf{x}_1) \cdot \mathbf{R} = |\mathbf{x}_0 - \mathbf{x}_1| \mathbf{e}_3 & \text{in Eq. (3.23),} \end{cases}$$

where \mathbf{e}_3 is given by $\mathbf{e}_3 = (0, 0, 1)$. All of the calculations in Eqs. (3.21)–(3.23) and the evaluations of $(\mathbf{E}|\mathbf{F})_{a,c}^b$ are conducted in $O(N_t^3)$ computation. The detailed expressions of $(\mathbf{E}|\mathbf{F})_{a,c}^b$ and the recursive computation are presented in Appendix A.

3.1.3. Some numerical techniques for efficient CQ-FMBEM

Two typical techniques that enhance the stability and efficiency of the CQ-FMBEM are presented. The first is scaling of the multipole moments (3.12) and (3.13) with the modified spherical Bessel functions i_a and k_a . $i_a(z)$ and $k_a(z)$ exponentially tend to infinity and zero for a large argument z , respectively. This fact sometimes causes instability of the translation formulas (3.18)–(3.20) when cell size is large. The second is the truncation of M2L translations. Some M2L translations for the retarded potential calculation can be neglected because the fundamental solution in Laplace-domain rapidly approaches to zero if the distance between field and source points $r = |\mathbf{x} - \mathbf{y}|$ is large.

Scaling of modified spherical Bessel function

When the absolute value of the argument $|z|$ is large, the asymptotic expressions of $i_a(z)$ and $k_a(z)$ are given by

$$i_a(z) \sim \frac{e^z}{2z}, \quad k_a(z) \sim \frac{e^{-z}}{z}. \quad (3.24)$$

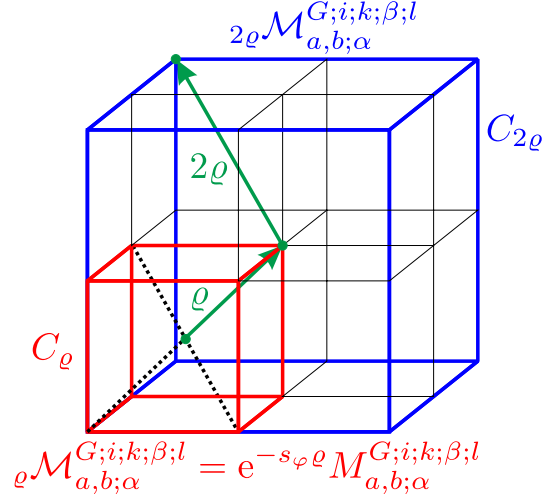


Figure 3.2.: Scaling for M2M moment translated from C_ρ to $C_{2\rho}$ using half diagonal length of cube cell.

Therefore, the scaled modified spherical Bessel functions \check{i}_a and \check{k}_a are defined by

$$\check{i}_a(z) = e^{-z} i_a(z), \quad \check{k}_a(z) = e^z k_a(z). \quad (3.25)$$

Scaling of multipole and local expansions

To utilize the scaled modified spherical Bessel functions in Eq. (3.25), the multipole and local expansions and the translation operators also have to be modified. Taking into account ρ , which is the half diagonal length of a cube cell C_ρ as shown in Fig. 3.2, the scaled multipole moment $\rho \mathcal{M}_{a,b;\alpha}^{G;i;k;\beta;l}$, the scaled local expansion coefficient $\rho \mathcal{L}_{a,b;\alpha}^{G;i;k;\beta;l}$, and the scaled functions $\rho \mathcal{F}_{a,b}^\varphi$ and $\rho \mathcal{O}_{a,b}^\varphi$ are defined as follows:

$$\rho \mathcal{M}_{a,b;\alpha}^{G;i;k;\beta;l} = e^{-s_\varphi \rho} M_{a,b;\alpha}^{G;i;k;\beta;l}, \quad \rho \mathcal{L}_{a,b;\alpha}^{G;i;k;\beta;l} = e^{s_\varphi \rho} L_{a,b;\alpha}^{G;i;k;\beta;l}, \quad (3.26)$$

$$\rho \mathcal{F}_{a,b}^\varphi = e^{-s_\varphi \rho} F_{a,b}^\varphi, \quad \rho \mathcal{O}_{a,b}^\varphi = e^{s_\varphi \rho} O_{a,b}^\varphi. \quad (3.27)$$

Consequently, the scaled multipole and local expansions for $G_{\gamma\alpha}^{i;k;\beta;l}$ are recast as follows:

$$G_{\gamma\alpha}^{i;k;\beta;l} = \sum_{a=0}^{\infty} \sum_{b=-a}^a \frac{s_\varphi(2a+1)}{4\pi} \left[\rho \mathcal{O}_{a,b}^\varphi(\mathbf{x}_\gamma - \mathbf{y}_0) \rho \mathcal{M}_{a,b;\alpha}^{G;i;k;\beta;l}(\mathbf{y}_0) \right]_{s=\lambda_\beta^l}, \quad (3.28)$$

$$G_{\gamma\alpha}^{i;k;\beta;l} = \sum_{a=0}^{\infty} \sum_{b=-a}^a \frac{s_\varphi(2a+1)}{4\pi} \left[\rho \mathcal{F}_{a,b}^\varphi(\mathbf{x}_\gamma - \mathbf{x}_0) \rho \mathcal{L}_{a,b;\alpha}^{G;i;k;\beta;l}(\mathbf{x}_0) \right]_{s=\lambda_\beta^l}. \quad (3.29)$$

The scaled multipole and local expansions for $H_{\gamma\alpha}^{i;k;\beta;l}$ can be obtained in the same manner as the ones for $G_{\gamma\alpha}^{i;k;\beta;l}$.

3. Acceleration of CQ-BEM

Scaling of M2M, M2L, and L2L

Considering the sizes of cells before and after translations, the scaling of translation formulas (M2M, M2L, and L2L) for Eqs. (3.28) and (3.29) can be obtained. Taking into account the variation of cell size from ϱ to 2ϱ as shown in Fig. 3.2, the scaling of M2M formulas (3.21) is expressed as follows:

$$\left\{ \begin{aligned} \varrho \tilde{\mathcal{M}}_{a,d;\alpha}^{G;i;k;\beta;l}(\mathbf{y}_0) &= \sum_{b=-a}^a \varrho \mathcal{M}_{a,b;\alpha}^{G;i;k;\beta;l}(\mathbf{y}_0) D_{db}^a(\mathbf{R}^T), & (3.30a) \\ 2\varrho \tilde{\mathcal{M}}_{c,d;\alpha}^{G;i;k;\beta;l}(\mathbf{y}_1) &= \sum_{a=|d|}^{\infty} (\mathcal{M}|\mathcal{M})_{c,a}^d(\mathbf{y}_0 \rightarrow \mathbf{y}_1; s_\varphi) \varrho \tilde{\mathcal{M}}_{a,d;\alpha}^{G;i;k;\beta;l}(\mathbf{y}_0), & (3.30b) \\ 2\varrho \mathcal{M}_{c,b;\alpha}^{G;i;k;\beta;l}(\mathbf{y}_1) &= \sum_{d=-c}^c 2\varrho \tilde{\mathcal{M}}_{c,d;\alpha}^{G;i;k;\beta;l}(\mathbf{y}_1) D_{bd}^c(\mathbf{R}), & (3.30c) \end{aligned} \right.$$

where $(\mathcal{E}|\mathcal{F})_{a,c}^b$ ($\mathcal{E}, \mathcal{F} = \mathcal{M}$ or \mathcal{L}) is the scaled translation operator, and the detail is given in Appendix A. The scaled M2L and L2L formulas can be obtained by analogous modifications of Eqs. (3.22) and (3.23) as follows:

$$\left\{ \begin{aligned} \varrho \tilde{\mathcal{M}}_{a,d;\alpha}^{G;i;k;\beta;l}(\mathbf{y}_1) &= \sum_{b=-a}^a \varrho \mathcal{M}_{a,b;\alpha}^{G;i;k;\beta;l}(\mathbf{y}_1) D_{db}^a(\mathbf{R}^T), & (3.31a) \\ \varrho \tilde{\mathcal{L}}_{c,d;\alpha}^{G;i;k;\beta;l}(\mathbf{x}_1) &= \sum_{a=|d|}^{\infty} e^{-s_\varphi(d_{M2L}-2\varrho)} (\mathcal{M}|\mathcal{L})_{c,a}^d(\mathbf{y}_1 \rightarrow \mathbf{x}_1; s_\varphi) \varrho \tilde{\mathcal{M}}_{a,d;\alpha}^{G;i;k;\beta;l}(\mathbf{y}_1), & (3.31b) \\ \varrho \mathcal{L}_{c,b;\alpha}^{G;i;k;\beta;l}(\mathbf{x}_1) &= \sum_{d=-c}^c \varrho \tilde{\mathcal{L}}_{c,d;\alpha}^{G;i;k;\beta;l}(\mathbf{x}_1) D_{bd}^c(\mathbf{R}), & (3.31c) \end{aligned} \right.$$

$$\left\{ \begin{aligned} 2\varrho \tilde{\mathcal{L}}_{a,d;\alpha}^{G;i;k;\beta;l}(\mathbf{x}_1) &= \sum_{b=-a}^a 2\varrho \mathcal{L}_{a,b;\alpha}^{G;i;k;\beta;l}(\mathbf{x}_1) D_{db}^a(\mathbf{R}^T), & (3.32a) \\ \varrho \tilde{\mathcal{L}}_{c,d;\alpha}^{G;i;k;\beta;l}(\mathbf{x}_0) &= \sum_{a=|d|}^{\infty} (\mathcal{L}|\mathcal{L})_{c,a}^d(\mathbf{x}_1 \rightarrow \mathbf{x}_0; s_\varphi) 2\varrho \tilde{\mathcal{L}}_{a,d;\alpha}^{G;i;k;\beta;l}(\mathbf{x}_1), & (3.32b) \\ \varrho \mathcal{L}_{c,b;\alpha}^{G;i;k;\beta;l}(\mathbf{x}_0) &= \sum_{d=-c}^c \varrho \tilde{\mathcal{L}}_{c,d;\alpha}^{G;i;k;\beta;l}(\mathbf{x}_0) D_{bd}^c(\mathbf{R}). & (3.32c) \end{aligned} \right.$$

In Eq. (3.31), d_{M2L} denotes the distance between the multipole point \mathbf{y}_1 and local expansion point \mathbf{x}_1 as shown in Fig. 3.1.

Truncation of M2L

From Eq. (3.31b), the M2L moment tends to zero for a large argument $s_\varphi(d_{M2L} - 2\varrho)$, where $d_{M2L} - 2\varrho$ corresponds to the minimum distance between two cells r_{\min} , and it holds that $d_{M2L} - 2\varrho \leq r_{\min}$ as shown in Fig. 3.3. Negligibly small values of $\varrho \tilde{\mathcal{L}}_{c,d;\alpha}^{G;i;k;\beta;l}(\mathbf{x}_1)$ in M2L (3.31) are

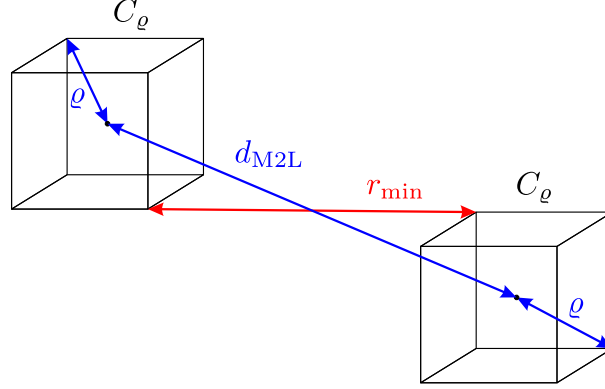


Figure 3.3.: Distance between two cells in M2L translation.

excluded from the translation process in order to accelerate the FMM calculation. To this end, the asymptotic behavior of M2L including $\exp[-s_\varphi(d_{\text{M2L}} - 2\rho)]$ is investigated. The truncation condition is expressed as follows:

$$\Re[s_\varphi(d_{\text{M2L}} - 2\rho)] > b \log 10, \quad (3.33)$$

where b is the number of significant figures required in M2L computation. The truncation procedure is briefly summarized as follows:

1. $s_\varphi(d_{\text{M2L}} - 2\rho)$ is evaluated before M2L.
2. The truncation condition defined in Eq. (3.33) is calculated.
3. If the truncation condition defined in Eq. (3.33) is satisfied, M2L is neglected. However, when Eq. (3.33) is not satisfied, M2L must be conducted as usual.

This truncation technique can be applied to the large number of M2L translations to save computational time. The truncation parameter b is given by $b = 20$ in this study.

3.1.4. Computational complexity

We briefly conclude the computational complexity of our proposed method for N and M_e here. The computational complexity of one matrix-vector product for spatial components is considered as $O(M_e)$ or $O(M_e \log M_e)$ owing to use of the FMM [62]. The computational complexities of FMM and FFT are dominant in the time-marching process presented in Section 3.1.1. The number of FMM implementation is $O(N^2)$, and the number of FFT calculations is $O(NM_e)$. Therefore, the computational complexity of FMM is $O(N^2M_e)$ or $O(N^2M_e \log M_e)$, while the one for FFT is $O(N^2M_e \log N)$. In practical numerical computations, the computational time of FMM usually becomes much larger than that of FFT, and $O(N^2M_e)$ or $O(N^2M_e \log M_e)$ is considered as the total computational complexity of the proposed method. On the other hand, the memory complexity is $O(NM_e)$ owing to the FMM [62].

3. Acceleration of CQ-BEM

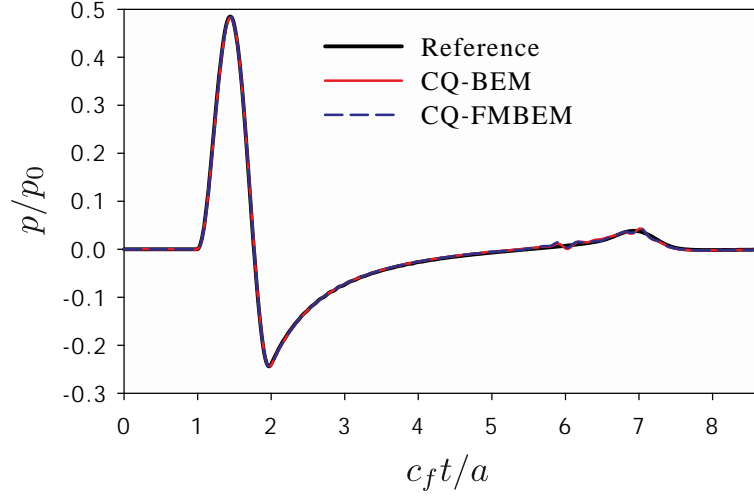


Figure 3.4.: Time variations of p/p_0 obtained by CQ-BEM and CQ-FMBEM using RK3 at point X in Fig. 2.3 when $c_f \Delta t/a = 0.069$.

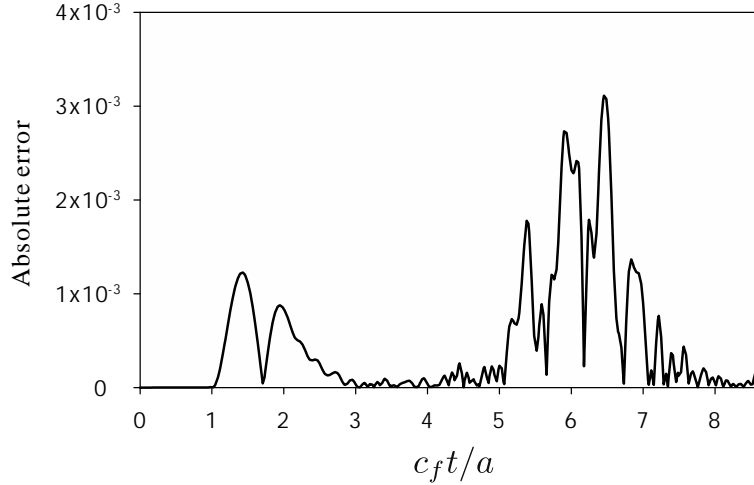


Figure 3.5.: Absolute errors between p/p_0 obtained by CQ-BEM and CQ-FMBEM, which are shown in Fig. 3.4.

3.1.5. Numerical results

To verify the accuracy and to demonstrate the computational efficiency of the proposed CQ-FMBEM, some numerical examples are presented in this section. The same analysis model as Section 2.3 depicted in Fig. 2.3 is used for this numerical simulation. The truncation number for the summation of multipole and local expansions, such as Eqs. (3.10) and (3.11), is chosen as $N_t = 10$ for all simulations in this study.

First, the comparison of numerical solutions obtained by the CQ-BEMs with and without the FMM for accuracy verification. Fig. 3.4 shows numerical solutions for the same simulation as Fig. 2.7 when $c_f \Delta t/a = 0.069$, and the dashed line is obtained by the CQ-FMBEM with RK3. As we

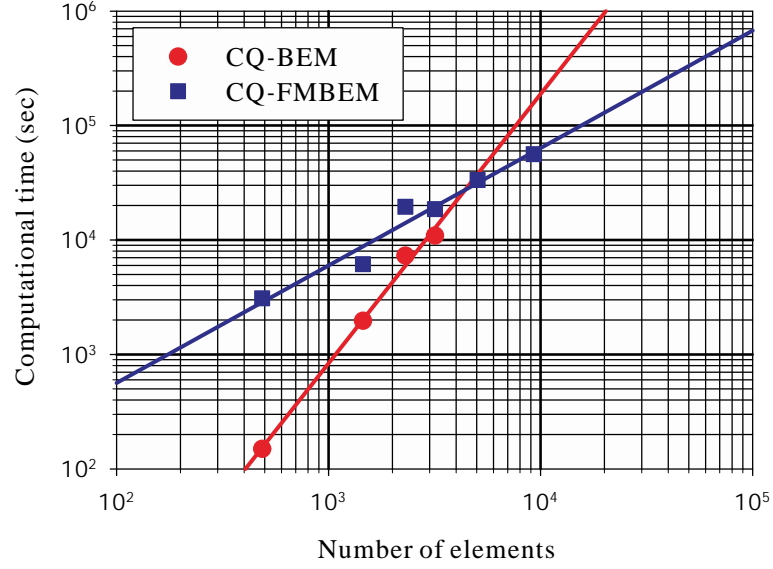


Figure 3.6.: Computational time comparison between CQ-BEM and CQ-FMBEM using RK3 for 3-D acoustic wave problem.

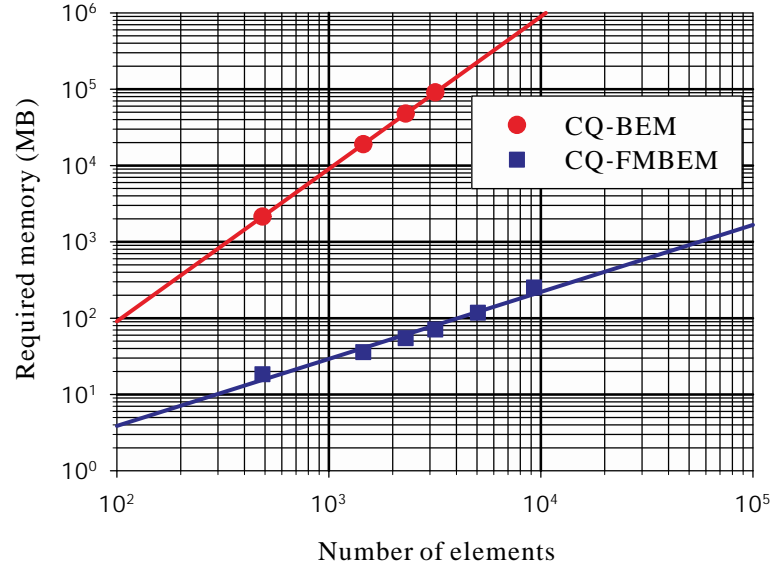


Figure 3.7.: Required memory comparison between CQ-BEM and CQ-FMBEM using RK3 for 3-D acoustic wave problem.

can see from Fig. 3.4, the waveforms obtained by the CQ-BEM and CQ-FMBEM are very similar. On the other hand, the absolute errors between p/p_0 obtained by CQ-BEM and CQ-FMBEM are plotted in Fig. 3.5. These errors are caused by the approximation in the FMM and considered as sufficiently small from Fig. 3.5.

Second, the computational efficiency of CQ-FMBEM is confirmed. All of the computations here are conducted by a single processor. Discretized BIE (2.33) is numerically solved by both CQ-BEM

3. Acceleration of CQ-BEM

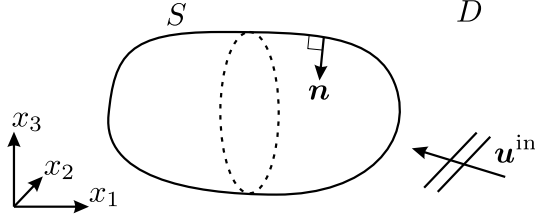


Figure 3.8.: Analysis model for elastic wave scattering by an obstacle in a 3-D infinite domain

and CQ-FMBEM, and the non-preconditioned GMRES [74], which is one of the Krylov subspace solvers, is used. In the CQ-BEM, all of the influence functions (2.30) are stored after the calculations for all elements and time steps.

The computational time and required memory for both CQ-BEM and CQ-FMBEM with RK3 are shown in Figs. 3.6 and 3.7, respectively, when $c_f \Delta t / a = 0.069$ and $N = 128$. As shown in Fig. 3.6, the CQ-FMBEM is faster than the CQ-BEM when the number of elements M_e is $M_e = 5000$ or more. Moreover, the memory required by the CQ-FMBEM is much less than that by the CQ-BEM as shown in Fig. 3.7. Consequently, the CQ-FMBEM is more efficient for large-scale problems than the CQ-BEM.

3.1.6. CQ-FMBEM for 3-D elastic wave problems

The CQ-FMBEM is applied to 3-D elastic wave problems in this section. The CQ-FMBEM for this problem has been developed by Maruyama *et al.* [55]. Only the formulation of BIE and multipole and local expansions are presented because the calculation algorithm is same as the one for 3-D acoustic problems.

Let S be a closed boundary with unit normal vector \mathbf{n} in \mathbb{R}^3 as depicted in Fig. 3.8. D is an exterior domain, which is a homogeneous, isotropic, and linearly elastic solid. Disregarding the body force, the displacement \mathbf{u} satisfies the following governing equation:

$$c_T^2 \nabla^2 \mathbf{u}(\mathbf{x}, t) + (c_L^2 + c_T^2) \nabla \nabla \cdot \mathbf{u}(\mathbf{x}, t) = \ddot{\mathbf{u}}(\mathbf{x}, t) \quad \mathbf{x} \in D, \quad (3.34)$$

where c_L and c_T are the velocities of P and S waves, respectively, and expressed using the density ρ and the Lamé constants λ and μ as follows:

$$c_L = \sqrt{\frac{\lambda + 2\mu}{\rho}}, \quad c_T = \sqrt{\frac{\mu}{\rho}}.$$

We assume that the solution \mathbf{u} of Eq. (3.34) satisfies the following initial condition:

$$\mathbf{u}^{\text{sc}}(\mathbf{x}, 0) = \dot{\mathbf{u}}^{\text{sc}}(\mathbf{x}, 0) = \mathbf{0} \quad \mathbf{x} \in D. \quad (3.35)$$

Considering the Sommerfeld radiation condition for scattered waves and initial condition (3.35), the

time-domain BIE for displacement \mathbf{u} is formulated by means of the usual manner as follows:

$$\begin{aligned} \mathbf{C}(\mathbf{x})\mathbf{u}(\mathbf{x}, t) = & \mathbf{u}^{\text{in}}(\mathbf{x}, t) + \int_0^t \int_S \mathbf{U}(\mathbf{x}, \mathbf{y}, t - \tau) \cdot \mathbf{t}(\mathbf{y}, \tau) dS_y d\tau \\ & - \int_0^t \text{p.v.} \int_S \mathbf{T}(\mathbf{x}, \mathbf{y}, t - \tau) \cdot \mathbf{u}(\mathbf{y}, \tau) dS_y d\tau, \end{aligned} \quad (3.36)$$

where $\mathbf{C}(\mathbf{x})$ is also the free term [14] depending on the boundary shape at \mathbf{x} , and \mathbf{t} is the traction force. \mathbf{U} and \mathbf{T} are the fundamental displacement and traction solutions for 3-D elastodynamic problems in time-domain, respectively [1]. The displacement formulation defined in Eq. (3.36) is used for the boundary element analysis of elastic wave scattering in this chapter.

CQ-FMBEM formulation

In numerically solving BIE (3.36), the convolution integrals are evaluated by means of the IRK-based CQM, and the surface integrals over the boundary S are discretized by the piecewise constant approximation. The discretized BIE at n -th and i -th sub-step in time is written as follows:

$$\begin{aligned} \frac{1}{2} \mathbf{u}_\gamma^{i;n} = & \mathbf{u}_\gamma^{\text{in};i;n} + \sum_{k=0}^n \sum_{\alpha=1}^{M_e} \sum_{j=1}^m \left[\mathcal{U}_{\gamma\alpha}^{ij;n-k} \cdot \mathbf{t}_\alpha^{j;k} - \mathcal{T}_{\gamma\alpha}^{ij;n-k} \cdot \mathbf{u}_\alpha^{j;k} \right] \\ & (i = 1, \dots, m), \quad (n = 0, \dots, N-1), \end{aligned} \quad (3.37)$$

where

$$\mathbf{p}_\gamma^{i;n} = \mathbf{p}(\mathbf{x}_\gamma, (n + c_i)\Delta t), \quad (\mathbf{p} = \mathbf{u}, \mathbf{t}, \text{ or } \mathbf{u}^{\text{in}}).$$

In Eq. (3.37), $\mathcal{U}_{\gamma\alpha}^{ij;\kappa}$ and $\mathcal{T}_{\gamma\alpha}^{ij;\kappa}$ are the influence functions defined by

$$\mathcal{U}_{\gamma\alpha}^{ij;\kappa} = \tilde{\mathcal{F}}_{l\kappa}^{-1} \left[\sum_{\beta=1}^m \left(\mathbf{E}_\beta(\zeta_l) \right)_{ij} \int_{S_\alpha} \hat{\mathbf{U}}(\mathbf{x}_\gamma, \mathbf{y}, \lambda_\beta^l) dS_y \right], \quad (3.38)$$

$$\mathcal{T}_{\gamma\alpha}^{ij;\kappa} = \tilde{\mathcal{F}}_{l\kappa}^{-1} \left[\sum_{\beta=1}^m \left(\mathbf{E}_\beta(\zeta_l) \right)_{ij} \text{p.v.} \int_{S_\alpha} \hat{\mathbf{T}}(\mathbf{x}_\gamma, \mathbf{y}, \lambda_\beta^l) dS_y \right], \quad (3.39)$$

where $\hat{\mathbf{U}}$ and $\hat{\mathbf{T}}$ are the Laplace-domain fundamental solutions for displacement and traction, respectively. Rearranging Eq. (3.37) according to the time step, the following expression is obtained.

$$\begin{aligned} \sum_{\alpha=1}^M \sum_{j=1}^m \left[\left(\frac{1}{2} I \delta_{\gamma\alpha} \delta_{ij} + \mathcal{T}_{\gamma\alpha}^{ij;0} \right) \cdot \mathbf{u}_\alpha^{j;n} - \mathcal{U}_{\gamma\alpha}^{ij;0} \cdot \mathbf{t}_\alpha^{j;n} \right] \\ = \mathbf{u}_\gamma^{\text{in};i;n} - \sum_{k=0}^{n-1} \sum_{\alpha=1}^M \sum_{j=1}^m \left[\mathcal{T}_{\gamma\alpha}^{ij;n-k} \cdot \mathbf{u}_\alpha^{j;k} - \mathcal{U}_{\gamma\alpha}^{ij;n-k} \cdot \mathbf{t}_\alpha^{j;k} \right]. \end{aligned} \quad (3.40)$$

3. Acceleration of CQ-BEM

The matrix-vector calculation of retarded potential terms in the right-hand side of Eq. (3.40) is rapidly evaluated by the FMM in order to reduce the computational cost. Only the multipole and local expansions are presented here because the time-stepping procedure and translation theorems are same as the CQ-FMBEM for 3-D acoustic wave problems.

In order to derive the multipole and local expansions, $\mathbf{U}_{I;\gamma\alpha}^{i;k;\beta;l}$ and $\mathbf{T}_{I;\gamma\alpha}^{i;k;\beta;l}$ are defined by

$$\mathbf{U}_{I;\gamma\alpha}^{i;k;\beta;l} = \left[\int_{S_\alpha} \hat{U}_{IK}(\mathbf{x}_\gamma, \mathbf{y}, \lambda_\beta^l) dS_y \right] \mathbf{t}_{K;\alpha}^{i;k;\beta;l}, \quad (3.41)$$

$$\mathbf{T}_{I;\gamma\alpha}^{i;k;\beta;l} = \left[\int_{S_\alpha} \hat{T}_{IK}(\mathbf{x}_\gamma, \mathbf{y}, \lambda_\beta^l) dS_y \right] \mathbf{u}_{K;\alpha}^{i;k;\beta;l}, \quad (3.42)$$

where

$$\mathbf{u}_{K;\alpha}^{i;k;\beta;l} = \sum_{j=1}^m \left(\mathbf{E}_\beta(\zeta_l) \right)_{ij} u_{K;\alpha}^{j;k}, \quad \mathbf{t}_{K;\alpha}^{i;k;\beta;l} = \sum_{j=1}^m \left(\mathbf{E}_\beta(\zeta_l) \right)_{ij} t_{K;\alpha}^{j;k}.$$

\hat{U} and \hat{T} in Eqs. (3.41) and (3.42) are expressed using the fundamental solution of modified Helmholtz equation \hat{G}^φ as follows:

$$\hat{U}_{IK}(\mathbf{x}, \mathbf{y}, s) = \frac{1}{\mu} \left[\hat{G}^T(\mathbf{x}, \mathbf{y}, s) \delta_{IK} + \frac{1}{s_T^2} \frac{\partial^2}{\partial x_I \partial y_K} \left(\hat{G}^T(\mathbf{x}, \mathbf{y}, s) - \hat{G}^L(\mathbf{x}, \mathbf{y}, s) \right) \right], \quad (3.43)$$

$$\hat{T}_{IK}(\mathbf{x}, \mathbf{y}, s) = n_J(\mathbf{y}) C_{KJpq} \frac{\partial}{\partial y_q} \hat{U}_{Ip}(\mathbf{x}, \mathbf{y}, s), \quad (3.44)$$

where C_{ijkl} is a component of the elastic modulus tensor. The multipole and local expansions for Laplace-domain fundamental solutions can be derived in a similar way to the ones in frequency-domain [99, 17].

Taking into account the scaling of modified Bessel functions, substituting Eqs. (3.4a), (3.43), and (3.44) into Eqs. (3.41) and (3.42) yields the following multipole expansions:

$$\begin{aligned} \mathbf{U}_{I;\gamma\alpha}^{i;k;\beta;l} = & \sum_{a=0}^{\infty} \sum_{b=-a}^a \left[A_a \left\{ \frac{\partial}{\partial x_I} {}_e\mathcal{O}_{a,b}^L(\mathbf{x}_\gamma - \mathbf{y}_0) \right\} {}_e\mathcal{M}_{a,b;\alpha}^{U_L;i;k;\beta;l}(\mathbf{y}_0) \right. \\ & \left. + B_a e_{tIJ} \left\{ \frac{\partial}{\partial x_J} {}_e\mathcal{O}_{a,b}^T(\mathbf{x}_\gamma - \mathbf{y}_0) \right\} {}_e\mathcal{M}_{t,a,b;\alpha}^{U_T;i;k;\beta;l}(\mathbf{y}_0) \right]_{s=\lambda_\beta^l}, \end{aligned} \quad (3.45)$$

$$\begin{aligned} \mathbf{T}_{I;\gamma\alpha}^{i;k;\beta;l} = & \sum_{a=0}^{\infty} \sum_{b=-a}^a \left[A_a \left\{ \frac{\partial}{\partial x_I} {}_e\mathcal{O}_{a,b}^L(\mathbf{x}_\gamma - \mathbf{y}_0) \right\} {}_e\mathcal{M}_{a,b;\alpha}^{T_L;i;k;\beta;l}(\mathbf{y}_0) \right. \\ & \left. + B_a e_{tIJ} \left\{ \frac{\partial}{\partial x_J} {}_e\mathcal{O}_{a,b}^T(\mathbf{x}_\gamma - \mathbf{y}_0) \right\} {}_e\mathcal{M}_{t,a,b;\alpha}^{T_T;i;k;\beta;l}(\mathbf{y}_0) \right]_{s=\lambda_\beta^l}, \end{aligned} \quad (3.46)$$

where ${}_e\mathcal{M}_{a,b;\alpha}^{\Pi_L;i;k;\beta;l}$ and ${}_e\mathcal{M}_{t,a,b;\alpha}^{\Pi_T;i;k;\beta;l}$ are the scaled multipole moments with respect to P and S waves, respectively, and the superscript Π is $\Pi = U$ or T . In addition, e_{ijk} indicates a component

3.1. Fast multipole accelerated CQ-BEM (CQ-FMBEM)

of the 3-D permutation tensor, and A_a and B_a are defined by

$$A_a = -\frac{s_L(2a+1)}{4\pi\mu s_T^2}, \quad B_a = \frac{2a+1}{4\pi\mu s_T}.$$

In Eqs. (3.45) and (3.46), each of $\mathbf{U}_{I;\gamma\alpha}^{i;k;\beta;l}$ and $\mathbf{T}_{I;\gamma\alpha}^{i;k;\beta;l}$ has four multipole moments: one for P waves (${}_e\mathcal{M}_{a,b;\alpha}^{\Pi_L;i;k;\beta;l}$) and the others for S waves (${}_e\mathcal{M}_{t,a,b;\alpha}^{\Pi_T;i;k;\beta;l}$, $t = 1, 2, 3$). The explicit expressions of the multipole moments in Eqs. (3.45) and (3.46) are shown as follows:

$${}_e\mathcal{M}_{a,b;\alpha}^{U_L;i;k;\beta;l}(\mathbf{y}_0) = \mathbf{t}_{K;\alpha}^{i;k;\beta;l} \int_{S_\alpha} \left[\frac{\partial}{\partial y_K} {}_e\bar{\mathcal{F}}_{a,b}^L(\mathbf{y} - \mathbf{y}_0) \right] dS_y, \quad (3.47)$$

$${}_e\mathcal{M}_{t,a,b;\alpha}^{U_T;i;k;\beta;l}(\mathbf{y}_0) = \mathbf{t}_{K;\alpha}^{i;k;\beta;l} \int_{S_\alpha} e_{tJK} \left[\frac{\partial}{\partial y_J} {}_e\bar{\mathcal{F}}_{a,b}^T(\mathbf{y} - \mathbf{y}_0) \right] dS_y, \quad (3.48)$$

$${}_e\mathcal{M}_{a,b;\alpha}^{T_L;i;k;\beta;l}(\mathbf{y}_0) = \mathbf{u}_{K;\alpha}^{i;k;\beta;l} \int_{S_\alpha} C_{KJpq} n_J(\mathbf{y}) \left[\frac{\partial}{\partial y_p \partial y_q} {}_e\bar{\mathcal{F}}_{a,b}^L(\mathbf{y} - \mathbf{y}_0) \right] dS_y, \quad (3.49)$$

$${}_e\mathcal{M}_{t,a,b;\alpha}^{T_T;i;k;\beta;l}(\mathbf{y}_0) = \mathbf{u}_{K;\alpha}^{i;k;\beta;l} \int_{S_\alpha} e_{tup} C_{KJpq} n_J(\mathbf{y}) \left[\frac{\partial}{\partial y_q \partial y_u} {}_e\bar{\mathcal{F}}_{a,b}^T(\mathbf{y} - \mathbf{y}_0) \right] dS_y. \quad (3.50)$$

The local expansions for $\mathbf{U}_{I;\gamma\alpha}^{i;k;\beta;l}$ and $\mathbf{T}_{I;\gamma\alpha}^{i;k;\beta;l}$ are obtained by substituting Eq. (3.4b) into Eqs. (3.41) and (3.42) as follows:

$$\begin{aligned} \mathbf{U}_{I;\gamma\alpha}^{i;k;\beta;l} = & \sum_{a=0}^{\infty} \sum_{b=-a}^a \left[A_a \left\{ \frac{\partial}{\partial x_I} {}_e\mathcal{F}_{a,b}^L(\mathbf{x}_\gamma - \mathbf{x}_0) \right\} {}_e\mathcal{L}_{a,b;\alpha}^{U_L;i;k;\beta;l}(\mathbf{x}_0) \right. \\ & \left. + B_a e_{tIJ} \left\{ \frac{\partial}{\partial x_J} {}_e\mathcal{F}_{a,b}^T(\mathbf{x}_\gamma - \mathbf{x}_0) \right\} {}_e\mathcal{L}_{t,a,b;\alpha}^{U_T;i;k;\beta;l}(\mathbf{x}_0) \right]_{s=\lambda_\beta^I}, \end{aligned} \quad (3.51)$$

$$\begin{aligned} \mathbf{T}_{I;\gamma\alpha}^{i;k;\beta;l} = & \sum_{a=0}^{\infty} \sum_{b=-a}^a \left[A_a \left\{ \frac{\partial}{\partial x_I} {}_e\mathcal{F}_{a,b}^L(\mathbf{x}_\gamma - \mathbf{x}_0) \right\} {}_e\mathcal{L}_{a,b;\alpha}^{T_L;i;k;\beta;l}(\mathbf{x}_0) \right. \\ & \left. + B_a e_{tIJ} \left\{ \frac{\partial}{\partial x_J} {}_e\mathcal{F}_{a,b}^T(\mathbf{x}_\gamma - \mathbf{x}_0) \right\} {}_e\mathcal{L}_{t,a,b;\alpha}^{T_T;i;k;\beta;l}(\mathbf{x}_0) \right]_{s=\lambda_\beta^I}, \end{aligned} \quad (3.52)$$

where ${}_e\mathcal{L}_{a,b;\alpha}^{\Pi_L;i;k;\beta;l}$ and ${}_e\mathcal{L}_{t,a,b;\alpha}^{\Pi_T;i;k;\beta;l}$ are the coefficients of local expansion with respect to P and S waves, respectively. The coefficients of local expansion can be written by replacing ${}_e\bar{\mathcal{F}}_{a,b}^\varphi(\mathbf{y} - \mathbf{y}_0)$ by ${}_e\bar{\mathcal{O}}_{a,b}^\varphi(\mathbf{y} - \mathbf{x}_0)$ in Eqs. (3.47)–(3.50) as follows:

$${}_e\mathcal{L}_{a,b;\alpha}^{U_L;i;k;\beta;l}(\mathbf{x}_0) = \mathbf{t}_{K;\alpha}^{i;k;\beta;l} \int_{S_\alpha} \left[\frac{\partial}{\partial y_K} {}_e\bar{\mathcal{O}}_{a,b}^L(\mathbf{y} - \mathbf{x}_0) \right] dS_y, \quad (3.53)$$

$${}_e\mathcal{L}_{t,a,b;\alpha}^{U_T;i;k;\beta;l}(\mathbf{x}_0) = \mathbf{t}_{K;\alpha}^{i;k;\beta;l} \int_{S_\alpha} e_{tJK} \left[\frac{\partial}{\partial y_J} {}_e\bar{\mathcal{O}}_{a,b}^T(\mathbf{y} - \mathbf{x}_0) \right] dS_y, \quad (3.54)$$

$${}_e\mathcal{L}_{a,b;\alpha}^{T_L;i;k;\beta;l}(\mathbf{x}_0) = \mathbf{u}_{K;\alpha}^{i;k;\beta;l} \int_{S_\alpha} C_{KJpq} n_J(\mathbf{y}) \left[\frac{\partial}{\partial y_p \partial y_q} {}_e\bar{\mathcal{O}}_{a,b}^L(\mathbf{y} - \mathbf{x}_0) \right] dS_y, \quad (3.55)$$

3. Acceleration of CQ-BEM

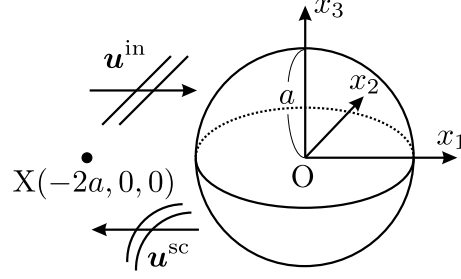


Figure 3.9.: Elastic wave scattering by a spherical cavity subjected to an incident plane wave.

$${}_{\rho}\mathcal{L}_{t,a,b;\alpha}^{TT;i;k;\beta;l}(\mathbf{x}_0) = \mathbf{u}_{K;\alpha}^{i;k;\beta;l} \int_{S_{\alpha}} e_{tup} C_{KJpq} n_J(\mathbf{y}) \left[\frac{\partial}{\partial y_q \partial y_u} {}_{\rho}\bar{\mathcal{O}}_{a,b}^T(\mathbf{y} - \mathbf{x}_0) \right] dS_y. \quad (3.56)$$

In Eqs. (3.47)–(3.50) and Eqs. (3.53)–(3.56), ${}_{\rho}\bar{\mathcal{O}}_{a,b}^{\varphi}$ and ${}_{\rho}\bar{\mathcal{F}}_{a,b}^{\varphi}$ are defined by

$${}_{\rho}\bar{\mathcal{F}}_{a,b}^{\varphi} = e^{-s_{\varphi}\rho} \bar{\mathcal{F}}_{a,b}^{\varphi}, \quad {}_{\rho}\bar{\mathcal{O}}_{a,b}^{\varphi} = e^{s_{\varphi}\rho} \bar{\mathcal{O}}_{a,b}^{\varphi}. \quad (3.57)$$

If ${}_{\rho}\mathcal{M}_{a,b;\alpha}^{G;i;k;\beta;l}$, ${}_{\rho}\mathcal{L}_{a,b;\alpha}^{G;i;k;\beta;l}$, and s_{φ} in Eqs. (3.30)–(3.32) are replaced with ${}_{\rho}\mathcal{M}_{a,b;\alpha}^{\Pi_L;i;k;\beta;l}$, ${}_{\rho}\mathcal{L}_{a,b;\alpha}^{\Pi_L;i;k;\beta;l}$, and s_L , respectively, the translation formulas for the P wave moments are derived. Similarly, replacing ${}_{\rho}\mathcal{M}_{a,b;\alpha}^{G;i;k;\beta;l}$, ${}_{\rho}\mathcal{L}_{a,b;\alpha}^{G;i;k;\beta;l}$, and s_{φ} in Eqs. (3.30)–(3.32) by ${}_{\rho}\mathcal{M}_{t,a,b;\alpha}^{\Pi_T;i;k;\beta;l}$, ${}_{\rho}\mathcal{L}_{t,a,b;\alpha}^{\Pi_T;i;k;\beta;l}$, and s_T , respectively, the translation formulas for the S wave moments are also obtained.

Numerical results

The scattering of an incident plane wave by a spherical cavity is numerically solved to show the accuracy and efficiency of the CQ-FMBEM for 3-D elastodynamics. The computational time and required memory are confirmed by comparing the results from CQ-BEMs with and without FMM. The boundary condition on S is assumed to be $\mathbf{t} = \mathbf{0}$, and Poisson's ratio ν is given by $\nu = 0.25$.

An incident plane P wave scattering by a spherical cavity with radius a as depicted in Fig. 3.9, is numerically solved to verify the accuracy of the CQ-FMBEM for 3-D elastodynamics. Displacement fields at the point X in Fig. 3.9 are investigated for CQ-FMBEMs based on different schemes and various time increments. The following Ricker wave [71] with amplitude u_0 is used as an incident plane wave.

$$\begin{cases} \mathbf{u}^{\text{in}}(\mathbf{x}, t) = \frac{\sqrt{\pi}}{2} u_0 \mathbf{d}_{\varphi} (\alpha - 0.5) e^{-\alpha}, \\ \alpha = \left[\pi f^{\text{in}} \left(t - t_s - \frac{x_1 + a}{c_L} \right) \right]^2, \end{cases} \quad (3.58a)$$

$$\alpha = \left[\pi f^{\text{in}} \left(t - t_s - \frac{x_1 + a}{c_L} \right) \right]^2, \quad (3.58b)$$

where \mathbf{d}_{φ} is the displacement vector of the incident wave, and $\varphi = L, TV$, or TH and indicates a P, SV, or SH wave, respectively. In this section, we present only the results of P wave incidence, and therefore, $\varphi = L$ and $\mathbf{d}_L = (1, 0, 0)$ are given. In addition, f^{in} is the center frequency of

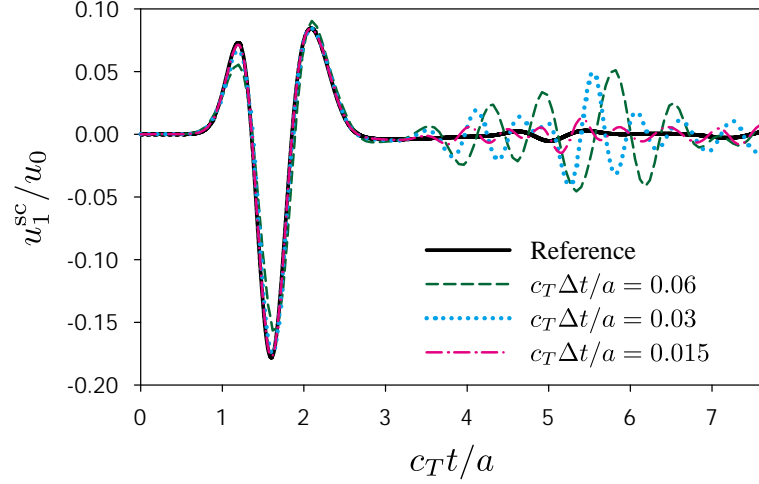


Figure 3.10.: Time variations of u_1^{sc}/u_0 obtained by using BDF2 at point X in Fig. 3.9 when $M_e = 9280$.

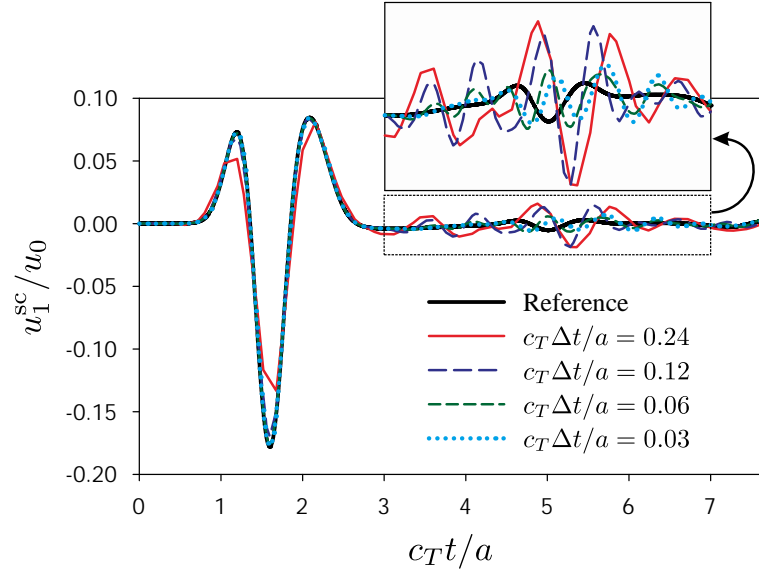


Figure 3.11.: Time variations of u_1^{sc}/u_0 obtained by using RK2 at point X in Fig. 3.9 when $M_e = 9280$.

the incident wave, and t_s is the peak time parameter. In this analysis, $t_s = 1/f^{\text{in}}$ and $f^{\text{in}} = ac_L/\lambda_L^{\text{in}}$ are considered, where λ_L^{in} is the P wavelength with respect to f^{in} and given by $\lambda_L^{\text{in}}/a = \sqrt{3}$. The boundary surface of the cavity is discretized into $M_e = 9280$ flatly triangular boundary elements. The reference transient solutions are constructed by the inverse Fourier transform because this problem has also been analytically solved in the frequency-domain by Pao and Mow [67].

The time variations of u_1^{sc}/u_0 at point X in Fig. 3.9 obtained by BDF2, RK2, and RK3 are shown for different time increments in Figs. 3.10, 3.11, and 3.12, respectively. As seen from Fig. 3.10, the BDF2 with the smallest time increment $c_T \Delta t/a = 0.015$, can yield very good results at the

3. Acceleration of CQ-BEM

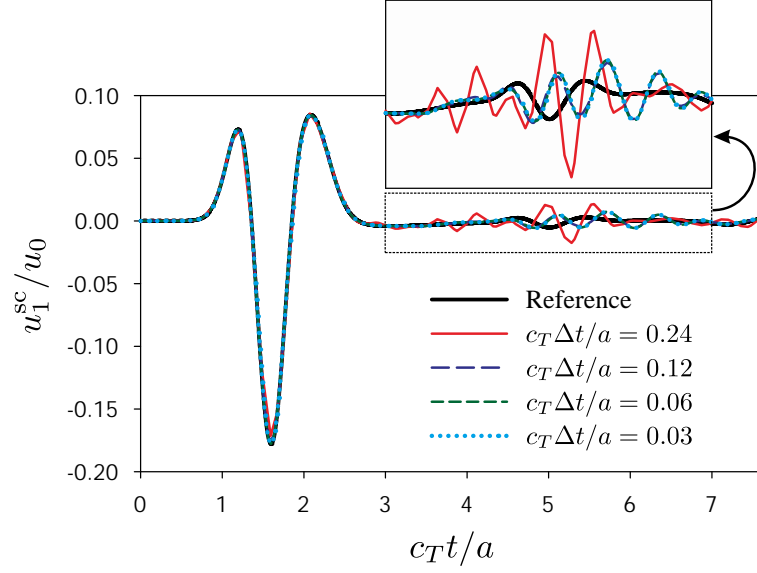


Figure 3.12.: Time variations of u_1^{sc}/u_0 obtained by using RK3 at point X in Fig. 3.9 when $M_e = 9280$.

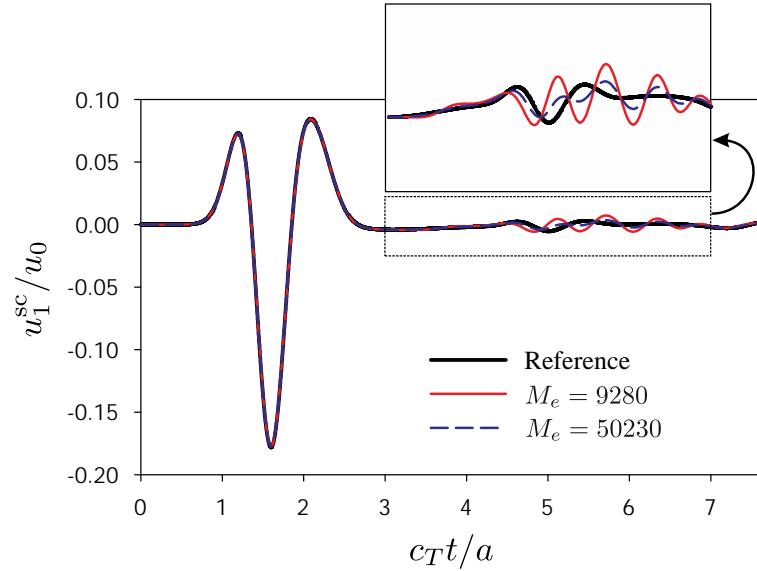


Figure 3.13.: Time variations of u_1^{sc}/u_0 obtained by using RK3 at point X in Fig. 3.9 when $c_T \Delta t/a = 0.06$.

time up to $c_T t/a = 3$. However, u_1^{sc}/u_0 is not accurate compared with the reference solutions after $c_T t/a = 3$, and fluctuations can be seen clearly. In particular, larger time increments, e.g., $c_T \Delta t/a = 0.06$ or 0.03 , give less accurate results. Consequently, a small time increment is required for accurate computation of u_1^{sc}/u_0 for the time range between $c_T t/a = 4$ to 7 .

As shown in Figs. 3.11 and 3.12, better accuracy can be obtained by the RK2 and RK3 for the cases of $c_T \Delta t/a = 0.06$ and 0.03 than that by the BDF2. The fluctuations of u_1^{sc}/u_0 increase with

3.1. Fast multipole accelerated CQ-BEM (CQ-FMBEM)

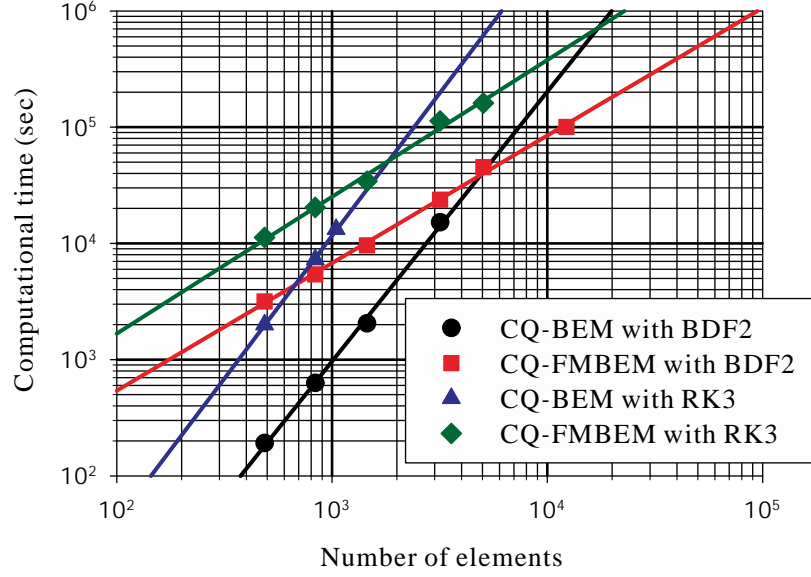


Figure 3.14.: Computational time comparison between CQ-BEM and CQ-FMBEM using BDF2 and RK3 for 3-D elastic wave problem.

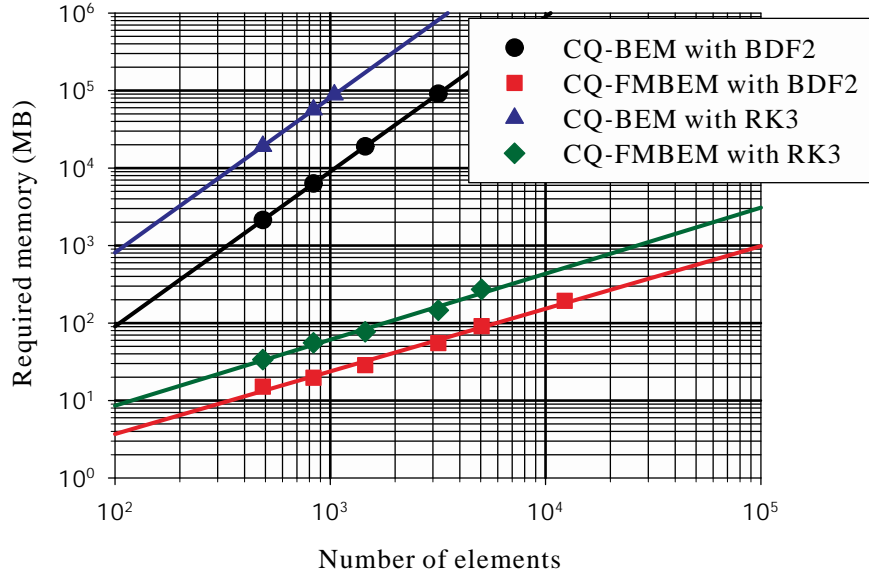


Figure 3.15.: Required memory comparison between CQ-BEM and CQ-FMBEM using BDF2 and RK3 for 3-D elastic wave problem.

increasing time increments. u_1^{sc}/u_0 calculated by the RK2 and RK3 using $c_T \Delta t/a = 0.03$ and 0.06 seem to be sufficiently accurate with the exception of a slight oscillation at about $c_T t/a = 5$.

The effect of spatial discretization of the BIE on the numerical solutions is next investigated. Fig. 3.13 shows u_1^{sc}/u_0 as a function of time at point X in Fig. 3.9 in the cases of $M_e = 9280$ and 50230 . These results are calculated by the RK3 using $c_T \Delta t/a = 0.06$. As expected, a large number of boundary elements, $M_e = 50230$, give more accurate results than $M_e = 9280$. The accuracy of the

3. Acceleration of CQ-BEM

Table 3.1.: Computational time and required memory of CQ-FMBEM when $N = 128$ and $M_e = 5048$.

	BDF2 ($m = 1$)	RK2	RK3
Computational time (sec)	45291	115860	161140
Required memory (MB)	91	174	272

numerical results can be improved either by using high order elements for the spatial discretization or by increasing the number of boundary elements.

The computational time and memory needed by the CQ-FMBEM with BDF2 and RK3 are shown in Figs. 3.14 and 3.15, respectively. The time increment $c_T \Delta t/a = 0.08$ and the total time step $N = 128$ are used here, and all computations are performed by a single processor. As shown in Fig. 3.14, the CQ-FMBEM with BDF2 is faster than the CQ-BEM with BDF2 when the number of elements M_e is $M_e = 5000$ or more. Moreover, the memory required by the CQ-FMBEM is much less than that by the CQ-BEM as shown in Fig. 3.15. The CQ-BEM with BDF2 could not be performed when the number of elements M_e is $M_e = 4000$ or more because of memory restriction. The similar behavior is seen for RK3. Consequently, the CQ-FMBEM is more efficient for large-scale problems than the CQ-BEM.

Next, the relation between the stage number of IRK method m and the computational efficiency of the proposed method is considered. The sub-matrix of influence functions becomes $3m \times 3m$ size as shown in Eqs. (3.38) and (3.39). However, the argument λ_β^l used in Eqs. (3.38) and (3.39), which corresponds to the Laplace parameter, has m components per l . Only m kinds of translation operators for each of M2M, M2L, and L2L are required in the FMM although the multiplications in the translation theorem and near-field contribution require $O(m^2)$ calculation. Therefore, for small m and large M_e , it is expected that the combination of the FMM and IRK-based CQ-BEM can reduce the computational cost as the stage number of the IRK method increases. Table 3.1 presents the computational time and memory for BDF2, RK2, and RK3 when $N = 128$ and $M_e = 5048$. As shown in Table 3.1, the computational time seems to be not $O(m^2)$ but faster than it. However, the behavior of computational time with respect to m is not stable because the M2L truncation depends on λ_β^l . On the other hand, the memory complexity for m is $O(m)$, and this fact is obviously confirmed from Table 3.1.

3.1.7. CQ-FMBEM for 3-D coupled acoustic-elastic wave problems

In this section, the formulation and numerical results of the CQ-FMBEM for the 3-D coupled acoustic-elastic wave problems are presented. The CQ-FMBEM for this problem has been developed by Maruyama *et al.* [53].

Let S be a closed interface between a fluid domain D^f and solid domain D^s as depicted in Fig. 3.16. The superscripts of normal vector \mathbf{n} , f and s , indicate respective domains, and \mathbf{s} denotes the unit tangential vector to S . Disregarding the body force, the pressure p in D^f and displacement \mathbf{u}

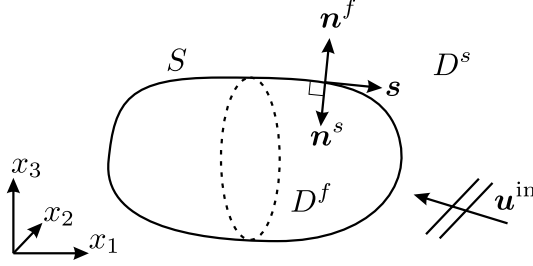


Figure 3.16.: Analysis model 3-D for coupled acoustic-elastic wave problems

in D^s satisfy the following governing equations:

$$c_f^2 \nabla^2 p(\mathbf{x}, t) = \ddot{p}(\mathbf{x}, t) \quad \mathbf{x} \in D^f, \quad (3.59)$$

$$c_T^2 \nabla^2 \mathbf{u}(\mathbf{x}, t) + (c_L^2 - c_T^2) \nabla \nabla \cdot \mathbf{u}(\mathbf{x}, t) = \ddot{\mathbf{u}}(\mathbf{x}, t) \quad \mathbf{x} \in D^s. \quad (3.60)$$

Taking into account the continuity of displacement and traction force on the interface S , the interface conditions are given as follows:

$$-\rho_f \mathbf{n}^f(\mathbf{x}) \cdot \ddot{\mathbf{u}}(\mathbf{x}, t) = q(\mathbf{x}, t) \quad \mathbf{x} \in S, \quad (3.61)$$

$$\mathbf{n}^s(\mathbf{x}) \cdot \mathbf{t}(\mathbf{x}, t) = -p(\mathbf{x}, t) \quad \mathbf{x} \in S, \quad (3.62)$$

$$\mathbf{s}(\mathbf{x}) \cdot \mathbf{t}(\mathbf{x}, t) = 0 \quad \mathbf{x} \in S, \quad (3.63)$$

where ρ_f is the density of fluid. Assuming that the incident wave exists in D^s and that D^f is closed inner domain as depicted in Fig. 3.16, the initial conditions for wave scattering problems are given as follows:

$$\mathbf{u}(\mathbf{x}, 0) = \mathbf{u}^{\text{in}}(\mathbf{x}, 0) \quad \mathbf{x} \in D^s, \quad (3.64)$$

$$\mathbf{u}(\mathbf{x}, 0) = \dot{\mathbf{u}}(\mathbf{x}, 0) = \mathbf{0} \quad \mathbf{x} \in S, \quad (3.65)$$

$$p(\mathbf{x}, 0) = \dot{p}(\mathbf{x}, 0) = 0 \quad \mathbf{x} \in D^f, S. \quad (3.66)$$

Using boundary conditions (3.61)–(3.63), the time-domain BIEs for pressure (2.27) and displacement (3.36) can be solved simultaneously.

Substituting Eqs. (3.61)–(3.63) into BIEs (2.27) and (3.36) and assuming that $p^{\text{in}} = 0$ yield the following BIEs:

$$\begin{aligned} C(\mathbf{x})\eta(\mathbf{x}, t) = & \rho_f \int_0^t \int_S G(\mathbf{x}, \mathbf{y}, t - \tau) \mathbf{n}^f(\mathbf{y}) \cdot \ddot{\mathbf{u}}(\mathbf{y}, \tau) dS_y d\tau \\ & - \int_0^t \text{p.v.} \int_S H(\mathbf{x}, \mathbf{y}, t - \tau) \eta(\mathbf{y}, \tau) dS_y d\tau, \end{aligned} \quad (3.67)$$

3. Acceleration of CQ-BEM

$$\begin{aligned} \mathbf{C}(\mathbf{x}) \cdot \mathbf{u}(\mathbf{x}, t) = & \mathbf{u}^{\text{in}}(\mathbf{x}, t) + \int_0^t \int_S \mathbf{U}(\mathbf{x}, \mathbf{y}, t - \tau) \cdot \mathbf{n}^s(\mathbf{y}) \eta(\mathbf{y}, \tau) dS_y d\tau \\ & - \int_0^t \text{p.v.} \int_S \mathbf{T}(\mathbf{x}, \mathbf{y}, t - \tau) \cdot \mathbf{u}(\mathbf{y}, \tau) dS_y d\tau, \end{aligned} \quad (3.68)$$

where η is defined by $\eta = \mathbf{n}^s \cdot \mathbf{t}$. The second derivative of displacement with respect to time $\ddot{\mathbf{u}}$ is contained in the right-hand side of Eq. (3.67). This second derivative has to be numerically treated by some techniques in order to simultaneously solve Eqs. (3.67) and (3.68). Using the CQM formulation, it is easy to treat time differential terms.

Taking into account the identity of convolution integral

$$\frac{d}{dt} (k * g)(t) = (\dot{k} * g)(t) + k(0)g(t)$$

and initial condition (3.65), the second term in the right-hand side of Eq. (3.67) can be modified as follows:

$$\begin{aligned} \rho_f \int_0^t \int_S G(\mathbf{x}, \mathbf{y}, t - \tau) \mathbf{n}^f(\mathbf{y}) \cdot \ddot{\mathbf{u}}(\mathbf{y}, \tau) dS_y d\tau \\ = \rho_f \int_0^t \int_S \ddot{G}(\mathbf{x}, \mathbf{y}, t - \tau) \mathbf{n}^f(\mathbf{y}) \cdot \mathbf{u}(\mathbf{y}, \tau) dS_y d\tau. \end{aligned} \quad (3.69)$$

As shown in Eq. (3.69), derivatives of quantity are no longer included. Next, the discretization of Eqs. (3.67) and (3.68) and the numerical treatment of differentiated fundamental solution \ddot{G} in Eq.(3.69) using the CQM are presented.

CQ-BEM formulation

In numerically solving the BIEs (3.67) and (3.68), the convolution integrals are evaluated by means of the IRK-based CQM, and the surface integrals over the interface S are discretized by the piecewise constant approximation. The discretized BIEs at n -th and i -th sub-step in time are written as follows:

$$\frac{1}{2} \eta_{\gamma}^{i;n} = \sum_{k=0}^n \sum_{\alpha=1}^M \sum_{j=1}^m \left[\rho_f \mathcal{D}_{\gamma\alpha}^{ij;n-k} \mathbf{n}_{\alpha}^f \cdot \mathbf{u}_{\alpha}^{j;k} - \mathcal{H}_{\gamma\alpha}^{ij;n-k} \eta_{\alpha}^{j;k} \right], \quad (3.70)$$

$$\frac{1}{2} \mathbf{u}_{\gamma}^{i;n} = \mathbf{u}_{\gamma}^{\text{in};i;n} + \sum_{k=0}^n \sum_{\alpha=1}^M \sum_{j=1}^m \left[\mathcal{U}_{\gamma\alpha}^{ij;n-k} \cdot \mathbf{n}_{\alpha}^s \eta_{\alpha}^{j;k} - \mathcal{T}_{\gamma\alpha}^{ij;n-k} \cdot \mathbf{u}_{\alpha}^{j;k} \right], \quad (3.71)$$

where $\mathcal{D}_{\gamma\alpha}^{ij;\kappa}$ is the influence function with respect to the differentiated fundamental solution \ddot{G} and given as follows:

3.1. Fast multipole accelerated CQ-BEM (CQ-FMBEM)

$$\mathcal{D}_{\gamma\alpha}^{ij;\kappa} = \tilde{\mathcal{F}}_{l\kappa}^{-1} \left[\sum_{\beta=1}^m (\lambda_{\beta}^l)^2 \left(\mathbf{E}_{\beta}(\zeta_l) \right)_{ij} \int_{S_{\alpha}} \hat{G}(\mathbf{x}_{\gamma}, \mathbf{y}, \lambda_{\beta}^l) dS_y \right]. \quad (3.72)$$

$(\lambda_{\beta}^l)^2$ in Eq. (3.72) is difference between $\mathcal{D}_{\gamma\alpha}^{ij;\kappa}$ and $\mathcal{G}_{\gamma\alpha}^{ij;\kappa}$ in Eq. (2.29). This term is caused by the differentiation with respect to time because Laplace-domain kernel functions are used here. The Laplace transform of time differentiated function is given as follows:

$$\mathcal{L} [\dot{k}(t)] = s\hat{k}(s).$$

From the above, BIEs (3.67) and (3.68) can be solved simultaneously with the easy treatment of the second derivative of displacement.

We confirm the numerical errors of calculating the second differentiation of fundamental solution in the CQM through numerical experiment. Therefore, the following convolution integral is computed in two ways, and their results are compared.

$$\begin{cases} u(t) = \int_0^t G(\mathbf{x}, \mathbf{y}, t - \tau) \ddot{\psi}(\tau) d\tau & 0 < t, \\ \psi(t) = t^3 e^t H(t), \end{cases} \quad (3.73a)$$

$$(3.73b)$$

where G is specifically described as follows:

$$G(\mathbf{x}, \mathbf{y}, t) = \frac{1}{4\pi r} \delta \left(t - \frac{r}{c_f} \right), \quad (3.74)$$

where $\delta(\cdot)$ is the Dirac delta distribution. The exact solution of u in Eq. (3.73) can be obtained as follows:

$$u(t) = \frac{1}{4\pi r} \ddot{\psi} \left(t - \frac{r}{c_f} \right). \quad (3.75)$$

We investigate the relative errors caused by numerical computation of Eq. (3.73) in the following two ways.

case 1 The CQM is applied to Eq. (3.73a) after differentiation of ψ . In other words, the following equation is evaluated by means of the CQM.

$$\bar{u}(t) = \int_0^t G(\mathbf{x}, \mathbf{y}, t - \tau) (\tau^3 + 6\tau^2 + 6\tau) e^{\tau} d\tau. \quad (3.76)$$

case 2 As well as the proposed method, the convolution integral including the second differentiation of fundamental solution is computed by the CQM. Namely, the following equation is computed by the CQM.

$$\bar{u}(t) = \int_0^t \ddot{G}(\mathbf{x}, \mathbf{y}, t - \tau) \tau^3 e^{\tau} d\tau. \quad (3.77)$$

3. Acceleration of CQ-BEM

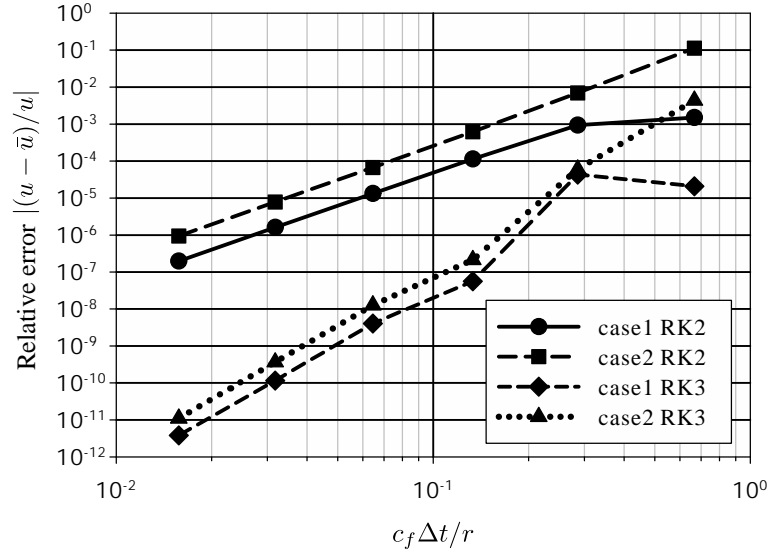


Figure 3.17.: Relative errors for calculating convolution integral (3.73) vs. time increments using IRK-based CQM with RK2 and RK3.

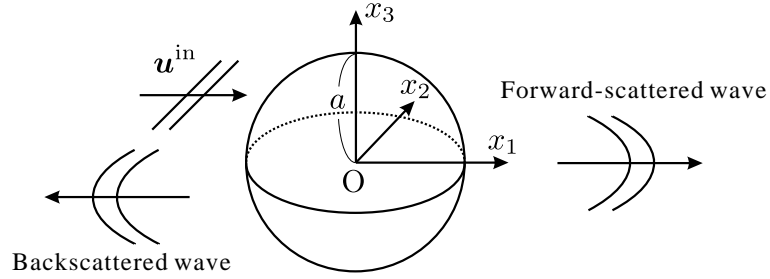


Figure 3.18.: Elastic wave scattering by a spherical obstacle subjected to an incident plane wave.

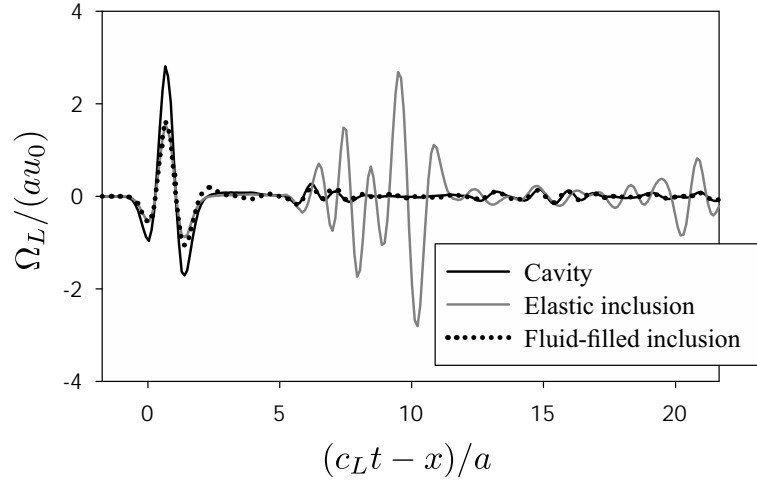
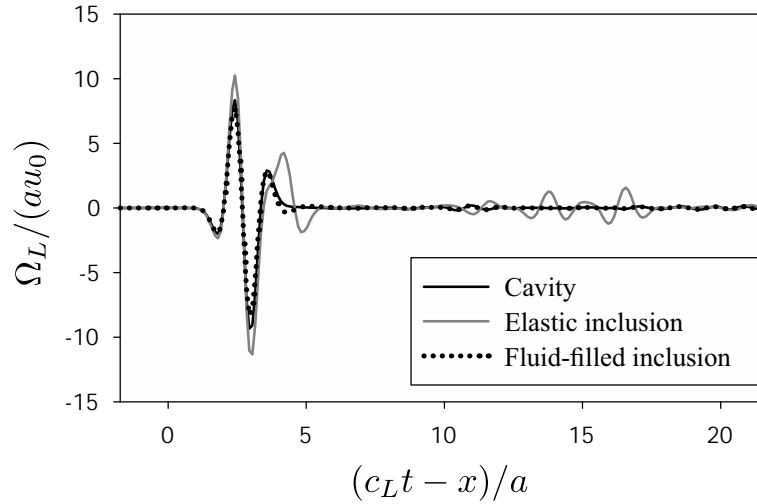
The total analysis time is $c_f t/r = 2$, and we investigate computational errors varying the time increment $c_f \Delta t/r$. In addition, the RK2 and RK3 are used for the CQM. The relative errors $|(u - \bar{u})/u|$ caused by both cases are plotted in Fig. 3.17. As we can see from Fig. 3.17, behavior of errors is unstable when $c_f \Delta t/r$ is comparatively large. However, the slopes of relative errors caused by case 1 and case 2 are identical, and their behavior is stable when $c_f \Delta t/r$ is sufficiently small. An increase of computational error from case 1 to case2 is considered as caused by the rapid fluctuation of differentiated fundamental solution. However, we can use the numerical approach of case 2 if $c_f \Delta t/r$ is sufficiently small.

Numerical results

The numerical examples deal with the scattering problems of an incident plane wave by a spherical cavity, elastic inclusion, and fluid-filled inclusion as depicted in Fig. 3.18. In this section, the far-field approximations of scattered wave $u^{sc;far}$ are evaluated, and their details can be found in

Table 3.2.: Material constants for base material and inclusions.

	P wave velocity	S wave velocity	Density
Base material	c_L	c_T	ρ
Elastic inclusion	$c_L/\sqrt{3}$	$c_T/\sqrt{3}$	$\rho/2$
Fluid-filled inclusion	$c_L/\sqrt{3}$	—	$\rho/2$


 Figure 3.19.: Time variations of far-field backscattered amplitude $\Omega_L/(au_0)$ for various obstacles subjected to an incident plane P wave.

 Figure 3.20.: Time variations of far-field forward-scattered amplitude $\Omega_L/(au_0)$ for various obstacles subjected to an incident plane P wave.

Appendix B. The Ricker wave described in Eq. (3.58) is used as an incident plane wave. We present numerical results of P and SV wave incidence, and \mathbf{d}_φ is given by $\mathbf{d}_L = (1, 0, 0)$ and $\mathbf{d}_{TV} = (0, 1, 0)$. Time parameters are set as $\lambda_L^{\text{in}}/a = \sqrt{3}$, $t_s = 1/f^{\text{in}}$, $c_T \Delta t/a = 0.12$, and

3. Acceleration of CQ-BEM

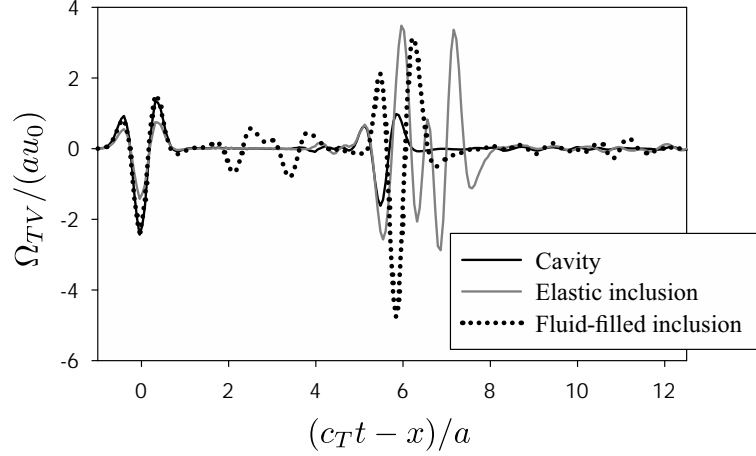


Figure 3.21.: Time variations of far-field backscattered amplitude $\Omega_{TV}/(au_0)$ for various obstacles subjected to an incident plane SV wave.

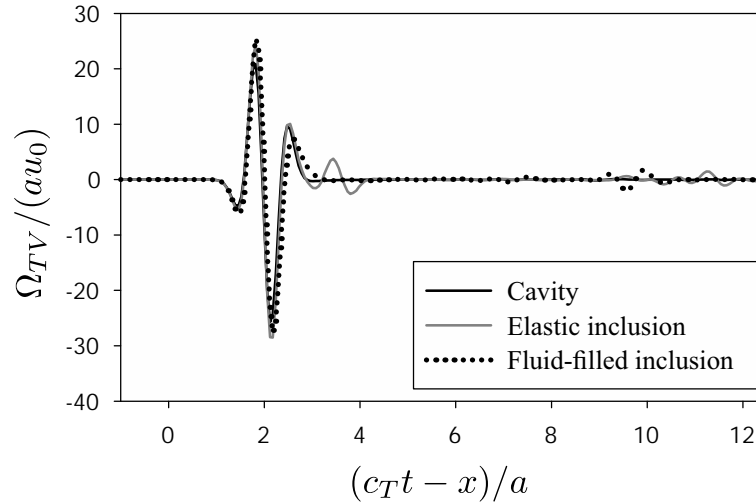


Figure 3.22.: Time variations of far-field forward-scattered amplitude $\Omega_{TV}/(au_0)$ for various obstacles subjected to an incident plane SV wave.

$N = 128$. In addition, the RK3 is used for the CQM. Material constants for base material, elastic inclusion, and fluid-filled inclusion are shown in Table 3.2, and Poisson's ratio of base material ν is given by $\nu = 0.25$. As shown in Table 3.2, the acoustic impedance of elastic inclusion for P wave is identical with the one of fluid-filled inclusion. For all numerical simulations in this section, the surface of obstacle is divided into $M_e = 9280$ flatly triangular boundary elements.

Figs. 3.19 and 3.20 show the time histories of $\Omega_L/(au_0)$ corresponding to backscattered and forward-scattered waves, respectively, when an incident plane P wave is scattered by a various spherical obstacle. Ω_φ is the far-field scattered amplitude and found in Appendix B. As shown in Fig. 3.19, the amplitudes of the first wave at about $(c_L t - x)/a = 0.7$ generated by elastic and fluid-filled inclusions are almost same because their acoustic impedances for P wave are identical.

Table 3.3.: Computational time (sec).

	Cavity	Elastic inclusion	Fluid-filled inclusion
P wave scattering	41959	220103	114366
S wave scattering	41999	223366	114952

In addition, the phase of waveform at about $(c_L t - x)/a = 0.7$ is the inverse of incident wave, and then, large amplitude waves arrive in the case of elastic inclusion. These phenomena have also been observed in the previous 2-D simulation [64]. On the other hand, there is only slight difference among far-field forward-scattered waves by various obstacles as shown in Fig. 3.20.

Figs. 3.21 and 3.22 show the time histories of $\Omega_{TV}/(au_0)$ corresponding to backscattered and forward-scattered waves, respectively, when an incident plane SV wave is scattered by various spherical obstacles. In this simulation, \hat{v} in Appendix B is given by $\hat{v} = (0, 1, 0)$. As shown in Fig. 3.21, the amplitudes of the first wave in the cases of cavity and fluid-filled inclusion are almost same, and the one in the case of elastic inclusion is comparatively small. This is because S waves are completely reflected on the cavity and fluid-solid interfaces. In addition, the secondary waves at about $(c_T t - x)/a = 6.0$ are greatly dissimilar among different obstacles. There is only slight difference among far-field forward-scattered waves as shown in Fig. 3.22 similarly to the case of P wave scattering.

The computational time required for solving the boundary value problems is shown in Table 3.3. The numerical simulations were conducted using the OpenMP parallelization with 24 threads. As shown in Table 3.3, the most expensive case costs about 3 days.

3.2. Acceleration for number of time steps

The acceleration of CQ-BEM for the number of elements using the FMM had been discussed until the previous section. However, there remains the issue of computational cost with respect to the number of time steps N , and the computational complexity of CQ-FMBEM with respect to N is still $O(N^2)$. This computational complexity prevents the application of CQ-FMBEM to a long time analysis. Therefore, the time-marching process of CQ-FMBEM is improved using the rapid convolution algorithm [31] without error increasing in this section. A new M2L truncation condition can be introduced through the rapid convolution algorithm. Consequently, the total computational complexity of a new CQ-FMBEM becomes about $O(NM_e \log N \log M_e)$, and that is demonstrated by showing some numerical results.

3.2.1. New time-marching process of CQ-FMBEM

In this section, the calculation process of matrix-vector products with respect to time for Eq.(3.3) is improved by using the rapid convolution algorithm. The right-hand side of Eq. (3.3) consists of the Toeplitz matrix depicted in Fig. 3.23 (a) and the boundary value vector. Moreover, we can use

3. Acceleration of CQ-BEM

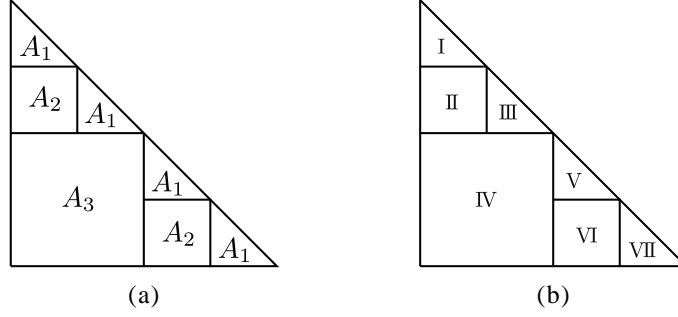


Figure 3.23.: (a) Coefficient matrix structure for time and (b) calculation order of sub-matrix in the rapid convolution algorithm [31].

Algorithm 1 Select h at n -th step.

```

1:  $i \leftarrow n$ 
2: for  $j = 0, \dots$  do
3:    $k \leftarrow 2^j$ 
4:   if  $k = i$  then
5:      $h \leftarrow k$ 
6:     exit
7:   else if  $k > i$  then
8:      $i \leftarrow i - 2^{j-1}$ 
9:     goto 2
10:  end if
11: end for

```

only past boundary values, i.e. $\mathbf{q}^0, \dots, \mathbf{q}^{n-1}$ at n -th step. This type of matrix-vector products can be evaluated by the rapid algorithm using FFT with $O(N \log^2 N)$ computational complexity [31]. In this algorithm, the product of $2^n \times 2^n$ sub-matrix and 2^n dimensional sub-vector is calculated at every time step because of using the FFT.

According to [31], the multiplication of sub-matrix and sub-vector is conducted in the order shown in Fig. 3.23 (b). Specifically, we calculate the following matrix-vector product at n -th step.

$$\begin{Bmatrix} \mathbf{S}^n \\ \mathbf{S}^{n+1} \\ \vdots \\ \mathbf{S}^{n+h-1} \end{Bmatrix} = \begin{bmatrix} \mathbf{G}^h & \mathbf{G}^{h-1} & \dots & \mathbf{G}^1 \\ \mathbf{G}^{h+1} & \mathbf{G}^h & \dots & \mathbf{G}^2 \\ \vdots & \vdots & & \vdots \\ \mathbf{G}^{2h-1} & \mathbf{G}^{2h-2} & \dots & \mathbf{G}^h \end{bmatrix} \begin{Bmatrix} \mathbf{q}^{n-h} \\ \mathbf{q}^{n-h+1} \\ \vdots \\ \mathbf{q}^{n-1} \end{Bmatrix}. \quad (3.78)$$

Then, the resulting vector \mathbf{S}^κ is used to update \mathbf{R}^κ as follows:

$$\mathbf{R}^\kappa + \mathbf{S}^\kappa \Rightarrow \mathbf{R}^\kappa \quad \text{for } \kappa = n, \dots, n + h - 1.$$

An appropriate h has to be chosen for efficient computation using the FFT, and h at n -th step can be determined by Algorithm 1. As shown in Algorithm 1, h is always an exponent of two.

Now, we explain the computational procedure of Eq. (3.78) using the rapid convolution algorithm. The Fourier-domain influence function $\tilde{\mathcal{G}}_{\gamma\alpha}^{ij;l}$ is defined by

$$\tilde{\mathcal{G}}_{\gamma\alpha}^{ij;l} = \tilde{\mathcal{F}}_{\kappa l} [\mathcal{G}_{\gamma\alpha}^{ij;\kappa}] = \sum_{\beta=1}^m \left(\mathbf{E}_{\beta}(\zeta_l) \right)_{ij} \int_{S_{\alpha}} \hat{G}(\mathbf{x}_{\gamma}, \mathbf{y}, \lambda_{\beta}^l) dS_y, \quad (3.79)$$

and the corresponding component of matrix in Eq. (3.78) is described as $\tilde{\mathbf{G}}^l$. The computational procedure of the rapid convolution algorithm at n -th step is summarized as follows:

1. The vector consisting of $2h$ components $\{\mathbf{q}^{n-h}, \dots, \mathbf{q}^{n-1}, 0, \dots, 0\}^T$ is transformed by discrete Fourier transform (2.10) as follows:

$$\{\tilde{\mathbf{q}}^0, \dots, \tilde{\mathbf{q}}^{2h-1}\}^T = \tilde{\mathcal{F}} \left[\{\mathbf{q}^{n-h}, \dots, \mathbf{q}^{n-1}, 0, \dots, 0\}^T \right]. \quad (3.80)$$

2. The components of Fourier-domain matrix $\tilde{\mathbf{G}}^l$ and the vector in the left-hand side of Eq. (3.80) are multiplied, and the resulting vector is transformed by inverse discrete Fourier transform (2.11) as follows:

$$\{\mathbf{P}^0, \dots, \mathbf{P}^{2h-1}\}^T = \tilde{\mathcal{F}}^{-1} \left[\{\tilde{\mathbf{G}}^0 \tilde{\mathbf{q}}^0, \dots, \tilde{\mathbf{G}}^{2h-1} \tilde{\mathbf{q}}^{2h-1}\}^T \right]. \quad (3.81)$$

In the right-hand side of Eq. (3.81), $\tilde{\mathbf{G}}^l \tilde{\mathbf{q}}^l$ for each l includes the matrix-vector products with respect to space. Therefore, the spatial matrix-vector products are rapidly evaluated by the FMM. In addition, the following identity is also used for the efficient calculation of the right-hand side of Eq. (3.81).

$$\tilde{\mathbf{G}}^{2h-l} \tilde{\mathbf{q}}^{2h-l} = \overline{\tilde{\mathbf{G}}^l \tilde{\mathbf{q}}^l} \quad (l = 1, \dots, h-1). \quad (3.82)$$

As a result of Eq. (3.82), $h+1$ spatial matrix-vector products are required in the right-hand side of Eq. (3.81).

3. Considering the relation between \mathbf{S}^{κ} in the left-hand side of Eq. (3.78) and \mathbf{P}^{κ} in the left-hand side of Eq. (3.81),

$$\{\mathbf{S}^n, \dots, \mathbf{S}^{n+h-1}\}^T = \{\mathbf{P}^h, \dots, \mathbf{P}^{2h-1}\}^T, \quad (3.83)$$

\mathbf{S}^{κ} can be determined, and \mathbf{R}^{κ} can be updated.

In order to use the FFT for the forward and inverse discrete Fourier transforms in the above, L is given by $L = 2h$. In the total calculation process of retarded potential term, the computational complexities of FFT and FMM are about $O(NM_e \log^2 N)$ and $O(NM_e \log N \log M_e)$, respectively. The computational time of FFT is usually much smaller than that of FMM, and therefore, the total computational complexity is considered as about $O(NM_e \log N \log M_e)$. In addition, the memory requirement of the proposed CQ-FMBEM is in $O(NM_e)$ order.

3.2.2. Truncation condition for M2L using arrival time of influence waves

A new condition is introduced to the truncation of M2L in this section. The attenuative feature of Laplace-domain fundamental solution has been used for the conventional M2L truncation in Section 3.1.3. Moreover, arrival time of influence waves is considered for the additional truncation condition.

As shown in Eq. (3.78), the influence functions from first to $(2h - 1)$ -th step are used for the evaluation of influence waves at n -th step. Therefore, the M2L calculation between two cells which satisfy the following condition can be neglected.

$$c_\varphi \Delta t (2h - 1 + c_m) < d_{\text{M2L}} - 2\varrho, \quad (3.84)$$

where $d_{\text{M2L}} - 2\varrho$ is used instead of the minimum distance between two cells r_{\min} , similarly to Section 3.1.3. The notations, d_{M2L} , ϱ , and r_{\min} , are found in Fig. 3.3. This new truncation is effective in sub-matrices near the diagonal of Toeplitz matrix with respect to time because it is expected that many components before arrival of influence waves are included in them.

3.2.3. Numerical results

To verify accuracy and to demonstrate the computational efficiency of the new CQ-FMBEM, some numerical results are presented here. The same analysis model as Section 2.3 depicted in Fig. 2.3 is used for this numerical simulation. All numerical simulations in this section are conducted using the RK3.

First, we compare numerical solutions obtained by the conventional CQ-FMBEM presented in Section 3.1 with the ones obtained by the new CQ-FMBEM proposed in this section. Fig. 3.24 shows the time histories of p/p_0 at point X in Fig. 2.3 when $c_f \Delta t/a = 0.069$. As we can see from Fig. 3.24, the waveforms of p/p_0 obtained by the conventional and new CQ-FMBEMs are very similar. On the other hand, absolute errors between p/p_0 obtained by the conventional and new CQ-FMBEMs are plotted in Fig. 3.25. These errors are caused by the rapid convolution algorithm and new M2L truncation. Comparing between Figs. 3.5 and 3.25, the magnitude of errors in Fig. 3.25 is very small compared with that caused by the FMM.

Second, the computational efficiency of the new CQ-FMBEM is presented when computations are conducted by a single processor. The computational time varying the number of elements M_e for both conventional and new CQ-FMBEMs is shown in Fig. 3.26. As shown in Fig. 3.26, the new CQ-FMBEM is much faster than the conventional one. The slopes of regression lines for the conventional and new CQ-FMBEMs are larger than $O(M_e)$ and a little smaller than $O(M_e \log M_e)$. On the other hand, the computational time varying the number of time steps N for both conventional and new CQ-FMBEMs are shown in Fig. 3.27. As shown in Fig. 3.27, the slopes of regression lines for the conventional and new CQ-FMBEMs are greatly different. The slope of regression line for the new CQ-FMBEM is very similar to $O(N \log N)$ although the one for the conventional CQ-FMBEM is about $O(N^2)$. From the above, the total computational complexity of the new

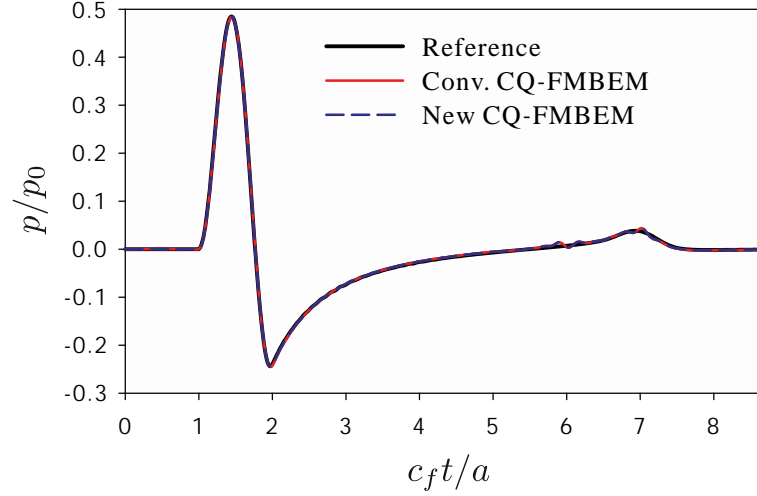


Figure 3.24.: Time variations of p/p_0 obtained by conventional and new CQ-FMBEMs using RK3 at point X in Fig. 2.3 when $c_f \Delta t/a = 0.069$.

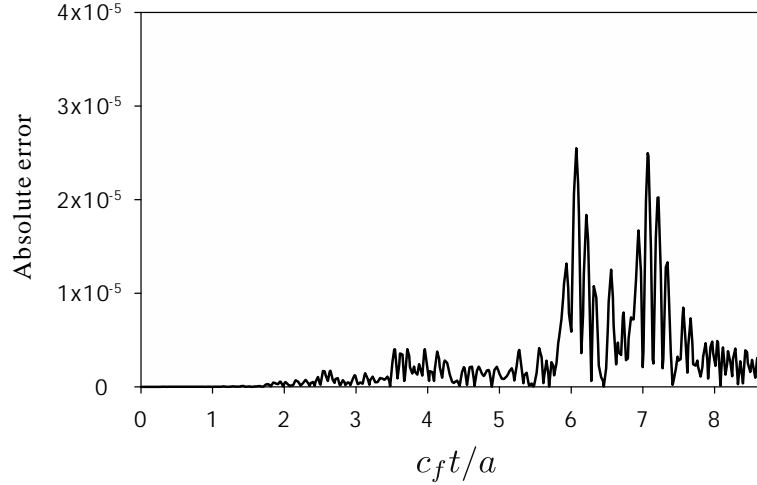


Figure 3.25.: Absolute errors between p/p_0 obtained by conventional and new CQ-FMBEMs, which are plotted in Fig. 3.24.

CQ-FMBEM is considered as $O(NM_e \log N \log M_e)$, which is much faster than the conventional $O(N^2 M_e \log M_e)$.

Finally, the situation of M2L truncation is presented in Fig. 3.28 when $N = 128$ and $M = 3176$. The ratio of the truncated number to the total number of M2L moments is plotted in Fig. 3.28. The case of using only conventional condition (3.33) is presented in Fig. 3.28 (a). As shown in Fig. 3.28 (a), the ratio of M2L truncation is about 0.2 on every sub-matrix. On the other hand, the case of using both conventional and new conditions is presented in Fig. 3.28 (b). The ratio of M2L truncation becomes large as the sub-matrix approaches the diagonal. This is because the new M2L truncation condition (3.84) is effective in the sub-matrices of small size.

3. Acceleration of CQ-BEM

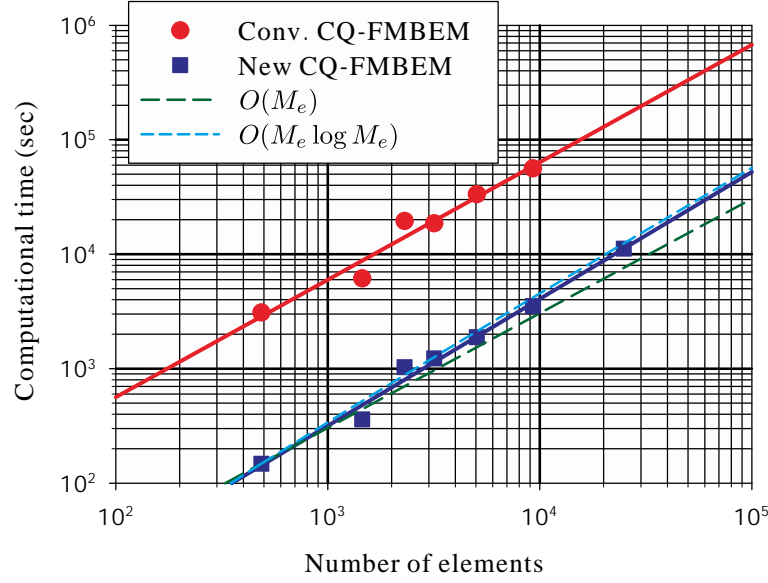


Figure 3.26.: Computational time comparison between conventional and new CQ-FMBEMs using RK3 for 3-D acoustic wave problem varying the number of elements M_e .

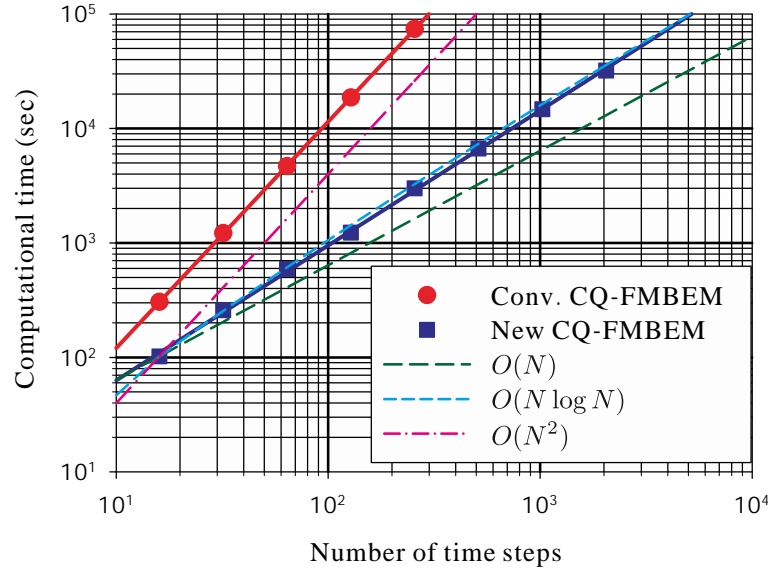


Figure 3.27.: Computational time comparison between conventional and new CQ-FMBEMs using RK3 for 3-D acoustic wave problem varying the number of time steps N .

3.3. Concluding remarks

- In Chapter 3, we have successfully applied the FMM to the IRK-based CQ-BEM for 3-D acoustic and elastic wave problems and their coupled one. Moreover, the application of the rapid convolution algorithm to the time-marching process in CQ-FMBEM has been shown, and it has significantly improved the computational efficiency of the CQ-FMBEM with re-

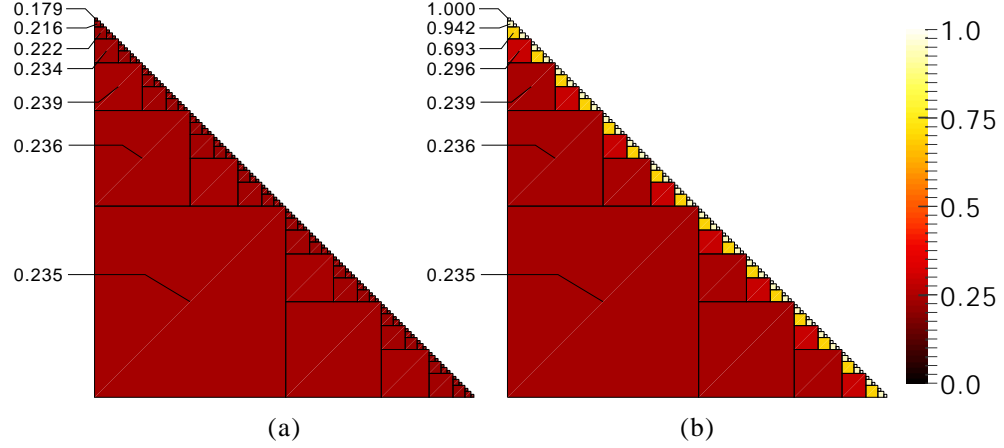


Figure 3.28.: Ratio of M2L truncation for each sub-matrix in triangular Toeplitz system using (a) only conventional truncation condition (3.33) and (b) both conventional and new ones when $N = 128$ and $M_e = 3176$.

spect to the number of time steps.

- In the CQ-FMBEM, many M2L moments can be truncated using condition (3.33) because the FMM calculation is carried out in Laplace-domain. Using the rapid convolution algorithm [31] enables the additional truncation condition (3.84) for M2L calculation. The additional condition is effective in the small sub-matrices near the diagonal of the coefficient matrix with respect to time.
- The other fast CQ-BEM proposed by Banjai and Kachanovska [8], which is based on the \mathcal{H} -matrix, requires $O(NM_e \log M_e)$ memory. Their method [8] can be more widely applied to various problems than our proposed CQ-FMBEM because the applicability of our method depends on the multipole expansion of fundamental solutions. However, our proposed CQ-FMBEM requires only $O(NM_e)$ memory and less than their method.
- In Chapters 2 and 3, only the combination of collocation method and piecewise constant approximation has been used for the spatial discretization. There remains some problems in accuracy with respect to spatial discretization as shown in Section 3.1.6. However, it is not very difficult to use the higher order element or to apply the Galerkin discretization to the proposed CQ-FMBEM. It is emphasized that the computational and memory complexities are not changed if these improvements of spatial discretization are considered.

Chapter 4

3-D Simulation of Higher-harmonic Waves Due to an Interface Crack of Bi-material

The boundary element formulation and numerical implementation for wave scattering by an interface crack with contact boundary conditions between two semi-infinite elastic solids are presented in this chapter. For this problem, the numerical method has been developed and some higher-harmonic simulations have been implemented by Maruyama *et al.* [54]. First, the BIE is formulated for wave scattering by an interface crack. Second, the contact boundary conditions on the interface crack are described, and the procedure of numerical implementation is explained using the flow chart. Finally, we show some numerical results and discuss the characteristic of the higher-harmonic generation.

4.1. Problem statement and BIE

A 3-D boundary element analysis model for nonlinear ultrasonic simulation is considered for two-layered semi-infinite media including debonding areas as shown in Fig. 4.1. This model consists of two semi-infinite domains D^I and D^{II} , which are homogeneous, isotropic, and linearly elastic solids, and the interfaces between them, S_h and S_d , denote bonding and debonding areas, respectively. In addition, \mathbf{n}^ς is defined as a unit outer normal vector to D^ς ($\varsigma = I$ or II), where the superscript denotes the respective domain. Disregarding the body force, displacement \mathbf{u} satisfies the following governing equation in each domain.

$$(c_T^\varsigma)^2 \nabla^2 \mathbf{u}^\varsigma(\mathbf{x}, t) + \left[(c_L^\varsigma)^2 - (c_T^\varsigma)^2 \right] \nabla \nabla \cdot \mathbf{u}^\varsigma(\mathbf{x}, t) = \ddot{\mathbf{u}}^\varsigma(\mathbf{x}, t) \quad \mathbf{x} \in D^\varsigma. \quad (4.1)$$

In this study, a plane wave is used as the incident wave in order to investigate fundamental motions of an interface crack with contact boundary conditions. For the layered media subjected to an incident plane wave, the free field formulation [37] is usually used in the BEM in order to enhance the computational efficiency and accuracy. We assume that the interface S_h is flat and that the

4. 3-D Simulation of Higher-harmonic Waves Due to an Interface Crack of Bi-material

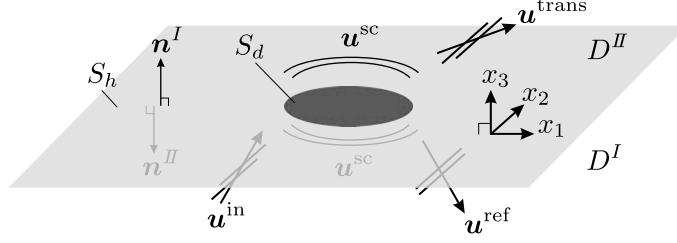


Figure 4.1.: Analysis model for wave scattering by a debonding area on bi-material interface in 3-D.

boundary conditions on S_h are given by the following continuity of displacement and traction:

$$\mathbf{u}^I = \mathbf{u}^{II}, \quad \mathbf{t}^I = -\mathbf{t}^{II}. \quad (4.2)$$

We also assume that \mathbf{u}^{in} exists in D^I . Then, the free field \mathbf{u}^{free} , which consists of incident wave \mathbf{u}^{in} , reflected wave \mathbf{u}^{ref} , and transmitted wave $\mathbf{u}^{\text{trans}}$, can be calculated analytically as presented in Appendix C, and the following relations hold.

$$\mathbf{u}^{\text{free};I} = \mathbf{u}^{\text{in};I} + \mathbf{u}^{\text{ref};I}, \quad \mathbf{u}^{\text{free};II} = \mathbf{u}^{\text{trans};II}. \quad (4.3)$$

Moreover, the superposition principle holds in D^I and D^{II} because they are linearly elastic solids. Therefore, defining the scattered wave \mathbf{u}^{sc} as the disturbance of \mathbf{u}^{free} by the debonding area S_d , the total displacement field \mathbf{u} is described as follows:

$$\mathbf{u} = \mathbf{u}^{\text{free}} + \mathbf{u}^{\text{sc}}. \quad (4.4)$$

Considering the initial condition

$$\mathbf{u}^{\text{sc};\zeta}(\mathbf{x}, 0) = \dot{\mathbf{u}}^{\text{sc};\zeta}(\mathbf{x}, 0) = \mathbf{0} \quad \mathbf{x} \in D^\zeta \quad (4.5)$$

and that \mathbf{u}^{sc} satisfies the Sommerfeld radiation condition, the BIE can be formulated for \mathbf{u}^{sc} as follows:

$$\begin{aligned} \frac{1}{2} \mathbf{u}^{\text{sc};\zeta}(\mathbf{x}, t) &= \int_0^t \int_{S_h+S_d} \mathbf{U}^\zeta(\mathbf{x}, \mathbf{y}, t-\tau) \cdot \mathbf{t}^{\text{sc};\zeta}(\mathbf{y}, \tau) dS_y d\tau \\ &\quad - \int_0^t \text{p.v.} \int_{S_h+S_d} \mathbf{T}^\zeta(\mathbf{x}, \mathbf{y}, t-\tau) \cdot \mathbf{u}^{\text{sc};\zeta}(\mathbf{y}, \tau) dS_y d\tau \quad \mathbf{x} \in S_h, S_d. \end{aligned} \quad (4.6)$$

Substituting Eq. (4.4) into Eq. (4.6), the BIE can be rewritten for the total wave field \mathbf{u} as follows:

$$\begin{aligned} \int_0^t \int_{S_h+S_d} \mathbf{U}^\zeta(\mathbf{x}, \mathbf{y}, t-\tau) \cdot \mathbf{t}^\zeta(\mathbf{y}, \tau) dS_y d\tau - \int_0^t \text{p.v.} \int_{S_h+S_d} \mathbf{T}^\zeta(\mathbf{x}, \mathbf{y}, t-\tau) \cdot \mathbf{u}^\zeta(\mathbf{y}, \tau) dS_y d\tau \\ - \frac{1}{2} \mathbf{u}^\zeta(\mathbf{x}, t) = \mathbf{g}^{\text{free};\zeta}(\mathbf{x}, t) \quad \mathbf{x} \in S_h, S_d, \end{aligned} \quad (4.7)$$

where \mathbf{g}^{free} is equivalent to the left-hand side of Eq. (4.7) in which \mathbf{u} and \mathbf{t} are replaced with \mathbf{u}^{free} and \mathbf{t}^{free} , respectively. Therefore, \mathbf{g}^{free} is the known quantity in the boundary element analysis.

4.2. Discretization of BIE and contact boundary conditions

The asymptotic behavior of stress field in the vicinity of interface crack front between dissimilar materials shows an oscillating singularity [96, 69]. This fact is also known for the anisotropic bi-material [90]. However, it is cumbersome to use the special element which can describe the proper behavior of displacement and stress in the vicinity of crack front. The usual element (specifically, piecewise linear element) has been used for the vicinity of crack front by Wünsche *et al.* [97], and They obtained accurate solutions. Moreover, in this study, we evaluate displacement at far-field as the received wave. Therefore, it is expected that sufficiently accurate solutions are obtained if the usual elements are used for the interpolation of quantities in the vicinity of the interface crack front.

In numerically solving BIE (4.7), the convolution integrals are evaluated by means of the IRK based CQM, and the surface integrals over S_h and S_d are discretized by the piecewise constant boundary elements. If the interface including the debonding area is divided into M_e boundary elements, the discretized BIE at n -th step and i -th sub-step in time are written as follows:

$$\sum_{\alpha=1}^{M_e} \sum_{j=1}^m \left[\mathcal{U}_{\gamma\alpha}^{s;j;0} \cdot \mathbf{t}_{\alpha}^{s;j;n} - \left\{ \mathcal{T}_{\gamma\alpha}^{s;j;0} + \frac{1}{2} I \delta_{\gamma\alpha} \delta_{ij} \right\} \cdot \mathbf{u}_{\alpha}^{s;j;n} \right] = \mathbf{g}_{\gamma}^{\text{free};s;i;n} - \sum_{k=0}^{n-1} \sum_{\alpha=1}^{M_e} \sum_{j=1}^m \left[\mathcal{U}_{\gamma\alpha}^{s;j;n-k} \cdot \left\{ \mathbf{t}_{\alpha}^{s;j;k} - \mathbf{t}_{\alpha}^{\text{free};s;j;k} \right\} - \mathcal{T}_{\gamma\alpha}^{s;j;n-k} \cdot \left\{ \mathbf{u}_{\alpha}^{s;j;k} - \mathbf{u}_{\alpha}^{\text{free};s;j;k} \right\} \right], \quad (4.8)$$

where $\mathbf{g}_{\gamma}^{\text{free};s;i;n}$ is equivalent to the left-hand side of Eq. (4.8) in which $\mathbf{u}_{\alpha}^{s;j;n}$ and $\mathbf{t}_{\alpha}^{s;j;n}$ are replaced with $\mathbf{u}_{\alpha}^{\text{free};s;j;n}$ and $\mathbf{t}_{\alpha}^{\text{free};s;j;n}$, respectively. For n -th time step, all of the quantities on the right-hand side of Eq. (4.8) are known. Therefore, considering the boundary conditions on S_h and S_d , the unknown values $\mathbf{u}_{\alpha}^{s;j;n}$ and $\mathbf{t}_{\alpha}^{s;j;n}$ can be obtained by solving Eq. (4.8). In additions, the underlined portion in Eq. (4.8) is rapidly evaluated by the FMM as presented in Section 3.1.6.

4.2.1. Nonlinear interface conditions

In order to simultaneously solve BIEs (4.8) with $\varsigma = I$ and II , the appropriate boundary conditions should be selected at each time step. Eq. (4.2) holds on the bonding interface S_h . For the debonding area S_d , we consider three types of interface state in a similar way to the previous researches [38, 39, 77]. The interface phases consist of "separation", "stick", and "slip" as shown in Fig. 4.2, and they are summarized as follows:

4. 3-D Simulation of Higher-harmonic Waves Due to an Interface Crack of Bi-material

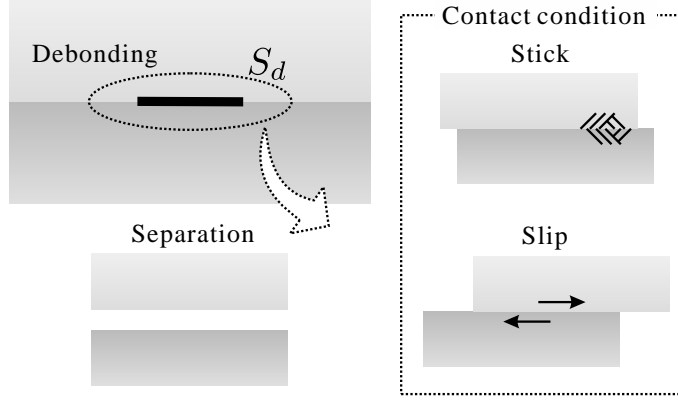


Figure 4.2.: Contact phases on debonding area S_d .

Separation

The separation phase means that two surfaces of upper and lower materials are separated with no traction as depicted in the lower left of Fig. 4.2. Thus, the following traction-free condition is given for this phase.

$$\mathbf{t}^I = \mathbf{t}^{II} = \mathbf{0}. \quad (4.9)$$

Stick contact

For the stick phase, the surfaces of two materials are contacting and not relatively moving due to the static friction force as depicted in the upper right of Fig. 4.2. However, the discontinuity of relative displacement in tangential direction is allowed unlike the perfect bonding on S_h . From the above, the interface conditions are given as follows:

$$[u_3] = -u_g, \quad [\dot{\mathbf{u}}_s] = \mathbf{0}, \quad \mathbf{t}^I = -\mathbf{t}^{II}, \quad (4.10)$$

where $[\mathbf{u}]$ is the crack opening displacement (COD) and defined by $[\mathbf{u}] = \mathbf{u}^{II} - \mathbf{u}^I$, and \mathbf{u}_s indicates the displacement vector in the plane of a crack surface. u_g denotes the pre-opening displacement of the debonding surface.

Slip contact

Although the slip phase is also contact state similarly to the stick phase, it allows the relatively tangential movement with dynamic friction force. The traction force is continuous in any direction because the surfaces of two materials are contacting under this phase. The friction force is evaluated by using the Coulomb friction law in this study, and therefore, the following interface conditions

are given for this phase.

$$[u_3] = -u_g, \quad t_3^I = -t_3^{II}, \quad \mathbf{t}_s^I = -\mathbf{t}_s^{II} = \frac{[\dot{\mathbf{u}}_s]}{[\dot{\mathbf{u}}_s]} \mu_d (-t_3^I), \quad (4.11)$$

where μ_d is the dynamic friction coefficient, and \mathbf{t}_s is the traction vector in the plane of a crack surface. The moving direction defined by $[\dot{\mathbf{u}}_s]/[\dot{\mathbf{u}}_s]$ is significant to the determination of friction force vector in the dynamic problem [39, 56, 59].

4.2.2. Modification of BIE

The interface conditions for the stick and slip phases (4.10) and (4.11) contain the tangential velocities of COD, and it is difficult to accurately compute them using ordinary numerical differentiation, such as backward differentiation. Moreover, the tangential velocity of COD consists of x_1 - and x_2 -components in 3-D problems although it is enough to evaluate $\text{sgn}([u_1])$ in the 2-D case [39, 77]. Therefore, the BIE is modified to the appropriate form in order to accurately evaluate the tangential velocity of COD.

The vector \mathbf{w} is defined by $\mathbf{w} = (\dot{u}_1, \dot{u}_2, u_3)$, and discretized BIE (4.8) is modified to the one for \mathbf{w} . Taking into account initial condition (4.5), the BIE for scattered wave (4.6) can be modified to the following expression in a similar way to the modification in Section 3.1.7.

$$\begin{aligned} \frac{1}{2} \mathbf{w}^{\text{sc};\varsigma}(\mathbf{x}, t) = & \int_0^t \int_{S_h+S_d} \mathbf{X}^\varsigma(\mathbf{x}, \mathbf{y}, t-\tau) \cdot \mathbf{t}^{\text{sc};\varsigma}(\mathbf{y}, \tau) dS_y d\tau \\ & - \int_0^t \text{p.v.} \int_{S_h+S_d} \mathbf{Y}^\varsigma(\mathbf{x}, \mathbf{y}, t-\tau) \cdot \mathbf{w}^{\text{sc};\varsigma}(\mathbf{y}, \tau) dS_y d\tau \quad \mathbf{x} \in S_h, S_d, \end{aligned} \quad (4.12)$$

where \mathbf{X} and \mathbf{Y} are defined by

$$\mathbf{X} = \begin{bmatrix} \dot{U}_{11} & \dot{U}_{12} & \dot{U}_{13} \\ \dot{U}_{21} & \dot{U}_{22} & \dot{U}_{23} \\ U_{31} & U_{32} & U_{33} \end{bmatrix}, \quad \mathbf{Y} = \begin{bmatrix} T_{11} & T_{12} & \dot{T}_{13} \\ T_{21} & T_{22} & \dot{T}_{23} \\ \Gamma_{31} & \Gamma_{32} & T_{33} \end{bmatrix}, \quad (4.13)$$

respectively, and $\mathbf{\Gamma}$ is

$$\mathbf{\Gamma}(\mathbf{x}, \mathbf{y}, t) = \int_0^t \mathbf{T}(\mathbf{x}, \mathbf{y}, \tau) d\tau.$$

The discretized BIE for \mathbf{w} can be obtained in a similar manner to derivation of Eq. (4.8) as follows:

$$\begin{aligned} \sum_{\alpha=1}^{M_e} \sum_{j=1}^m \left[\mathcal{X}_{\gamma\alpha}^{\varsigma;ij;0} \cdot \mathbf{t}_\alpha^{\varsigma;j;n} - \left\{ \mathcal{Y}_{\gamma\alpha}^{\varsigma;ij;0} + \frac{1}{2} I \delta_{\gamma\alpha} \delta_{ij} \right\} \cdot \mathbf{w}_\alpha^{\varsigma;j;n} \right] = \mathbf{h}_\gamma^{\text{free};\varsigma;i;n} \\ - \sum_{k=0}^{n-1} \sum_{\alpha=1}^{M_e} \sum_{j=1}^m \left[\mathcal{X}_{\gamma\alpha}^{\varsigma;ij;n-k} \cdot \left\{ \mathbf{t}_\alpha^{\varsigma;j;k} - \mathbf{t}_\alpha^{\text{free};\varsigma;j;k} \right\} - \mathcal{Y}_{\gamma\alpha}^{\varsigma;ij;n-k} \cdot \left\{ \mathbf{w}_\alpha^{\varsigma;j;k} - \mathbf{w}_\alpha^{\text{free};\varsigma;j;k} \right\} \right], \end{aligned} \quad (4.14)$$

4. 3-D Simulation of Higher-harmonic Waves Due to an Interface Crack of Bi-material

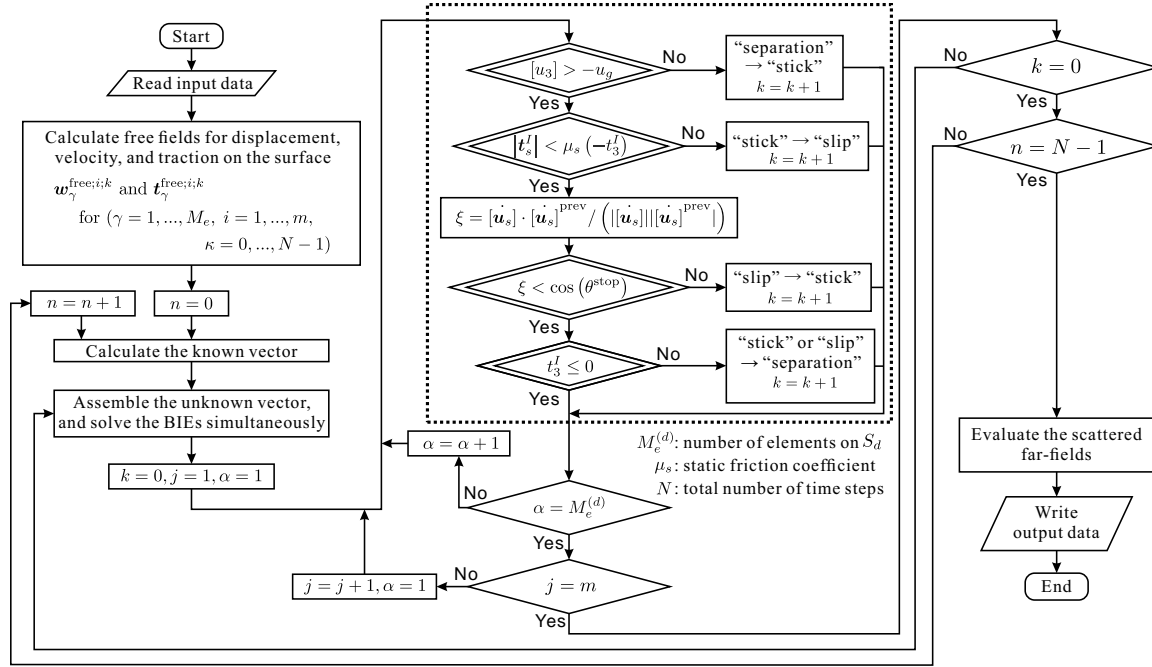


Figure 4.3.: Flowchart of numerical procedure for nonlinear analysis.

where $\mathbf{h}_\gamma^{\text{free};\varsigma;i;n}$ is equivalent to the left-hand side of Eq. (4.14) in which $\mathbf{w}_\alpha^{s;j;n}$ and $\mathbf{t}_\alpha^{s;j;n}$ are replaced with $\mathbf{w}_\alpha^{\text{free};\varsigma;j;n}$ and $\mathbf{t}_\alpha^{\text{free};\varsigma;j;n}$, respectively. The influence functions $\mathcal{X}_{\gamma\alpha}^{\varphi;ij;\kappa}$ and $\mathcal{Y}_{\gamma\alpha}^{\varphi;ij;\kappa}$ correspond to \mathbf{X} and \mathbf{Y} , respectively, and contain time differentiation and integration. However, these can be easily evaluated by considering the following identities with respect to the Laplace transform:

$$\mathcal{L}[\dot{k}(t)] = s\hat{k}(s), \quad \mathcal{L}\left[\int_0^t k(\tau)d\tau\right] = \frac{1}{s}\hat{k}(s).$$

Using discretized BIE (4.14) and dealing with the tangential velocities of COD as variables, the direction of relative movement and tangential traction on the debonding area in the slip phase can be evaluated precisely.

4.3. Numerical procedure for nonlinear analysis

The transition and constraint conditions for the iterative calculation of nonlinear analysis are presented in this section. The overall procedure of numerical simulation is shown in Fig. 4.3. At a time step in the CQ-BEM, discretized BIE (4.14) is solved assuming that the interface conditions on each element are the same as those at the previous time step. If the additional constraint conditions enclosed by the double rhombuses in Fig. 4.3 are not satisfied by the obtained solutions, the interface condition on the element, which is one of separation, stick, and slip, is changed to another condition, and then, the system of equations is assembled and solved again. After conducting the

iterative calculations, if both the boundary and constraint conditions on all elements are satisfied, the time step proceeds to the next one.

Some remarks concerning the numerical calculations are summarized as follows:

- At the initial time step, the interface condition of separation is given for all elements on the debonding area S_d if the pre-opening displacement $g > 0$. On the other hand, all elements are taken to be the stick phase if $u_g = 0$.
- There are two options for the phase shift from separation to one of two contact conditions, i.e. slip and stick. In this study, the priority is given to the change from separation to stick if $[u_3] > -u_g$ for the separation condition is violated on the element. In practice, it is considered that the slip is not started unless the tangential force exceeds the static friction force which is generated by the contact of debonding surfaces.
- The stick phase is changed to the slip one if the tangential traction force exceeds the static friction force. Specifically, this transition occurs if the following condition is violated.

$$|t_s^I| < \mu_s (-t_3^I), \quad (4.15)$$

where μ_s is the static friction coefficient. On the other hand, the transition from contact state to separation is caused if the following condition is violated.

$$t_3^I \leq 0. \quad (4.16)$$

- In numerical calculations, it is difficult to achieve the condition $|\dot{[u_s]}| = 0$ exactly in the transition from stick to slip. Therefore, we set $|\dot{[u_s]}| = 0$ if the following condition is not satisfied.

$$\frac{[\dot{u_s}] \cdot [\dot{u_s}]^{\text{prev}}}{|[\dot{u_s}]| |[\dot{u_s}]^{\text{prev}}|} = \xi < \cos(\theta^{\text{stop}}), \quad (4.17)$$

where the superscript "prev" indicates the quantity at the previous time step. Violating Eq. (4.17) means that the direction of relatively tangential movement is changed more than θ^{stop} . Considering the 2-D local coordinate system (s_1, s_2) on the debonding surface in which s_1 is parallel to $[\dot{u_s}]^{\text{prev}} / |[\dot{u_s}]^{\text{prev}}|$ as depicted in Fig. 4.4, a sign of s_1 -component of $[\dot{u_s}] / |[\dot{u_s}]|$ is different from the one of $[\dot{u_s}]^{\text{prev}} / |[\dot{u_s}]^{\text{prev}}|$ if the direction of relatively tangential movement is changed more than 90° . Therefore, θ^{stop} is given by 90° in this study.

4.4. Numerical results

In this section, we present some numerical results for two types of material combination using the analysis model depicted in Fig. 4.5. The first is a penny-shaped debonding area on the steel-steel

4. 3-D Simulation of Higher-harmonic Waves Due to an Interface Crack of Bi-material

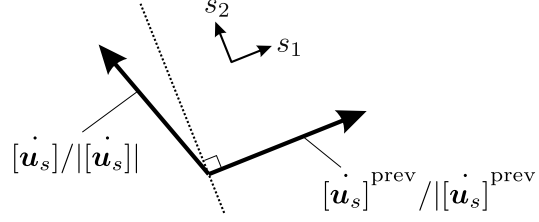


Figure 4.4.: Local coordinate system for stopping condition of relatively tangential movement.

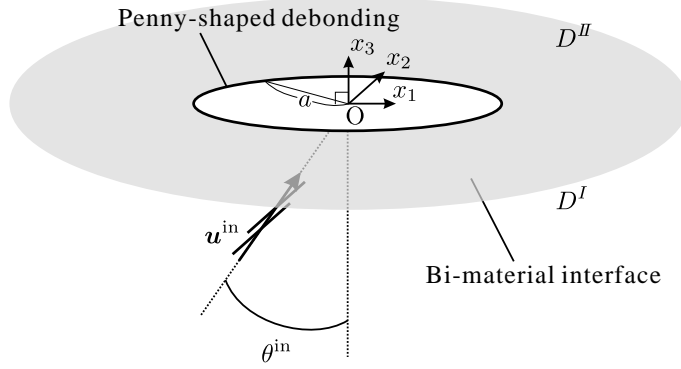


Figure 4.5.: An incident plane wave scattering by a penny-shaped interface crack with radius a .

interface subjected to an incident plane wave, and this model is equivalent to a crack in an infinite elastic solid. The second is a penny-shaped debonding area on the interface of the steel-aluminum coupled medium subjected to an incident plane wave. Numerical results of scattering problems due to normal incidence of P and S waves and oblique incidence of P wave are shown for both cases. In advance of the nonlinear ultrasonic simulation, we show numerical results for the linear problem to verify the numerical method. The CQ-FMBEM with RK2 is used for all numerical simulations in this section.

4.4.1. Accuracy verification

To verify accuracy of the proposed CQ-FMBEM, we solve the scattering problem by an interface crack when the debonding area is always separated. The material constants of D^I and D^{II} are given by identical values, and therefore, this problem is equivalent to the scattering problem by a penny-shaped crack in an infinite domain. If the material constants of D^I and D^{II} are identical, we omit the superscripts I and II . We use an incident plane P wave normal to the crack face for this verification, and it is defined by the monotonically increasing function as follows:

$$u_i^{\text{in}}(\mathbf{x}, t) = -u_0 \delta_{i3} \frac{c_T}{c_L} \frac{c_L t - x_3}{a} H(c_L t - x_3). \quad (4.18)$$

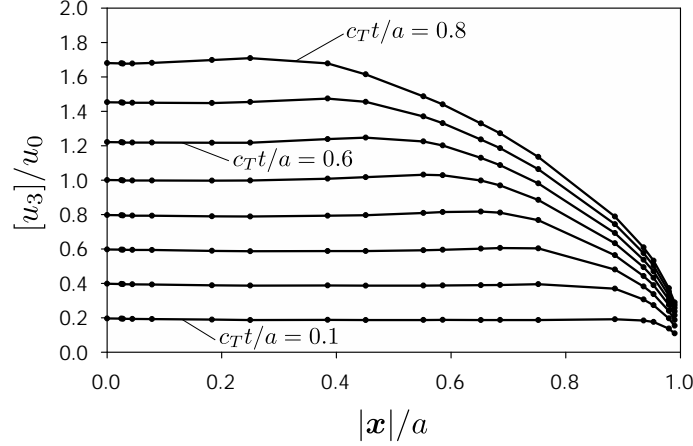


Figure 4.6.: Vertical COD on S_d at each several time steps $c_T t/a$ when a penny-shaped crack is subjected to normal incidence of P wave.

Time increment Δt is taken as $c_T \Delta t/a = 0.1$, and Poisson's ratio ν is given by $\nu = 0.3$. Vertical CODs at each several time steps are shown in Fig. 4.6. As shown in Fig. 4.6, the CODs near the center point of the penny-shaped crack becomes about $2c_T t/a$ from $c_T t/a = 0.1$ to 0.5 because the incident wave is completely reflected on S_d . The diffracted P wave reaches the center point of crack at $c_T t/a \simeq 0.53$. Therefore, the CODs are larger than $2c_T t/a$ due to the influence of diffracted waves after $c_T t/a = 0.6$. From the above, it seems that the proposed CQ-FMBEM is verified.

4.4.2. Nonlinear ultrasonic simulation

Next, we present numerical results of the nonlinear ultrasonic simulation considering the nonlinear interface conditions. The following sinusoidal burst wave with n^{in} cycles is used as an incident wave in this simulation.

$$\begin{cases} \mathbf{u}^{\text{in}}(\mathbf{x}, t) = u_0 \mathbf{d}_\varphi \sin(2\pi \Lambda_\varphi^I) H(\Lambda_\varphi^I) H(n^{\text{in}} - \Lambda_\varphi^I), & (4.19a) \\ \Lambda_\varphi^I = f^{\text{in}} \left(t - \frac{\mathbf{p} \cdot (\mathbf{x} - \boldsymbol{\chi})}{c_\varphi^I} \right), & (4.19b) \end{cases}$$

where $\varphi = L, TV$, or TH and indicates a P, SV, or SH wave, respectively. \mathbf{p} is the propagation vector of the incident plane wave and given by $\mathbf{p} = (\sin \theta^{\text{in}}, 0, \cos \theta^{\text{in}})$ using the incident angle θ^{in} . The displacement vector is given by $\mathbf{d}_L = \mathbf{p}$ for the incident P wave, and we assume that $\mathbf{d}_{TH} = (0, 1, 0)$ and $\mathbf{d}_{TV} = \mathbf{d}_{TH} \times \mathbf{p}$ in this study. $\boldsymbol{\chi}$ is a point on the wavefront of the incident wave at $t = 0$ and given by $\boldsymbol{\chi} = (-a, 0, 0)$. n^{in} is given by $n^{\text{in}} = 3$ in this section. The free-fields are calculated from Eq. (4.19) as presented in Appendix C. The far-field approximation of scattered wave (see Appendix B) is used for the frequency spectrum analysis. The time increment is taken to be $f^{\text{in}} \Delta t = 0.08$, and material constants for steel and aluminum media are shown in Table 4.1. The static and dynamic friction coefficients for steel-steel and steel-aluminum interfaces are also shown in Table 4.2 [22].

4. 3-D Simulation of Higher-harmonic Waves Due to an Interface Crack of Bi-material

Table 4.1.: Material constants for steel and aluminum.

	c_L [m/s]	c_T [m/s]	ρ [kg/m ³]
Steel	5800	3100	7690
Aluminum	6400	3040	2700

Table 4.2.: Friction coefficients for steel-steel and steel-aluminum interfaces.

	μ_s	μ_d
Steel-steel	0.74	0.57
Steel-aluminum	0.61	0.47

In some numerical simulations, we consider the static compressive stress normal to the debonding area σ^{st} . Adding σ^{st} into the free-field of traction, σ^{st} can be considered in the case that $g = 0$ because σ^{st} does not cause COD at $t \leq 0$ due to the stick state. In this study, σ^{st} is given over the debonding area uniformly.

We explain some symbols used for the frequency spectrum analysis of nonlinear ultrasonic waves here. A_ω , $A_{2\omega}$, and $A_{3\omega}$ indicate the Fourier amplitudes corresponding to fundamental frequency, 2nd higher-harmonic component, and 3rd higher-harmonic component, respectively. This type of the symbol with superscript 0 such as A_ω^0 , $A_{2\omega}^0$, or $A_{3\omega}^0$, indicates the quantity in the case that $u_g/u_0 = \sigma^{\text{st}}/\sigma_0 = 0.0$. The nondimensionalization parameter σ_0 is the maximum stress of the incident wave and given by

$$\sigma_0 = 2\pi u_0 f^{\text{in}} \rho c_\varphi, \quad (4.20)$$

where φ is taken to be same as the incident wave.

Debonding area on steel-steel interface

The scattering problems by a penny-shaped crack in an infinite elastic solid are numerically solved by the proposed CQ-FMBEM. Therefore, the material constants of steel are used for D^I and D^{II} , and we omit the superscripts I and II .

Numerical results using an incident plane P wave with $\theta^{\text{in}} = 0^\circ$ are shown. Time histories of vertical displacement on the top and bottom surfaces at the center point of a crack are shown in Figs. 4.7 and 4.8 when the center wavenumbers of the incident wave are given by $k_T a = 2\pi a f^{\text{in}}/c_T = 2.0$ and 5.2, respectively. Opening and closing of crack faces, i.e. clapping motions, are repeated periodically as shown in Fig. 4.7. The crack faces are rapidly closed by the diffracted wave after the opening of crack faces. On the other hand, the waveforms of displacement in the case $k_T a = 5.2$ are not clearly periodic as we can see in Fig. 4.8. If the frequency of incident wave is higher than the eigenfrequency of mode I for the linear system, it takes time that the vibration of crack faces

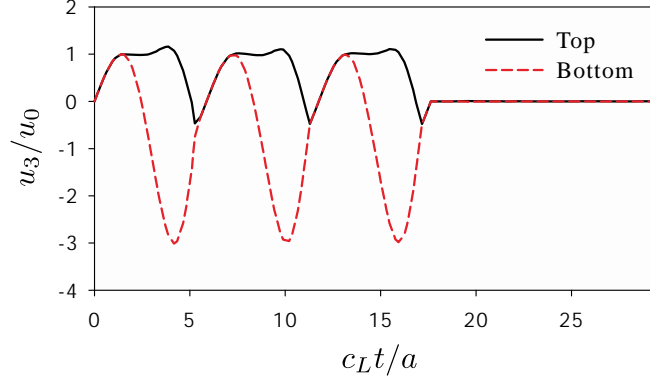


Figure 4.7.: Time variations of vertical displacement at the center point of a penny-shaped crack subjected to an incident plane P wave when $k_T a = 2.0$ and $\sigma^{\text{st}}/\sigma_0 = 0$.

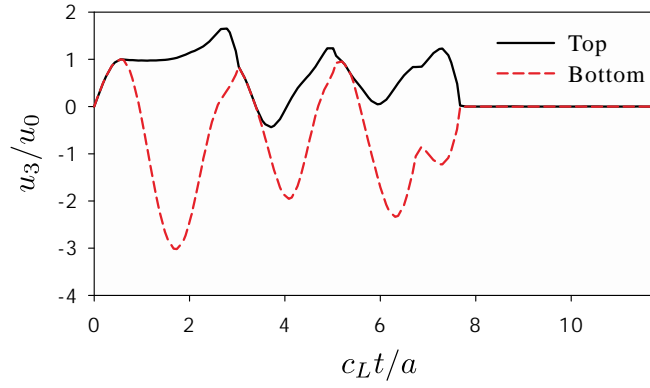


Figure 4.8.: Time variations of vertical displacement at the center point of a penny-shaped crack subjected to an incident plane P wave when $k_T a = 5.2$ and $\sigma^{\text{st}}/\sigma_0 = 0$.

becomes periodic. This is because the arrival time of diffracted waves is large compared with the period of incident wave.

The frequency spectra of far-field amplitude of backscattered P wave $\Omega_L/(au_0)$ are shown in Figs. 4.9 and 4.10 when $k_T a = 2.0$ and 5.2 , respectively. They are normalized by the maximum value around the fundamental frequency in each spectrum, and the time history of $\Omega_L/(au_0)$ is shown in each small window in Figs. 4.9 and 4.10. From Fig. 4.9, the similar waveform to [38] is obtained, and some rapid fluctuations can be seen. It is confirmed that this sharp waveform includes higher-harmonic components of 2nd, 3rd, 4th, etc. orders. Similarly, the sharp waveform is obtained in the case that $k_T a = 5.2$ as shown in Fig. 4.10. As described in Eqs. (B.2) and (B.6), the far-field scattered wave depends on the velocity of the COD [35]. Therefore, the sharp waveforms are constructed from the rapid fluctuation of the velocity of COD due to the closing motion of crack faces, and higher-harmonic waves are generated strongly.

Time histories of vertical COD at the center point of a crack for various static compressive stress $\sigma^{\text{st}}/\sigma_0$ are shown in Figs. 4.11 and 4.12 when $k_T a = 2.0$ and 5.2 , respectively. The normalized

4. 3-D Simulation of Higher-harmonic Waves Due to an Interface Crack of Bi-material

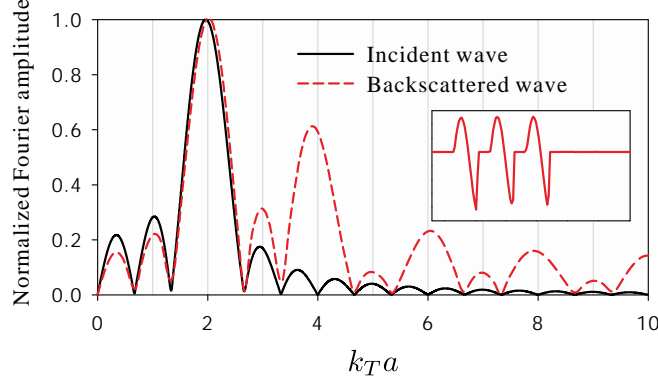


Figure 4.9.: Normalized frequency spectrum of far-field amplitude of backscattered P wave $\Omega_L/(au_0)$ when $k_T a = 2.0$ and $\sigma^{\text{st}}/\sigma_0 = 0$.

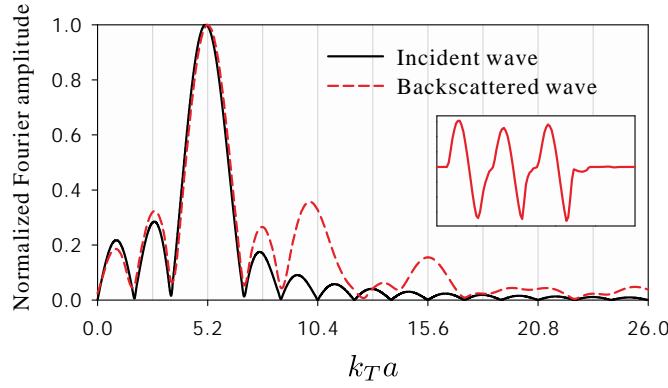


Figure 4.10.: Normalized frequency spectrum of far-field amplitude of backscattered P wave $\Omega_L/(au_0)$ when $k_T a = 5.2$ and $\sigma^{\text{st}}/\sigma_0 = 0$.

Fourier amplitudes corresponding to the 2nd and 3rd higher-harmonic components, $A_{2\omega}/A_{2\omega}^0$ and $A_{3\omega}/A_{3\omega}^0$, are plotted in Figs. 4.13 and 4.14. From Fig. 4.11, amplitude of vertical COD decreases monotonously in the case that $k_T a = 2.0$ as $\sigma^{\text{st}}/\sigma_0$ increases. Correspondingly, $A_{2\omega}/A_{2\omega}^0$ is decreasing as shown in Fig. 4.13. On the other hand, the vertical COD in the case that $k_T a = 5.2$ shows different behavior as we can see from Fig. 4.12. The waveform of the vertical COD becomes similar to the case that $k_T a = 2.0$ as $\sigma^{\text{st}}/\sigma_0$ increase from $\sigma^{\text{st}}/\sigma_0 = 0.0$ to 0.4. Then, amplitude of the vertical COD decreases with a little phase shift. Due to this fact, there is a peak of $A_{2\omega}/A_{2\omega}^0$ around $\sigma^{\text{st}}/\sigma_0 = 0.2$ in Fig. 4.14 although the amplitude of the vertical COD in the case that $\sigma^{\text{st}}/\sigma_0 = 0.0$ is largest. From the above, the behavior of 2nd higher-harmonic generation is significantly influenced by f^{in} and $\sigma^{\text{st}}/\sigma_0$. The behavior of $A_{3\omega}/A_{3\omega}^0$ is similar in both cases as shown in Figs. 4.13 and 4.14.

Next, time histories of horizontal COD at the center point of a penny-shaped crack subjected to an incident plane SV wave for various $\sigma^{\text{st}}/\sigma_0$ are shown in Fig. 4.15 when $k_T a = 2.0$. In this simulation, φ and \hat{v} are given by $\varphi = TV$ and $\hat{v} = (1, 0, 0)$, respectively. The normalized Fourier

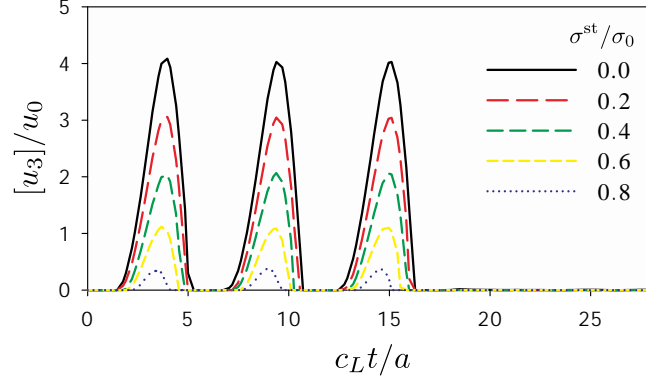


Figure 4.11.: Time variations of vertical COD at the center point of a penny-shaped crack subjected to an incident plane P wave varying σ^{st}/σ_0 when $k_T a = 2.0$.

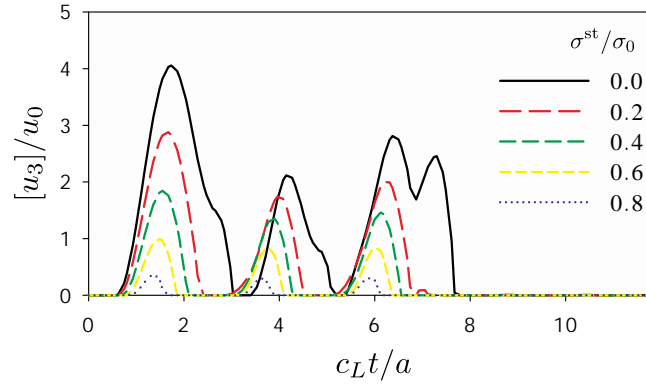


Figure 4.12.: Time variations of vertical COD at the center point of a penny-shaped crack subjected to an incident plane P wave varying σ^{st}/σ_0 when $k_T a = 5.2$.

amplitude corresponding to the 3rd higher-harmonic component $A_{3\omega}/A_{3\omega}^0$ is also plotted in Fig. 4.16. The slip between crack faces does not occur in the case that about $\sigma^{st}/\sigma_0 > 1.35$ because $\mu_s = 0.74$. From Fig. 4.15, the amplitude of horizontal COD decreases, and the waveform becomes similar to the square wave as σ^{st}/σ_0 increases. $A_{3\omega}/A_{3\omega}^0$ peaks at about $\sigma^{st}/\sigma_0 = 0.6$ and decreases after the peak as shown in Fig. 4.16. The comparatively large 3rd higher-harmonic wave is generated in the case that $\sigma^{st}/\sigma_0 = 1.2$ although σ^{st}/σ_0 is near the nonslip condition $\sigma^{st}/\sigma_0 \simeq 1.35$. This is because $\mu_s > \mu_d$, and the crack faces are hard to stop once they begin to slip. Conversely, the 3rd higher-harmonic component decreases gently if $\mu_s = \mu_d$, and this fact has been presented from solving the antiplane shear wave problems by Meziane *et al.* [59]. The normalized frequency spectrum in the case that $\sigma^{st}/\sigma_0 = 0.6$, when a most large 3rd higher-harmonic wave is generated, is shown in Fig. 4.17. From the small window of Fig. 4.17, the waveform of $\Omega_{TV}/(au_0)$ is similar to the triangular wave. It is also confirmed from the frequency spectrum in Fig. 4.17 that the 3rd higher-harmonic wave is generated.

Finally, numerical results for the oblique incidence of P wave with $\sigma^{st}/\sigma_0 = 0.0$ are presented.

4. 3-D Simulation of Higher-harmonic Waves Due to an Interface Crack of Bi-material

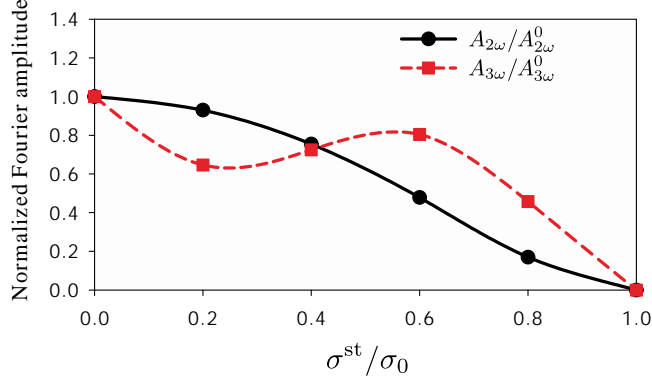


Figure 4.13.: Normalized Fourier amplitude of $\Omega_L/(au_0)$ corresponding to 2nd and 3rd higher-harmonic components, $A_{2\omega}/A_{2\omega}^0$ and $A_{3\omega}/A_{3\omega}^0$, in backscattered P waves varying σ^{st}/σ_0 when $k_Ta = 2.0$.

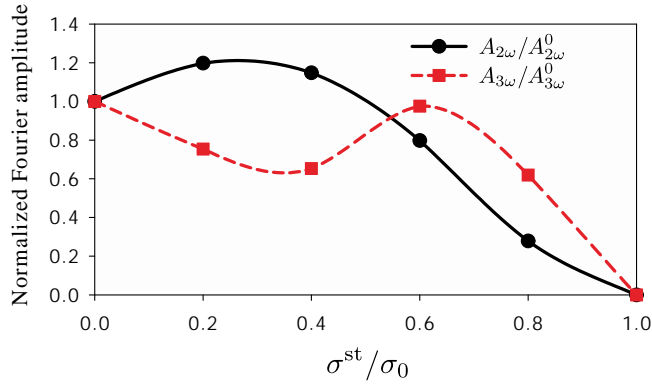


Figure 4.14.: Normalized Fourier amplitude of $\Omega_L/(au_0)$ corresponding to 2nd and 3rd higher-harmonic components, $A_{2\omega}/A_{2\omega}^0$ and $A_{3\omega}/A_{3\omega}^0$, in backscattered P waves varying σ^{st}/σ_0 when $k_Ta = 5.2$.

Time histories and normalized frequency spectra of $\Omega_L/(au_0)$ varying θ^{in} in the case that $k_Ta = 2.0$ are presented in Figs. 4.18 and 4.19, respectively. The interval of incident angle is 15° . In order to compare them with the different frequency cases, the corresponding numerical results in the case that $k_Ta = 5.2$ are also shown in Figs. 4.20 and 4.21. From Figs. 4.18 and 4.19, the amplitude of $\Omega_L/(au_0)$ and the higher-harmonic components decrease as the θ^{in} increases. On the other hand, from Fig. 4.20, it can also be seen that the amplitude of $\Omega_L/(au_0)$ decreases as the θ^{in} increases. However, the amplitude is very small when θ^{in} is 45° or more, and the waveforms of $\Omega_L/(au_0)$ become comparatively flat. Therefore, it is confirmed that there are many low frequency components in the frequency spectra of Fig. 4.21. In addition, the locations of peak near $k_Ta = 5.2$ are shifted because the scattered waves are distorted and have their aftereffects as shown in Fig. 4.20. From the above, behavior of scattered waves and their frequency spectra is significantly different among different f^{in} . Therefore, the size estimation of debonding area is considered as possible using this behavior.

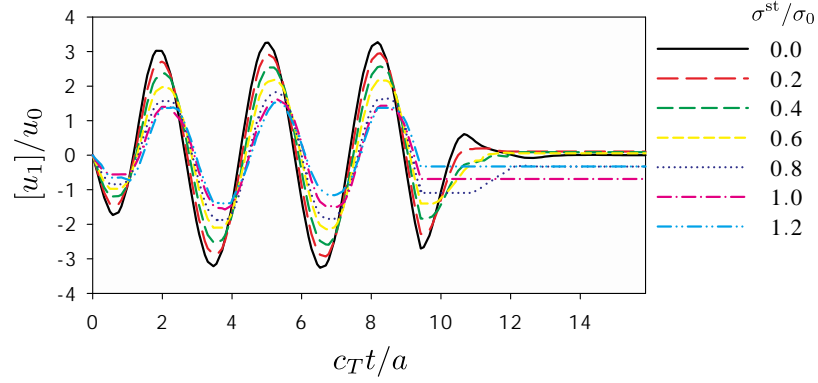


Figure 4.15.: Time variations of horizontal COD at the center of a penny-shaped crack subjected to an incidence plane SV wave varying $\sigma^{\text{st}}/\sigma_0$ when $k_T a = 2.0$.

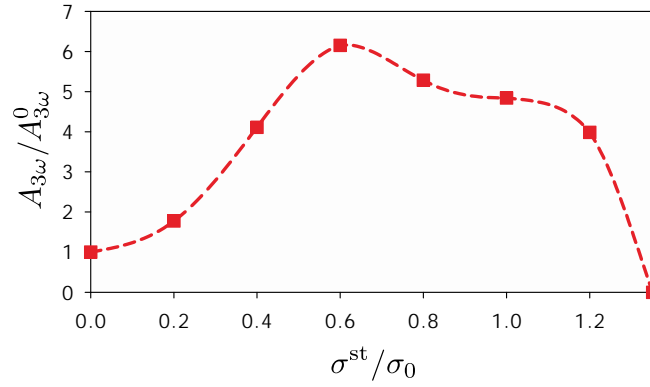


Figure 4.16.: Normalized Fourier amplitude corresponding to 3rd higher-harmonic component $A_{3\omega}/A_{3\omega}^0$ in far-field backscattered SV waves varying $\sigma^{\text{st}}/\sigma_0$ when $k_T a = 2.0$.

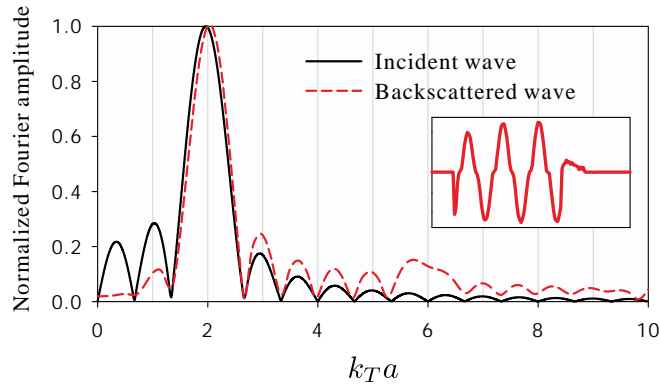


Figure 4.17.: Normalized frequency spectrum of far-field amplitude of backscattered SV wave $\Omega_{TV}/(au_0)$ when $k_T a = 2.0$ and $\sigma^{\text{st}}/\sigma_0 = 0.6$.

4. 3-D Simulation of Higher-harmonic Waves Due to an Interface Crack of Bi-material

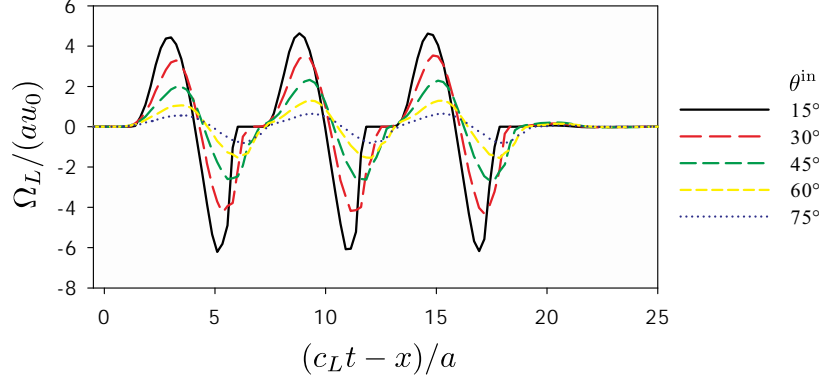


Figure 4.18.: Time variations of far-field amplitude of backscattered P wave $\Omega_L/(au_0)$ varying θ^{in} when $k_T a = 2.0$ and $\sigma^{st}/\sigma_0 = 0.0$.

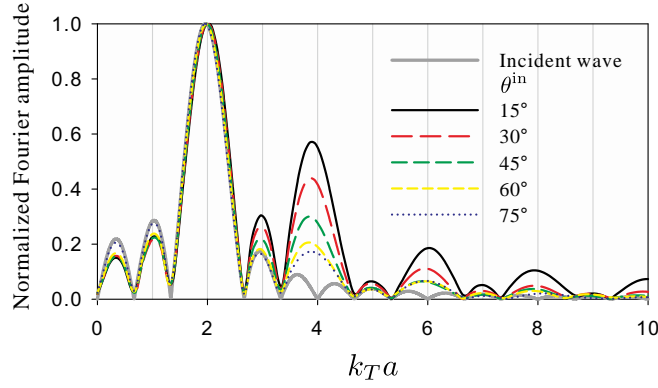


Figure 4.19.: Normalized frequency spectra of far-field amplitude of backscattered P wave $\Omega_L/(au_0)$ varying θ^{in} when $k_T a = 2.0$ and $\sigma^{st}/\sigma_0 = 0.0$.

Debonding area on steel-aluminum interface

Numerical results for the scattering problems by a penny-shaped debonding area on the steel-aluminum interface are presented. The material constants of steel and aluminum in Table 4.1 are used for D^I and D^{II} , respectively, and the friction coefficients in the bottom of Table 4.2 are used for this simulation. In Fig. 4.22, the absolute values of the reflection and transmission coefficients for displacement are shown. $R^{a,b}$ and $T^{a,b}$ indicate the reflection and transmission coefficients, respectively, and the first and second superscripts denote the wave modes before and after its conversion, respectively. In Fig. 4.22, the rapid fluctuation can be seen at $\theta^{in} \simeq 65^\circ$, and this incident angle is the critical angle for the P-P transmission. In this section, numerical results under the similar conditions to the previous section are presented in order to compare between the steel-steel and steel-aluminum cases.

Time histories of vertical displacement on the top and bottom surfaces at the center point of an interface crack are shown in Figs. 4.23 and 4.24 when $k_T^I a = 2.0$ and 5.2, respectively. Although the behavior in the case that $k_T^I a = 2.0$ is similar to the one in Fig. 4.7, the amplitude of displacement is

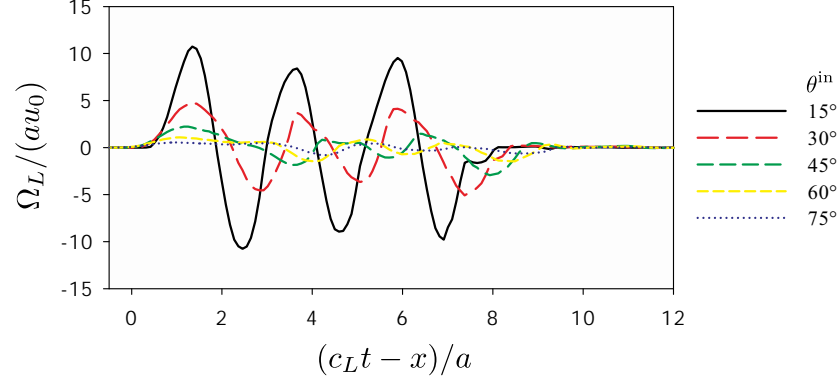


Figure 4.20.: Time variations of far-field amplitude of backscattered P wave $\Omega_L/(au_0)$ varying θ^{in} when $k_T a = 5.2$ and $\sigma^{st}/\sigma_0 = 0.0$.

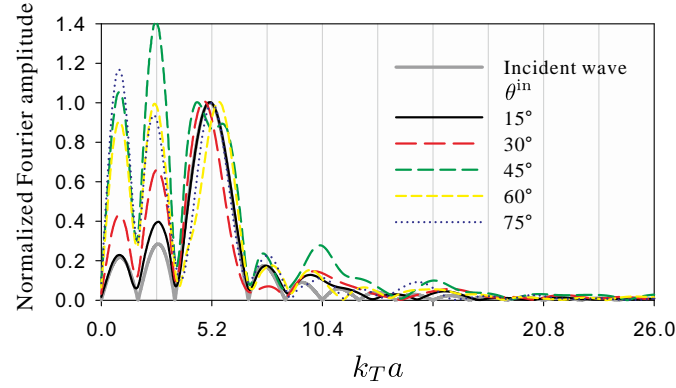


Figure 4.21.: Normalized frequency spectra of far-field amplitude of backscattered P wave $\Omega_L/(au_0)$ varying θ^{in} when $k_T a = 5.2$ and $\sigma^{st}/\sigma_0 = 0.0$.

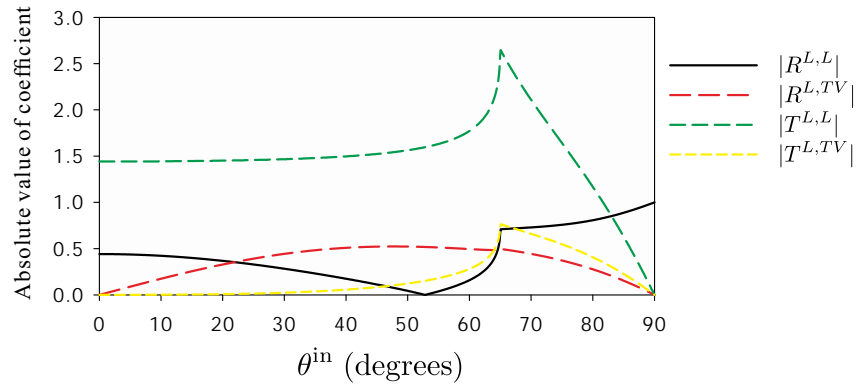


Figure 4.22.: Absolute values of reflection and transmission coefficients for displacement when a semi-infinite and flat interface between steel and aluminum is subjected to an incident plane P wave with incident angle θ^{in} .

4. 3-D Simulation of Higher-harmonic Waves Due to an Interface Crack of Bi-material

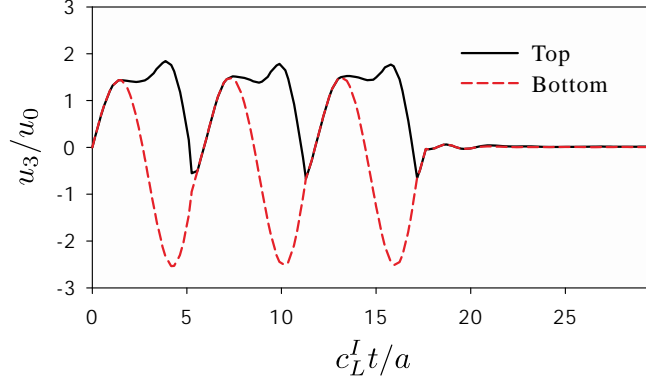


Figure 4.23.: Time variations of vertical displacement on the center point of a penny-shaped interface crack subjected to an incident plane P wave when $k_T^I a = 2.0$ and $\sigma^{\text{st}}/\sigma_0 = 0$.

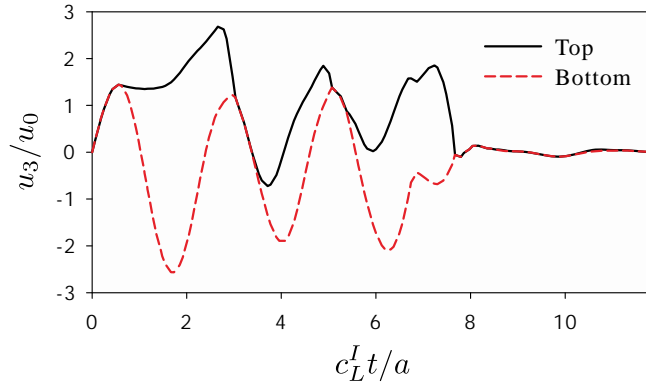


Figure 4.24.: Time variations of vertical displacement on the center point of a penny-shaped interface crack subjected to an incident plane P wave when $k_T^I a = 5.2$ and $\sigma^{\text{st}}/\sigma_0 = 0$.

different due to reflection and transmission coefficients as shown in Fig. 4.23. For normal incidence of P wave, the reflection and transmission coefficients are $|R^{L,L}| \simeq 0.44$ and $|T^{L,L}| \simeq 1.44$, respectively. The amplitude of displacement in the case that $k_T^I a = 5.2$ is also influenced due to this fact as shown in Fig. 4.24. However, the difference between Figs. 4.8 and 4.24 is large compared with the case that $k_T^I a = 2.0$. This difference in behavior of waveform is caused by the difference of wave velocities between steel and aluminum. It seems that this effect is significant in the high frequency case.

The normalized frequency spectra of far-field amplitude of backscattered P wave $\Omega_L/(au_0)$ are shown in Figs. 4.25 and 4.26 when $k_T^I a = 2.0$ and 5.2 , respectively. They show almost same behavior as the ones in Figs. 4.9 and 4.10.

Time histories of vertical COD at the center point of an interface crack for various static compressive stress $\sigma^{\text{st}}/\sigma_0$ are shown in Figs. 4.27 and 4.28 when $k_T^I a = 2.0$ and 5.2 , respectively. The normalized Fourier amplitudes corresponding to the 2nd and 3rd higher-harmonic components, $A_{2\omega}/A_{2\omega}^0$ and $A_{3\omega}/A_{3\omega}^0$, are also plotted in Figs. 4.13 and 4.14. Note that the static compressive

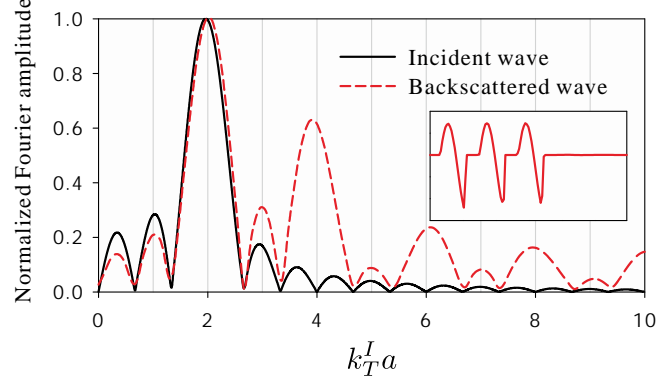


Figure 4.25.: Normalized frequency spectrum of far-field amplitude of backscattered P wave $\Omega_L/(au_0)$ when $k_T^I a = 2.0$ and $\sigma^{\text{st}}/\sigma_0 = 0$.

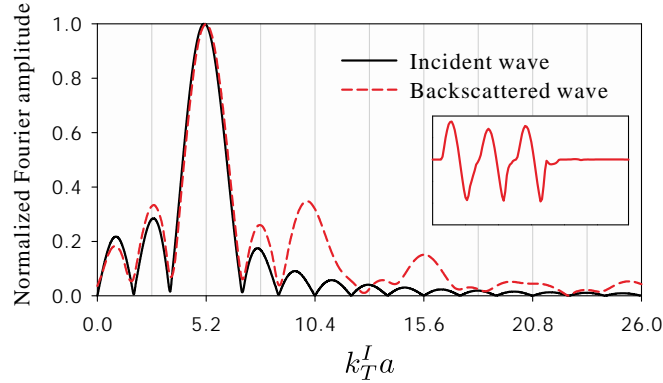


Figure 4.26.: Normalized frequency spectrum of far-field amplitude of backscattered P wave $\Omega_L/(au_0)$ when $k_T^I a = 5.2$ and $\sigma^{\text{st}}/\sigma_0 = 0$.

stress $\sigma^{\text{st}}/\sigma_0$ given here is different from the ones in the case of steel-steel interface because the transmission coefficient for stress is $|T_{\sigma}^{L,L}| \simeq 0.56$ in this case. The opening of crack faces does not occur if $\sigma^{\text{st}}/\sigma_0 \geq |T_{\sigma}^{L,L}|$. However, the behavior in the cases that $k_T^I a = 2.0$ and 5.2 are very similar to the cases of steel-steel interface.

Next, time histories of horizontal COD at the center point of a penny-shaped interface crack subjected to an incident plane SV wave varying $\sigma^{\text{st}}/\sigma_0$ are shown in Fig. 4.31 when $k_T^I a = 2.0$. The normalized Fourier amplitude corresponding to 3rd higher-harmonic components in the far-field backscattered SV wave $\Omega_{TV}/(au_0)$ is also plotted in Fig. 4.32. In this case, the transmission coefficient for stress corresponding to SV-SV transmission is significant, and $|T_{\sigma}^{TV,TV}| \simeq 0.51$. Therefore, the slip between crack faces does not occur if $\sigma^{\text{st}}/\sigma_0 > |T_{\sigma}^{TV,TV}|/\mu_s \simeq 0.84$. Similarly to the case of steel-steel interface, the amplitude of horizontal COD decreases, and the waveform becomes similar to the square wave as $\sigma^{\text{st}}/\sigma_0$ increases in Fig. 4.31. As shown in Fig. 4.32, the peak of $A_{3\omega}/A_{3\omega}^0$ is located about at $\sigma^{\text{st}}/\sigma_0 = 0.4$. Thus, the normalized frequency spectrum in the case that $\sigma^{\text{st}}/\sigma_0 = 0.4$ is shown in Fig. 4.33. From Fig. 4.33, the waveform of $\Omega_{TV}/(au_0)$ is

4. 3-D Simulation of Higher-harmonic Waves Due to an Interface Crack of Bi-material

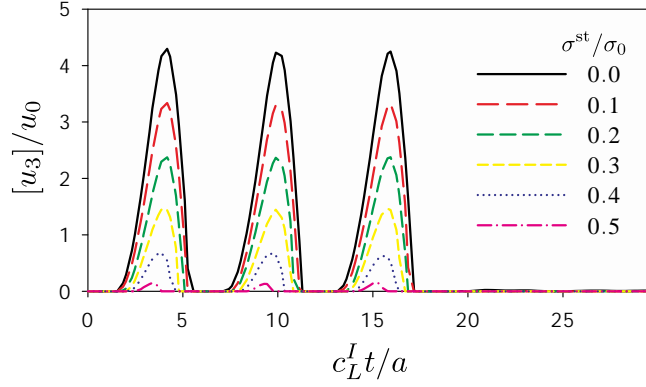


Figure 4.27.: Time variations of vertical COD at the center point of a penny-shaped interface crack subjected to an incident plane P wave varying $\sigma^{\text{st}}/\sigma_0$ when $k_T^I a = 2.0$.

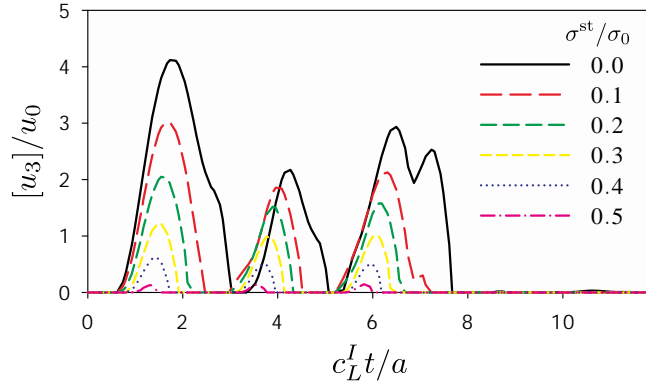


Figure 4.28.: Time variations of vertical COD at the center point of a penny-shaped interface crack subjected to an incident plane P wave varying $\sigma^{\text{st}}/\sigma_0$ when $k_T^I a = 5.2$.

similar to the triangular wave, and it is confirmed that the 3rd higher-harmonic wave is generated.

Finally, numerical results for the oblique incidence of P wave with $\sigma^{\text{st}}/\sigma_0 = 0.0$ are presented. Time histories and normalized frequency spectra of far-field amplitude of backscattered P wave $\Omega_L/(au_0)$ varying θ^{in} in the case that $k_T^I a = 2.0$ and 5.2 are presented in Figs. 4.34–4.21. We should pay attention to the behavior near the critical angle which is about 65° here. Hence, the results with $\theta^{\text{in}} = 65^\circ$ are added into Figs. 4.34–4.37. From Figs. 4.34 and 4.36, the amplitudes of $\Omega_L/(au_0)$ are smaller than those in Figs. 4.18 and 4.20 due to the reflection and transmission coefficients. It is remarkable that the amplitude of $\Omega_L/(au_0)$ in the case that $\theta^{\text{in}} = 65^\circ$ is much larger than those with $\theta^{\text{in}} = 60^\circ$ and 70° . This is because the reflection and transmission coefficients are much larger than those with other θ^{in} , and the large COD is then generated. However, the features of frequency components of $\Omega_L/(au_0)$ are similar to the ones with $\theta^{\text{in}} = 60^\circ$ and 70° as shown in Figs. 4.35 and 4.37.

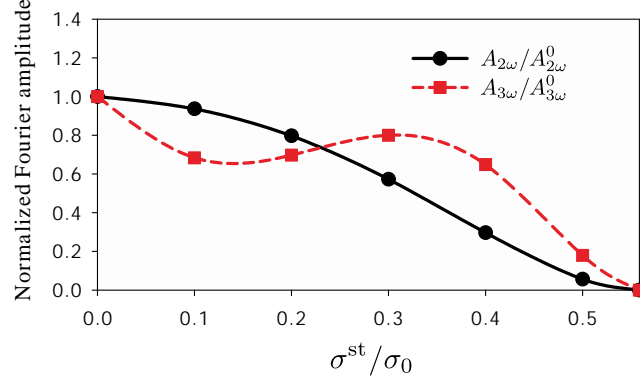


Figure 4.29.: Normalized Fourier amplitude of $\Omega_L/(au_0)$ corresponding to 2nd and 3rd higher-harmonic components, $A_{2\omega}/A_{2\omega}^0$ and $A_{3\omega}/A_{3\omega}^0$, in backscattered P waves varying σ^{st}/σ_0 when $k_T^I a = 2.0$.

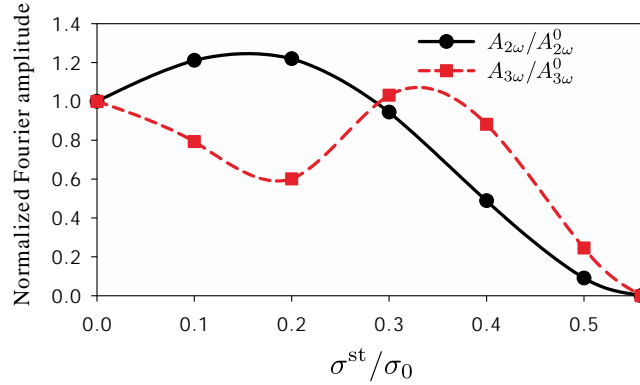


Figure 4.30.: Normalized Fourier amplitude of $\Omega_L/(au_0)$ corresponding to 2nd and 3rd higher-harmonic components, $A_{2\omega}/A_{2\omega}^0$ and $A_{3\omega}/A_{3\omega}^0$, in backscattered P waves varying σ^{st}/σ_0 when $k_T^I a = 5.2$.

4.5. Concluding remarks

- In Chapter 4, we have applied the CQ-FMBEM to the nonlinear ultrasonic simulation for the debonding area on the interface of two semi-infinite elastic solids. We have conducted some numerical simulations for the steel-steel and steel-aluminum interfaces and investigated the characteristic of higher-harmonic generation due to the static compressive stress. Moreover, the numerical results have been compared between the cases of steel-steel and steel-aluminum interfaces.
- We have successfully reproduced the clapping motion and friction on the crack faces and observed the higher-harmonic generation using the presented contact model of crack faces. The clapping motion and dynamic friction of crack faces have generated the every order of higher-harmonic waves and odd order of ones, respectively. Therefore, it is considered that the presented model is valid.

4. 3-D Simulation of Higher-harmonic Waves Due to an Interface Crack of Bi-material

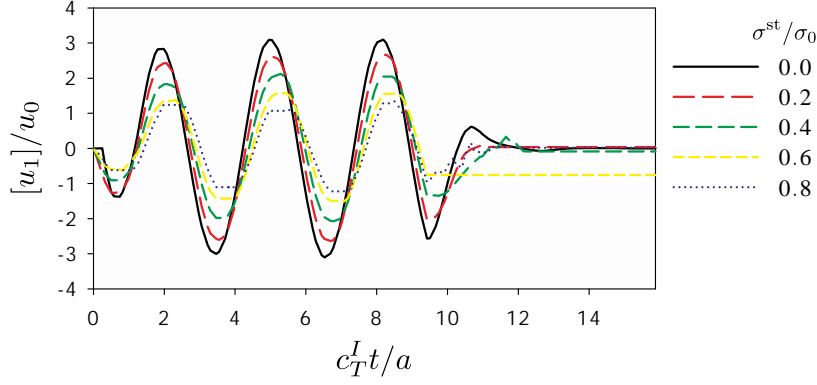


Figure 4.31.: Time variations of horizontal COD at the center of a penny-shaped interface crack subjected to an incidence plane SV wave varying $\sigma^{\text{st}}/\sigma_0$ when $k_T^I a = 2.0$.

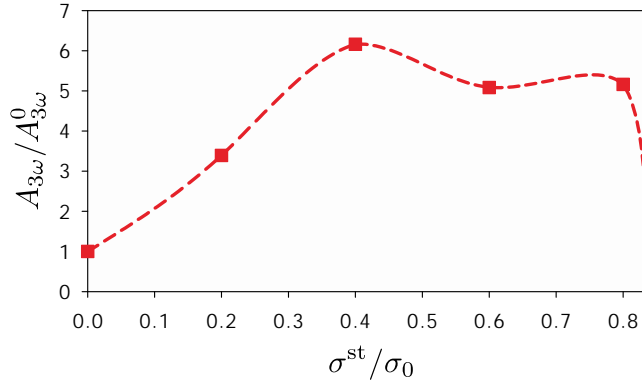


Figure 4.32.: Normalized Fourier amplitude corresponding to 3rd higher-harmonic component $A_{3\omega}/A_{3\omega}^0$ in far-field backscattered SV waves varying $\sigma^{\text{st}}/\sigma_0$ when $k_T^I a = 2.0$.

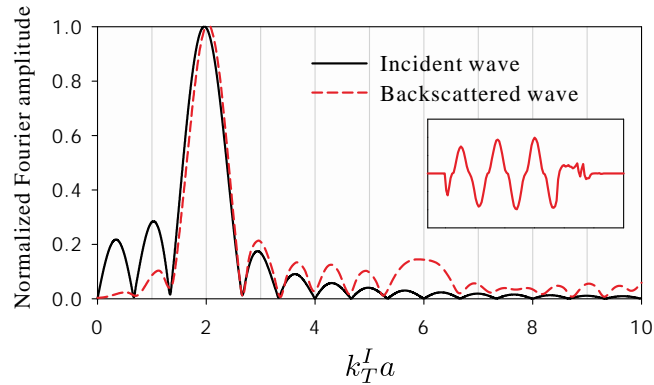


Figure 4.33.: Normalized frequency spectrum of far-field amplitude of backscattered SV wave $\Omega_{TV}/(au_0)$ when $k_T^I a = 2.0$ and $\sigma^{\text{st}}/\sigma_0 = 0.4$.

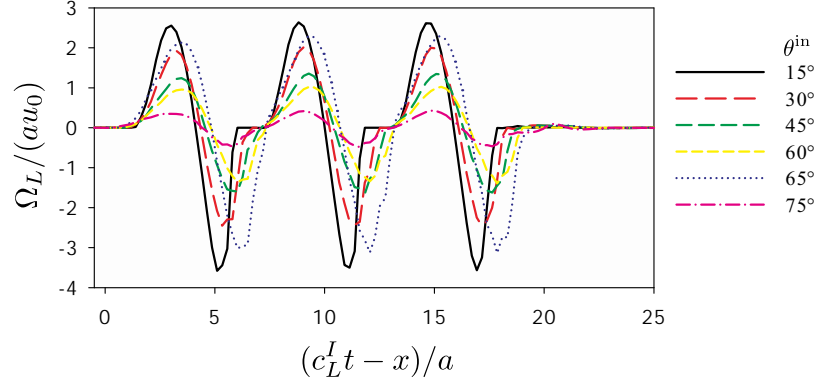


Figure 4.34.: Time variations of far-field amplitude of backscattered P wave $\Omega_L/(au_0)$ varying θ^{in} when $k_T^I a = 2.0$ and $\sigma^{st}/\sigma_0 = 0.0$.

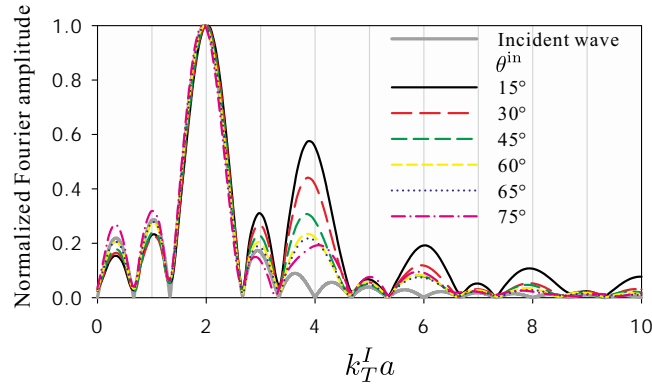


Figure 4.35.: Normalized frequency spectra of far-field amplitude of backscattered P wave $\Omega_L/(au_0)$ varying θ^{in} when $k_T^I a = 2.0$ and $\sigma^{st}/\sigma_0 = 0.0$.

- In the high frequency cases, i.e. $k_T a = 5.2$, the scattered waves sometimes have been distorted strongly. Then, many low frequency components are contained in their frequency spectra. However, we could not observe the sub-harmonic generation.
- In the case of the steel-aluminum interface, the reflection and transmission coefficients significantly effect in the results. For the normal incidence of P and SV waves, the amplitude of COD greatly depends on these coefficients. Moreover, scattered waves obtained by using the incident angle near the critical one have much larger amplitude than the others. However, the behavior of frequency spectra is not very different from others in the presented numerical results.

4. 3-D Simulation of Higher-harmonic Waves Due to an Interface Crack of Bi-material

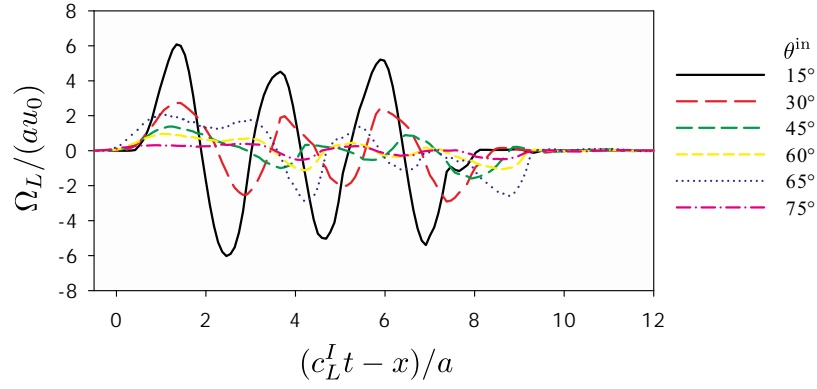


Figure 4.36.: Time variations of far-field amplitude of backscattered P wave $\Omega_L/(au_0)$ varying θ^{in} when $k_T^I a = 5.2$ and $\sigma^{st}/\sigma_0 = 0.0$.

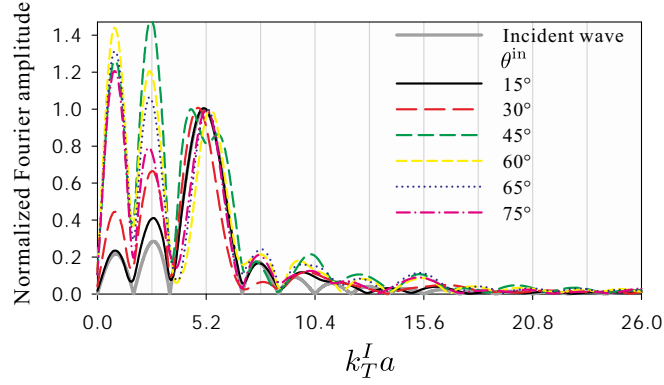


Figure 4.37.: Normalized frequency spectra of far-field amplitude of backscattered P wave $\Omega_L/(au_0)$ varying θ^{in} when $k_T^I a = 5.2$ and $\sigma^{st}/\sigma_0 = 0.0$.

Chapter 5

2-D Simulation of Nonlinear Ultrasonic Waves Due to Interior and Surface Breaking Cracks

In this chapter, the boundary element formulations and numerical results for 2-D simulation of higher- and sub-harmonic generation are presented. We consider the scattering problems by cracks in an infinite elastic solid and surface breaking cracks in an elastic half-space. The frequency response characteristic of linear systems is important for the sub-harmonic simulation, and we consider complex shape and arrangement of cracks. Therefore, the Galerkin method is used for spatial discretization in this simulation. In general, the Galerkin BEM requires expensive computational cost and produces accurate solutions compared with the collocation BEM. Moreover, although the collocation hypersingular BIE is known to require a $C^{1,\alpha}$ continuity for displacement on boundaries, usual C^0 basis functions are allowed to use in the variational one [12, 40].

In this chapter, the hypersingular integral (p.f. integral) in the BIE for crack problems is regularized only to strong singular one (p.v. integral), where p.f. denotes the finite part of a divergent integral. This is because it is not very difficult to analytically calculate the integration of the static part of fundamental solutions over a straight-line element for 2-D elastodynamics.

5.1. Problem statement and BIE

In this section, we present the problem statements and formulation of BIE for the scattering problems by cracks in an infinite domain and surface breaking cracks in a half-space.

5.1.1. Scattering problem by cracks in infinite domain

Scalar wave scattering problems by a crack have been come down to the hypersingular BIE by Martin and Rizzo [50]. Then, the counterpart for elastodynamic problems has been numerically solved by BEMs. The hypersingular BIE is effective in dealing with crack problems for infinite and semi-infinite domains and also used in this study.

5. 2-D Simulation of Nonlinear Ultrasonic Waves Due to Interior and Surface Breaking Cracks

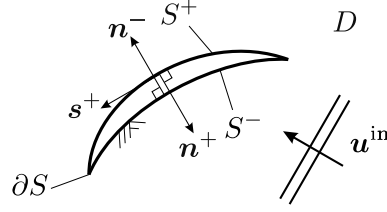


Figure 5.1.: Analysis model for elastic wave scattering by a crack in a 2-D infinite domain.

Let S be a smooth curved crack surface in \mathbb{R}^2 as depicted in Fig. 5.1. D is a homogeneous, isotropic, and linearly elastic solid, and S consists of S^+ and S^- called positive and negative sides of crack face, respectively ($S = S^+ \cup S^-$ and $S^+ \cap S^- = \emptyset$). \mathbf{n}^+ and \mathbf{n}^- are the unit normal vectors to S^+ and S^- , respectively. \mathbf{s}^+ is the unit tangential vector to S^+ . Disregarding the body force, we consider the problem to find the solution \mathbf{u} which satisfies the following equations:

$$c_T^2 \nabla^2 \mathbf{u}(\mathbf{x}, t) + (c_L^2 + c_T^2) \nabla \nabla \cdot \mathbf{u}(\mathbf{x}, t) = \ddot{\mathbf{u}}(\mathbf{x}, t) \quad \mathbf{x} \in D \left(\equiv \mathbb{R}^2 \setminus S \right), \quad (5.1)$$

$$\mathbf{t}^+(\mathbf{x}, t) + \mathbf{t}^-(\mathbf{x}, t) = \mathbf{0} \quad \mathbf{x} \in S, \quad (5.2)$$

$$[\mathbf{u}](\mathbf{x}, t) \left(\equiv \mathbf{u}^+(\mathbf{x}, t) - \mathbf{u}^-(\mathbf{x}, t) \right) = \mathbf{0} \quad \mathbf{x} \in \partial S, \quad (5.3)$$

$$\mathbf{u}^{\text{sc}}(\mathbf{x}, 0) = \dot{\mathbf{u}}^{\text{sc}}(\mathbf{x}, 0) = \mathbf{0} \quad \mathbf{x} \in D, \quad (5.4)$$

where the superscript \pm indicates the each side of crack face. Eq. (5.2) indicates traction continuity over crack faces. Eq. (5.3) denotes that the COD at the crack tip ∂S is equal to zero, and this condition ensures the uniqueness of solution in crack problems. Eq. (5.4) is the initial condition and indicates that there are no scattered waves at $t \leq 0$.

Considering the Sommerfeld radiation condition for scattered waves and initial and boundary conditions (5.4) and (5.2), the scattered displacement fields can be expressed in the following integral representation:

$$\mathbf{u}^{\text{sc}}(\mathbf{x}, t) = - \int_0^t \int_{S^+} \mathbf{T}^+(\mathbf{x}, \mathbf{y}, t - \tau) \cdot [\mathbf{u}^{\text{sc}}](\mathbf{y}, \tau) dS_y d\tau \quad \mathbf{x} \in D. \quad (5.5)$$

Then, substituting $\mathbf{u}^{\text{sc}} = \mathbf{u} - \mathbf{u}^{\text{in}}$ into Eq. (5.5) and considering the continuity of \mathbf{u}^{in} over crack faces yield

$$\mathbf{u}(\mathbf{x}, t) = \mathbf{u}^{\text{in}}(\mathbf{x}, t) - \int_0^t \int_{S^+} \mathbf{T}^+(\mathbf{x}, \mathbf{y}, t - \tau) \cdot [\mathbf{u}](\mathbf{y}, \tau) dS_y d\tau \quad \mathbf{x} \in D. \quad (5.6)$$

The traction operator with respect to \mathbf{x} is multiplied from the left in both hand sides of Eq. (5.6). Then, taking the limit that $\mathbf{x} \in D \rightarrow \mathbf{x} \in S^+$, the collocation hypersingular BIE can be obtained as follows:

$$\mathbf{t}^+(\mathbf{x}, t) = \mathbf{t}^{\text{in};+}(\mathbf{x}, t) - \int_0^t \text{p.f.} \int_{S^+} \mathbf{W}^+(\mathbf{x}, \mathbf{y}, t - \tau) \cdot [\mathbf{u}](\mathbf{y}, \tau) dS_y d\tau \quad \mathbf{x} \in S^+, \quad (5.7)$$

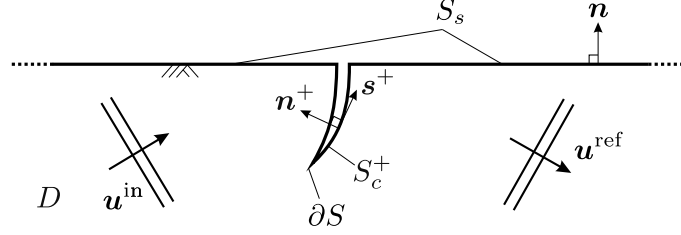


Figure 5.2.: Analysis model for wave scattering by a surface breaking crack in a 2-D elastic half-space.

where \mathbf{W}^+ is the hypersingular kernel corresponding to \mathbf{n}^+ and given as follows:

$$W_{bj}^+(\mathbf{x}, \mathbf{y}, t) = n_a^+(\mathbf{x}) n_k^+(\mathbf{y}) C_{baic} C_{jkpq} \frac{\partial}{\partial x_c} \frac{\partial}{\partial y_q} U_{ip}(\mathbf{x}, \mathbf{y}, t). \quad (5.8)$$

Note that the hypersingular kernel \mathbf{W} for 2-D problems has singularity of order $1/r^2$ as $r \downarrow 0$. Multiplying the weight function ψ and integrating over the surface S^+ with respect to \mathbf{x} , the variational hypersingular BIE can be derived as follows:

$$\begin{aligned} \int_{S^+} \psi(\mathbf{x}) \mathbf{t}^+(\mathbf{x}, t) dS_x &= \int_{S^+} \psi(\mathbf{x}) \mathbf{t}^{\text{in};+}(\mathbf{x}, t) dS_x \\ &\quad - \int_0^t \int_{S^+} \psi(\mathbf{x}) \text{p.f.} \int_{S^+} \mathbf{W}^+(\mathbf{x}, \mathbf{y}, t - \tau) \cdot [\mathbf{u}](\mathbf{y}, \tau) dS_y dS_x d\tau. \end{aligned} \quad (5.9)$$

Both collocation and variational BIEs contain p.f. integrals as the result of taking of the limit to the boundary. Eq. (5.9) is the BIE which is used for the boundary element analysis in this study.

5.1.2. Scattering problem by surface breaking cracks in half-space

Next, we show the variational formulation of BIE for the scattering problem by a surface breaking crack in an elastic half-space. In this study, the full-space fundamental solutions are used for solving the initial and boundary value problem. Then, the scattered far-fields are evaluated by means of approximated Green's functions for an elastic half-space. The similar boundary element analyses for the traction-free crack have been implemented in frequency-domain by Zhang and Achenbach [102, 103].

Let S_s and S_c be flat free surface and smooth curved crack face, respectively in \mathbb{R}^2 as depicted in Fig. 5.2. We assume that the governing equation and boundary conditions on crack face S_c are same as Eqs. (5.1)–(5.4). In addition, the boundary condition on the free-surface S_s is given by

$$\mathbf{t}(\mathbf{x}, t) = \mathbf{0} \quad \mathbf{x} \in S_s. \quad (5.10)$$

Therefore, we can obtain the following integral representation of scattered waves in D by means of

5. 2-D Simulation of Nonlinear Ultrasonic Waves Due to Interior and Surface Breaking Cracks

a similar manner to the crack problems in an infinite domain.

$$\begin{aligned} \mathbf{u}^{\text{sc}}(\mathbf{x}, t) = & - \int_0^t \int_{S_s} \mathbf{T}(\mathbf{x}, \mathbf{y}, t - \tau) \cdot \mathbf{u}^{\text{sc}}(\mathbf{y}, \tau) dS_y d\tau \\ & - \int_0^t \int_{S_c^+} \mathbf{T}^+(\mathbf{x}, \mathbf{y}, t - \tau) \cdot [\mathbf{u}](\mathbf{y}, \tau) dS_y d\tau \quad \mathbf{x} \in D, \end{aligned} \quad (5.11)$$

where the scattered wave is defined as the disturbance of free-field \mathbf{u}^{free} by a crack. Multiplying the traction operator corresponding to \mathbf{x} from the left in both sides of Eq. (5.11) and taking the limit that $\mathbf{x} \in D \rightarrow \mathbf{x} \in S_s, S_c^+$, the hypersingular BIE for the surface breaking crack is obtained as follows:

$$\begin{aligned} \mathbf{t}^{\text{sc};+}(\mathbf{x}, t) = & - \int_0^t \text{p.f.} \int_{S_s} \mathbf{W}^+(\mathbf{x}, \mathbf{y}, t - \tau) \cdot \mathbf{u}^{\text{sc}}(\mathbf{y}, \tau) dS_y d\tau \\ & - \int_0^t \text{p.f.} \int_{S_c^+} \mathbf{W}^+(\mathbf{x}, \mathbf{y}, t - \tau) \cdot [\mathbf{u}](\mathbf{y}, \tau) dS_y d\tau \quad \mathbf{x} \in S_s, S_c^+. \end{aligned} \quad (5.12)$$

Taking the free-field of traction $\mathbf{t}^{\text{free}} (\equiv \mathbf{t} - \mathbf{t}^{\text{sc}})$ into account, we can obtain the following expression:

$$\begin{aligned} \mathbf{t}^+(\mathbf{x}, t) = & \mathbf{t}^{\text{free};+}(\mathbf{x}, t) - \int_0^t \text{p.f.} \int_{S_s} \mathbf{W}^+(\mathbf{x}, \mathbf{y}, t - \tau) \cdot \mathbf{u}^{\text{sc}}(\mathbf{y}, \tau) dS_y d\tau \\ & - \int_0^t \text{p.f.} \int_{S_c^+} \mathbf{W}^+(\mathbf{x}, \mathbf{y}, t - \tau) \cdot [\mathbf{u}](\mathbf{y}, \tau) dS_y d\tau \quad \mathbf{x} \in S_s, S_c^+, \end{aligned} \quad (5.13)$$

where \mathbf{t}^{free} consists of incident and reflected waves and satisfies governing equation (5.1) and boundary condition (5.10). The variational formulation corresponding to Eq. (5.13) can be derived using the weight function ψ as follows:

$$\begin{aligned} \int_{S_c^+} \psi(\mathbf{x}) \mathbf{t}^+(\mathbf{x}, t) dS_x = & \int_{S_c^+} \psi(\mathbf{x}) \mathbf{t}^{\text{free};+}(\mathbf{x}, t) dS_x \\ & - \int_0^t \int_{S_s \cup S_c^+} \psi(\mathbf{x}) \text{p.f.} \int_{S_s} \mathbf{W}^+(\mathbf{x}, \mathbf{y}, t - \tau) \cdot \mathbf{u}^{\text{sc}}(\mathbf{y}, \tau) dS_y dS_x d\tau \\ & - \int_0^t \int_{S_s \cup S_c^+} \psi(\mathbf{x}) \text{p.f.} \int_{S_c^+} \mathbf{W}^+(\mathbf{x}, \mathbf{y}, t - \tau) \cdot [\mathbf{u}](\mathbf{y}, \tau) dS_y dS_x d\tau. \end{aligned} \quad (5.14)$$

The scattered wave \mathbf{u}^{sc} is used for the variable on free-surface, while the COD $[\mathbf{u}]$ is the one on crack face as shown in Eq. (5.14). Considering appropriate boundary conditions on crack face, Eqs. (5.9) and (5.14) can be solved numerically. In order to accurately evaluate the p.f. integral which contains the hypersingular kernel, the regularization technique is used for relaxing the singularity.

5.2. Regularization of BIE

In this section, the regularization of hypersingular BIE is presented. The superscript $+$ is hereinafter omitted in this chapter.

According to [93], the second term in the right-hand side of Eq. (5.9) can be regularized from p.f. integral to p.v. one as follows:

$$\begin{aligned}
& \int_0^t \int_S \psi(\mathbf{x}) \text{p.f.} \int_S W_{bj}(\mathbf{x}, \mathbf{y}, t - \tau) [u_j](\mathbf{y}, \tau) dS_y dS_x d\tau \\
&= e_{de} e_{ck} C_{baic} \int_0^t \int_S \psi(\mathbf{x}) n_a(\mathbf{x}) \text{p.v.} \int_S \Sigma_{ikj}(\mathbf{x}, \mathbf{y}, t - \tau) n_e(\mathbf{y}) \frac{\partial [u_j](\mathbf{y}, \tau)}{\partial y_d} dS_y dS_x d\tau \\
&- \rho C_{baic} \int_0^t \int_S \psi(\mathbf{x}) n_a(\mathbf{x}) \int_S \ddot{U}_{ij}(\mathbf{x}, \mathbf{y}, t - \tau) n_c(\mathbf{y}) [u_j](\mathbf{y}, \tau) dS_y dS_x d\tau \\
&- e_{ck} C_{baic} \int_0^t \int_S \psi(\mathbf{x}) n_a(\mathbf{x}) \int_S s_d(\mathbf{y}) \frac{\partial}{\partial y_d} \left[\Sigma_{ikj}(\mathbf{x}, \mathbf{y}, t - \tau) [u_j](\mathbf{y}, \tau) \right] dS_y dS_x d\tau, \quad (5.15)
\end{aligned}$$

where e_{ij} is a component of the 2-D permutation tensor. Σ is the fundamental solution with respect to stress and has an singularity of order $1/r$ as $r \downarrow 0$ (so-called strong singularity). Note that this singularity is not related with stress singularity at crack tips and sometimes called non-physical singularity. The third term in the right-hand side of Eq. (5.15) contains the tangential derivative $s_d(\mathbf{y}) \partial / \partial y_d$ and vanishes when $[u]$ is equal to zero at the edges of boundary S as described in Eq. (5.3). It therefore vanishes in the case that crack is located on the inside of material.

Now, we show the regularized BIEs corresponding to Eqs. (5.9) and (5.14). The regularized BIE for the scattering problem by cracks in an infinite domain can be obtained as follows:

$$\begin{aligned}
& \int_S \psi(\mathbf{x}) t_b(\mathbf{x}, t) dS_x = \int_S \psi(\mathbf{x}) t_b^{\text{in}}(\mathbf{x}, t) dS_x \\
&+ e_{de} e_{ck} C_{baic} \int_0^t \int_S \psi(\mathbf{x}) n_a(\mathbf{x}) \text{p.v.} \int_S \Sigma_{ikj}(\mathbf{x}, \mathbf{y}, t - \tau) n_e(\mathbf{y}) \frac{\partial [u_j](\mathbf{y}, \tau)}{\partial y_d} dS_y dS_x d\tau \\
&- \rho C_{baic} \int_0^t \int_S \psi(\mathbf{x}) n_a(\mathbf{x}) \int_S \ddot{U}_{ij}(\mathbf{x}, \mathbf{y}, t - \tau) n_c(\mathbf{y}) [u_j](\mathbf{y}, \tau) dS_y dS_x d\tau, \quad (5.16)
\end{aligned}$$

where boundary condition (5.3) is used. On the other hand, the regularized BIE for the scattering problem by surface breaking cracks in an elastic half-space can be written as follows:

5. 2-D Simulation of Nonlinear Ultrasonic Waves Due to Interior and Surface Breaking Cracks

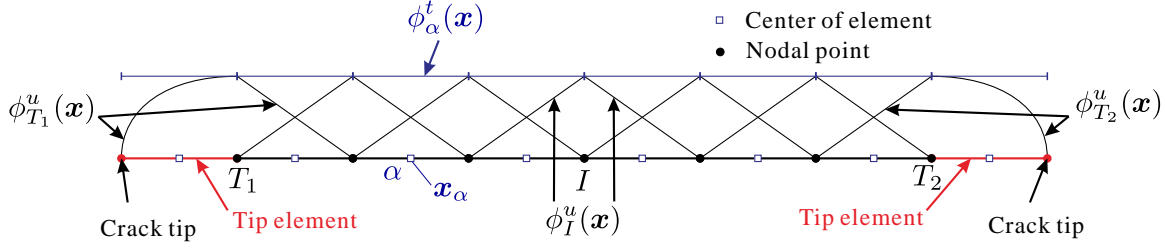


Figure 5.3.: Spatial shape functions with respect to displacement and traction for a crack in an infinite domain.

$$\begin{aligned}
 \int_{S_c} \psi(\mathbf{x}) t_b(\mathbf{x}, t) dS_x &= \int_{S_c} \psi(\mathbf{x}) t_b^{\text{free}}(\mathbf{x}, t) dS_x \\
 &+ e_{de} e_{ck} C_{baic} \int_0^t \int_{S_s \cup S_c} \psi(\mathbf{x}) n_a(\mathbf{x}) \text{p.v.} \int_{S_s} \Sigma_{ikj}(\mathbf{x}, \mathbf{y}, t - \tau) n_e(\mathbf{y}) \frac{\partial u_j^{\text{sc}}(\mathbf{y}, \tau)}{\partial y_d} dS_y dS_x d\tau \\
 &- \rho C_{baic} \int_0^t \int_{S_s \cup S_c} \psi(\mathbf{x}) n_a(\mathbf{x}) \int_{S_s} \ddot{U}_{ij}(\mathbf{x}, \mathbf{y}, t - \tau) n_c(\mathbf{y}) u_j^{\text{sc}}(\mathbf{y}, \tau) dS_y dS_x d\tau \\
 &- e_{ck} C_{baic} \int_0^t \int_{S_s \cup S_c} \psi(\mathbf{x}) n_a(\mathbf{x}) \int_{S_s} s_d(\mathbf{y}) \frac{\partial}{\partial y_d} \left[\Sigma_{ikj}(\mathbf{x}, \mathbf{y}, t - \tau) u_j^{\text{sc}}(\mathbf{y}, \tau) \right] dS_y dS_x d\tau \\
 &+ e_{de} e_{ck} C_{baic} \int_0^t \int_{S_s \cup S_c} \psi(\mathbf{x}) n_a(\mathbf{x}) \text{p.v.} \int_{S_c} \Sigma_{ikj}(\mathbf{x}, \mathbf{y}, t - \tau) n_e(\mathbf{y}) \frac{\partial [u_j](\mathbf{y}, \tau)}{\partial y_d} dS_y dS_x d\tau \\
 &- \rho C_{baic} \int_0^t \int_{S_s \cup S_c} \psi(\mathbf{x}) n_a(\mathbf{x}) \int_{S_c} \ddot{U}_{ij}(\mathbf{x}, \mathbf{y}, t - \tau) n_c(\mathbf{y}) [u_j](\mathbf{y}, \tau) dS_y dS_x d\tau \\
 &- e_{ck} C_{baic} \int_0^t \int_{S_s \cup S_c} \psi(\mathbf{x}) n_a(\mathbf{x}) \int_{S_c} s_d(\mathbf{y}) \frac{\partial}{\partial y_d} \left[\Sigma_{ikj}(\mathbf{x}, \mathbf{y}, t - \tau) [u_j](\mathbf{y}, \tau) \right] dS_y dS_x d\tau. \quad (5.17)
 \end{aligned}$$

5.3. Discretization of BIE

Next, the time and spatial discretization using the IRK based-CQM [48] and Galerkin method, respectively, is presented. In this study, we use straight-line elements for division of surfaces, S , S_c , and S_s . For interpolation of quantities, different shape functions between displacement and traction are taken because we consider the continuity and discontinuity of displacement and traction between two adjacent elements, respectively. Specifically, the piecewise linear interpolation and tip element are used for $[\mathbf{u}]$ and \mathbf{u}^{sc} , and \mathbf{t} is interpolated by the piecewise constant shape function. The shape functions with respect to these variables for a crack in an infinite domain are presented in Fig. 5.3. Using the Galerkin method, the weight functions ψ are taken to be same as the corresponding shape functions of variable considered in each BIE. Therefore, ψ is different between BIEs for displacement and traction.

5.3.1. Scattering problem by cracks in infinite domain

First, we discretize the BIE for scattering problems by cracks in an infinite domain. If the boundary S in Eq. (5.16) is divided into M_e straight-line elements consisting of M_d nodal points, the discretized BIEs for $[\mathbf{u}]$ and \mathbf{t} at n -th and i -th sub-step in time can be written as follows:

$$\sum_{j=1}^m \sum_{J=1}^{M_d} \mathcal{W}_{IJ}^{ij;0} \cdot [\mathbf{u}]_J^{j;n} = - \sum_{\alpha=1}^{M_e} \mathbf{t}_{\alpha}^{i;n} \phi_{\alpha}^t \int_{\text{supp}(\phi_I^u) \cap S_{\alpha}} \phi_I^u(\mathbf{x}) dS_x + \int_{\text{supp}(\phi_I^u)} \phi_I^u(\mathbf{x}) \mathbf{t}^{\text{in}}(\mathbf{x}, (n + c_i)\Delta t) dS_x - \sum_{k=0}^{n-1} \sum_{j=1}^m \sum_{J=1}^{M_d} \mathcal{W}_{IJ}^{ij;n-k} \cdot [\mathbf{u}]_J^{j;k}, \quad (5.18)$$

$$\mathbf{t}_{\alpha}^{i;n} \phi_{\alpha}^t \phi_{\alpha}^t \int_{S_{\alpha}} dS_x = \phi_{\alpha}^t \int_{S_{\alpha}} \mathbf{t}^{\text{in}}(\mathbf{x}, (n + c_i)\Delta t) dS_x - \sum_{k=0}^n \sum_{j=1}^m \sum_{J=1}^{M_d} \tilde{\mathcal{W}}_{\alpha J}^{ij;n-k} \cdot [\mathbf{u}]_J^{j;k}, \quad (5.19)$$

where subscripts I and J indicate the indices of nodal point. In addition, $\text{supp}(\phi)$ denotes the support of ϕ , and $\int_{S_{\alpha}} dS_x$ in the left hand side of Eq. (5.19) is equal to the length of α -th element. The specific expressions of $[\mathbf{u}]_I^{i;n}$ and $\mathbf{t}_{\alpha}^{i;n}$ are

$$[\mathbf{u}]_I^{i;n} = [\mathbf{u}](\mathbf{x}_I, (n + c_i)\Delta t), \quad \mathbf{t}_{\alpha}^{i;n} = \mathbf{t}(\mathbf{x}_{\alpha}, (n + c_i)\Delta t),$$

where \mathbf{x}_I is the position vector of I -th nodal point. The influence functions $\mathcal{W}_{IJ}^{ij;\kappa}$ and $\tilde{\mathcal{W}}_{\alpha J}^{ij;\kappa}$ in Eqs. (5.18) and (5.19) are given by

$$\mathcal{W}_{IJ}^{ij;\kappa} = \tilde{\mathcal{F}}_{l\kappa}^{-1} \left[\sum_{\beta=1}^m \left(\mathbf{E}_{\beta}(\zeta_l) \right)_{ij} \int_{\text{supp}(\phi_I^u)} \phi_I^u(\mathbf{x}) \mathcal{W}_J^{\beta;l}(\mathbf{x}) dS_x \right], \quad (5.20)$$

$$\tilde{\mathcal{W}}_{\alpha J}^{ij;\kappa} = \tilde{\mathcal{F}}_{l\kappa}^{-1} \left[\sum_{\beta=1}^m \left(\mathbf{E}_{\beta}(\zeta_l) \right)_{ij} \phi_{\alpha}^t \int_{S_{\alpha}} \mathcal{W}_J^{\beta;l}(\mathbf{x}) dS_x \right], \quad (5.21)$$

where

$$\begin{aligned} \left(\mathcal{W}_J^{\beta;l}(\mathbf{x}) \right)_{bj} &= e_{de} e_{ck} C_{baic} n_a(\mathbf{x}) \text{p.v.} \int_{\text{supp}(\phi_J^u)} \hat{\Sigma}_{ikj}(\mathbf{x}, \mathbf{y}, \lambda_{\beta}^l) n_e(\mathbf{y}) \frac{\partial \phi_J^u(\mathbf{y})}{\partial y_d} dS_y \\ &\quad - \rho \left(\lambda_{\beta}^l \right)^2 C_{baic} n_a(\mathbf{x}) \int_{\text{supp}(\phi_J^u)} \hat{U}_{ij}(\mathbf{x}, \mathbf{y}, \lambda_{\beta}^l) n_c(\mathbf{y}) \phi_J^u(\mathbf{y}) dS_y \\ &\quad - e_{ck} n_a(\mathbf{x}) C_{baic} \int_{\text{supp}(\phi_J^u)} s_d(\mathbf{y}) \frac{\partial}{\partial y_d} \left[\hat{\Sigma}_{ikj}(\mathbf{x}, \mathbf{y}, \lambda_{\beta}^l) \phi_J^u(\mathbf{y}) \right] dS_y. \end{aligned} \quad (5.22)$$

In Eq. (5.22), \hat{U} and $\hat{\Sigma}$ are the 2-D fundamental solutions corresponding to displacement and stress in Laplace-domain. Note that the underlined term in the right-hand side of Eq. (5.22) is canceled by boundary condition (5.3) for a crack on the inside of materials.

In this study, we use two types of special shape functions for displacement $\phi_{T_1}^u$ and $\phi_{T_2}^u$ on the tip elements (see Fig. 5.3) in order to describe the proper behavior of COD at the crack tip. If \mathbf{y}_1 and

5. 2-D Simulation of Nonlinear Ultrasonic Waves Due to Interior and Surface Breaking Cracks

\mathbf{y}_2 are the left and right edges of element, respectively, the specific expressions of $\phi_{T_1}^u$ and $\phi_{T_2}^u$ are shown as follows:

$$\phi_{T_1}^u(\mathbf{y}) = \sqrt{\frac{|\mathbf{y} - \mathbf{y}_1|}{|\mathbf{y}_2 - \mathbf{y}_1|}}, \quad \phi_{T_2}^u(\mathbf{y}) = \sqrt{\frac{|\mathbf{y} - \mathbf{y}_2|}{|\mathbf{y}_1 - \mathbf{y}_2|}}.$$

Note that the derivatives of shape functions on tip elements have additional singularity of order $1/\sqrt{r}$ corresponding to the stress singularity as $\mathbf{y} \rightarrow \partial S$. Therefore, the coordinate transformation is used for the first term in the right-hand side of Eq. (5.22) before the numerical integration using the standard Gaussian quadrature.

We summarize the procedure of transformation as follows:

1. The interval of integration over the line element is transformed from $[\mathbf{y}_1, \mathbf{y}_2]$ to $[0, 1]$. If the kernel function is $A(\mathbf{y})$, the integral is transformed as follows:

$$\int_{\mathbf{y}_1}^{\mathbf{y}_2} A(\mathbf{y}) dS_y = l_e \int_0^1 A(l) dl, \quad (5.23)$$

where $l_e = |\mathbf{y}_2 - \mathbf{y}_1|$, and $\mathbf{y} = \mathbf{y}_1 + (\mathbf{y}_2 - \mathbf{y}_1)l$.

2. The integral variable l is changed to appropriate one l^* considering the location of crack tip. When the crack tip is located at $l = 0$, the relation between l and l^* is taken as

$$l = (l^*)^2, \quad J^*(l^*) = 2l^*,$$

where J^* is the Jacobian corresponding to coordinate transformation as l to l^* . On the other hand,

$$l = 1 - (1 - l^*)^2, \quad J^*(l^*) = 2(1 - l^*)$$

for the case that the crack tip is located at $l = 1$. Then, the Jacobian corresponding to each l^* can cancel the singularity of order $1/\sqrt{r}$, and Eq. (5.23) is rewritten as follows:

$$l_e \int_0^1 A(l) dl = l_e \int_0^1 A(l^*) J^*(l^*) dl^*. \quad (5.24)$$

3. In order to use the standard Gaussian quadrature, l^* is transformed to f with interval $[-1, 1]$ as follows:

$$l_e \int_0^1 A(l^*) J^*(l^*) dl^* = \frac{1}{2} l_e \int_{-1}^1 A(f) J^*(f) df, \quad (5.25)$$

where f is given by $l^* = (f + 1)/2$. Using Eq. (5.25), the integrals of $\hat{\Sigma}$ for tip elements can be evaluated accurately.

In this study, all integrals of static parts of \hat{U} and $\hat{\Sigma}$ are analytically calculated.

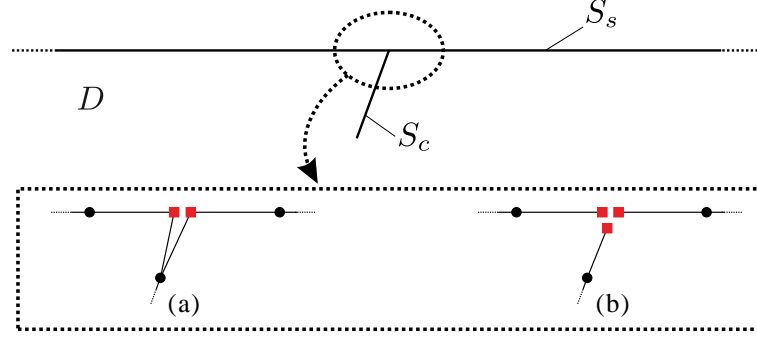


Figure 5.4.: (a) Double node model and (b) triple node model for connection point between surface breaking crack and free-surface.

5.3.2. Scattering problem by surface breaking cracks in half-space

Second, we discretize the BIE for scattering problems by a surface breaking crack in an elastic half-space. For the connection point between the surface breaking crack and free-surface, we need to consider discontinuity of displacement. The double node model as depicted in Fig. 5.4 (a) is usually utilized for this type of problem, where square nodal points are in the same position. If we use the double node model, boundaries S_s and S_c are considered as continuous and closed. Therefore, the fourth and seventh terms in the right-hand side of Eq. (5.17) can be canceled. However, the triple node model as depicted in Fig. 5.4 (b) is utilized in this study because the manageability of nonlinear iterative calculation becomes much easier than the case of double node model.

If the boundaries S_c and S_s in Eq. (5.16) is divided into M_c and M_s straight-line elements consisting of M_d nodal points, the discretized BIEs for $[u]$ and u^{sc} , and t at n -th and i -th sub-step in time are written as follows:

$$\sum_{j=1}^m \sum_{J=1}^{M_d} \mathcal{W}_{IJ}^{ij;0} \cdot v_J^{j;n} = - \sum_{\alpha=1}^{M_c} t_{\alpha}^{i;n} \phi_{\alpha}^t \int_{\text{supp}(\phi_I^u) \cap S_{\alpha}} \phi_I^u(x) dS_x + \int_{\text{supp}(\phi_I^u)} \phi_I^u(x) t^{\text{free}}(x, (n + c_i)\Delta t) dS_x - \sum_{k=0}^{n-1} \sum_{j=1}^m \sum_{J=1}^{M_d} \mathcal{W}_{IJ}^{ij;n-k} \cdot v_J^{j;k}, \quad (5.26)$$

$$t_{\alpha}^{i;n} \phi_{\alpha}^t \phi_{\alpha}^t \int_{S_{\alpha}} dS_x = \phi_{\alpha}^t \int_{S_{\alpha}} t^{\text{free}}(x, (n + c_i)\Delta t) dS_x - \sum_{k=0}^n \sum_{j=1}^m \sum_{J=1}^{M_d} \tilde{\mathcal{W}}_{\alpha J}^{ij;n-k} \cdot v_J^{j;k}. \quad (5.27)$$

In Eqs. (5.26) and (5.27),

$$v_I^{i;n} = \left\{ \begin{array}{l} [u]_I^{i;n} \\ u_{sc;i;n} \end{array} \right\} \text{ when } I\text{-th nodal point belongs to } \left\{ \begin{array}{l} S_c \\ S_s \end{array} \right\}.$$

For the calculation of influence functions in Eqs. (5.26) and (5.27), the underlined term in the right-hand side of Eq. (5.22) has to be evaluated. This term can be modified into the following

5. 2-D Simulation of Nonlinear Ultrasonic Waves Due to Interior and Surface Breaking Cracks

expression and easily evaluated for 2-D problems.

$$\begin{aligned}
e_{ck}n_a(\mathbf{x})C_{baic} \int_{\text{supp}(\phi_J^u)} s_d(\mathbf{y}) \frac{\partial}{\partial y_d} \left[\hat{\Sigma}_{ikj}(\mathbf{x}, \mathbf{y}, \lambda_\beta^l) \phi_J^u(\mathbf{y}) \right] dS_y \\
= e_{ck}n_a(\mathbf{x})C_{baic} \sum_{S_e \in \text{supp}(\phi_J^u)} \int_{S_e} s_d(\mathbf{y}) \frac{\partial}{\partial y_d} \left[\hat{\Sigma}_{ikj}(\mathbf{x}, \mathbf{y}, \lambda_\beta^l) \phi_J^u(\mathbf{y}) \right] dS_y \\
= e_{ck}n_a(\mathbf{x})C_{baic} \sum_{S_e \in \text{supp}(\phi_J^u)} \left[\hat{\Sigma}_{ikj}(\mathbf{x}, \mathbf{y}, \lambda_\beta^l) \phi_J^u(\mathbf{y}) \right]_{\mathbf{y}=\mathbf{y}_1}^{\mathbf{y}=\mathbf{y}_2}, \quad (5.28)
\end{aligned}$$

where S_e is an element area and has the interval $[\mathbf{y}_1, \mathbf{y}_2]$.

5.4. Nonlinear boundary conditions and numerical procedure

The nonlinear boundary conditions on crack faces are different from the ones for an interface crack in Section 4.2.1 because this problem is 2-D, and the formulations and variables are different. Therefore, the nonlinear boundary conditions and numerical procedure are briefly presented in this section.

In order to simultaneously solve BIEs (5.18) and (5.19), the appropriate boundary conditions should be selected at each time step. We also consider three types of state in a similar way to Section 4.2.1. The boundary conditions for separation, stick, and slip states are summarized as follows:

$$\begin{cases} \mathbf{t} = \mathbf{0} & : \text{separation,} & (5.29a) \\ [\mathbf{u}] \cdot \mathbf{n} = u_g, \quad [\dot{\mathbf{u}}] \cdot \mathbf{s} = 0 & : \text{stick,} & (5.29b) \\ [\mathbf{u}] \cdot \mathbf{n} = u_g, \quad \mathbf{t} \cdot \mathbf{s} = \text{sgn}([\dot{\mathbf{u}}] \cdot \mathbf{s}) \mu_d \mathbf{t} \cdot \mathbf{n} & : \text{slip.} & (5.29c) \end{cases}$$

As shown in Eq. (5.29c), the slip direction in the 2-D problem is positive or negative, and its evaluation is easier than the 3-D case.

The transition conditions for the iterative calculation are summarized as follows:

$$\begin{cases} [\mathbf{u}] \cdot \mathbf{n} \geq u_g & : \text{separation} \rightarrow \text{stick,} & (5.30a) \\ \mathbf{t} \cdot \mathbf{n} > 0 & : \text{stick or slip} \rightarrow \text{separation,} & (5.30b) \\ |\mathbf{t} \cdot \mathbf{s}| \geq \mu_s |\mathbf{t} \cdot \mathbf{n}| & : \text{stick} \rightarrow \text{slip,} & (5.30c) \\ \left([\dot{\mathbf{u}}] \cdot \mathbf{s} \right) / \left([\dot{\mathbf{u}}]^{\text{prev}} \cdot \mathbf{s} \right) \leq 0 & : \text{slip} \rightarrow \text{stick.} & (5.30d) \end{cases}$$

Eq. (5.30a) indicates that the phase is changed from separation to stick when the crack faces overlap. Eq. (5.30b) means that the normal tensile force to the crack face opens it. The right-hand side of Eq. (5.30c) corresponds to the maximum static friction force. The crack faces begin to slide relatively in the Coulomb friction law when the absolute value of tangential force exceeds the maximum static friction one. The transition condition from slip to stick is considered as $[\dot{\mathbf{u}}] \cdot \mathbf{s} = 0$ in practice. However, it is difficult to satisfy this condition in numerical simulation. Therefore, we assume that

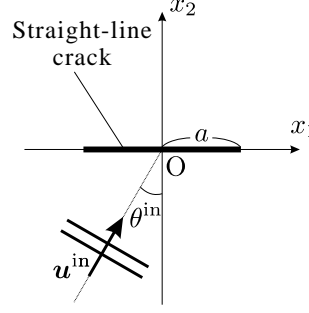


Figure 5.5.: A straight-line crack subjected to an incident plane wave.

the direction change of relatively tangential movement is "stop condition" as shown in Eq. (5.30d). If the left inequalities in Eq. (5.30) are satisfied, the corresponding right transition occurs.

Using boundary conditions (5.29), discretized BIEs (5.18) and (5.19) can be simultaneously solved. The iterative algorithm is similar to the case of interface crack in Section 4.3. In addition, discretized BIEs (5.18) and (5.19) are modified for the velocity of displacement tangential to the crack face as well as Section 4.2.2. The scattering problems by surface breaking cracks are also solved in a similar way to the one by cracks in an infinite elastic solid.

5.5. Numerical results

In this section, numerical results of the proposed IRK-based CQ-BEM are presented. Before the sub-harmonic generation, the linear problem is first solved in order to verify the proposed method for the crack problem. Second, the higher-harmonic simulation is conducted to validate the contact model of crack faces. Finally, numerical results of sub-harmonic generation due to cracks in an infinite domain and a surface breaking crack in a half-space are presented. The non-accelerated CQ-BEM with RK2 is used for all numerical simulations in this section.

5.5.1. Linear problem

In advance of the nonlinear ultrasonic simulation, the numerical results for the traction-free crack are shown in order to verify the proposed IRK-based CQ-BEM. We compute the stress intensity factor (SIF) of mode I for straight-line crack subjected to an incident plane P wave as depicted in Fig. 5.5, where a is the half length of a crack. The incident plane P wave is defined by the monotonically increasing function as follows:

$$u^{\text{in}}(\mathbf{x}, t) = -u_0 \mathbf{d}_L \frac{c_L}{a} \left(t - \frac{\mathbf{p} \cdot (\mathbf{x} - \boldsymbol{\chi})}{c_L} \right) H \left(t - \frac{\mathbf{p} \cdot (\mathbf{x} - \boldsymbol{\chi})}{c_L} \right). \quad (5.31)$$

\mathbf{p} , \mathbf{d}_L , and $\boldsymbol{\chi}$ are given by $\mathbf{p} = \mathbf{d}_L = (\sin \theta^{\text{in}}, \cos \theta^{\text{in}})$ and $\boldsymbol{\chi} = (-a, 0)$ in this simulation, respectively. The crack surface S is divided into 40 boundary elements, time increment Δt is taken

5. 2-D Simulation of Nonlinear Ultrasonic Waves Due to Interior and Surface Breaking Cracks

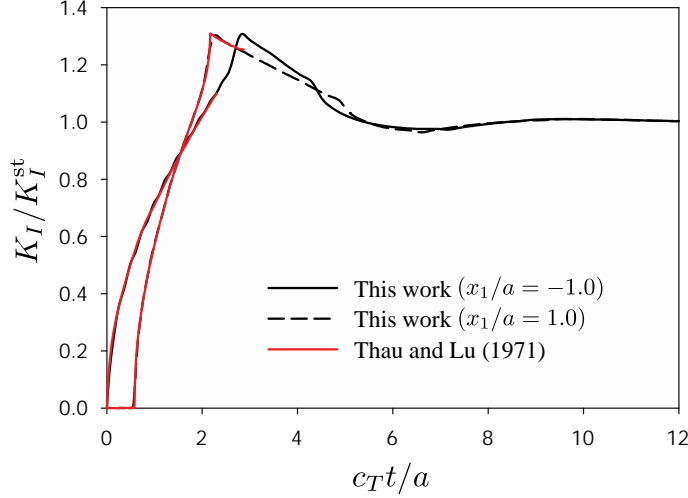


Figure 5.6.: Time variations of dynamic SIF of mode I when $\theta^{\text{in}} = 30^\circ$.

as $c_T \Delta/a = 0.05$, and Poisson's ratio ν is given by $\nu = 0.25$. The mode I dynamic SIF can be calculated from COD near the crack tip as follows:

$$K_I(t) = -\frac{\mu\sqrt{2\pi}}{4(1-\nu)} \lim_{\varepsilon \rightarrow 0} \frac{1}{\sqrt{\varepsilon}} [\mathbf{u}](\varepsilon, t) \cdot \mathbf{n}(\varepsilon), \quad (5.32)$$

where ε is the distance from the crack tip.

Time histories of dynamic SIF of mode I corresponding to the crack tips at $x_1/a = -1.0$ and 1.0 are shown in Fig. 5.6 when a straight-line crack is subjected to an incident plane P wave with $\theta^{\text{in}} = 30^\circ$. The dynamic SIFs shown here are normalized by the exact solution of static problems $K_I^{\text{st}} = \sigma_{22}\sqrt{\pi a}$. The short time exact solutions for this problem have been obtained by Thau and Lu [94], and they are plotted in the same figure for comparison. Both numerical solutions are in good agreement with the exact ones and converge to the static exact ones over time. Therefore, the scattering problem by a crack can be accurately solved using the proposed IRK-based CQ-BEM.

5.5.2. Higher-harmonic simulation

In order to validate the contact model of crack face, the numerical results of higher-harmonic simulation are presented in this section. The analysis model in Fig. 5.5 is also used for this simulation, and we confirm that our model can reproduce the clapping motion and friction on crack faces. θ^{in} is given by $\theta^{\text{in}} = 0^\circ$ here because fundamental motions on crack faces are investigated. The following sinusoidal burst wave with n^{in} cycles is used as the incident wave for this simulation.

$$\begin{cases} \mathbf{u}^{\text{in}}(\mathbf{x}, t) = u_0 \mathbf{d}_\varphi \sin(2\pi \Lambda_\varphi) H(\Lambda_\varphi) H(n^{\text{in}} - \Lambda_\varphi), & (5.33a) \end{cases}$$

$$\begin{cases} \Lambda_\varphi = f^{\text{in}} \left(t - \frac{\mathbf{p} \cdot (\mathbf{x} - \boldsymbol{\chi})}{c_\varphi} \right), & (5.33b) \end{cases}$$

where $\varphi = L$ or T because of the 2-D problem. The far-field approximated scattered wave is used for the spectrum analysis of scattered wave (see Appendix B). The time increment is taken as $f^{\text{in}}\Delta t = 0.05$, and Poisson's ratio of base material is given by $\nu = 0.3$ supposing steel. The friction coefficients are thus given by the top row of Table 4.2. n^{in} is taken as $n^{\text{in}} = 30$ because we conduct transient analysis for a sufficiently long time and investigate nearly stationary vibration.

First, some numerical results of P wave incidence are presented when $\theta^{\text{in}} = 0^\circ$, $k_T a = 3.0$, and $u_g/u_0 = 0.0$. Time histories of vertical COD at the center point of a crack is shown in Fig. 5.7 (a). On the other hand, time histories and normalized frequency spectra of far-field amplitude of backscattered P wave $\Omega_L/(u_0\sqrt{a})$ in Fig. 5.7 (b), and (c), respectively. In these figures, "linear" and "nonlinear" indicate the results obtained for the traction-free crack and the crack with contact boundary conditions, respectively. The small windows in the figures show the enlarged view of early parts. As shown in Fig. 5.7 (a), the vertical COD obtained by the presented model cannot take the negative value due to contact. From Fig. 5.7 (b), the waveform of $\Omega_L/(u_0\sqrt{a})$ is distorted by the clapping motion. Therefore, its frequency spectrum contains the higher harmonic components as shown in Fig. 5.7 (c). It is known that all (2nd, 3rd, 4th, etc.) orders of higher-harmonic waves are generated for the normal incidence of P wave [89], and that is reproduced by the presented numerical simulation.

Second, numerical results of S wave incidence are presented when $\theta^{\text{in}} = 0^\circ$, $k_T a = 3.0$, and $u_g/u_0 = 0.0$. In this case, the static compressive stress σ^{st} is given over a crack uniformly in order to generate the dynamic friction force. σ^{st} is given by $\sigma^{\text{st}}/\sigma_0 = 1.0$ here. If σ^{st} does not cause COD due to contact of crack faces, σ^{st} is only added into t^{in} or t^{free} in BIEs similarly to Chapter 4. Therefore, if we give u_g/u_0 as a parameter, $\sigma^{\text{st}}/\sigma_0$ is equal to zero in this study. The reverse is also true.

Time histories of tangential traction at the center point of a crack is shown in Fig. 5.8 (a). On the other hand, time histories and normalized frequency spectra of far-field amplitude of backscattered S wave $\Omega_T/(u_0\sqrt{a})$ in Fig. 5.8 (b), and (c), respectively. As shown in Fig. 5.8 (a), the tangential traction becomes similar to square wave due to dynamic friction force. Therefore, the waveform of $\Omega_T/(u_0\sqrt{a})$ is distorted and the amplitude becomes small as shown in Fig. 5.8 (b). From Fig. 5.8 (c), the 3rd higher-harmonic component is contained in the nonlinear case. It is known that odd order of higher-harmonic waves are generated due to pure shear motion with contact [89], and that is also reproduced. From the above, we can confirm that the presented numerical method can accurately simulate the clapping motion and dynamic friction on crack faces.

Finally, we investigate the characteristic of 2nd higher-harmonic generation varying pre-opening displacement g or static compressive stress σ^{st} when a straight-line crack is subjected to normal incidence of plane P wave. Normalized Fourier amplitudes corresponding to 2nd higher-harmonic wave $A_{2\omega}/A_{2\omega}^0$ for each $k_T a$ varying u_g/u_0 and $\sigma^{\text{st}}/\sigma_0$ are shown in Fig. 5.9 (a) and (b), respectively. The behavior of $A_{2\omega}/A_{2\omega}^0$ varying u_g/u_0 is different among various $k_T a$ as shown in Fig. 5.9 (a). However, the maximum value of $A_{2\omega}/A_{2\omega}^0$ for each $k_T a$ is located at $u_g/u_0 = 0.0$. This is because contact of crack faces is strongly caused if u_g/u_0 is small. On the other hand, behavior of $A_{2\omega}/A_{2\omega}^0$ varying $\sigma^{\text{st}}/\sigma_0$ is different. The maximum value of $A_{2\omega}/A_{2\omega}^0$ in the case that about

5. 2-D Simulation of Nonlinear Ultrasonic Waves Due to Interior and Surface Breaking Cracks

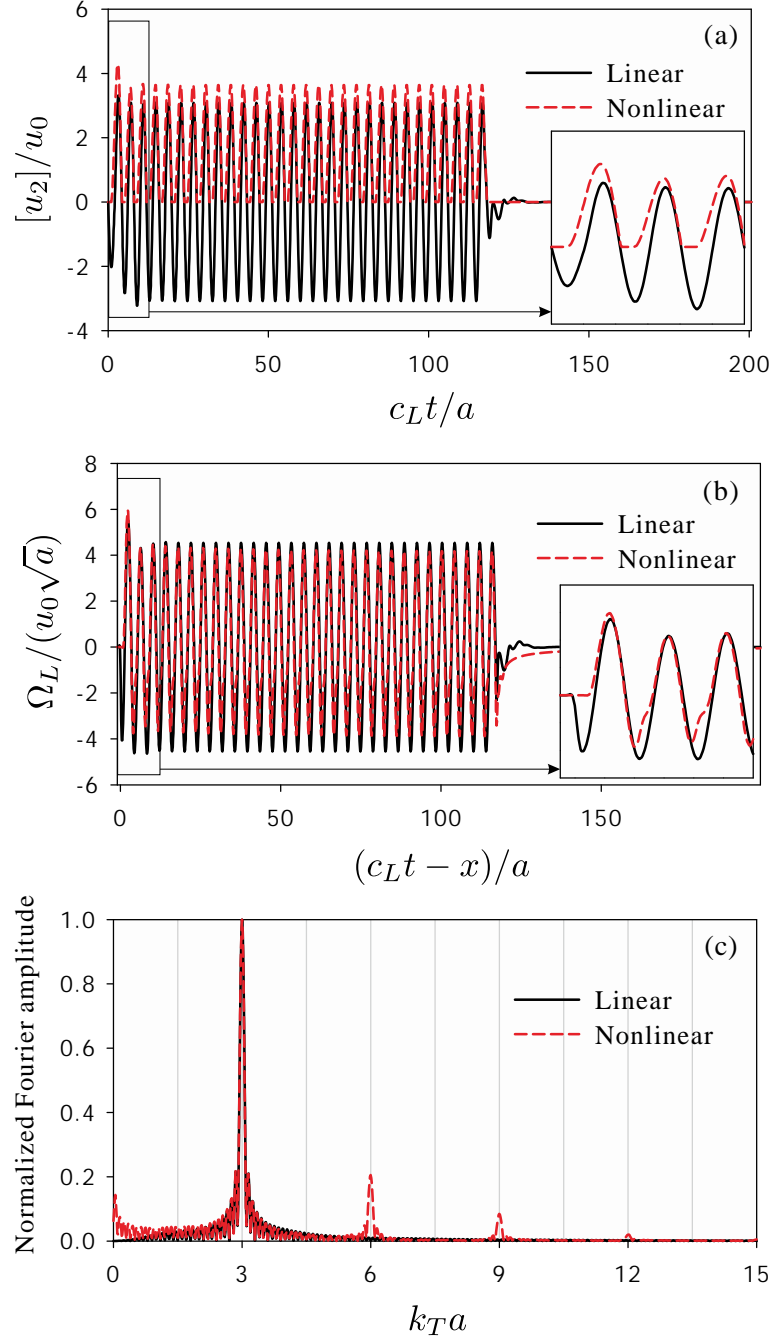


Figure 5.7.: Time variations of (a) COD at the center point of a crack and (b) far-field amplitude of backscattered P wave when a straight-line crack is subjected to an incident plane P wave. (c) is normalized frequency spectrum of far-field amplitude.

$k_T a < 1.2$ is located at $\sigma^{\text{st}}/\sigma_0 = 0.0$ as we can see Fig. 5.9 (b). However, the maximum value of $A_{2\omega}/A_{2\omega}^0$ for about $1.3 < k_T a$ is located at $\sigma^{\text{st}}/\sigma_0 > 0.0$. In addition, the maximum value of $A_{2\omega}/A_{2\omega}^0$ is located at about $\sigma^{\text{st}}/\sigma_0 = 0.4$ when $3.0 < k_T a < 5.5$. In order to investigate the detail, the time histories of far-field amplitude of backscattered P wave $\Omega_L/(u_0\sqrt{a})$ in the case that

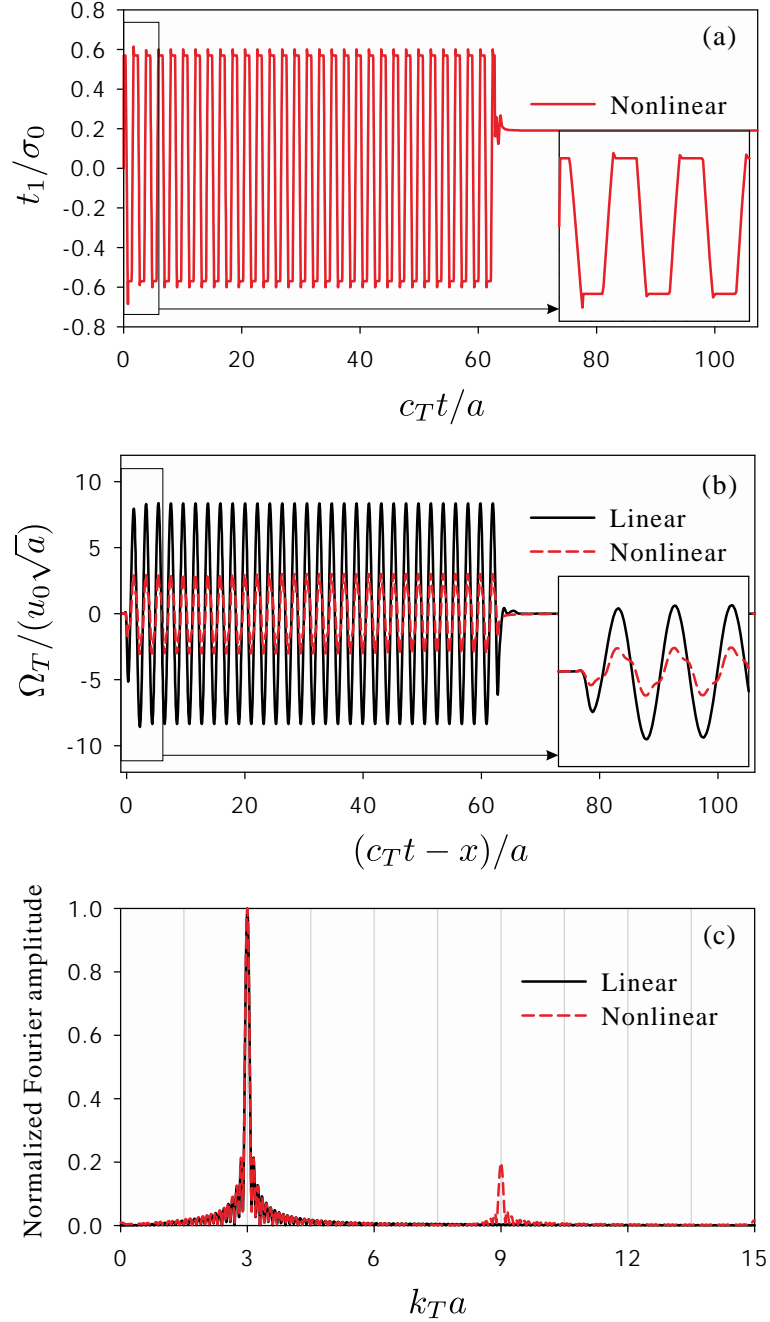


Figure 5.8.: Time variations of (a) tangential traction at the center point of a crack and (b) far-field amplitude of backscattered S wave when a straight-line crack is subjected to an incident plane S wave, and $\sigma^{\text{st}}/\sigma_0 = 1.0$. (c) is normalized frequency spectrum of far-field amplitude.

$k_T a = 5.0$ are shown in Fig. 5.10. As shown in Fig. 5.10, the amplitude of $\Omega_L/(u_0\sqrt{a})$ in the case that $\sigma^{\text{st}}/\sigma_0 = 0.4$ is comparatively small because the compressive static stress prevents crack faces from opening. However, the waveform is strongly distorted, and it is expected to contain many

5. 2-D Simulation of Nonlinear Ultrasonic Waves Due to Interior and Surface Breaking Cracks

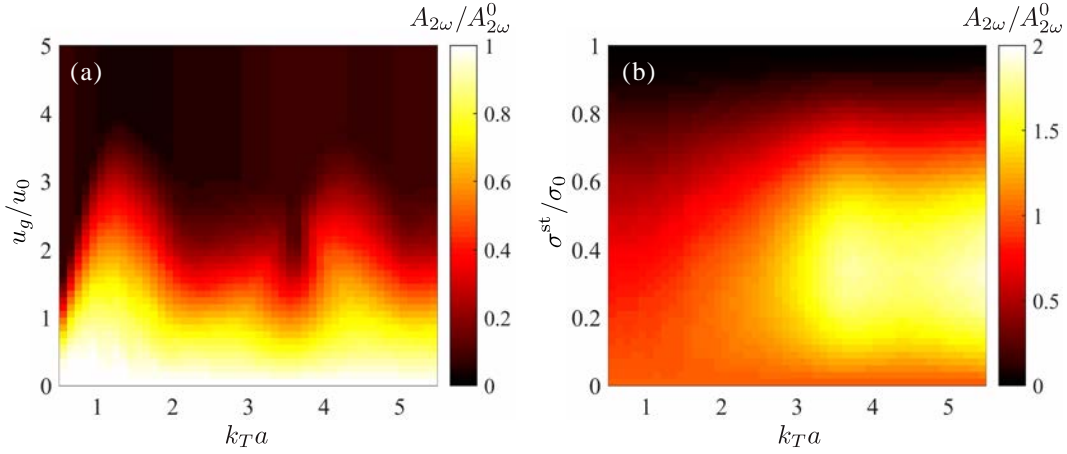


Figure 5.9.: Fourier amplitude corresponding to 2nd higher-harmonic wave normalized by the one when $u_g/u_0 = \sigma^{st}/\sigma_0 = 0.0$ for (a) various $k_T a$ and u_g/u_0 , and (b) various $k_T a$ and σ^{st}/σ_0 .

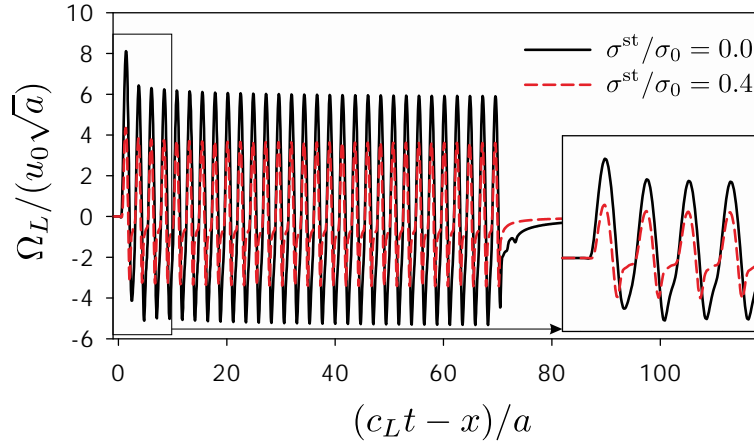


Figure 5.10.: Time variations of far-field amplitude of backscattered P wave when $k_T a = 5.0$.

higher-harmonic components.

From the above, there is optimal static compressive stress for the 2nd higher-harmonic generation when $k_T a$ is comparatively large. The branch point $k_T a \simeq 1.2$ is almost same as the first mode quasi-eigenfrequency in the linear system. It has been pointed out by some researchers that there is optimal static compressive stress for the 2nd higher-harmonic generation [15, 70, 87]. However, the presented 2-D numerical simulation revealed that this phenomenon has relation to quasi-eigenfrequency of the linear system containing a crack.

5.5.3. Simulation of sub-harmonic waves due to interior cracks

Some numerical results of sub-harmonic generation by cracks in an infinite domain are shown here. We consider two types of model for the numerical simulations as depicted in Fig. 5.11. The first is

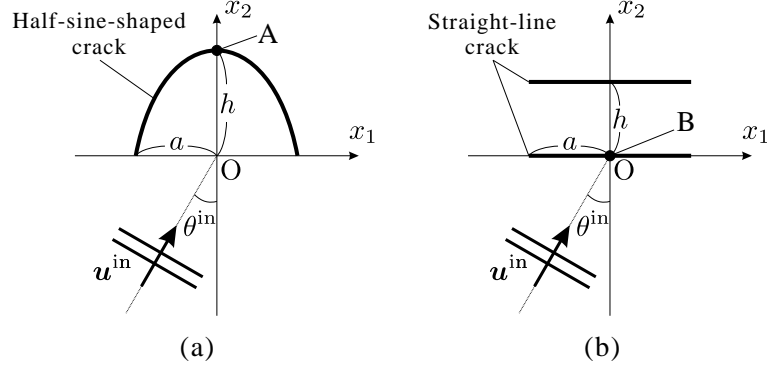


Figure 5.11.: Elastic wave scattering by (a) a half-sine-shaped crack and (b) two straight-line cracks arranged in parallel.

an incident wave scattering by a half-sine-shaped crack (Fig. 5.11 (a)), and the second is that by two cracks arranged in parallel (Fig. 5.11 (b)). In practice, it is not sure that cracks with the shape and arrangement presented here exist. However, our objective is to implement numerical simulations for the system in which the resonance is caused easily. In order to investigate the sub-harmonic generation in the case that contact boundary conditions on crack faces are added into such a system, the analysis models in Fig. 5.11 are selected in this study.

The time increment is taken as $f^{\text{in}} \Delta t = 0.05$, and Poisson's ratio of base material is given by $\nu = 0.3$ supposing steel. The friction coefficients are thus given by the top row of Table 4.2. The cycle number of the incident wave n^{in} is given by $n^{\text{in}} = 30$.

Sub-harmonic generation by a curved crack

First, numerical results obtained by solving the scattering problem by a curved crack as depicted in Fig. 5.11 (a) are shown. Fourier amplitude ratios of sub-harmonic component to fundamental one in backscattered P wave $A_{0.5\omega}/A_{\omega}$ for various $k_T a$, u_g/u_0 , and θ^{in} are shown in Figs. 5.12–5.16 when height h/a is varying. The area enclosed by a white line in Fig. 5.16 indicates the condition under which we can observe the sub-harmonic generation. Therefore, we could not observe the sub-harmonic generation when $0.0 \leq h/a \leq 1.5$ as shown in Figs. 5.12–5.15. For the case that $h/a = 2.0$ in Fig. 5.16, the sub-harmonic generation is caused under certain conditions except the symmetric case, i.e. $\theta^{\text{in}} = 0^\circ$. For instance of the sub-harmonic generation, the time history and normalized frequency spectrum of far-field amplitude of backscattered P wave are shown in Fig. 5.17 when $k_T a = 1.2$, $u_g/u_0 = 2.0$, $h/a = 2.0$, and $\theta^{\text{in}} = 60^\circ$. As shown in Fig. 5.17 (a), large and small amplitude is periodically repeated, and this motion becomes stable from the middle. This waveform is typical one which includes sub-harmonic components, and there is a clear peak corresponding to the sub-harmonic component in Fig. 5.17 (b). In this study, we define that sub-harmonic wave can be observed if such a waveform and frequency spectrum are confirmed. On the other hand, we could not observe the sub-harmonic generation even if $A_{0.5\omega}/A_{\omega}$ is large in the

5. 2-D Simulation of Nonlinear Ultrasonic Waves Due to Interior and Surface Breaking Cracks

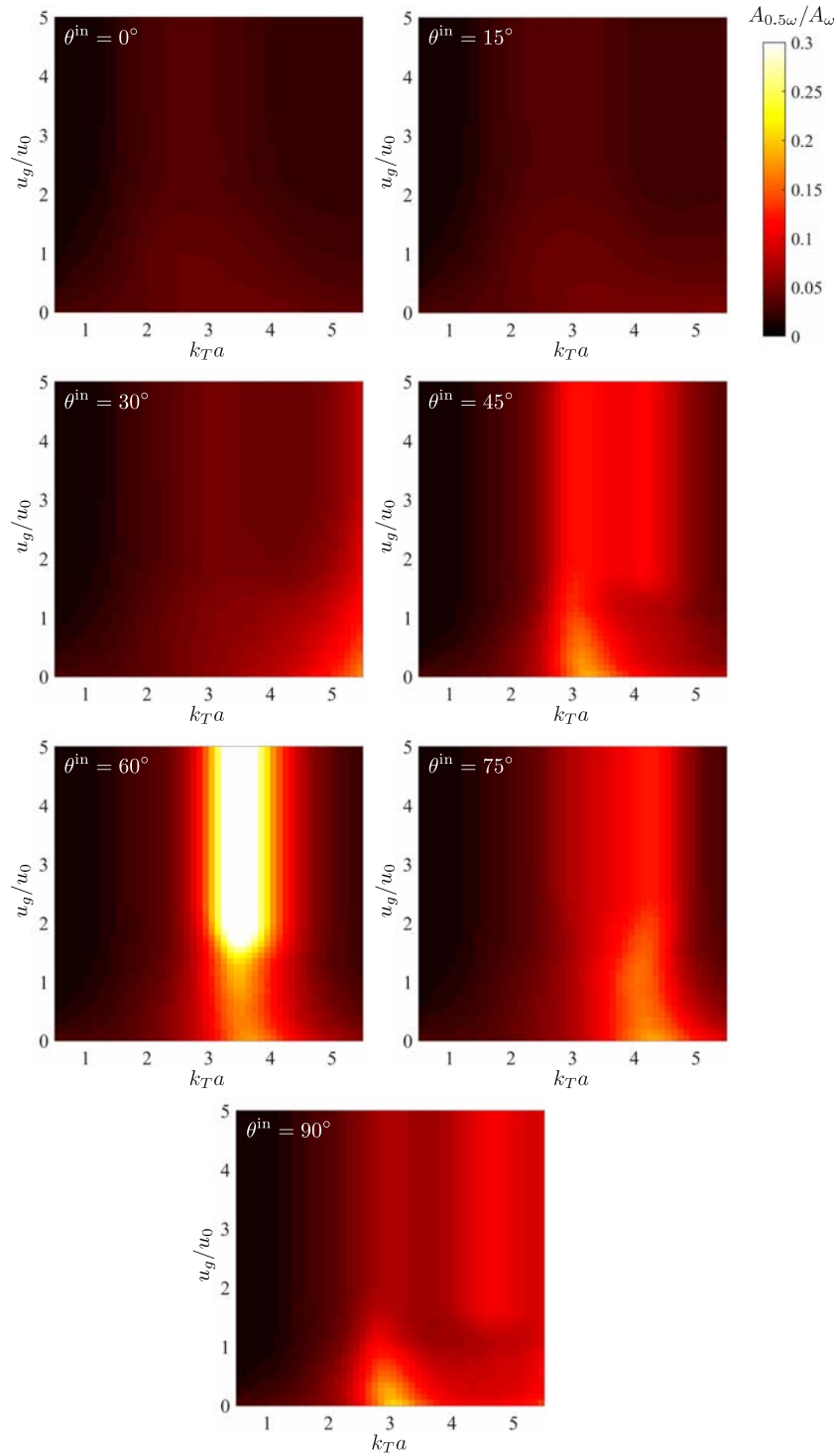


Figure 5.12.: Fourier amplitude ratio of sub-harmonic frequency to fundamental one for various wavenumber $k_T a$, pre-opening displacement u_g/u_0 , and incident angles θ^{in} when a half-sine-shaped crack is subjected to an incident plane P wave with $n^{in} = 30$ ($h/a = 0.0$).

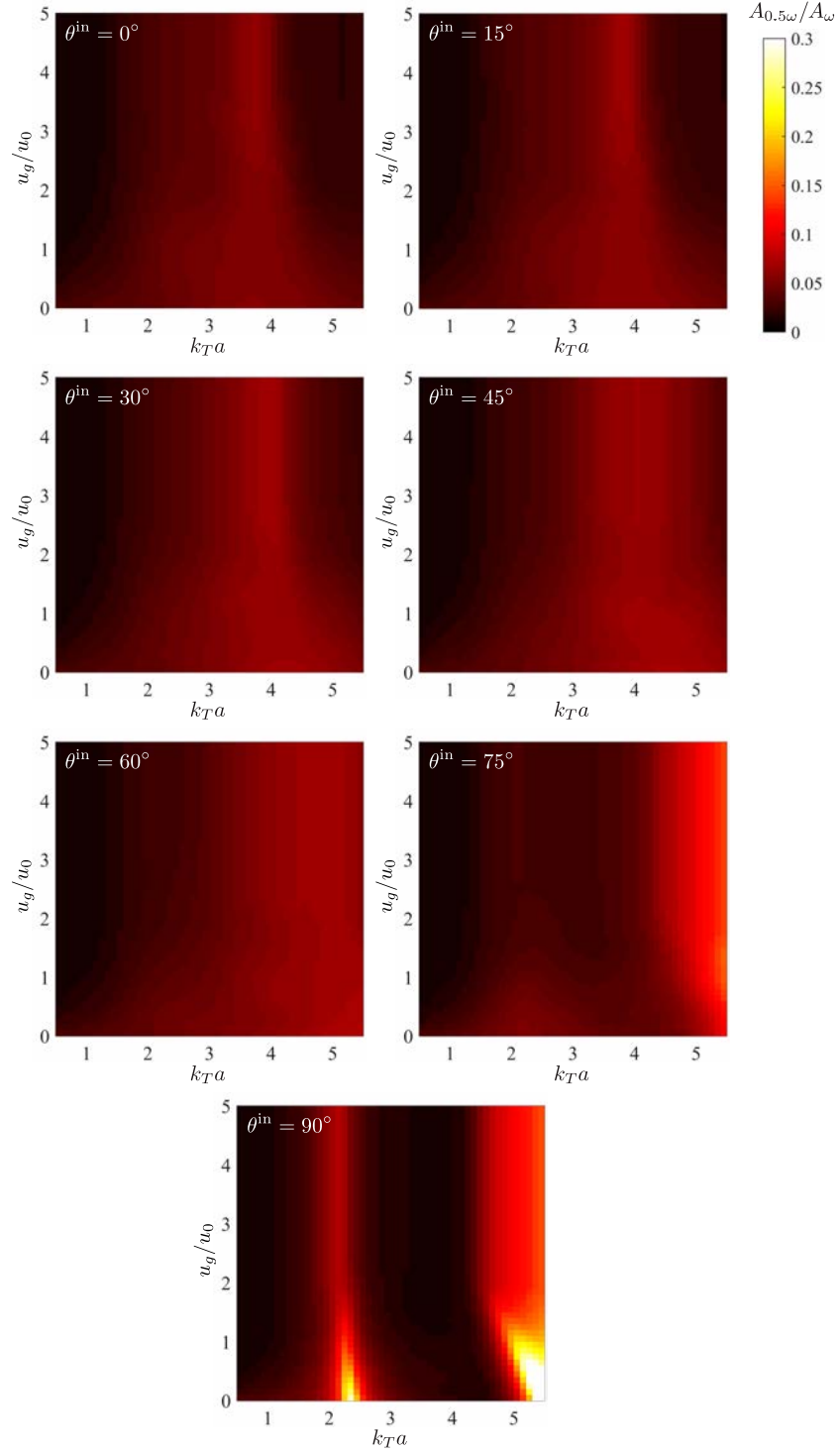


Figure 5.13.: Fourier amplitude ratio of sub-harmonic frequency to fundamental one for various wavenumber $k_T a$, pre-opening displacement u_g/u_0 , and incident angles θ^{in} when a half-sine-shaped crack is subjected to an incident plane P wave with $n^{in} = 30$ ($h/a = 0.5$).

5. 2-D Simulation of Nonlinear Ultrasonic Waves Due to Interior and Surface Breaking Cracks

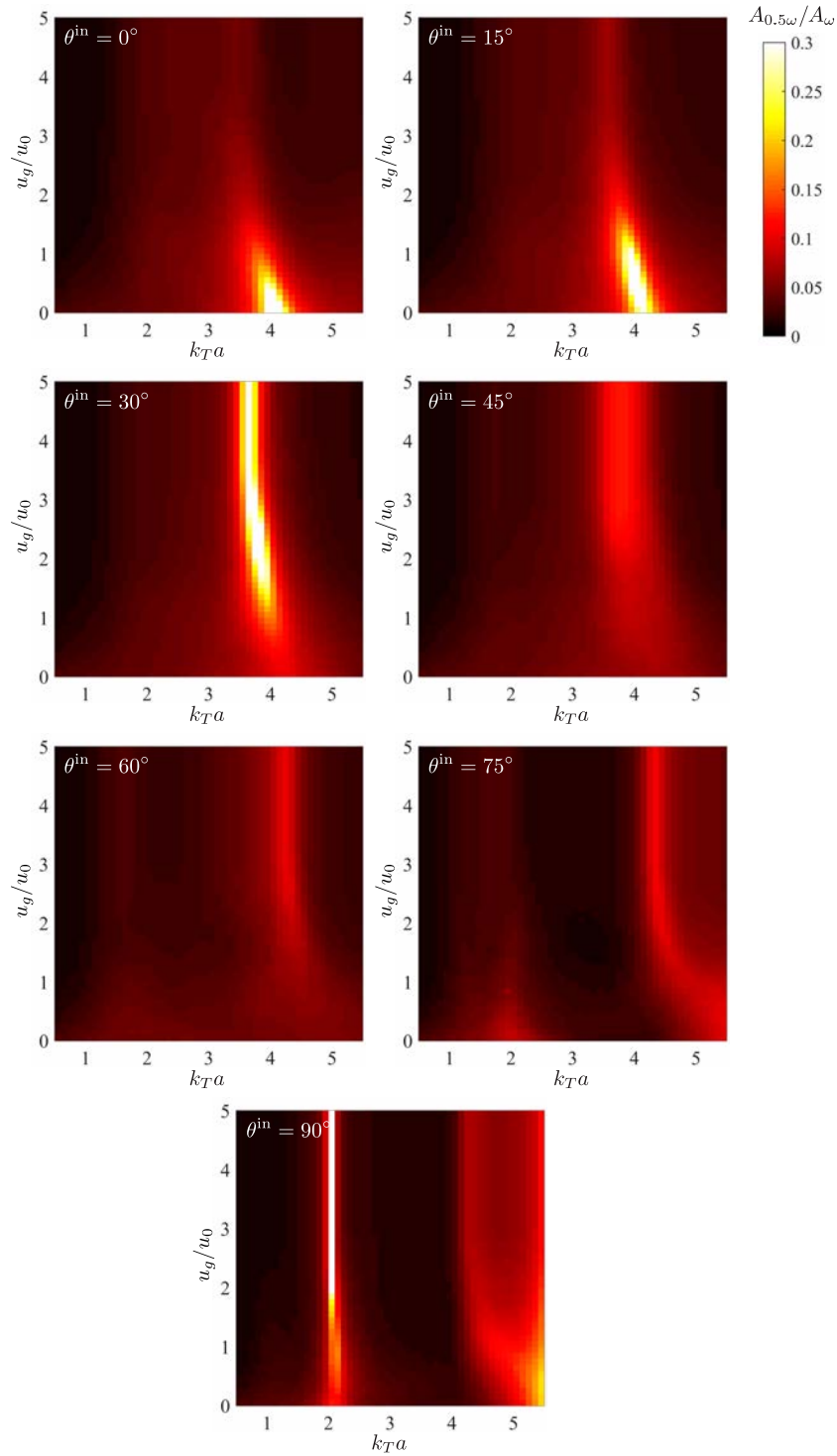


Figure 5.14.: Fourier amplitude ratio of sub-harmonic frequency to fundamental one for various wavenumber $k_T a$, pre-opening displacement u_g/u_0 , and incident angles θ^{in} when a half-sine-shaped crack is subjected to an incident plane P wave with $n^{in} = 30$ ($h/a = 1.0$).

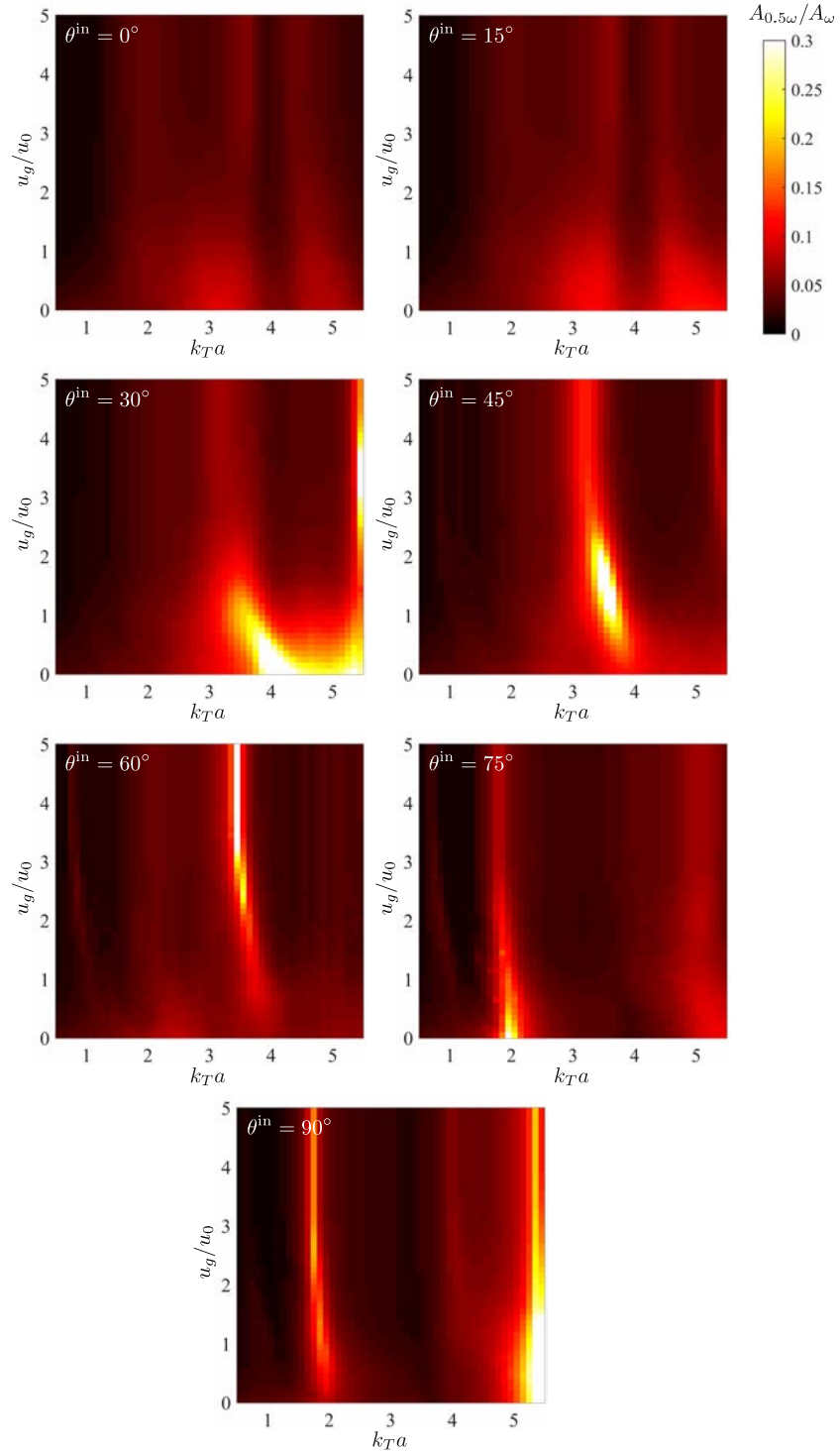


Figure 5.15.: Fourier amplitude ratio of sub-harmonic frequency to fundamental one for various wavenumber $k_T a$, pre-opening displacement u_g/u_0 , and incident angles θ^{in} when a half-sine-shaped crack is subjected to an incident plane P wave with $n^{in} = 30$ ($h/a = 1.5$).

5. 2-D Simulation of Nonlinear Ultrasonic Waves Due to Interior and Surface Breaking Cracks

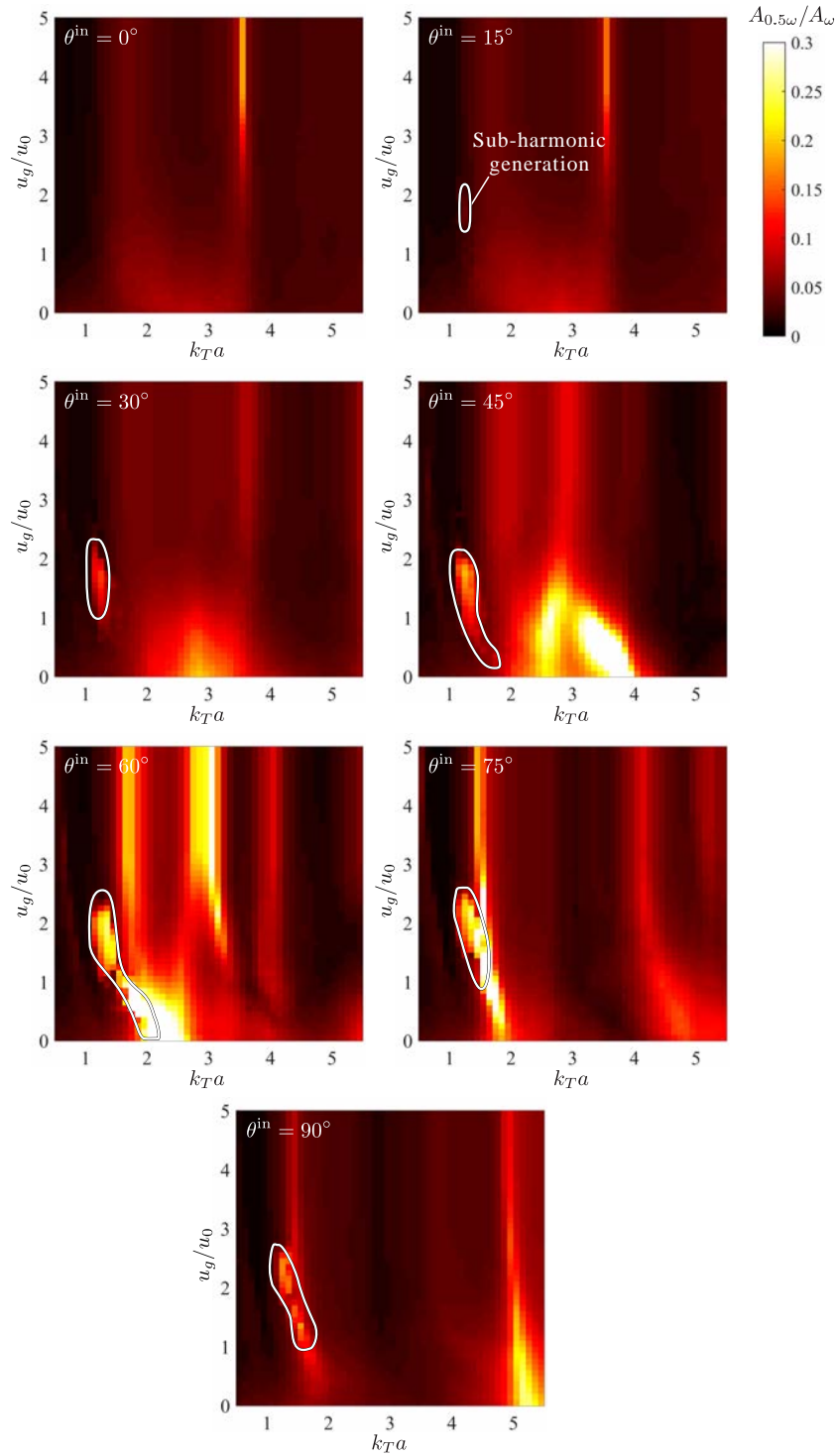


Figure 5.16.: Fourier amplitude ratio of sub-harmonic frequency to fundamental one for various wavenumber $k_T a$, pre-opening displacement u_g/u_0 , and incident angles θ^{in} when a half-sine-shaped crack is subjected to an incident plane P wave with $n^{\text{in}} = 30$ ($h/a = 2.0$).

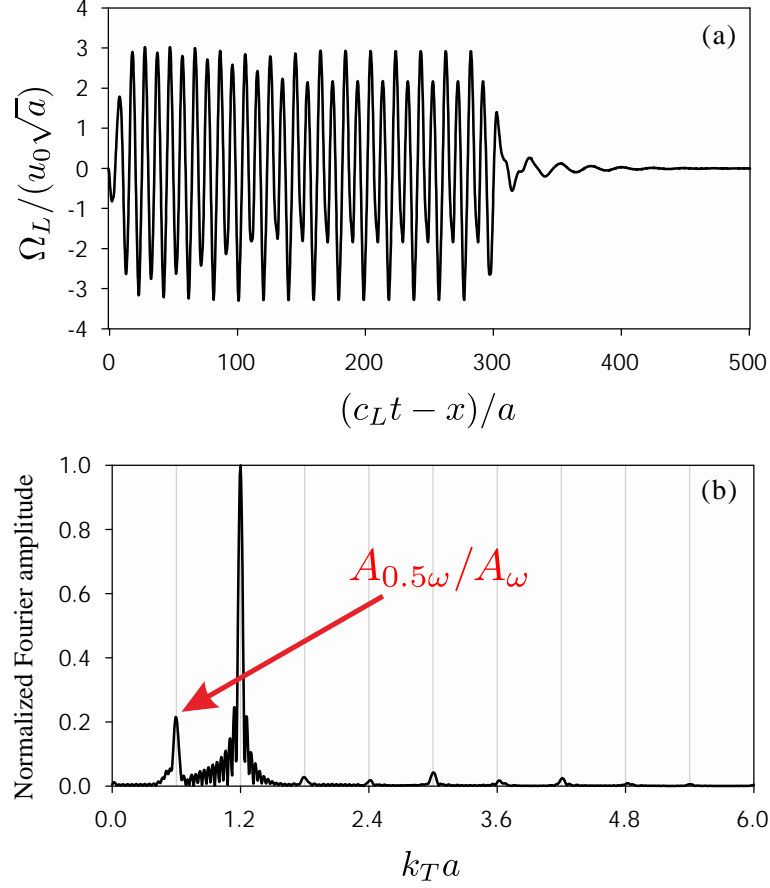


Figure 5.17.: (a) Time variation and (b) normalized frequency spectrum of far-field amplitude of backscattered P wave when a curved crack is subjected to an incident plane P wave ($k_T a = 1.2$, $u_g/u_0 = 2.0$, $h/a = 2.0$, and $\theta^{\text{in}} = 60^\circ$).

outside of white line. As an example of that, the time history and normalized frequency spectrum of far-field amplitude of backscattered P wave are shown in Fig. 5.18 when $k_T a = 2.5$, $u_g/u_0 = 0.0$, $h/a = 2.0$, and $\theta^{\text{in}} = 60^\circ$. As shown in Fig. 5.18 (a), the waveform of $\Omega_L / (u_0 \sqrt{a})$ is strongly distorted, and the value of A_ω is considered as small. Although $A_{0.5\omega}/A_\omega$ is comparatively large due to this fact, there is no peak corresponding to the sub-harmonic component as shown in Fig. 5.18 (b). In order to investigate the behavior of sub-harmonic generation varying u_g/u_0 , $A_{0.5\omega}/A_\omega$ for various u_g/u_0 is shown in Fig. 5.19 when $k_T a = 1.2$, $h/a = 2.0$, and $\theta^{\text{in}} = 60^\circ$. As shown in Fig. 5.19, $A_{0.5\omega}/A_\omega$ changes continuously without rapid fluctuation when u_g/u_0 is varying. In addition, the chaotic vibration, which has been observed in [88, 34], has never seen from the numerical results in this thesis.

In order to investigate the vibration around a crack when the sub-harmonic wave is generated, the displacement fields in the case that $k_T a = 1.2$, $u_g/u_0 = 2.0$, $h/a = 2.0$, and $\theta^{\text{in}} = 60^\circ$ from $f^{\text{in}} t = 20.0$ to 22.0 are presented in Fig. 5.20. The color depth of crack line indicates the phase of contact conditions as shown in the upper right of Fig. 5.20. These displacement fields are in the

5. 2-D Simulation of Nonlinear Ultrasonic Waves Due to Interior and Surface Breaking Cracks

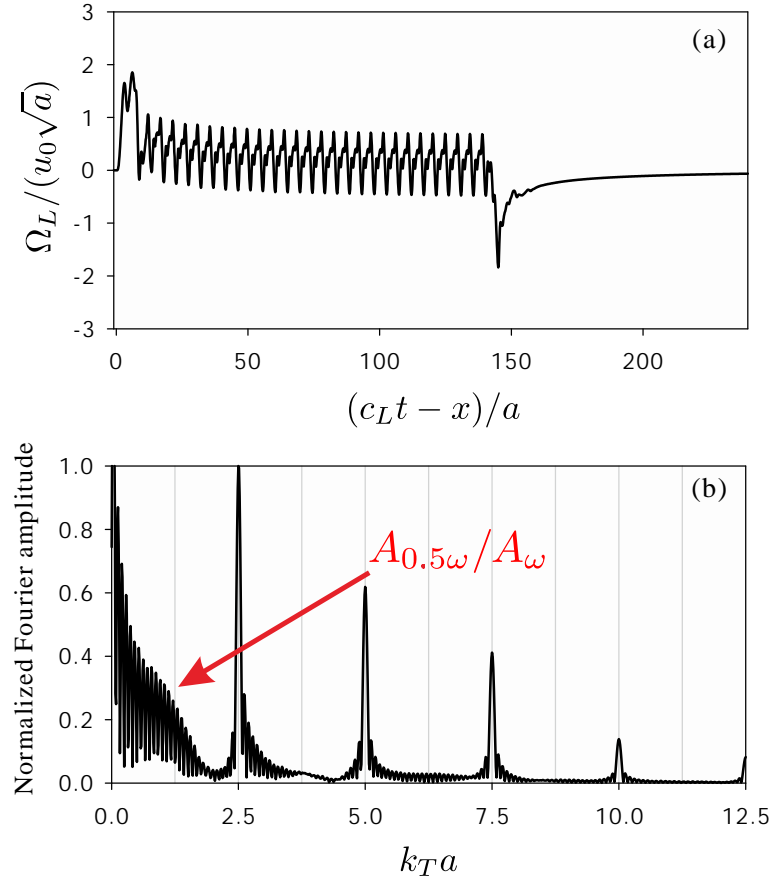


Figure 5.18.: (a) Time variation and (b) normalized frequency spectrum of far-field amplitude of backscattered P wave when a curved crack is subjected to an incident plane P wave ($k_T a = 2.5$, $u_g/u_0 = 0.0$, $h/a = 2.0$, and $\theta^{\text{in}} = 60^\circ$).

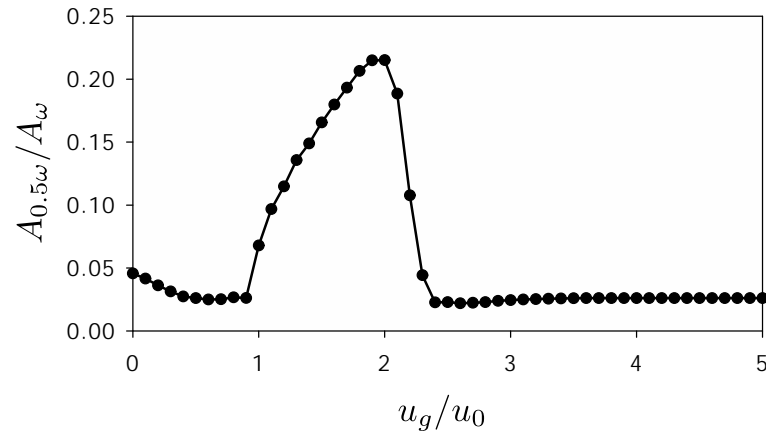


Figure 5.19.: Fourier amplitude ratio of sub-harmonic frequency to fundamental one for various pre-opening displacement u_g/u_0 when $k_T a = 1.2$, $h/a = 2.0$, and $\theta^{\text{in}} = 60^\circ$.

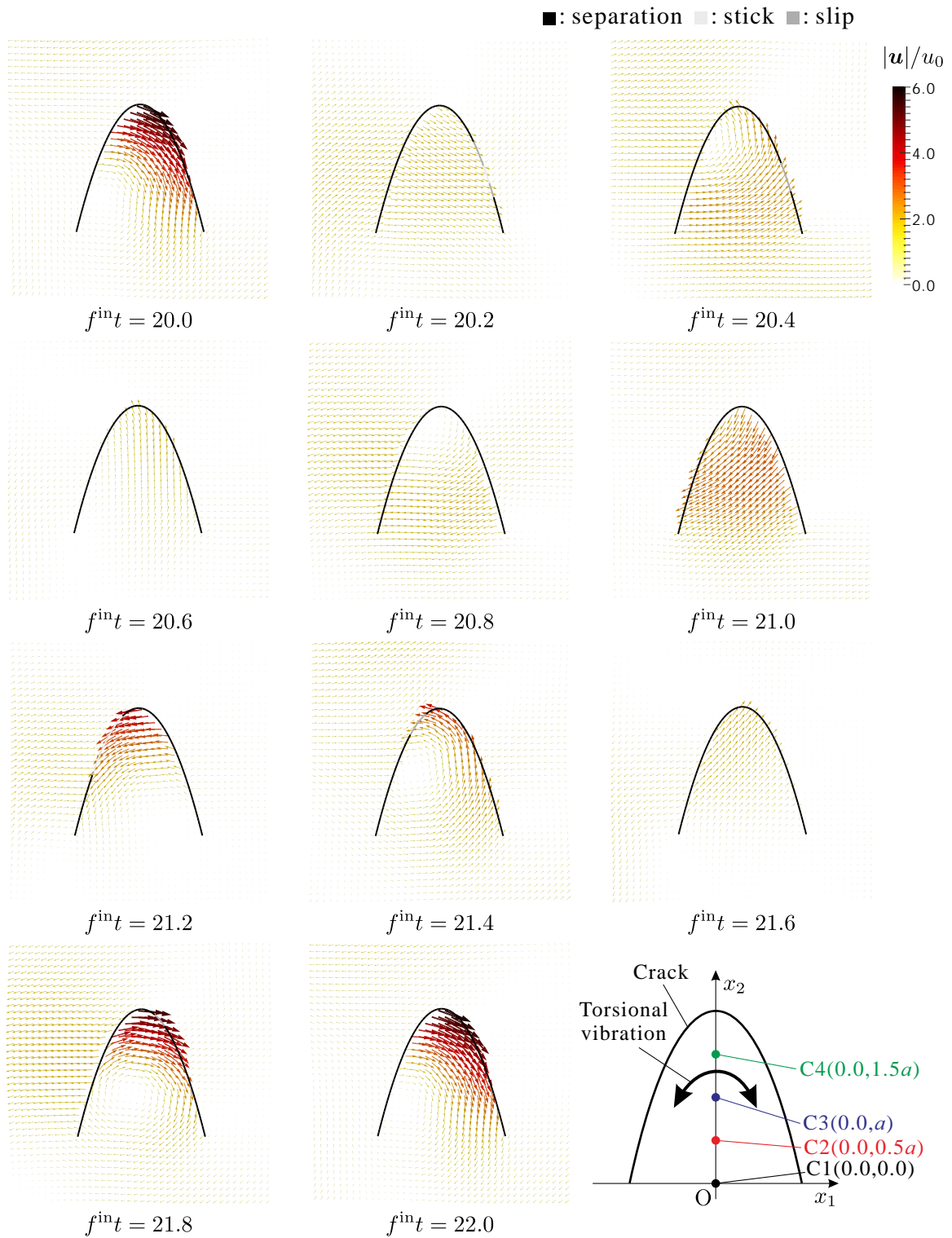


Figure 5.20.: Displacement fields around a curved crack from $f^{\text{int}} t = 20.0$ to 22.0 when $h/a = 2.0$, $\theta^{\text{in}} = 60^\circ$, $k_T a = 1.2$, and $u_g/u_0 = 2.0$.

5. 2-D Simulation of Nonlinear Ultrasonic Waves Due to Interior and Surface Breaking Cracks

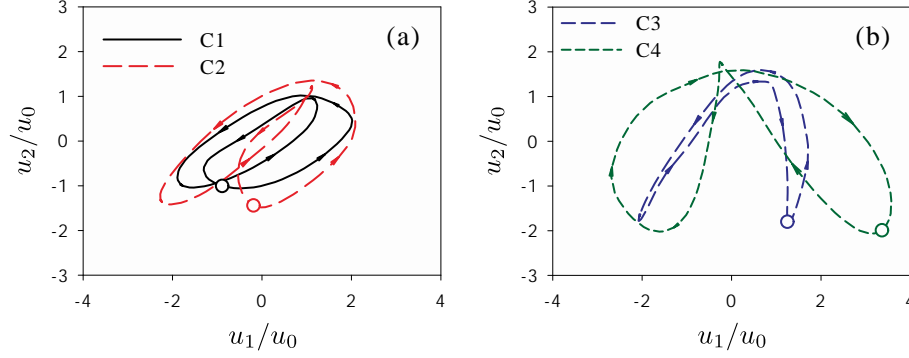


Figure 5.21.: Histories of displacement at points (a) C1 and C2, and (b) C3 and C4 in the lower right of Fig. 5.20 from $f^{\text{int}} = 20.0$ to 22.0 when $h/a = 2.0$, $\theta^{\text{in}} = 60^\circ$, $k_T a = 1.2$, and $u_g/u_0 = 2.0$.

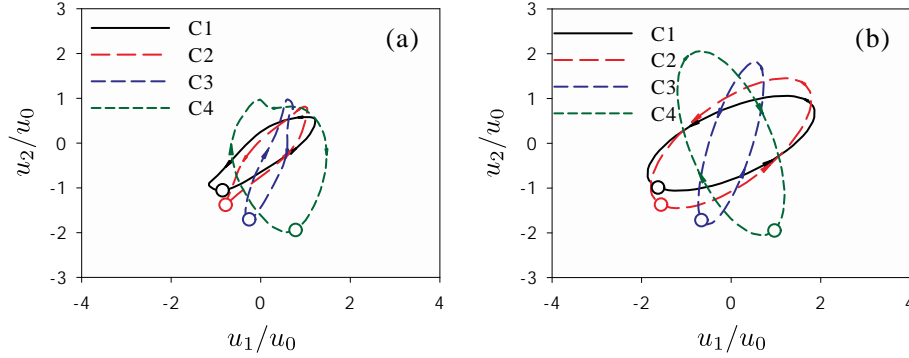


Figure 5.22.: Histories of displacement at points C1–C4 in the lower right of Fig. 5.20 from $f^{\text{int}} = 20.0$ to 21.0 when $h/a = 2.0$, $\theta^{\text{in}} = 60^\circ$, $k_T a = 1.2$, and (a) $u_g/u_0 = 0.5$ and (b) $u_g/u_0 = 3.0$.

nearly stationary vibration after the transient analysis is proceeded for a sufficiently long time. It can be obviously seen that the vibration period is double of $1/f^{\text{in}}$, especially in the inner part of a curved crack. Focusing there, the large displacement to right is generated at $f^{\text{int}} = 20.0$, and the friction is caused on the right side of crack at around $f^{\text{int}} = 20.2$ to 20.4. Then, the inner part is deformed to left with comparatively small amplitude at around $f^{\text{int}} = 21.0$. This part begins to be deformed to right again at around $f^{\text{int}} = 21.6$, and the state of displacement fields eventually returns to the first one at $f^{\text{int}} = 22.0$. From the above, it seems that the torsional vibration with the double period of incident wave as shown in lower right of Fig. 5.20 is generated by the contact of crack faces.

Histories of displacement at points C1–C4 in lower right of Fig. 5.20 from $f^{\text{int}} = 20.0$ to 22.0 are shown in Fig. 5.21. The circle in the figure indicates the displacement at $f^{\text{int}} = 20.0$. As shown in Fig. 5.21 (a), the displacement orbits at points C1 and C2 are distorted, and the locations return to the positions at $f^{\text{int}} = 20.0$ spending double of $1/f^{\text{in}}$. The cause of these phenomena is the contact of crack faces because the displacement orbit of harmonic vibration must be ellipse with the

period $1/f^{\text{in}}$. As shown in Fig. 5.21 (b), the torsional vibration like the lower right of Fig. 5.20 is observed at points C3 and C4. In addition, the direction of displacement at point C4 is rapidly changed because it is near the crack face. On the other hand, displacement orbits in the cases that the sub-harmonic generation could not be observed are presented in Fig. 5.22 for the time range from $f^{\text{in}}t = 20.0$ to 21.0. Fig. 5.22 (a) shows the case that $u_g/u_0 = 0.5$, and it can be seen that the displacement orbits are distorted by contact of crack faces. However, all of these periods are $1/f^{\text{in}}$ and different from ones in Fig. 5.21. The displacement orbit is almost ellipse with $1/f^{\text{in}}$ period in the case that $u_g/u_0 = 3.0$ as shown in Fig. 5.22 (b) because contact of crack faces hardly occurs.

From the above, the torsional vibration is generated as sub-harmonic resonance under certain conditions for the model in Fig. 5.11 (a). As a result, the sub-harmonic wave is contained in the scattered wave.

Sub-harmonic generation by two straight-line cracks arranged in parallel

Second, numerical results obtained by solving the scattering problem by two straight-line cracks in parallel as depicted in Fig. 5.11 (b) are shown. Fourier amplitude ratios of sub-harmonic component to fundamental one in backscattered P wave $A_{0.5\omega}/A_\omega$ for various k_Ta , u_g/u_0 , and θ^{in} are shown in Figs. 5.23–5.25 when the interval between two cracks h/a is varying. We could not observe the sub-harmonic generation when $h/a = 1.5$ as shown in Fig. 5.25. For the cases that $h/a = 0.5$ and 1.0 in Figs. 5.23 and 5.24, respectively, the sub-harmonic generation is caused under certain conditions except the case of parallel incidence to cracks, i.e. $\theta^{\text{in}} = 90^\circ$. For instance of the sub-harmonic generation, the time history and normalized frequency spectrum of far-field amplitude of backscattered P wave are shown in Fig. 5.26 when $k_Ta = 2.5$, $u_g/u_0 = 2.0$, $h/a = 0.5$, and $\theta^{\text{in}} = 0^\circ$. As shown in Fig. 5.26, the waveform of $\Omega_L/(u_0\sqrt{a})$ is the typical one which contains the sub-harmonic component, and there is a clear peak of $A_{0.5\omega}/A_\omega$ in the frequency spectrum. $A_{0.5\omega}/A_\omega$ for various u_g/u_0 is shown in Fig. 5.27 when $k_Ta = 2.5$, $h/a = 0.5$, and $\theta^{\text{in}} = 0^\circ$. In this case, $A_{0.5\omega}/A_\omega$ also changes continuously as shown in Fig. 5.27.

In order to investigate the vibration around cracks when the sub-harmonic wave is generated, the displacement fields in the case that $k_Ta = 2.5$, $u_g/u_0 = 2.0$, $h/a = 0.5$, and $\theta^{\text{in}} = 0^\circ$ from $f^{\text{in}}t = 20.0$ to 22.0 are presented in Fig. 5.28. It can be obviously seen that the vibration period is $2/f^{\text{in}}$, especially at the part between two cracks. Focusing there, the large displacement appears upward at $f^{\text{in}}t = 20.0$, and the displacement becomes small at around $f^{\text{in}}t = 20.2$ to 21.0. Then, contact of crack faces occurs on the lower crack at $f^{\text{in}}t = 21.2$, and upward large displacement is generated by diffracted waves at $f^{\text{in}}t = 21.6$ to 21.8. Finally, the displacement state returns to the first one at $f^{\text{in}}t = 22.0$. From the above, it seems that the bending vibration with the double period of incident wave as shown in lower right of Fig. 5.28 is generated by the contact of crack faces.

Histories of displacement at points D1–D4 in lower right of Fig. 5.28 from $f^{\text{in}}t = 20.0$ to 22.0 are shown in Fig. 5.29. As shown in Fig. 5.29 (a) and (b), all of the displacement orbits are strongly distorted, and the displacement returns to the position at $f^{\text{in}}t = 20.0$ spending double of $1/f^{\text{in}}$. From Fig. 5.29 (a), one upward and downward motion spends $2/f^{\text{in}}$, and it is therefore confirmed

5. 2-D Simulation of Nonlinear Ultrasonic Waves Due to Interior and Surface Breaking Cracks

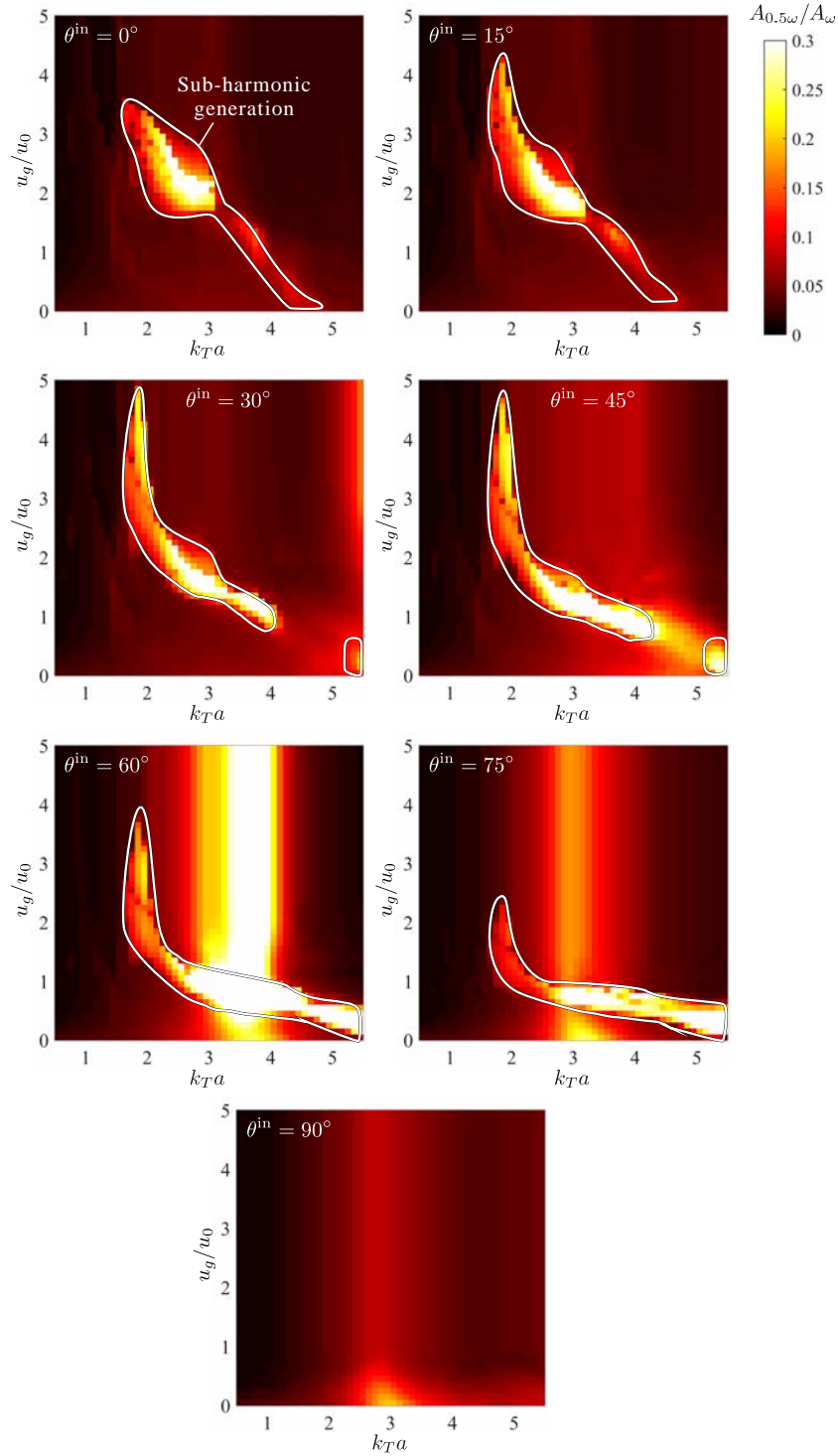


Figure 5.23.: Fourier amplitude ratio of sub-harmonic frequency to fundamental one for various wavenumber $k_T a$, pre-opening displacement u_g/u_0 , and incident angles θ^{in} when two straight-line cracks arranged in parallel are subjected to an incident plane P wave with $n^{in} = 30$ ($h/a = 0.5$).

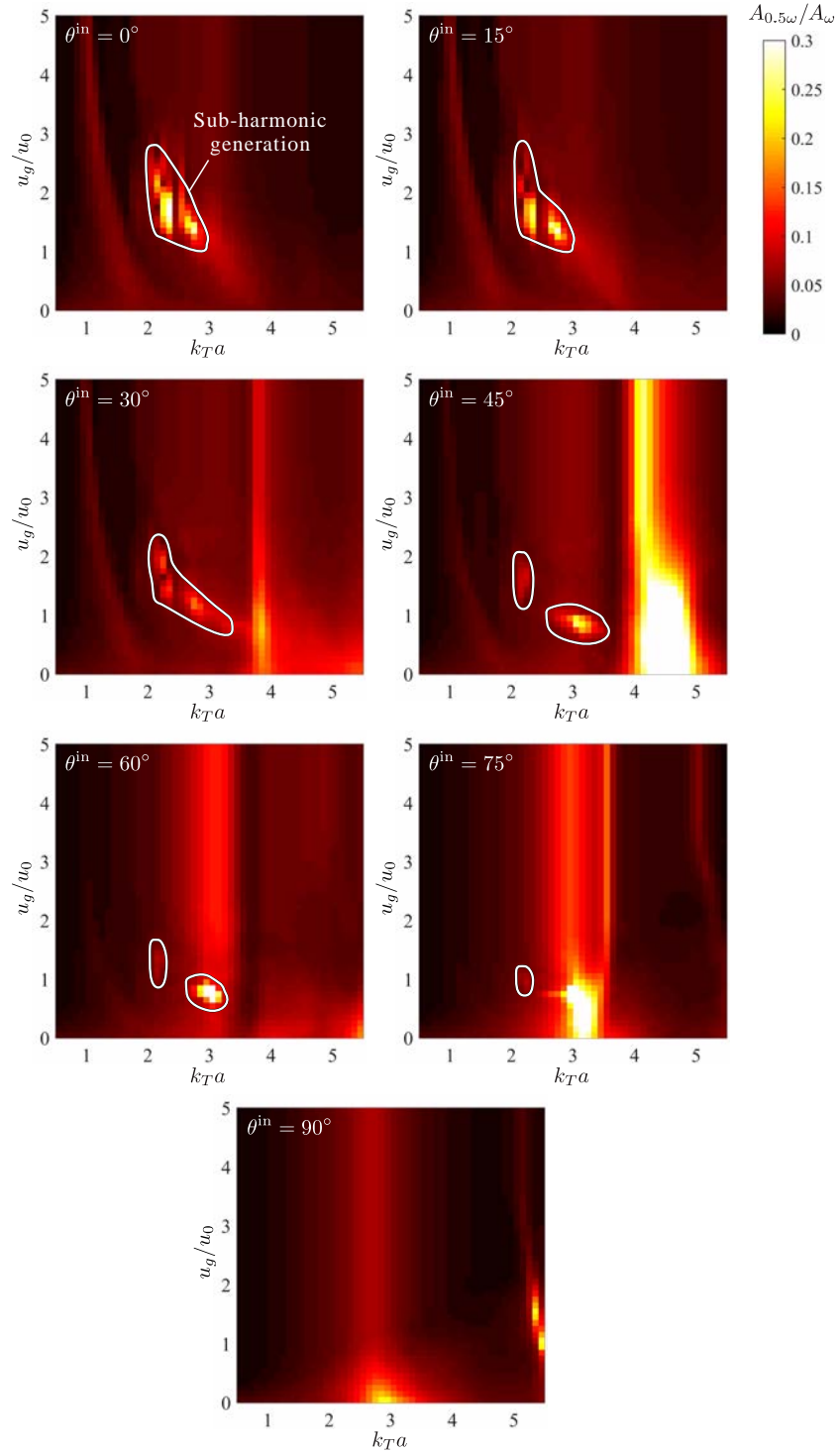


Figure 5.24.: Fourier amplitude ratio of sub-harmonic frequency to fundamental one for various wavenumber $k_T a$, pre-opening displacement u_g/u_0 , and incident angles θ^{in} when two straight-line cracks arranged in parallel are subjected to an incident plane P wave with $n^{in} = 30$ ($h/a = 1.0$).

5. 2-D Simulation of Nonlinear Ultrasonic Waves Due to Interior and Surface Breaking Cracks

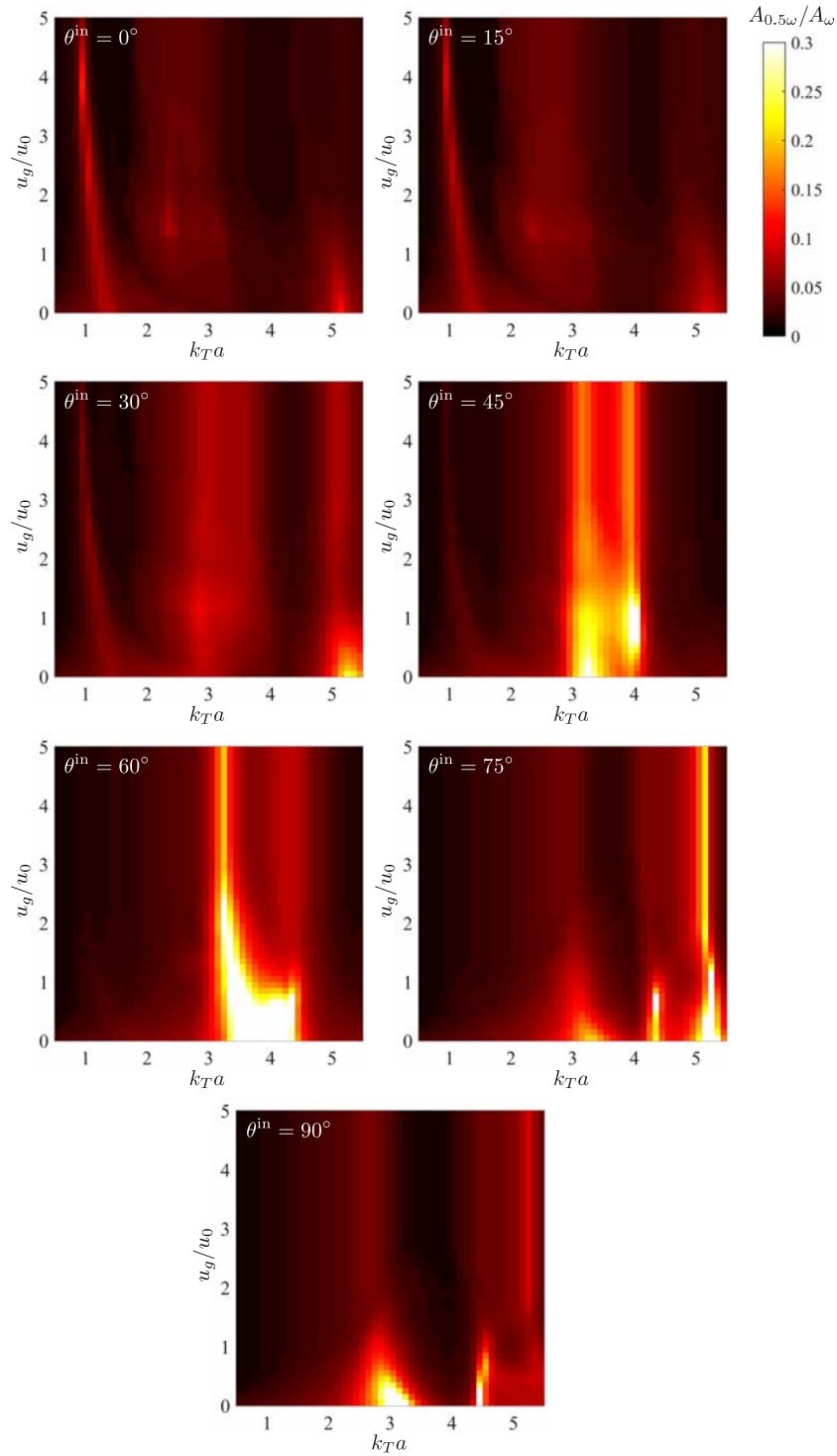


Figure 5.25.: Fourier amplitude ratio of sub-harmonic frequency to fundamental one for various wavenumber $k_T a$, pre-opening displacement u_g/u_0 , and incident angles θ^{in} when two straight-line cracks arranged in parallel are subjected to an incident plane P wave with $n^{in} = 30$ ($h/a = 1.5$).

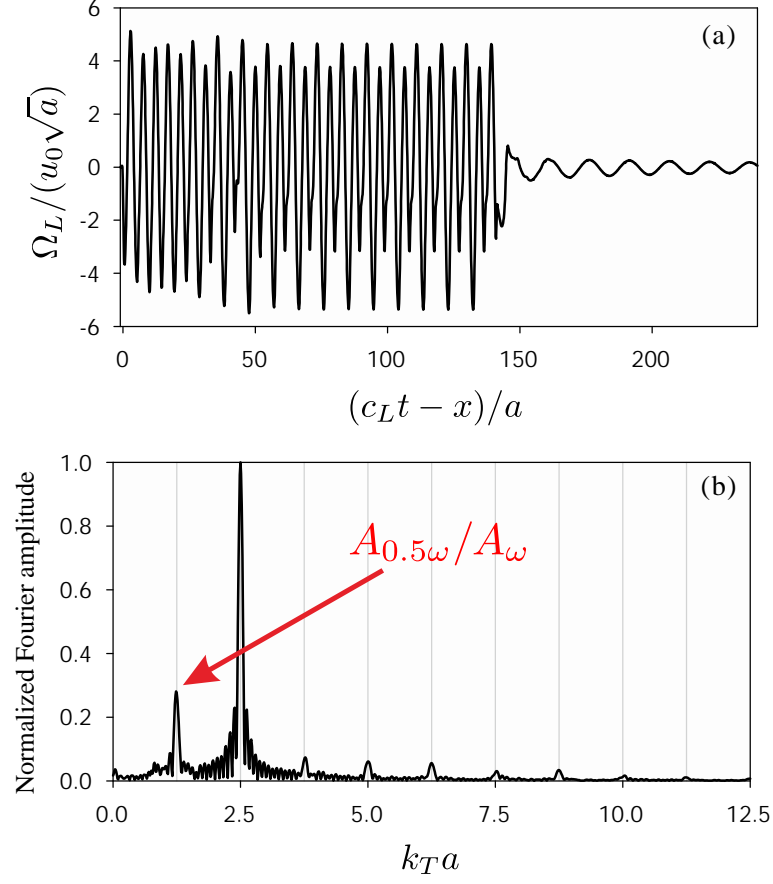


Figure 5.26.: (a) Time variation and (b) normalized frequency spectrum of far-field amplitude of backscattered P wave when two straight-line cracks arranged in parallel are subjected to an incident plane P wave ($k_T a = 2.5$, $u_g/u_0 = 2.0$, $h/a = 0.5$, and $\theta^{\text{in}} = 0^\circ$).

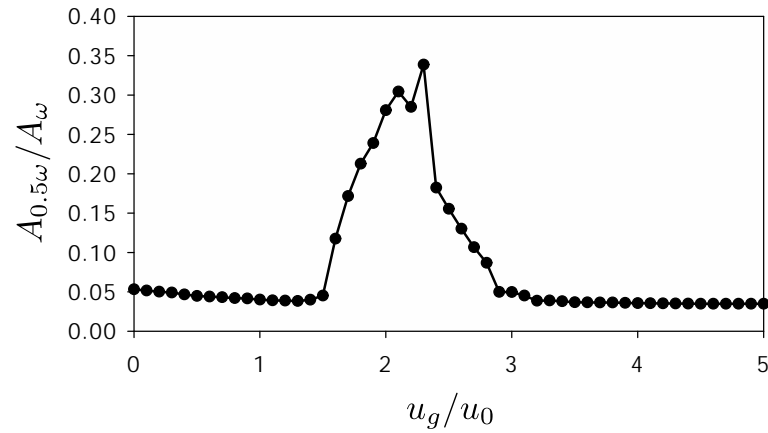


Figure 5.27.: Fourier amplitude ratio of sub-harmonic frequency to fundamental one for various pre-opening displacement u_g/u_0 when $k_T a = 2.5$, $h/a = 0.5$, and $\theta^{\text{in}} = 0^\circ$.

5. 2-D Simulation of Nonlinear Ultrasonic Waves Due to Interior and Surface Breaking Cracks

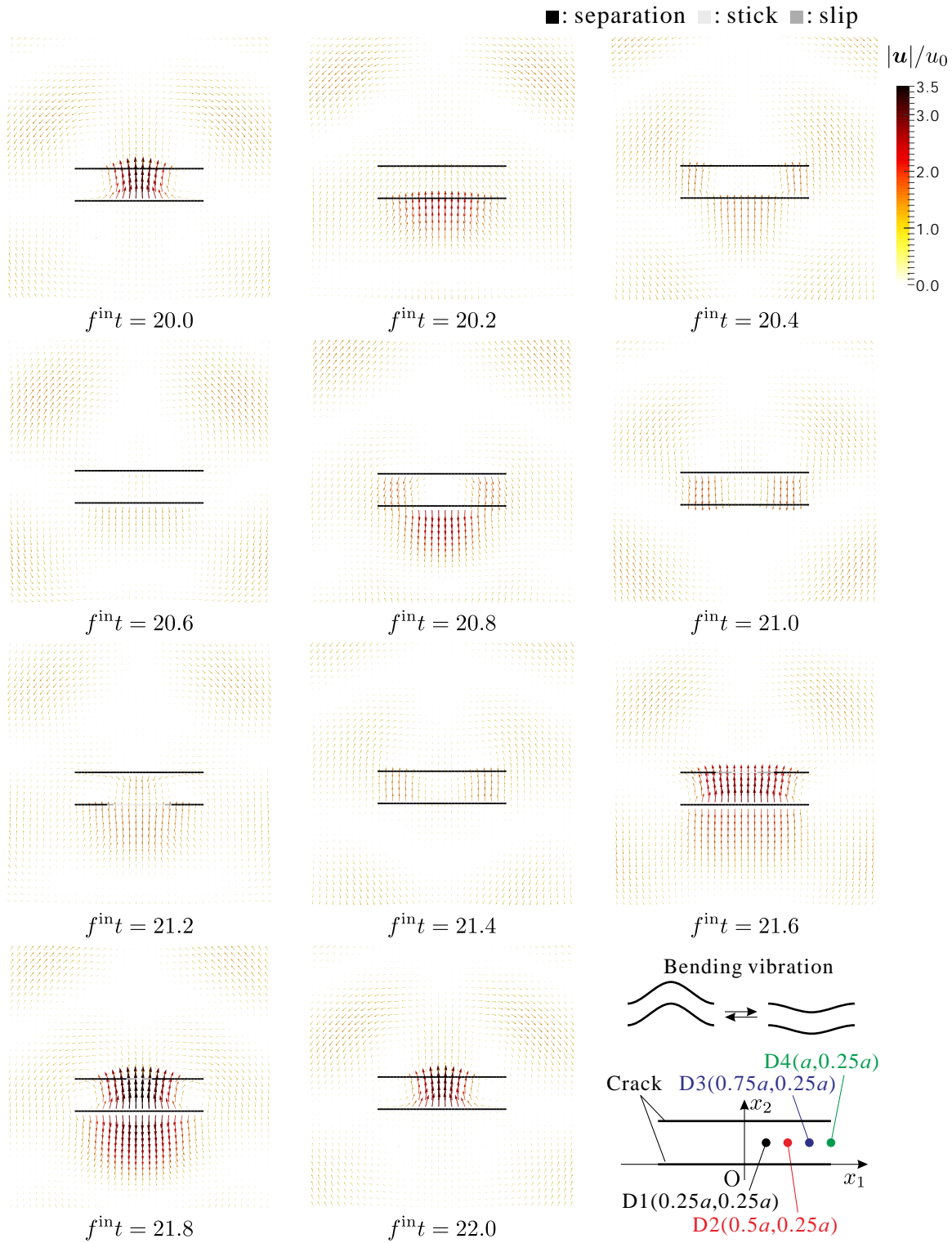


Figure 5.28.: Displacement fields around two cracks arranged in parallel from $f^{\text{in}}t = 20.0$ to 22.0 when $h/a = 0.5$, $\theta^{\text{in}} = 0^\circ$, $k_T a = 2.5$, and $u_g/u_0 = 2.0$.

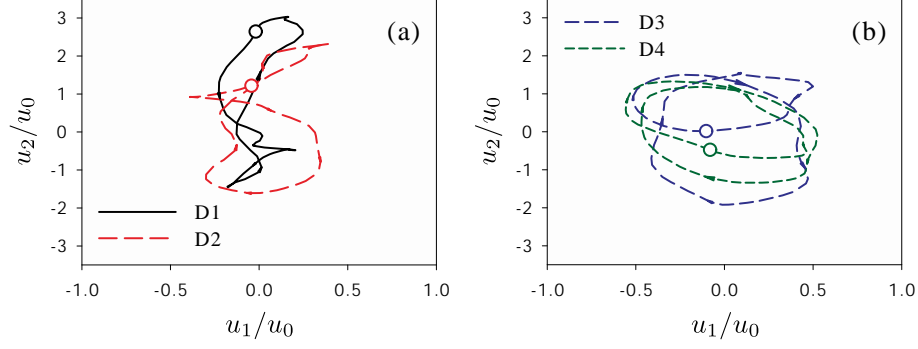


Figure 5.29.: Histories of displacement at points (a) D1 and D2, and (b) D3 and D4 in the lower right of Fig. 5.28 from $f^{\text{int}} = 20.0$ to 22.0 when $h/a = 0.5$, $\theta^{\text{in}} = 0^\circ$, $k_T a = 2.5$, and $u_g/u_0 = 2.0$.

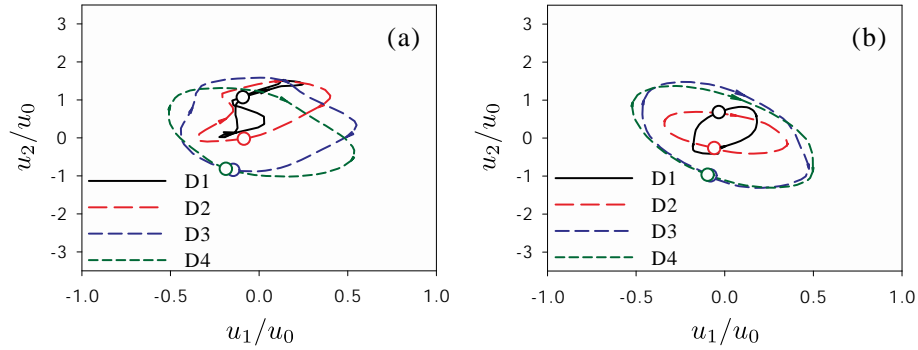


Figure 5.30.: Histories of displacement at points D1–D4 in the lower right of Fig. 5.28 from $f^{\text{int}} = 20.0$ to 21.0 when $h/a = 0.5$, $\theta^{\text{in}} = 0^\circ$, $k_T a = 2.5$, and (a) $u_g/u_0 = 1.0$ and (b) $u_g/u_0 = 3.0$.

that the bending vibration is generated. On the other hand, displacement orbits in the cases that the sub-harmonic generation could not be observed are presented in Fig. 5.30 for the time range from $f^{\text{int}} = 20.0$ to 21.0. Fig. 5.30 (a) shows the case that $u_g/u_0 = 1.0$, and it can be seen that the displacement orbits are distorted by contact of crack faces. However, all of these periods are $1/f^{\text{in}}$ and different from the ones in Fig. 5.29. The displacement orbit is almost ellipse with $1/f^{\text{in}}$ period in the case that $u_g/u_0 = 3.0$ as shown in Fig. 5.30 (b) because contact of crack faces hardly occurs.

From the above, the bending vibration is generated as sub-harmonic resonance under certain conditions for the model in Fig. 5.11 (b).

Relation between sub-harmonic generation and characteristic of frequency response

From numerical results of sub-harmonic generation by a curved crack and two straight-line cracks arranged in parallel, it seems that the sub-harmonic resonance such as torsional and bending vibrations, depends on the shape and arrangement of cracks. Therefore, it is presumed that the fre-

5. 2-D Simulation of Nonlinear Ultrasonic Waves Due to Interior and Surface Breaking Cracks

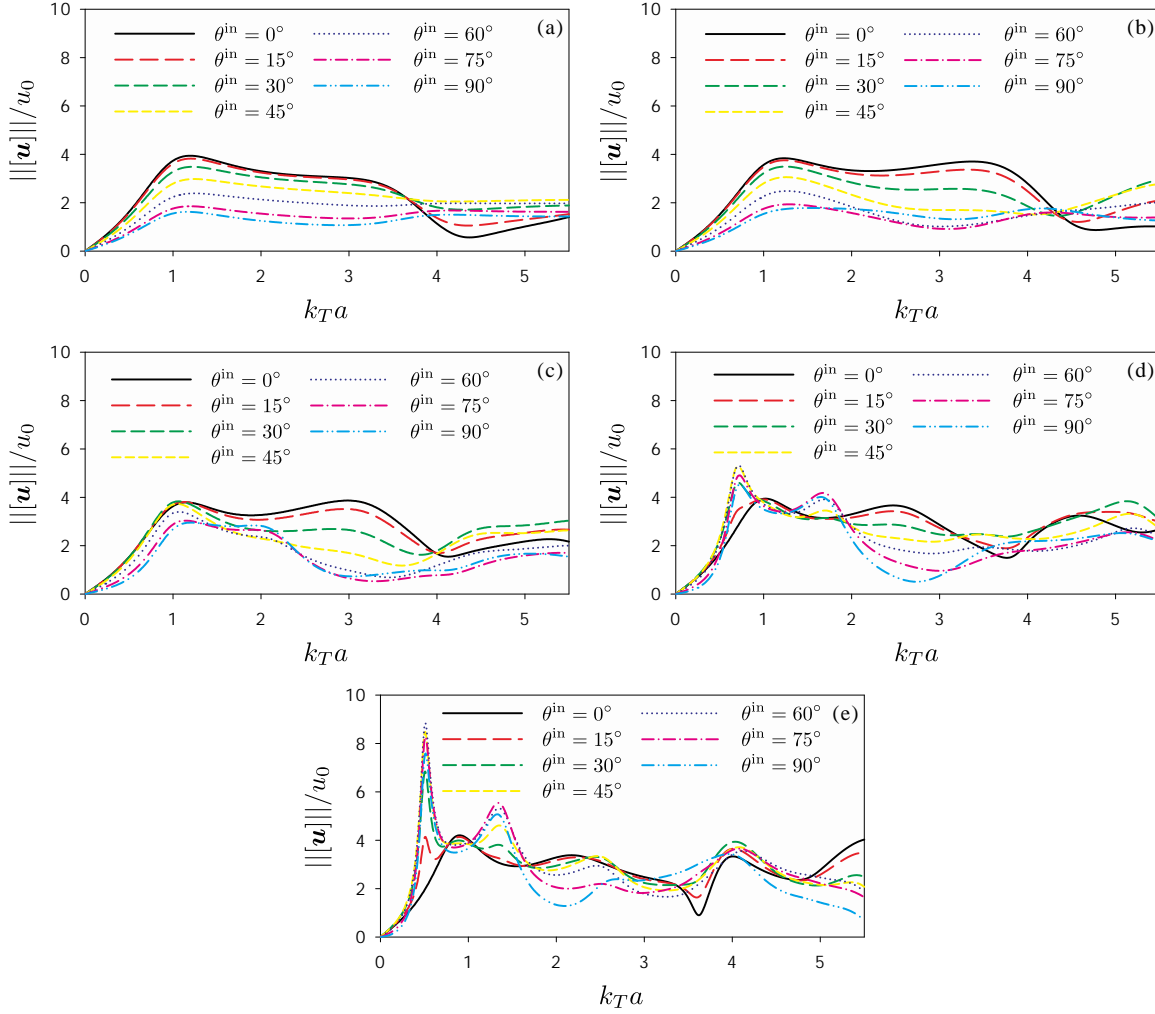


Figure 5.31.: Frequency responses for the model in Fig. 5.11 (a) using the frequency-domain BEM and assuming that crack faces are always separated. The norm $\|[\mathbf{u}]\|/u_0$ at point A in Fig. 5.11 (a) for various θ^{in} and $k_T a$ is plotted when (a) $h/a = 0.0$, (b) 0.5, (c) 1.0, (d) 1.5, and (e) 2.0.

quency response characteristic of the linear system containing cracks without contact of crack faces is important. That is investigated by solving the scattering problem for the same models using the frequency-domain BEM. In this study, the norm of COD $\|[\mathbf{u}]\|$ is considered as the factor of frequency response. The norm $\|\cdot\|$ is defined by

$$\|\mathbf{v}\| \equiv \sqrt{\sum_i v_i \bar{v}_i}. \quad (5.34)$$

The norm of COD $\|[\mathbf{u}]\|/u_0$ at points A in Fig. 5.11 (a) varying $k_T a$ is shown in Fig. 5.31 for various h/a and θ^{in} . All lines are smooth in Fig. 5.31 (a), (b), and (c) compared with the ones in Fig. 5.31 (d) and (e). $\|[\mathbf{u}]\|/u_0$ in Fig. 5.31 (d) shows a little rapid fluctuation at about $k_T a = 0.7$ when

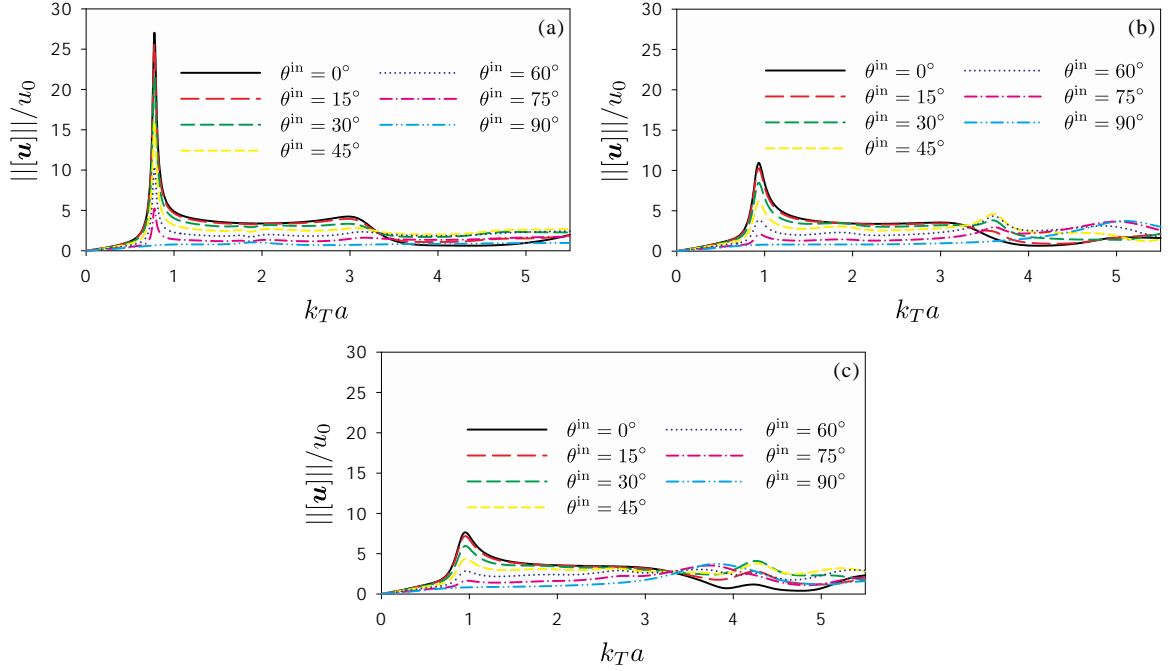


Figure 5.32.: Frequency responses for the model in Fig. 5.11 (b) using the frequency-domain BEM and assuming that crack faces are always separated. The norm $||[u]||/u_0$ at point B in Fig. 5.11 (b) for various θ^{in} and $k_T a$ is plotted when (a) $h/a = 0.5$, (b) 1.0, and (c) 1.5.

$30^\circ \leq \theta^{\text{in}} \leq 90^\circ$. As shown in Fig. 5.31 (e), $||[u]||/u_0$ has rapid fluctuation at about $k_T a = 0.5$ when $15^\circ \leq \theta^{\text{in}} \leq 90^\circ$. This fluctuation corresponds to the first mode quasi-eigenfrequency and seems to be important for the probability of sub-harmonic generation because the sub-harmonic generation could be observed when $h/a = 2.0$ and $15^\circ \leq \theta^{\text{in}} \leq 90^\circ$. In addition, the sub-harmonic generation could be observed in the case that $k_T a$ is a little larger than the double of $k_T a$ at the rapid fluctuation as shown in Fig. 5.16. h/a and θ^{in} are significant to the characteristic of frequency response, and they are therefore important for the sub-harmonic generation.

Next, the norm of COD $||[u]||/u_0$ at points B in Fig. 5.11 (b) varying $k_T a$ is shown in Fig. 5.32 for various h/a and θ^{in} . $||[u]||/u_0$ in Fig. 5.32 (a) shows rapid fluctuation at about $k_T a = 0.8$ when $0^\circ \leq \theta^{\text{in}} \leq 75^\circ$. As shown in Fig. 5.32 (a)–(c), the smaller h/a is, the more rapid the fluctuation of $||[u]||/u_0$ is. However, $||[u]||/u_0$ is gentle in the case that $\theta^{\text{in}} = 90^\circ$ because the multiple reflection hardly occurs between two cracks. It also seems that this fluctuation is important for the probability of sub-harmonic generation because the sub-harmonic generation could be observed only when $h/a = 0.5$ and 1.0 and $0^\circ \leq \theta^{\text{in}} \leq 75^\circ$. In addition, the the sub-harmonic generation could be observed in the case that $k_T a$ is larger than the double of $k_T a$ at the rapid fluctuation as shown in Figs. 5.23 and 5.24.

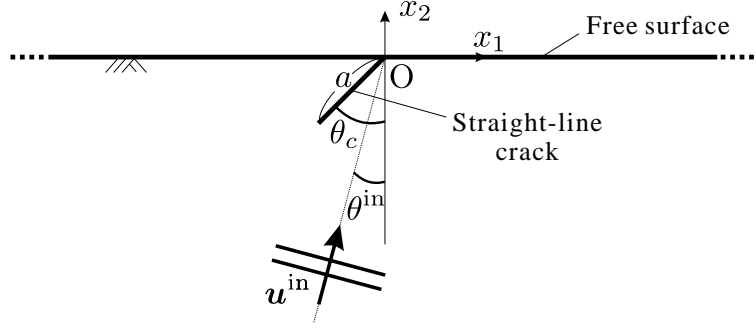


Figure 5.33.: Elastic wave scattering by a surface breaking crack in an elastic half-space.

5.5.4. Simulation of sub-harmonic waves due to a surface breaking crack

The numerical results of sub-harmonic generation by a surface breaking crack in an elastic half-space as depicted in Fig. 5.33 are presented. We assume that a straight-line crack with length a is connected to the free surface with the angle θ_c . An incident plane wave described in Eq. (5.33) with $\varphi = L$ (P wave) and $n^{\text{in}} = 15$ is used in this simulation. The far-field scattered waves and free fields are evaluated as presented in Appendices B and C, respectively.

Fourier amplitude ratios of sub-harmonic component to fundamental one in backscattered P wave $A_{0.5\omega}/A_\omega$ for various $k_T a$, u_g/u_0 , and θ^{in} are shown in Figs. 5.34–5.37 when the crack angle θ_c is varying. We could not observe the sub-harmonic generation when $0^\circ \leq \theta_c \leq 15^\circ$ in Figs. 5.34 and 5.35. However, for the case that $\theta_c = 30^\circ$ in Fig. 5.36, the sub-harmonic generation is slightly caused around $k_T a = 3.7$ and $u_g/u_0 = 0.0$. As shown in Fig. 5.37, the sub-harmonic generation can be obviously observed in the case that $\theta_c = 45^\circ$ compared with the case that $\theta_c = 30^\circ$. For instance of the sub-harmonic generation, the time history and normalized frequency spectrum of far-field amplitude of backscattered P wave are shown in Fig. 5.38 when $k_T a = 3.7$, $u_g/u_0 = 0.0$, $\theta_c = 45^\circ$, and $\theta^{\text{in}} = 75^\circ$. The typical sub-harmonic waveform and clear peak of $A_{0.5\omega}/A_\omega$ can be observed in Fig. 5.17 (a) and (b), respectively. $A_{0.5\omega}/A_\omega$ for various u_g/u_0 is shown in Fig. 5.39 when $k_T a = 3.7$, $\theta_c = 45^\circ$, and $\theta^{\text{in}} = 75^\circ$. It can be seen from Fig. 5.39 that $A_{0.5\omega}/A_\omega$ changes gently. However, the behavior is different from the cases of interior cracks, and the maximum value of $A_{0.5\omega}/A_\omega$ is observed at $u_g/u_0 = 0.0$.

In order to investigate the vibration around a surface breaking crack when the sub-harmonic wave is generated, the displacement fields in the case that $k_T a = 3.7$, $u_g/u_0 = 0.0$, $\theta_c = 45^\circ$, and $\theta^{\text{in}} = 75^\circ$ from $f^{\text{int}} t = 10.0$ to 12.0 are shown in Fig. 5.40. It can be obviously seen that the vibration period is double of $1/f^{\text{in}}$, especially around the crack. Focusing on the upper left of a surface breaking crack, the displacement to left at $f^{\text{int}} t = 10.0$ is observed, and the contact of crack faces is caused at $f^{\text{int}} t = 10.2$ to 10.4. Then, this part is deformed from upper left to upper right with large amplitude at $f^{\text{int}} t = 10.8$ to 11.6 without contact of crack faces. This part begins to be deformed to left again at around $f^{\text{int}} t = 11.8$, and the state of displacement eventually returns to the first one at $f^{\text{int}} t = 12.0$. From the above, it seems that the bending vibration of the convex part

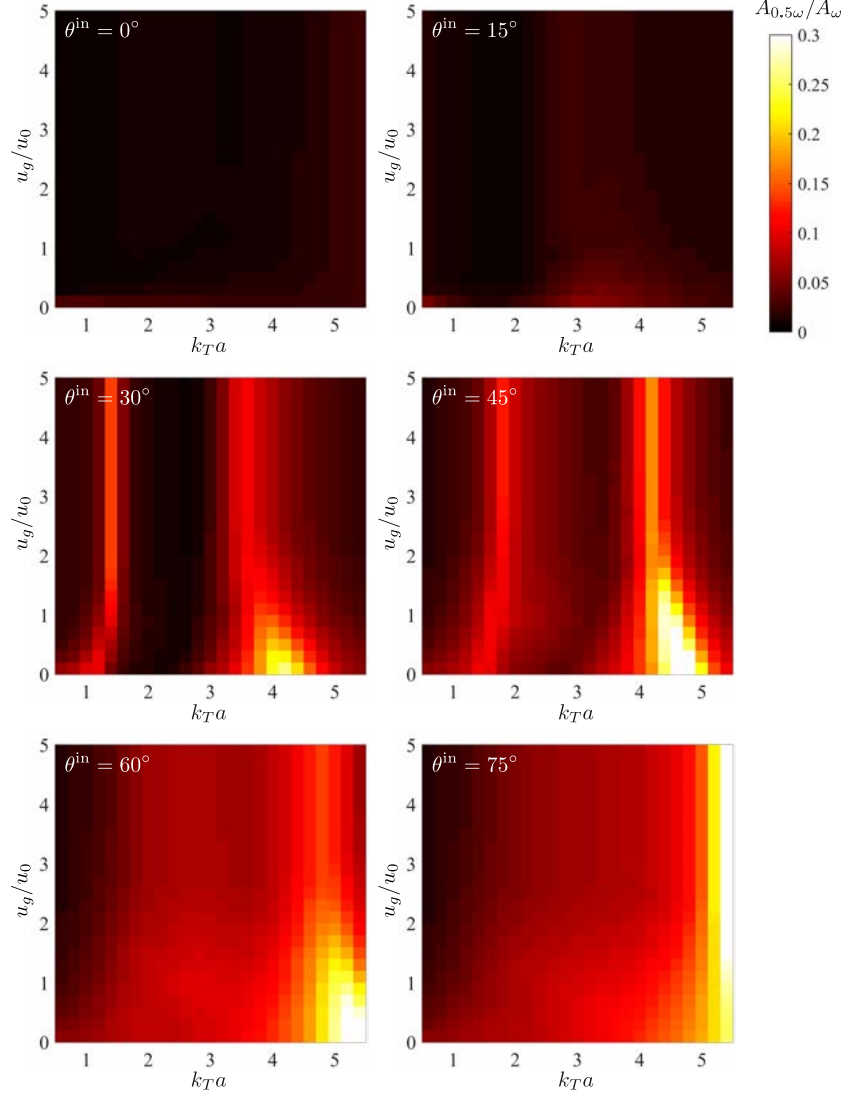


Figure 5.34.: Fourier amplitude ratio of sub-harmonic frequency to fundamental one for various wavenumber $k_T a$, pre-opening displacement u_g/u_0 , and incident angles θ^{in} when a surface breaking crack is subjected to an incident plane P wave with $n^{\text{in}} = 15$ ($\theta_c = 0^\circ$).

with the double period of incident wave as shown in lower right of Fig. 5.40, is generated due to the contact of crack faces.

The history of displacement at point E in lower right of Fig. 5.40 from $f^{\text{int}} = 10.0$ to 12.0 is shown in Fig. 5.41. The circle in the figure indicates the displacement at $f^{\text{int}} = 10.0$. As shown in Fig. 5.41, the displacement orbit is distorted, and the displacement returns to the position at $f^{\text{int}} = 10.0$ spending double of $1/f^{\text{in}}$. Therefore, the bending vibration of the convex part is generated as sub-harmonic resonance under certain conditions.

In order to investigate the relation with frequency responses, the norm of COD $||[\mathbf{u}]||/u_0$ at the

5. 2-D Simulation of Nonlinear Ultrasonic Waves Due to Interior and Surface Breaking Cracks

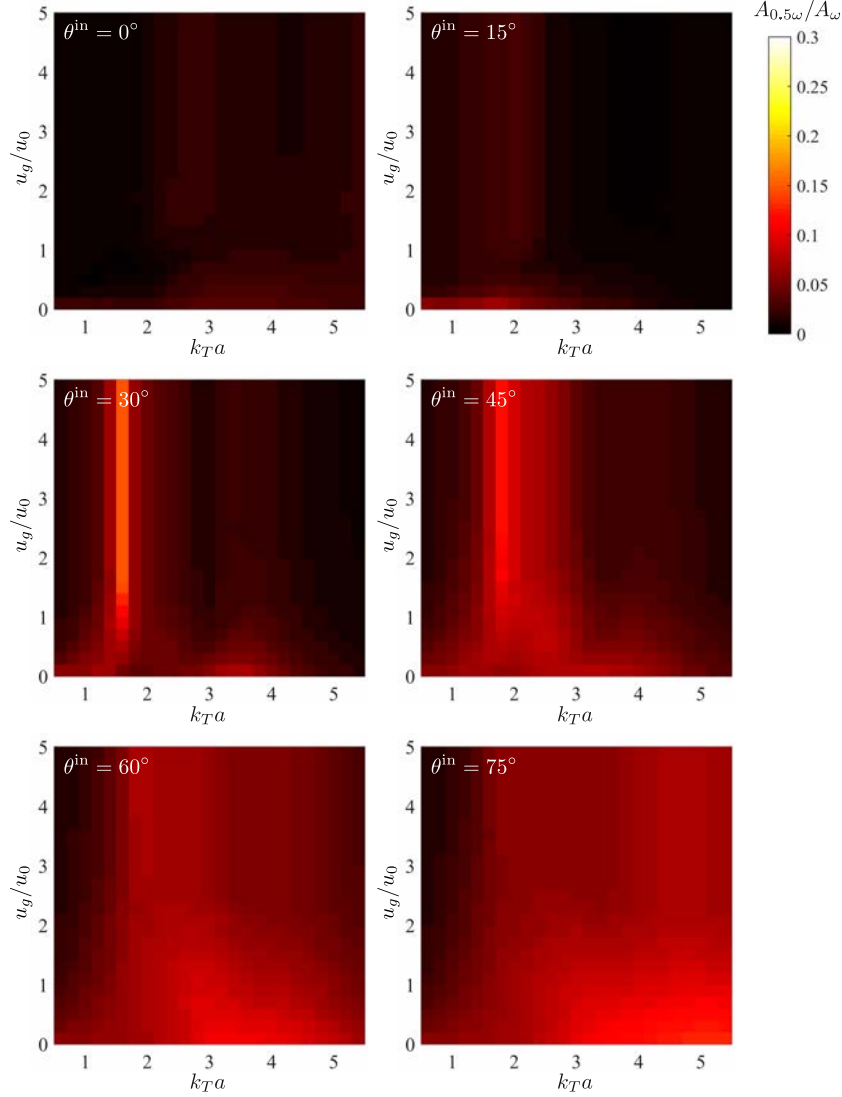


Figure 5.35.: Fourier amplitude ratio of sub-harmonic frequency to fundamental one for various wavenumber $k_T a$, pre-opening displacement u_g/u_0 , and incident angles θ^{in} when a surface breaking crack is subjected to an incident plane P wave with $n^{in} = 15$ ($\theta_c = 15^\circ$).

origin O in Fig. 5.33 varying $k_T a$ is shown in Fig. 5.42 for various θ_c . As shown in Fig. 5.42 (d), $||[\mathbf{u}]||/u_0$ has rapid fluctuation at about $k_T a = 1.1$ when $60^\circ \leq \theta^{in} \leq 75^\circ$ compared with others in Fig. 5.42 (a), (b), and (c). It also seems that this fluctuation is important for the probability of sub-harmonic generation. However, the sub-harmonic generation is caused in the case that $k_T a$ is larger than the triple of $k_T a$ at the rapid fluctuation as shown in Fig. 5.37. In addition, the optimal u_g/u_0 for the sub-harmonic generation is $u_g/u_0 = 0.0$ in this case. Therefore, the behavior of sub-harmonic generation is different between interior cracks and surface breaking crack. This may be because the one side of convex part is free surface without contact.

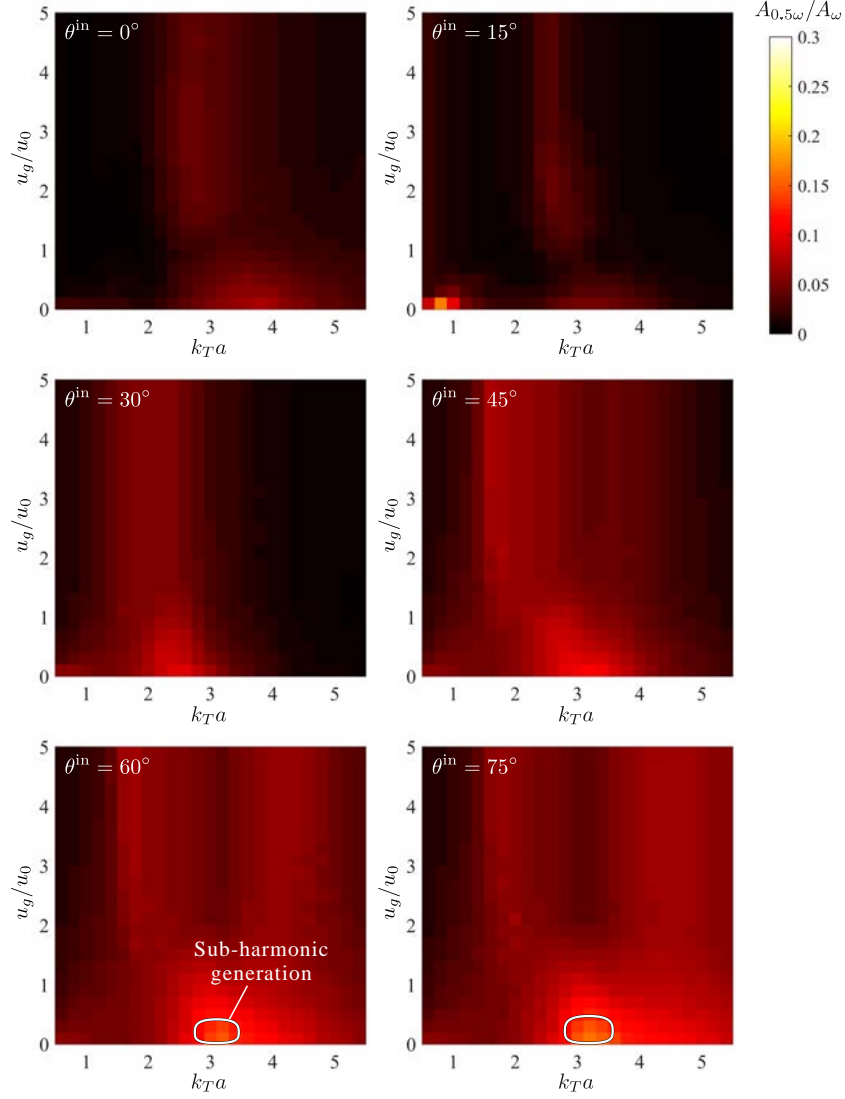


Figure 5.36.: Fourier amplitude ratio of sub-harmonic frequency to fundamental one for various wavenumber $k_T a$, pre-opening displacement u_g/u_0 , and incident angles θ^{in} when a surface breaking crack is subjected to an incident plane P wave with $n^{\text{in}} = 15$ ($\theta_c = 30^\circ$).

5.6. Concluding remarks

- In Chapter 5, we have applied the IRK-based CQ-BEM without any acceleration techniques to the 2-D elastic wave scattering problems by cracks in an infinite elastic solid and surface breaking cracks in an elastic half-space. Moreover, the contact boundary conditions on crack faces are considered, and the phenomena of higher- and sub-harmonic generation are investigated by the presented numerical method.
- The IRK-based CQ-BEM produces accurate solutions for the linear crack problems. We

5. 2-D Simulation of Nonlinear Ultrasonic Waves Due to Interior and Surface Breaking Cracks

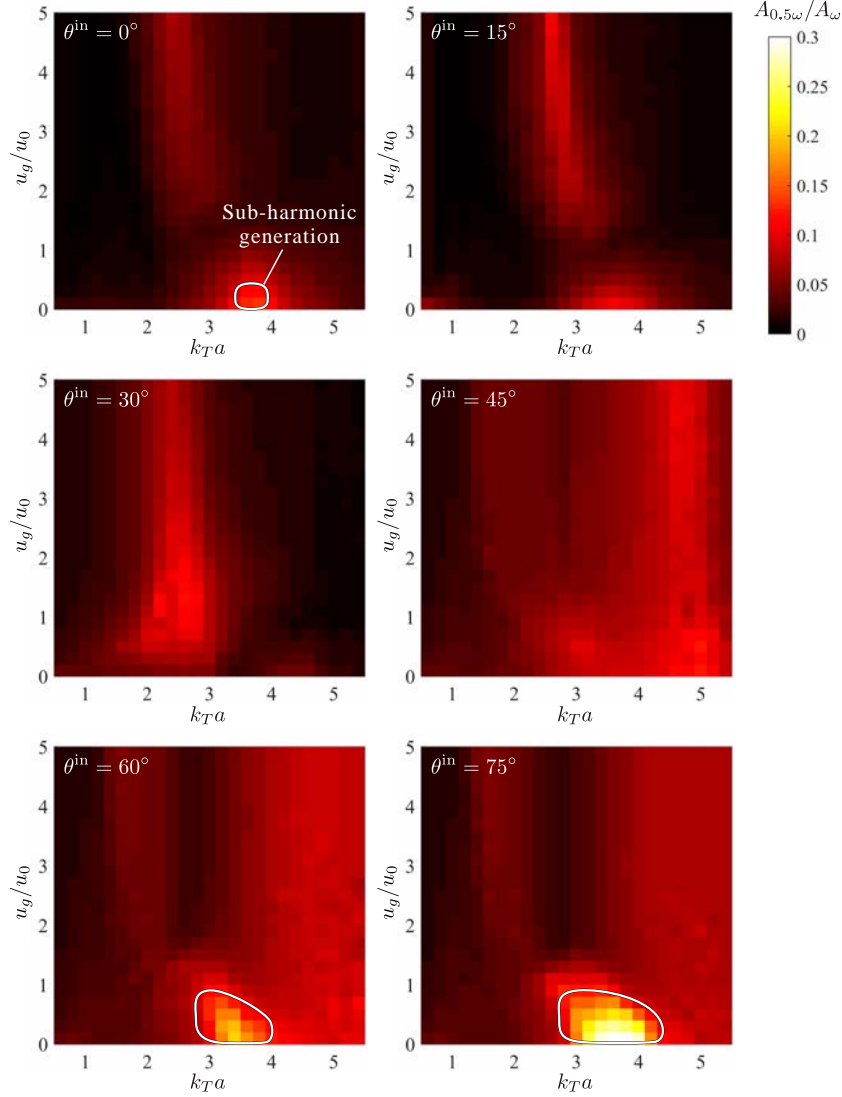


Figure 5.37.: Fourier amplitude ratio of sub-harmonic frequency to fundamental one for various wavenumber $k_T a$, pre-opening displacement u_g/u_0 , and incident angles θ^{in} when a surface breaking crack is subjected to an incident plane P wave with $n^{in} = 15$ ($\theta_c = 45^\circ$).

have also numerically solved the fundamental nonlinear ultrasonic problems such as normal incidence of P and S waves to a straight-line crack in order to validate the presented contact model. From these results, it could be confirmed that the proposed IRK-based CQ-BEM can accurately solve the crack problems with contact boundary conditions.

- We conducted the higher-harmonic simulation for a straight-line crack subjected to an incident plane P wave varying u_g/u_0 or σ^{st}/σ_0 . From the numerical results, the 2nd higher-harmonic wave is generated most strongly when $u_g/u_0 = \sigma^{st}/\sigma_0 = 0.0$ if the center frequency of incident wave is comparatively low. However, the 2nd higher-harmonic wave is

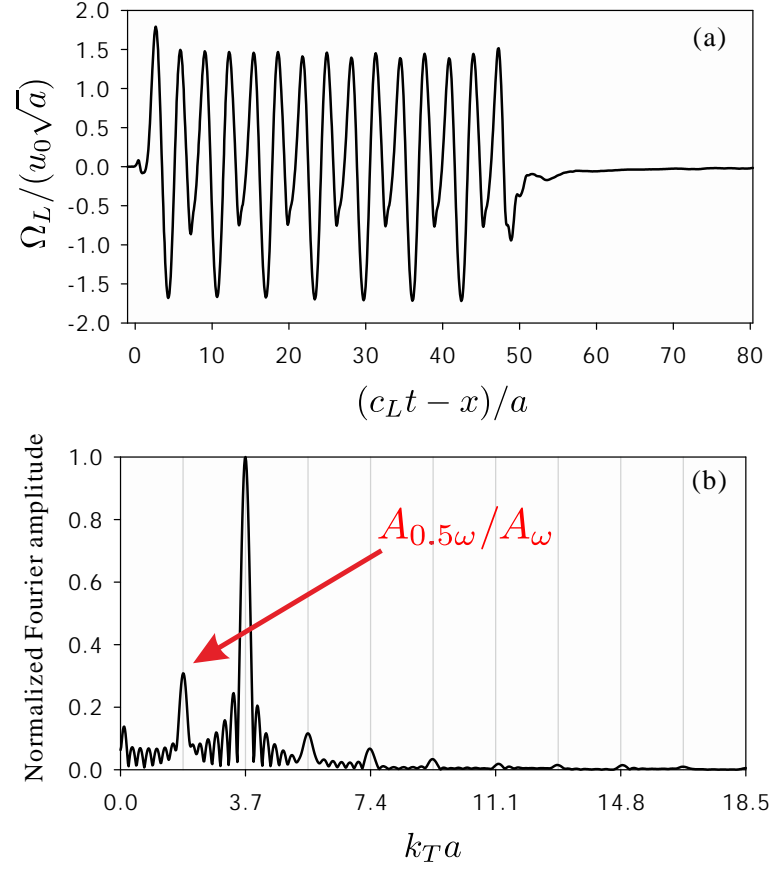


Figure 5.38.: (a) Time variation and (b) normalized frequency spectrum of far-field amplitude of backscattered P wave when a surface breaking crack is subjected to an incident plane P wave ($k_T a = 3.7$, $u_g/u_0 = 0.0$, $\theta_c = 45^\circ$, and $\theta^{\text{in}} = 75^\circ$).

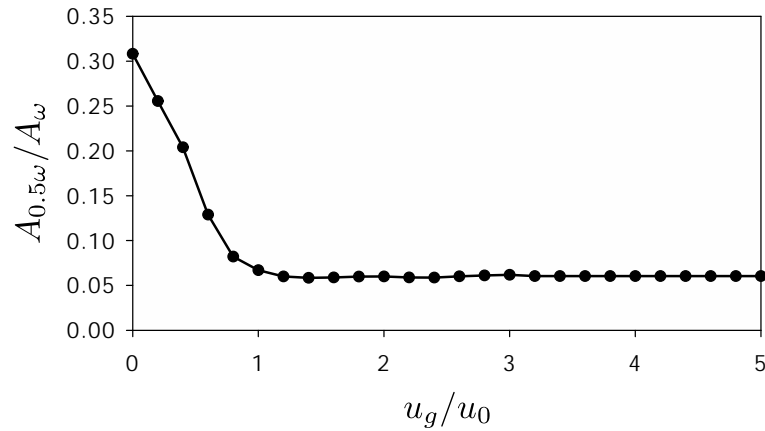


Figure 5.39.: Fourier amplitude ratio of sub-harmonic frequency to fundamental one for various pre-opening displacement u_g/u_0 when $k_T a = 3.7$, $\theta_c = 45^\circ$, and $\theta^{\text{in}} = 75^\circ$.

5. 2-D Simulation of Nonlinear Ultrasonic Waves Due to Interior and Surface Breaking Cracks

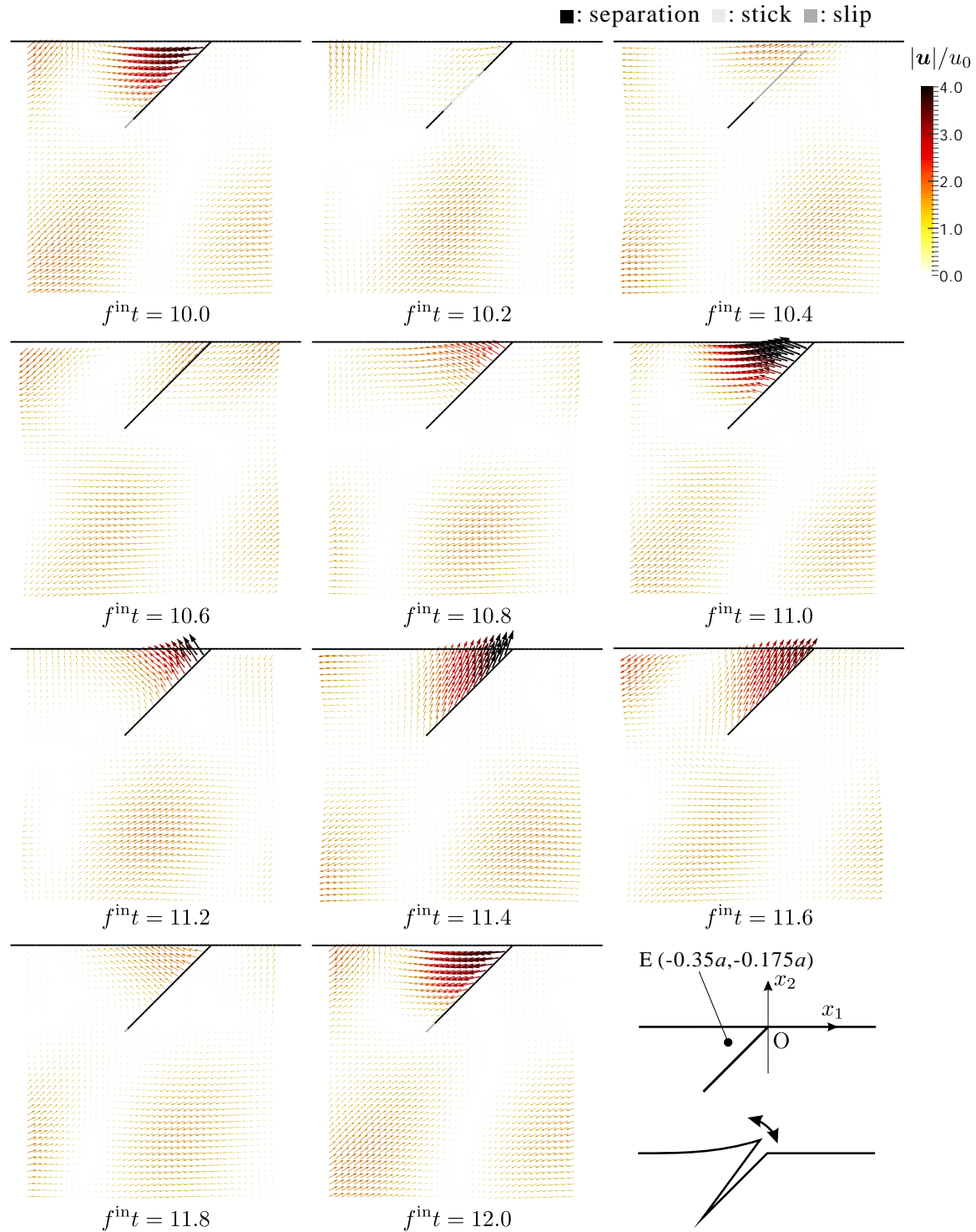


Figure 5.40.: Displacement fields around a surface breaking crack from $f^{\text{int}} = 10.0$ to 12.0 when $\theta_c = 45^\circ$, $\theta^{\text{in}} = 75^\circ$, $k_T a = 3.7$, and $u_g/u_0 = 0.0$.

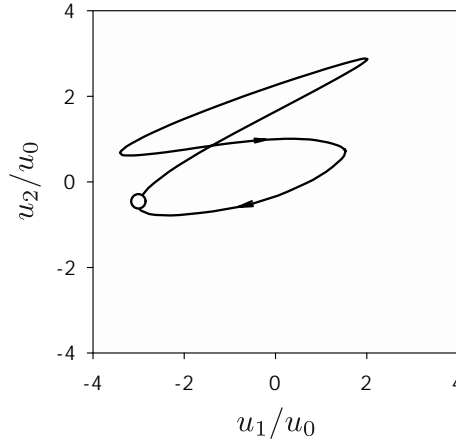


Figure 5.41.: History of displacement at point E in the lower right of Fig. 5.40 from $f^{\text{int}} t = 10.0$ to 12.0 when $\theta_c = 45^\circ$, $\theta^{\text{in}} = 75^\circ$, $k_{Ta} = 3.7$, and $u_g/u_0 = 0.0$.

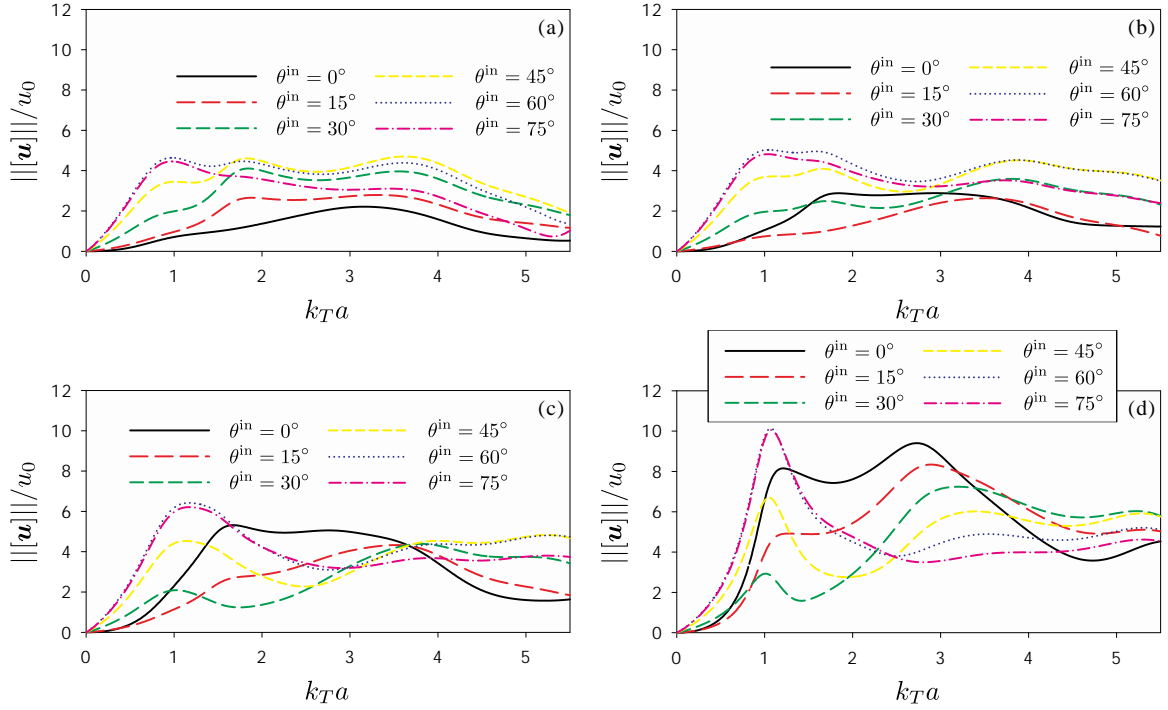


Figure 5.42.: Frequency responses for the model in Fig. 5.33 using the frequency-domain BEM and assuming that crack faces are always separated. The norm $||[\mathbf{u}]||/u_0$ at the origin O in Fig. 5.33 for various θ^{in} and k_{Ta} is plotted when (a) $\theta_c = 0^\circ$, (b) 15° , (c) 30° , and (d) 45° .

5. 2-D Simulation of Nonlinear Ultrasonic Waves Due to Interior and Surface Breaking Cracks

generated most strongly under some compressive static stress if the center frequency of incident wave is comparatively high. The border frequency of this phenomenon is near the first mode quasi-eigenfrequency of the linear system (about $k_T a = 1.2$).

- We have dealt with the scattering problems by a half-sine-shaped crack and two straight-line cracks arranged in parallel in an infinite elastic solid in this chapter. The torsional and bending vibrations with the double period of the incident wave are generated as the nonlinear sub-harmonic resonance. In addition, the characteristic of frequency response greatly depends on the crack shape and incident angle, and it seems that this characteristic is significantly related to the probability of sub-harmonic generation.
- We also implemented the 2-D simulation of nonlinear ultrasonic due to a surface breaking crack in an elastic half-space. The bending vibration of convex part with the double period of the incident wave is generated as the nonlinear sub-harmonic resonance. Similarly to the case of interior cracks, the characteristic of frequency response seems to be important for the sub-harmonic generation. However, the frequency behavior of sub-harmonic generation is different from the case of the interior crack.

Chapter 6

3-D Simulation of Nonlinear Ultrasonic Waves Due to Interior Cracks

In this chapter, the boundary element formulations and numerical results for the 3-D simulation of sub-harmonic generation are presented. We consider the scattering problems by cracks in an infinite domain. The fast CQ-BEM proposed in Chapter 3 is extended to the 3-D crack problems with contact boundary conditions. The Galerkin method is used for spatial discretization here, similarly to Chapter 5.

For 2-D problems, the regularization of hypersingular integrals to the strong singular one is enough to use the tip element as shown in Chapter 5. However, the analytical integration over elements at the crack front in 3-D problems is much more complicated than that in 2-D. Therefore, we regularize the hypersingular integrals to weakly singular ones, and all of the integrations over elements are evaluated numerically. Regularization techniques for the hypersingular BIE have been developed by many researchers [93]. For instance, the weakly singular formulations have been developed for the 3-D acoustic and elastic wave problems by Liu and Rizzo [44, 45]. Also, the direct numerical integration method of hypersingular integral has been developed by Guiggiani *et al.* [27]. In this study, we use the regularization method proposed by Nishimura and Kobayashi [61]. Their method is based on the stress function representation of differentiated fundamental solution and can relax the hypersingular integrals to weakly ones.

First, the formulation of time-domain BIE for crack problem is briefly explained. Second, the regularization and discretization are presented, and some remarks related with the application of FMM are summarized. Then, the computational cost and accuracy of the proposed CQ-FMBEM are demonstrated by solving linear crack problems. Finally, we implement 3-D sub-harmonic simulations and discuss the phenomena through obtained numerical results.

6.1. Problem statement and BIE

We show the initial and boundary conditions for 3-D crack problems in time-domain. Let S be a smooth curved crack surface in \mathbb{R}^3 bounded by a smooth edge ∂S as depicted in Fig. 6.1. D is a homogeneous, isotropic, and linearly elastic solid, and S consists of S^+ and S^- called positive and

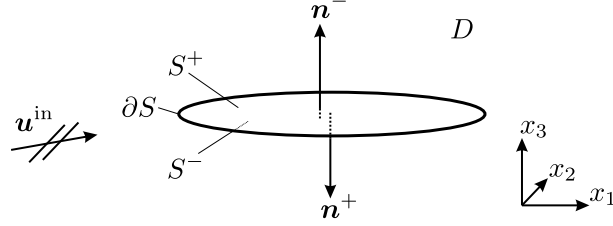


Figure 6.1.: Analysis model for elastic wave scattering by a crack in a 3-D infinite domain.

negative sides of crack face, respectively ($S = S^+ \cup S^-$ and $S^+ \cap S^- = \emptyset$). \mathbf{n} is the unit normal vector to the crack face, and the superscript \pm indicates its each side. Disregarding the body force, the problem is to find the solution \mathbf{u} which satisfies the following equations:

$$c_T^2 \nabla^2 \mathbf{u}(\mathbf{x}, t) + (c_L^2 + c_T^2) \nabla \nabla \cdot \mathbf{u}(\mathbf{x}, t) = \ddot{\mathbf{u}}(\mathbf{x}, t) \quad \mathbf{x} \in D \left(\equiv \mathbb{R}^3 \setminus S \right), \quad (6.1)$$

$$\mathbf{t}^+(\mathbf{x}, t) + \mathbf{t}^-(\mathbf{x}, t) = \mathbf{0} \quad \mathbf{x} \in S, \quad (6.2)$$

$$[\mathbf{u}](\mathbf{x}, t) \left(\equiv \mathbf{u}^+(\mathbf{x}, t) - \mathbf{u}^-(\mathbf{x}, t) \right) = \mathbf{0} \quad \mathbf{x} \in \partial S, \quad (6.3)$$

$$\mathbf{u}^{\text{sc}}(\mathbf{x}, 0) = \dot{\mathbf{u}}^{\text{sc}}(\mathbf{x}, 0) = \mathbf{0} \quad \mathbf{x} \in D. \quad (6.4)$$

Similarly to 2-D case in Chapter 5, the variational formulation of hypersingular BIE with weight function ψ can be derived as follows:

$$\begin{aligned} \int_{S^+} \psi(\mathbf{x}) \mathbf{t}^+(\mathbf{x}, t) dS_x &= \int_{S^+} \psi(\mathbf{x}) \mathbf{t}^{\text{in};+}(\mathbf{x}, t) dS_x \\ &\quad - \int_0^t \int_{S^+} \psi(\mathbf{x}) \text{p.f.} \int_{S^+} \mathbf{W}^+(\mathbf{x}, \mathbf{y}, t - \tau) \cdot [\mathbf{u}](\mathbf{y}, \tau) dS_y dS_x d\tau. \end{aligned} \quad (6.5)$$

The superscript $+$ is hereinafter omitted. In Eq. (6.5), \mathbf{W} is the 3-D hypersingular kernel in time-domain. Similarly to the 2-D case, it can be written as follows:

$$W_{bj}(\mathbf{x}, \mathbf{y}, t) = n_a(\mathbf{x}) n_k(\mathbf{y}) C_{baic} C_{jkpq} \frac{\partial}{\partial x_c} \frac{\partial}{\partial y_q} U_{ip}(\mathbf{x}, \mathbf{y}, t). \quad (6.6)$$

6.2. Regularization of BIE

In this section, the regularization of variational BIE (6.5) is presented. First, the stress function representation of differentiated fundamental solution in Laplace-domain is shown because we use the CQM and evaluate the integration of hypersingular kernel in Laplace-domain. According to [61], the stress function representation for differentiated fundamental solutions in Laplace-domain

elastodynamic problems is shown as follows:

$$C_{baic}C_{jkpq}\frac{\partial}{\partial x_c}\frac{\partial}{\partial y_q}\hat{U}_{ip}(\mathbf{x}, \mathbf{y}, s) = e_{acm}e_{bds}e_{jpn}e_{kqt}\frac{\partial}{\partial x_c}\frac{\partial}{\partial x_d}\frac{\partial}{\partial y_p}\frac{\partial}{\partial y_q}\hat{\Phi}_{msnt}(\mathbf{x}, \mathbf{y}, s) + \hat{\Psi}_{abjk}(\mathbf{x}, \mathbf{y}, s) + D_{abjk}\delta(\mathbf{x} - \mathbf{y}), \quad (6.7)$$

where $\hat{\Phi}$ is a function of order r as $r \downarrow 0$, and $\hat{\Psi}$ is a function which has an integrable singularity at $\mathbf{x} = \mathbf{y}$. In addition, \mathbf{D} is a constant tensor, and this term is canceled in the BIE. The specific expressions of $\hat{\Phi}$ and $\hat{\Psi}$ for isotropic media are given as follows:

$$\hat{\Phi}_{msnt}(\mathbf{x}, \mathbf{y}, s) = -\frac{1}{4\pi(\lambda + \mu)}\frac{\mu}{s_T^2}\left\{2\lambda\delta_{ms}\delta_{nt} + (\lambda + 2\mu)(\delta_{mt}\delta_{sn} + \delta_{st}\delta_{mn})\right\} \times \left(\frac{e^{-s_L r}}{r} - \frac{e^{-s_T r}}{r}\right), \quad (6.8)$$

$$\begin{aligned} \hat{\Psi}_{abjk}(\mathbf{x}, \mathbf{y}, s) = & \frac{1}{4\pi(\lambda + \mu)}\left[\mu s_T^2\left\{\lambda\delta_{ab}\delta_{jk}\mu(\delta_{aj}\delta_{bk} + \delta_{ak}\delta_{bj})\right\}\left(\frac{s_L^2}{s_T^2}\frac{e^{-s_L r}}{r} - \frac{s_T^2}{s_L^2}\frac{e^{-s_T r}}{r}\right)\right. \\ & - \left\{\lambda^2\delta_{ab}\delta_{jk}\delta_{pq} + \mu^2(\delta_{ap}\delta_{jq}\delta_{bk} + \delta_{bp}\delta_{kq}\delta_{aj} + \delta_{ap}\delta_{kq}\delta_{bj} + \delta_{bp}\delta_{jq}\delta_{ak})\right. \\ & \left. + 2\lambda\mu(\delta_{ab}\delta_{jp}\delta_{kq} + \delta_{jk}\delta_{ap}\delta_{bq})\right\}\frac{\partial}{\partial x_p}\frac{\partial}{\partial x_q}\left(\frac{e^{-s_L r}}{r} - \frac{e^{-s_T r}}{r}\right)\left. \right]. \quad (6.9) \end{aligned}$$

In addition, this decomposition has been extended to anisotropic elastodynamics by Becache *et al.* [11].

Taking into account the application of CQM, we consider the following integral containing the Laplace-domain hypersingular kernel $\hat{\mathbf{W}}$ corresponding to the second term in the right-hand side of Eq. (6.5):

$$\hat{I}^W = \int_S \psi(\mathbf{x}) \text{p.f.} \int_S \hat{W}_{bj}(\mathbf{x}, \mathbf{y}, s) \phi(\mathbf{y}) dS_y dS_x, \quad (6.10)$$

where ϕ is the spatial shape function for $[\mathbf{u}]$. Substituting Eq. (6.7) into Eq. (6.10) yields the following expression:

$$\begin{aligned} \hat{I}^W = & \int_S \psi(\mathbf{x}) n_a(\mathbf{x}) \\ & \times \text{p.f.} \int_S \phi(\mathbf{y}) n_k(\mathbf{y}) e_{acm}e_{bds}e_{jpn}e_{kqt}\frac{\partial}{\partial x_c}\frac{\partial}{\partial x_d}\frac{\partial}{\partial y_p}\frac{\partial}{\partial y_q}\hat{\Phi}_{msnt}(\mathbf{x}, \mathbf{y}, s) dS_y dS_x \\ & + \int_S \psi(\mathbf{x}) n_a(\mathbf{x}) \int_S \hat{\Psi}_{abjk}(\mathbf{x}, \mathbf{y}, s) \phi(\mathbf{y}) n_k(\mathbf{y}) dS_y dS_x. \quad (6.11) \end{aligned}$$

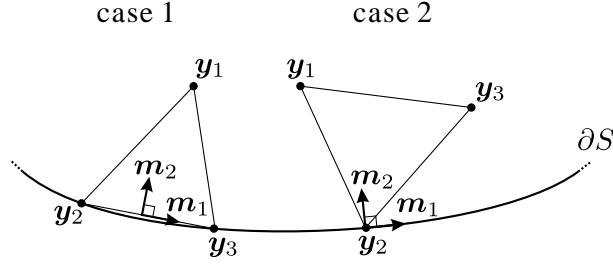


Figure 6.2.: Two types of triangular tip element for crack front.

Using Stokes' theorem and taking Eq. (6.3) into account, Eq. (6.11) can be regularized as follows:

$$\begin{aligned} \hat{I}^W = & \int_S e_{acm} n_a(\mathbf{x}) \frac{\partial \psi(\mathbf{x})}{\partial x_c} \int_S e_{kqt} n_k(\mathbf{y}) \frac{\partial \phi(\mathbf{y})}{\partial y_q} e_{bds} e_{jpn} \frac{\partial}{\partial x_d} \frac{\partial}{\partial y_p} \hat{\Phi}_{msnt}(\mathbf{x}, \mathbf{y}, s) dS_y dS_x \\ & - \oint_{\partial S} \psi(\mathbf{x}) \int_S e_{kqt} n_k(\mathbf{y}) \frac{\partial \phi(\mathbf{y})}{\partial y_q} e_{bds} e_{jpn} \frac{\partial}{\partial x_d} \frac{\partial}{\partial y_p} \hat{\Phi}_{msnt}(\mathbf{x}, \mathbf{y}, s) dS_y dx_m \\ & + \int_S \psi(\mathbf{x}) n_a(\mathbf{x}) \int_S \hat{\Psi}_{abjk}(\mathbf{x}, \mathbf{y}, s) \phi(\mathbf{y}) n_k(\mathbf{y}) dS_y dS_x. \end{aligned} \quad (6.12)$$

The second term in Eq. (6.12) includes the contour integral over the crack front with respect to \mathbf{x} . If we select the weight function ψ as $\psi = 0$ on ∂S , this term vanishes. The second derivative of $\hat{\Phi}$ in the first term of Eq. (6.12) has weak singularity of order $1/r$ as $r \downarrow 0$.

6.3. Discretization of BIE

The IRK-based CQM [48] is used for time discretization. For spatial discretization, the piecewise linear interpolation is used for $[\mathbf{u}]$ except elements which are located at the crack front. We utilize two types of tip element as depicted in Fig. 6.2 in order to accurately calculate COD near the crack front using flatly triangular elements. As shown in Fig. 6.2, \mathbf{m}_1 and \mathbf{m}_2 are the unit tangential and normal vectors to the crack front, respectively. The specific expressions of shape function ϕ_I^u for the two types of tip element are shown as follows:

case 1

$$\phi_1^u(\mathbf{y}) = \sqrt{\frac{\mathbf{m}_2 \cdot (\mathbf{y} - \mathbf{y}_2)}{\mathbf{m}_2 \cdot (\mathbf{y}_1 - \mathbf{y}_2)}}, \quad \phi_2^u(\mathbf{y}) = \phi_3^u(\mathbf{y}) = 0.$$

case 2

$$\begin{aligned} \phi_1^u(\mathbf{y}) &= \frac{\mathbf{m}_1 \cdot (\mathbf{y} - \mathbf{y}_3)}{\mathbf{m}_1 \cdot (\mathbf{y}_1 - \mathbf{y}_3)} \sqrt{\frac{\mathbf{m}_2 \cdot (\mathbf{y} - \mathbf{y}_2)}{\mathbf{m}_2 \cdot (\mathbf{y}_1 - \mathbf{y}_2)}}, \quad \phi_2^u(\mathbf{y}) = 0, \\ \phi_3^u(\mathbf{y}) &= \frac{\mathbf{m}_1 \cdot (\mathbf{y} - \mathbf{y}_1)}{\mathbf{m}_1 \cdot (\mathbf{y}_3 - \mathbf{y}_1)} \sqrt{\frac{\mathbf{m}_2 \cdot (\mathbf{y} - \mathbf{y}_2)}{\mathbf{m}_2 \cdot (\mathbf{y}_3 - \mathbf{y}_2)}}. \end{aligned}$$

Note that the derivatives of shape function for tip element have additional singularity of order $1/\sqrt{r}$ corresponding to stress singularity at the crack front.

On the other hand, the piecewise constant shape function ϕ^t is used for the interpolation of \mathbf{t} in order to describe the discontinuity of traction between two adjacent elements. Therefore, the weight functions for displacement ψ^u and traction ψ^t are different because the Galerkin method is used in this study. For simplicity, all of the weight functions ψ^u are however taken as piecewise linear functions. Thus, $\psi^u \neq \phi^u$ on tip elements.

If the m -stage Radau IIA method [33] is used for the IRK-based CQM, and the boundary S is divided into M_e flatly triangular elements composed of M_d nodal points, the discretized BIEs for $[\mathbf{u}]$ and \mathbf{t} at n -th and i -th sub-step in time are written as follows:

$$\begin{aligned} \sum_{J=1}^{M_d} \sum_{j=1}^m \left[\mathcal{W}_{IJ}^{ij;0} \cdot [\mathbf{u}]_J^{j;n} \right] &= - \sum_{\alpha=1}^{M_e} \mathbf{t}_{\alpha}^{i;n} \phi_{\alpha}^t \int_{\text{supp}(\psi_I^u) \cap S_{\alpha}} \psi_I^u(\mathbf{x}) dS_x \\ &+ \int_{\text{supp}(\psi_I^u)} \psi_I^u(\mathbf{x}) \mathbf{t}^{\text{in}}(\mathbf{x}, (n + c_i)\Delta t) dS_x - \sum_{k=0}^{n-1} \sum_{J=1}^{M_d} \sum_{j=1}^m \mathcal{W}_{IJ}^{ij;n-k} \cdot [\mathbf{u}]_J^{j;k}, \end{aligned} \quad (6.13)$$

$$\begin{aligned} \mathbf{t}_{\alpha}^{i;n} \phi_{\alpha}^t \phi_{\alpha}^t \int_{S_{\alpha}} dS_x &= \phi_{\alpha}^t \int_{S_{\alpha}} \mathbf{t}^{\text{in}}(\mathbf{x}, (n + c_i)\Delta t) dS_x \\ &- \sum_{k=0}^n \sum_{J=1}^{M_d} \sum_{j=1}^m \tilde{\mathcal{W}}_{\alpha J}^{ij;n-k} \cdot [\mathbf{u}]_J^{j;k}, \end{aligned} \quad (6.14)$$

where $\int_{S_{\alpha}} dS_x$ in the left hand side of Eq. (6.14) is equal to the area of α -th element. $\mathcal{W}_{IJ}^{ij;\kappa}$ and $\tilde{\mathcal{W}}_{\alpha J}^{ij;\kappa}$ in Eqs. (6.13) and (6.14) are influence functions and given as follows:

$$\mathcal{W}_{IJ}^{ij;\kappa} = \tilde{\mathcal{F}}_{l\kappa}^{-1} \left[\sum_{\beta=1}^m \left(\mathbf{E}_{\beta}(\zeta_l) \right)_{ij} \mathcal{Z}_{IJ}^{\beta;l} \right], \quad (6.15)$$

$$\begin{aligned} \left(\mathcal{Z}_{IJ}^{\beta;l} \right)_{bj} &= \int_{\text{supp}(\psi_I^u)} e_{acm} n_a(\mathbf{x}) \frac{\partial \psi_I^u(\mathbf{x})}{\partial x_c} \\ &\times \int_{\text{supp}(\phi_J^u)} e_{kqt} n_k(\mathbf{y}) \frac{\partial \phi_J^u(\mathbf{y})}{\partial y_q} e_{bds} e_{jpn} \frac{\partial}{\partial x_d} \frac{\partial}{\partial y_p} \hat{\Phi}_{msnt}(\mathbf{x}, \mathbf{y}, \lambda_{\beta}^l) dS_y dS_x \\ &+ \int_{\text{supp}(\psi_I^u)} \psi_I^u(\mathbf{x}) n_a(\mathbf{x}) \int_{\text{supp}(\phi_J^u)} \hat{\Psi}_{abjk}(\mathbf{x}, \mathbf{y}, \lambda_{\beta}^l) \phi_J^u(\mathbf{y}) n_k(\mathbf{y}) dS_y dS_x, \end{aligned} \quad (6.16)$$

$$\tilde{\mathcal{W}}_{\alpha J}^{ij;\kappa} = \tilde{\mathcal{F}}_{l\kappa}^{-1} \left[\sum_{\beta=1}^m \left(\mathbf{E}_{\beta}(\zeta_l) \right)_{ij} \tilde{\mathcal{Z}}_{\alpha J}^{\beta;l} \right], \quad (6.17)$$

$$\begin{aligned} \left(\tilde{\mathcal{Z}}_{\alpha J}^{\beta;l} \right)_{bj} &= -\phi_{\alpha}^t \oint_{\partial S_{\alpha}} \int_{\text{supp}(\phi_J^u)} e_{kqt} n_k(\mathbf{y}) \frac{\partial \phi_J^u(\mathbf{y})}{\partial y_q} e_{bds} e_{jpn} \frac{\partial}{\partial x_d} \frac{\partial}{\partial y_p} \hat{\Phi}_{msnt}(\mathbf{x}, \mathbf{y}, \lambda_{\beta}^l) dS_y dx_m \\ &+ \phi_{\alpha}^t \int_{S_{\alpha}} n_a(\mathbf{x}) \int_{\text{supp}(\phi_J^u)} \hat{\Psi}_{abjk}(\mathbf{x}, \mathbf{y}, \lambda_{\beta}^l) \phi_J^u(\mathbf{y}) n_k(\mathbf{y}) dS_y dS_x, \end{aligned} \quad (6.18)$$

6. 3-D Simulation of Nonlinear Ultrasonic Waves Due to Interior Cracks

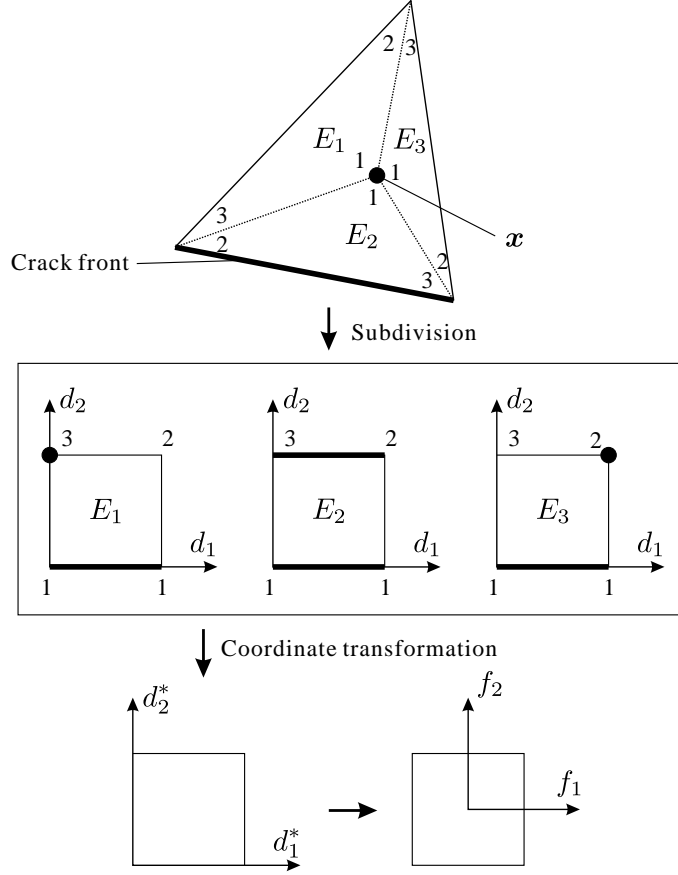


Figure 6.3.: Schematic of element subdivision and coordinate transformation for case 1 tip element in Fig. 6.2.

Table 6.1.: Relation between coordinate systems (d_1, d_2) and (d_1^*, d_2^*) for sub-elements E_1 , E_2 , and E_3 in Fig. 6.3.

E_1	E_2	E_3
$d_1 = (d_1^*)^2$	$d_1 = d_1^*$	$d_1 = 1 - (1 - d_1^*)^2$
$d_2 = 1 - (1 - d_2^*)^2$	$d_2 = 1 - (1 - d_2^*)^2$	$d_2 = 1 - (1 - d_2^*)^2$

where ∂S_α indicates the edge of S_α . Note that there are only weakly singular integrals in Eqs. (6.16) and (6.18). Therefore, applying the element subdivision [43] and the transformation of local coordinate system, we can accurately evaluate all of the integrals in Eqs. (6.16) and (6.18) using the standard Gaussian quadrature.

6.4. Numerical integration over element surfaces

In this study, we use the element subdivision [43] and the transformation of local coordinate system in order to cancel the weak singularities of order $1/r$ and $1/\sqrt{r}$. The similar regularization technique has been presented in [21]. For instance, we present regularization for the case 1 in Fig. 6.2 when field point \mathbf{x} is located on the same element. The integrals with respect to \mathbf{x} in Eqs. (6.16) and (6.18) are evaluated by the standard Gaussian quadrature after the calculation of integrals with respect to \mathbf{y} .

We summarize the procedure of the regularization as follows:

1. The element subdivision method is applied in order to regularize the singularity of order $1/r$ at the point $\mathbf{x} = \mathbf{y}$. The definitions of sub-elements E_1 , E_2 , and E_3 are shown in the above of Fig. 6.3. Then, the coordinate system of each sub-element is transformed into the local one (d_1, d_2) . We select (d_1, d_2) for each element as shown in the middle of Fig. 6.3, and the ranges of d_1 and d_2 for each element are $[0, 1]$. If the kernel function is $A(\mathbf{y})$, the integral is transformed as follows:

$$\int_{E_i} A(\mathbf{y}) dS_y = \int_0^1 \int_0^1 A(\mathbf{d}) J_d dd_1 dd_2 \quad (i = 1, 2, \text{ or } 3), \quad (6.19)$$

where J_d is the Jacobian of the coordinate transformation and can cancel the singularity of order $1/r$ at $d_2 = 0$ in the middle of Fig. 6.3.

2. In order to regularize the additional singularity of order $1/\sqrt{r}$ caused by the derivatives of shape function ϕ^u at the crack front, the additional transformation of local coordinate system is introduced. The coordinate system (d_1, d_2) is changed to (d_1^*, d_2^*) using the relations between old and new ones in Table 6.1 for each element as follows:

$$\int_0^1 \int_0^1 A(\mathbf{d}) J_d dd_1 dd_2 = \int_0^1 \int_0^1 A(\mathbf{d}^*) J_d J_d^* dd_1^* dd_2^*, \quad (6.20)$$

where J_d^* is also the Jacobian of the coordinate transformation. Consequently, the singularity of each sub-element is canceled by each J_d^* .

3. The coordinate system (d_1^*, d_2^*) is transformed to (f_1, f_2) , where the intervals of f_1 and f_2 are $[-1, 1]$. Then, the integrations over each sub-element are evaluated by the standard Gaussian quadrature.

The other cases of integration such as case 2 tip element or the case that \mathbf{x} is located at the edge of element, can be regularized in a similar way.

6.5. Application of FMM

The computational time and required memory often become significant issues for solving 3-D problems. Therefore, the proposed CQ-BEM is accelerated by the FMM as presented in Chapter 3.

6. 3-D Simulation of Nonlinear Ultrasonic Waves Due to Interior Cracks

The multipole and local expansions for non-regularized hypersingular kernel are used because the FMM for the regularized one requires much more computational time [100, 101]. The difference of accuracy between the FMM with and without regularization is not significant because the FMM calculation is implemented only for far-field contributions. In Chapter 3, we explained the computational algorithm of the CQ-FMBEM. Therefore, the multipole and local expansions and some remarks for this problem are presented here.

In order to derive the multipole and local expansions, $W_{b;IJ}^{i;k;\beta;l}$ and $\tilde{W}_{b;\alpha J}^{i;k;\beta;l}$ are defined by

$$W_{b;IJ}^{i;k;\beta;l} = \left[\int_{\text{supp}(\psi_I^u)} \psi_I^u(\mathbf{x}) \int_{\text{supp}(\phi_J^u)} \hat{W}_{bh}(\mathbf{x}, \mathbf{y}, \lambda_\beta^l) \phi_J^u(\mathbf{y}) dS_y dS_x \right] [\mathbf{u}_h]_J^{i;k;\beta;l}, \quad (6.21)$$

$$\tilde{W}_{b;IJ}^{i;k;\beta;l} = \left[\phi_\alpha^t \int_{S_\alpha} \int_{\text{supp}(\phi_J^u)} \hat{W}_{bh}(\mathbf{x}, \mathbf{y}, \lambda_\beta^l) \phi_J^u(\mathbf{y}) dS_y dS_x \right] [\mathbf{u}_h]_J^{i;k;\beta;l}, \quad (6.22)$$

where

$$[\mathbf{u}_h]_J^{i;k;\beta;l} = \sum_{j=1}^m \left(\mathbf{E}_\beta(\zeta_l) \right)_{ij} [u_h]_J^{j;k}.$$

The scaled multipole expansions for $W_{b;IJ}^{i;k;\beta;l}$ and $\tilde{W}_{b;\alpha J}^{i;k;\beta;l}$ without regularization are given by

$$\begin{aligned} W_{b;IJ}^{i;k;\beta;l} = & \sum_{v=0}^{\infty} \sum_{w=-v}^v \left[A_v \left\{ C_{bcad} \int_{\text{supp}(\psi_I^u)} n_c(\mathbf{x}) \psi_I^u(\mathbf{x}) \frac{\partial^2}{\partial x_a \partial x_d} {}_\rho \mathcal{O}_{v,w}^L(\mathbf{x} - \mathbf{y}_0) dS_x \right\} \right. \\ & \left. \times {}_\rho \mathcal{M}_{v,w;J}^{W_L;i;k;\beta;l}(\mathbf{y}_0) \right. \\ & \left. + B_v e_{oce} \left\{ C_{bcad} \int_{\text{supp}(\psi_I^u)} n_c(\mathbf{x}) \psi_I^u(\mathbf{x}) \frac{\partial^2}{\partial x_d \partial x_e} {}_\rho \mathcal{O}_{v,w}^T(\mathbf{x} - \mathbf{y}_0) dS_x \right\} {}_\rho \mathcal{M}_{o,v,w;J}^{W_T;i;k;\beta;l}(\mathbf{y}_0) \right]_{s=\lambda_\beta^l}, \end{aligned} \quad (6.23)$$

$$\begin{aligned} \tilde{W}_{b;IJ}^{i;k;\beta;l} = & \sum_{v=0}^{\infty} \sum_{w=-v}^v \left[A_v \left\{ C_{bcad} \phi_\alpha^t \int_{S_\alpha} n_c(\mathbf{x}) \frac{\partial^2}{\partial x_a \partial x_d} {}_\rho \mathcal{O}_{v,w}^L(\mathbf{x} - \mathbf{y}_0) dS_x \right\} {}_\rho \mathcal{M}_{v,w;J}^{W_L;i;k;\beta;l}(\mathbf{y}_0) \right. \\ & \left. + B_v e_{oce} \left\{ C_{bcad} \phi_\alpha^t \int_{S_\alpha} n_c(\mathbf{x}) \frac{\partial^2}{\partial x_d \partial x_e} {}_\rho \mathcal{O}_{v,w}^T(\mathbf{x} - \mathbf{y}_0) dS_x \right\} {}_\rho \mathcal{M}_{o,v,w;J}^{W_T;i;k;\beta;l}(\mathbf{y}_0) \right]_{s=\lambda_\beta^l}, \end{aligned} \quad (6.24)$$

where ${}_\rho \mathcal{M}_{v,w;J}^{W_L;i;k;\beta;l}$ and ${}_\rho \mathcal{M}_{o,v,w;J}^{W_T;i;k;\beta;l}$ are the scaled multipole moments with respect to P and S waves, respectively, and given by

$${}_\rho \mathcal{M}_{v,w;J}^{W_L;i;k;\beta;l}(\mathbf{y}_0) = [\mathbf{u}_h]_J^{i;k;\beta;l} \int_{\text{supp}(\phi_J)} C_{hfpq} n_f(\mathbf{y}) \left[\frac{\partial}{\partial y_p \partial y_q} {}_\rho \bar{\mathcal{F}}_{v,w}^L(\mathbf{y} - \mathbf{y}_0) \right] \phi_J(\mathbf{y}) dS_y, \quad (6.25)$$

$${}_\rho \mathcal{M}_{o,v,w;J}^{W_T;i;k;\beta;l}(\mathbf{y}_0) = [\mathbf{u}_h]_J^{i;k;\beta;l} \int_{\text{supp}(\phi_J)} e_{oup} C_{hfpq} n_f(\mathbf{y}) \left[\frac{\partial}{\partial y_q \partial y_u} {}_\rho \bar{\mathcal{F}}_{v,w}^T(\mathbf{y} - \mathbf{y}_0) \right] \phi_J(\mathbf{y}) dS_y. \quad (6.26)$$

Note that the double integrals with respect to \mathbf{x} and \mathbf{y} are separated, and therefore, far-field contributions can be rapidly evaluated using the FMM. The same translation theorems as $U_{b;\alpha\gamma}^{i;k;\beta;l}$ and $T_{b;\alpha\gamma}^{i;k;\beta;l}$ in Chapter 3 can be used for M2M, M2L, and L2L calculations.

However, the modified fast multipole algorithm for the Galerkin BEM (see Chapter 3 in [101]), has to be taken in order to ensure the following two identities because we canceled some terms in the regularization procedure from Eq. (6.11) to Eq. (6.12) using Eq. (6.3) and $\psi^u = 0$ on ∂S .

$$\begin{aligned} & \int_{\text{supp}(\psi_I^u)} \psi_I^u(\mathbf{x}) \text{p.f.} \int_{\text{supp}(\phi_J^u)} \hat{W}_{bj}(\mathbf{x}, \mathbf{y}, s) \phi_J^u(\mathbf{y}) dS_y dS_x \\ &= \int_{\text{supp}(\psi_I^u)} e_{acm} n_a(\mathbf{x}) \frac{\partial \psi_I^u(\mathbf{x})}{\partial x_c} \\ & \quad \times \int_{\text{supp}(\phi_J^u)} e_{kqt} n_k(\mathbf{y}) \frac{\partial \phi_J^u(\mathbf{y})}{\partial y_q} e_{bds} e_{jpn} \frac{\partial}{\partial x_d} \frac{\partial}{\partial y_p} \hat{\Phi}_{msnt}(\mathbf{x}, \mathbf{y}, s) dS_y dS_x \\ & \quad + \int_{\text{supp}(\psi_I^u)} \psi_I^u(\mathbf{x}) n_a(\mathbf{x}) \int_{\text{supp}(\phi_J^u)} \hat{\Psi}_{abjk}(\mathbf{x}, \mathbf{y}, s) \phi_J^u(\mathbf{y}) n_k(\mathbf{y}) dS_y dS_x, \end{aligned} \quad (6.27)$$

$$\begin{aligned} & \phi_\alpha^t \int_{S_\alpha} \text{p.f.} \int_{\text{supp}(\phi_J^u)} \hat{W}_{bj}(\mathbf{x}, \mathbf{y}, s) \phi_J^u(\mathbf{y}) dS_y dS_x \\ &= -\phi_\alpha^t \int_{\partial S_\alpha} \int_{\text{supp}(\phi_J^u)} e_{kqt} n_k(\mathbf{y}) \frac{\partial \phi_J^u(\mathbf{y})}{\partial y_q} e_{bds} e_{jpn} \frac{\partial}{\partial x_d} \frac{\partial}{\partial y_p} \hat{\Phi}_{msnt}(\mathbf{x}, \mathbf{y}, s) dS_y dx_m \\ & \quad + \phi_\alpha^t \int_{S_\alpha} n_a(\mathbf{x}) \int_{\text{supp}(\phi_J^u)} \hat{\Psi}_{abjk}(\mathbf{x}, \mathbf{y}, s) \phi_J^u(\mathbf{y}) n_k(\mathbf{y}) dS_y dS_x. \end{aligned} \quad (6.28)$$

Eq. (6.27) holds if ψ_I^u and ϕ_J^u are equal to zero at the edges of $\text{supp}(\psi_I^u)$ and $\text{supp}(\phi_J^u)$, respectively. Therefore, a set of multipole moments corresponding to ϕ_J^u is calculated for one \mathbf{y}_0 as shown in Fig. 6.4 (a). The coefficients of local expansion have to be calculated in a similar way. Then, the far-field contributions can be evaluated by using the fast multipole algorithm. Correspondingly to this fast multipole algorithm, the near-field contributions have to be evaluated as node to node. Similarly, Eq. (6.28) holds if $\phi_J^u = 0$ at the edges of $\text{supp}(\phi_J^u)$. Also in this case, a set of multipole moments corresponding to ϕ_J^u has to be calculated for one \mathbf{y}_0 as shown in Fig. 6.4 (b). As a result, the near-field contributions have to be evaluated as node to element. Taking into account these calculation ways and two identities (6.27) and (6.28), the counterpart of direct matrix-vector product can be evaluated by using the FMM. Other numerical procedures of CQ-FMBEM are same as the ones in Chapter 3.

6.6. Nonlinear boundary conditions and numerical procedure

The nonlinear boundary conditions and numerical procedure are briefly summarized in this section. In order to simultaneously solve discretized BIEs (6.13) and (6.14), the appropriate boundary conditions should be selected at each time step. We consider three types of state in a similar way to Section 4.2.1. The boundary conditions for separation, stick, and slip states are summarized as

6. 3-D Simulation of Nonlinear Ultrasonic Waves Due to Interior Cracks

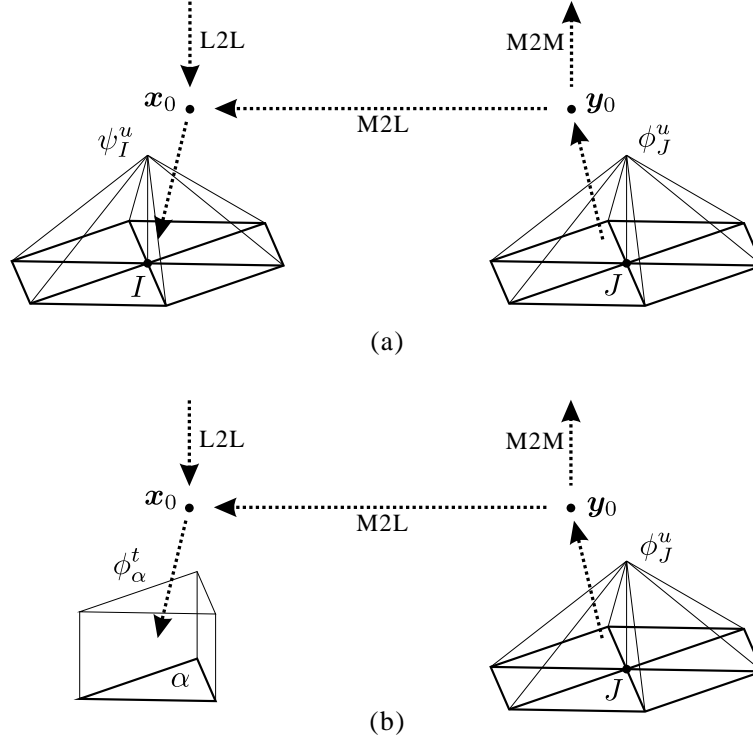


Figure 6.4.: Schematic of potential calculation to ensure (a) Eq. (6.27) and (b) Eq. (6.28).

follows:

$$\begin{cases} t = 0 & : \text{separation,} & (6.29a) \\ [u] \cdot n = u_g, \quad [\dot{u}_s] = 0 & : \text{stick,} & (6.29b) \\ [u] \cdot n = u_g, \quad t_s = \mu_d (t \cdot n) \frac{[\dot{u}_s]}{[\dot{u}_s]} & : \text{slip,} & (6.29c) \end{cases}$$

where the vectors with the subscript s indicate the ones which consist of the tangential components to the crack face. The transition conditions for the iterative calculation are also summarized as follows:

$$\begin{cases} [u] \cdot n \geq u_g & : \text{separation} \rightarrow \text{stick,} & (6.30a) \\ t \cdot n > 0 & : \text{stick or slip} \rightarrow \text{separation,} & (6.30b) \\ |t_s| \geq \mu_s |t \cdot n| & : \text{stick} \rightarrow \text{slip,} & (6.30c) \\ \frac{[\dot{u}_s] \cdot [\dot{u}_s]^{\text{prev}}}{|[\dot{u}_s]| |[\dot{u}_s]^{\text{prev}}|} < \cos(\theta^{\text{stop}}) & : \text{slip} \rightarrow \text{stick,} & (6.30d) \end{cases}$$

where θ^{stop} is given by 90° . If the left inequalities in Eq. (6.30) are satisfied, the corresponding right transition occurs.

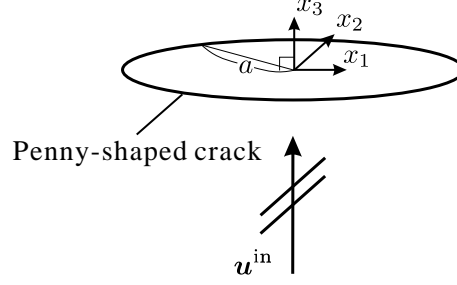


Figure 6.5.: A penny-shaped crack with radius a subjected to an incident plane P wave.

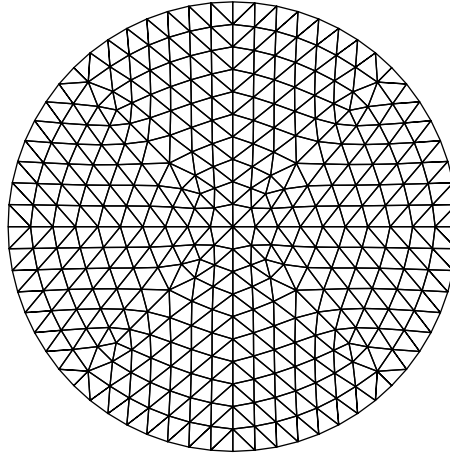


Figure 6.6.: Mesh structure of a penny-shaped crack when $M_e = 656$ and $M_d = 361$.

Using boundary conditions (6.29), discretized BIEs (6.13) and (6.14) can be simultaneously solved. The iterative algorithm is similar to the case of interface crack of bi-material in Section 4.3. In addition, discretized BIEs (6.13) and (6.14) are modified for the velocity of COD tangential to the crack face as well as Section 4.2.2.

6.7. Numerical results

In this section, numerical results of the proposed CQ-FMBEM for 3-D crack problems are presented. First, the linear problem is numerically solved in order to verify the accuracy and to demonstrate the computational efficiency. Second, the higher-harmonic simulation is carried out to validate the contact model of crack faces. Finally, numerical results of sub-harmonic generation due to cracks in an infinite domain are shown and compared with the ones for the 2-D case.

6.7.1. Linear problem

In advance of the nonlinear ultrasonic simulation, the numerical results for the traction-free crack are shown. The time histories of COD and SIF are computed for the accuracy verification when a

6. 3-D Simulation of Nonlinear Ultrasonic Waves Due to Interior Cracks

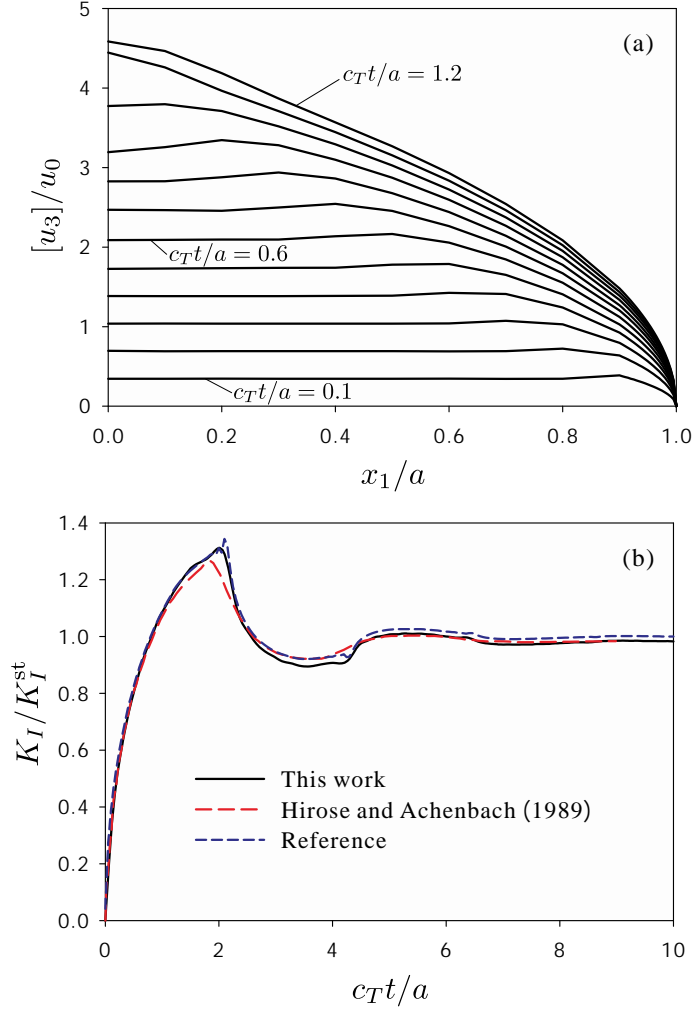


Figure 6.7.: (a) Vertical COD at each several time-steps and (b) time variations of normalized dynamic SIF when a penny-shaped crack is subjected to normal incidence of plane P wave.

penny-shaped crack is subjected to normal incidence of plane P wave as depicted in Fig. 6.5. The incident plane P wave is given by

$$u_i^{\text{in}}(\mathbf{x}, t) = -u_0 \delta_{i3} \frac{c_L t - x_3}{a} H(c_L t - x_3). \quad (6.31)$$

The crack surface is divided into 656 flatly triangular elements as depicted in Fig. 6.6, and time increment Δt is given by $c_T \Delta t/a = 0.1$. Poisson's ratio of base material ν is given by $\nu = 0.25$ in order to compare with reference solutions, and the CQ-FMBEM with RK3 is used here.

Vertical COD at several time steps on the positive part of x_1 -axis is shown in Fig. 6.7 (a). The vertical COD at $x_1/a = 0.0$ is constantly raised until about $c_T t/a = 0.6$ because the diffracted P wave arrives at about $c_T t/a = 0.58$. From $c_T t/a = 0.9$ to 1.2, the behavior of COD around the

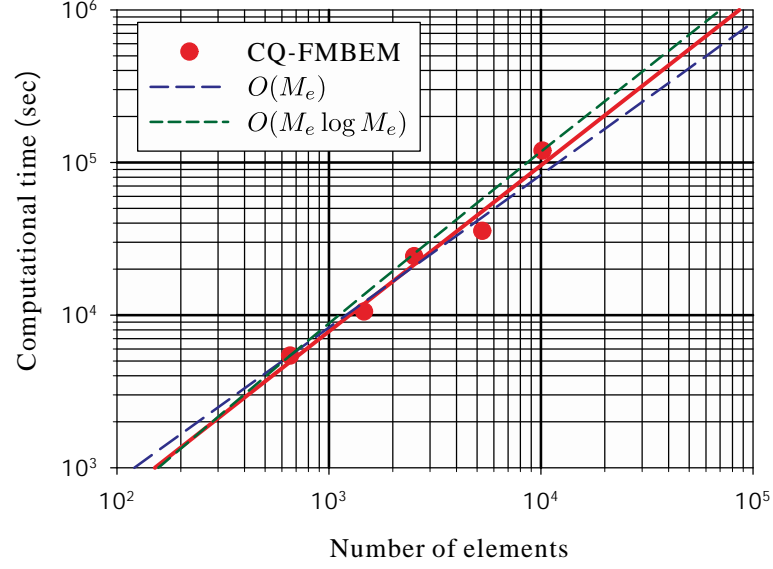


Figure 6.8.: Computational time of CQ-FMBEM using RK3 for 3-D crack problems varying the number of elements M_e when $N = 128$.

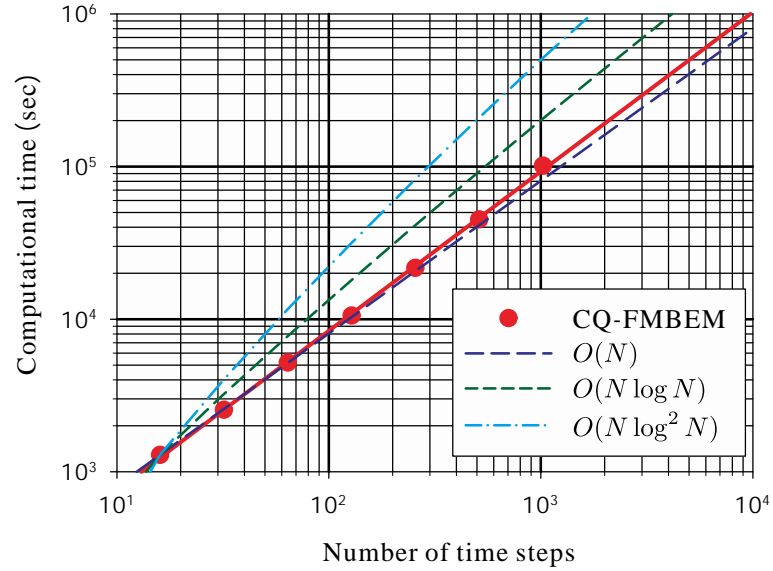


Figure 6.9.: Computational time of CQ-FMBEM using RK3 for 3-D crack problems varying the number of time steps N when $M_e = 1464$.

center of the crack is greatly different from an early time due to diffracted surface waves.

Next, the dynamic SIF of mode I is computed by the present method. According to [84], the dynamic SIF corresponding to mode I can be calculated by

$$K_I(t) = -\frac{\mu\sqrt{2\pi}}{4(1-\nu)} \lim_{\varepsilon \rightarrow 0} \frac{1}{\sqrt{\varepsilon}} [\mathbf{u}](\varepsilon, t) \cdot \mathbf{n}(\varepsilon), \quad (6.32)$$

6. 3-D Simulation of Nonlinear Ultrasonic Waves Due to Interior Cracks

where ε indicates the distance from the crack front. We normalize the dynamic SIF using the exact solution of static problems $K_I^{\text{st}} = 2\sigma_{33}\sqrt{a/\pi}$. The time history of dynamic SIF is presented in Fig. 6.7 (b). The solutions obtained by Hirose and Achenbach [35] are plotted in the same figure for comparison. They have used the conventional TD-BEM in which the collocation method is used for time and spatial discretization. On the other hand, this problem in frequency-domain can be come to a Fredholm integral equation of the second kind using the axisymmetric property, and it has been numerically solved by Rahman [68]. The transient solutions constructed by the inverse Fourier transform, which are called the "reference solutions", are also presented in Fig. 6.7 (b). The reference solutions have slight oscillation at about $c_T t/a = 2.1$ and 4.3 , when the waveform is rapidly fluctuated. However, the reference solutions are considered as most accurate in Fig. 6.7 (b). The behavior of solutions obtained by the proposed method and Hirose and Achenbach are very similar and both solutions converge to the static solution. At about $c_T t/a = 2.1$ and 4.3 , the solutions obtained by the proposed method seem to be more accurate.

The computational efficiency of the proposed method is confirmed by solving the same problem for different N and M_e . The computational time varying the number of elements M_e is shown in Fig. 6.8 when $N = 128$. The solid line in the figure indicates the regression one of numerical results. As shown in Fig. 6.8, the computational complexity for M_e seems to be about $O(M_e \log M_e)$. On the other hand, the computational time varying the number of time steps N is shown in Fig. 6.9 when $M_e = 1464$. When about $N < 200$, the computational complexity seems to be $O(N)$. However, the order of computational time seems to be $O(N \log N)$ for comparatively large N . This is because calculation of the influence functions for near-field contribution is most time-consuming with small N , and its complexity is $O(NM_e)$. Consequently, it seems that the total computational complexity of the proposed method is about $O(NM_e \log N \log M_e)$.

6.7.2. Higher-harmonic simulation

In order to validate the contact model of crack faces for 3-D problems, the numerical results of higher-harmonic simulation are presented here. Hereinafter, the CQ-FMBEM with RK2 is used for all nonlinear ultrasonic simulations. The analysis model in Fig. 6.5 is also used for this simulation, and we confirm that our model can reproduce the clapping motion and friction on crack faces similarly to the 2-D case in Section 5.5.2. The following sinusoidal burst wave with n^{in} cycles is used as the incident wave for the nonlinear ultrasonic simulation.

$$\begin{cases} \mathbf{u}^{\text{in}}(\mathbf{x}, t) = u_0 \mathbf{d}_\varphi \sin(2\pi\Lambda_\varphi) H(\Lambda_\varphi) H(n^{\text{in}} - \Lambda_\varphi), \\ \Lambda_\varphi = f^{\text{in}} \left(t - \frac{\mathbf{p} \cdot (\mathbf{x} - \boldsymbol{\chi})}{c_\varphi} \right). \end{cases} \quad (6.33a)$$

$$\quad (6.33b)$$

We assume that $\mathbf{d}_{TH} = (0, 1, 0)$ and $\mathbf{d}_{TV} = \mathbf{d}_{TH} \times \mathbf{p}$. The far-field approximation of scattered wave (see Appendix B) is used for the spectrum analysis. The time increment is taken as $f^{\text{in}}\Delta t = 0.05$, and Poisson's ratio of base material is given by $\nu = 0.3$ supposing steel. The friction coefficients are thus given by the top row of Table 4.2. n^{in} is given by $n^{\text{in}} = 15$ here.

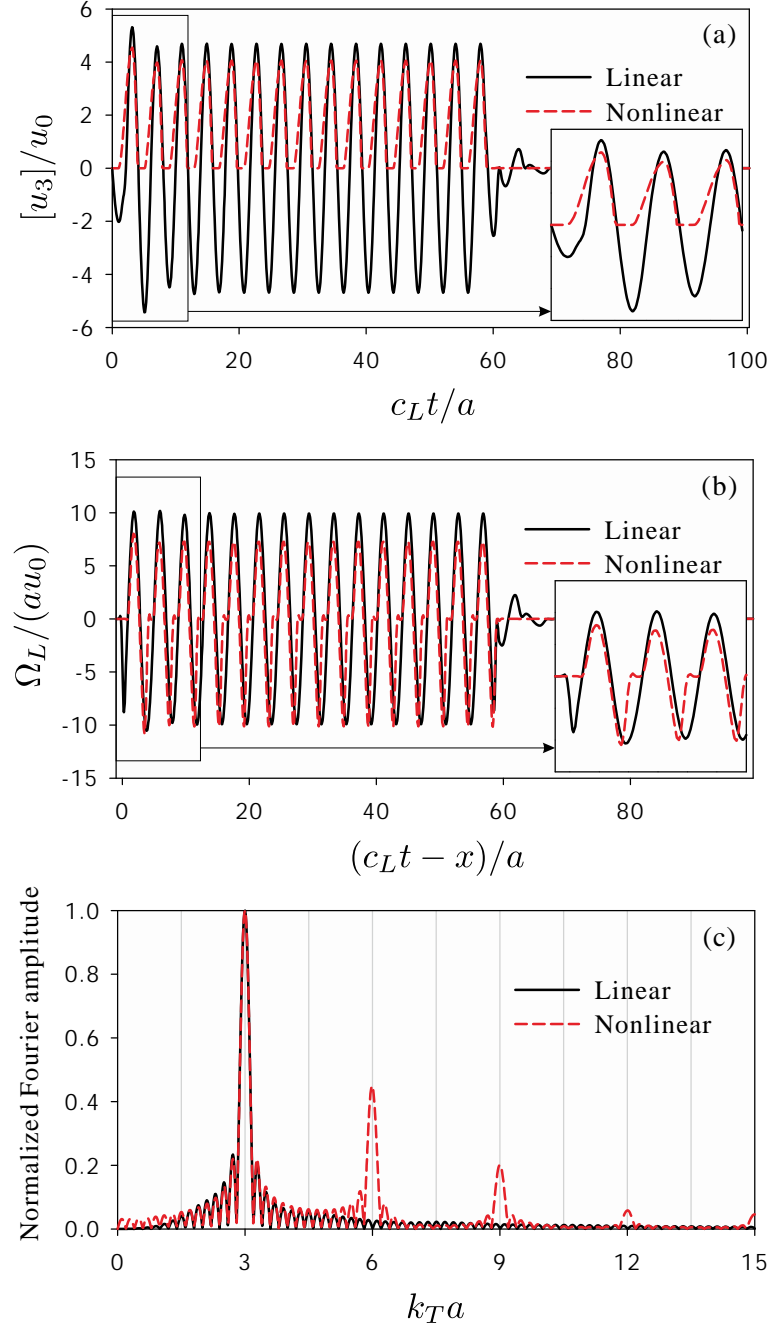


Figure 6.10.: Time variations of (a) COD at the center point of a crack and (b) far-field amplitude of backscattered P wave when a penny-shaped crack is subjected to an incident plane P wave. (c) is normalized frequency spectrum of far-field amplitude.

First, numerical results of P wave incidence are presented when $\theta^{\text{in}} = 0^\circ$, $k_T a = 3.0$, and $u_g/u_0 = 0.0$. Time histories of vertical COD at the center point of a crack are shown in Fig. 6.10 (a). Time histories and normalized frequency spectra of far-field amplitude of backscattered P wave are also presented in Fig. 6.10 (b), and (c), respectively. As shown in Fig. 6.10 (a), the vertical COD

6. 3-D Simulation of Nonlinear Ultrasonic Waves Due to Interior Cracks

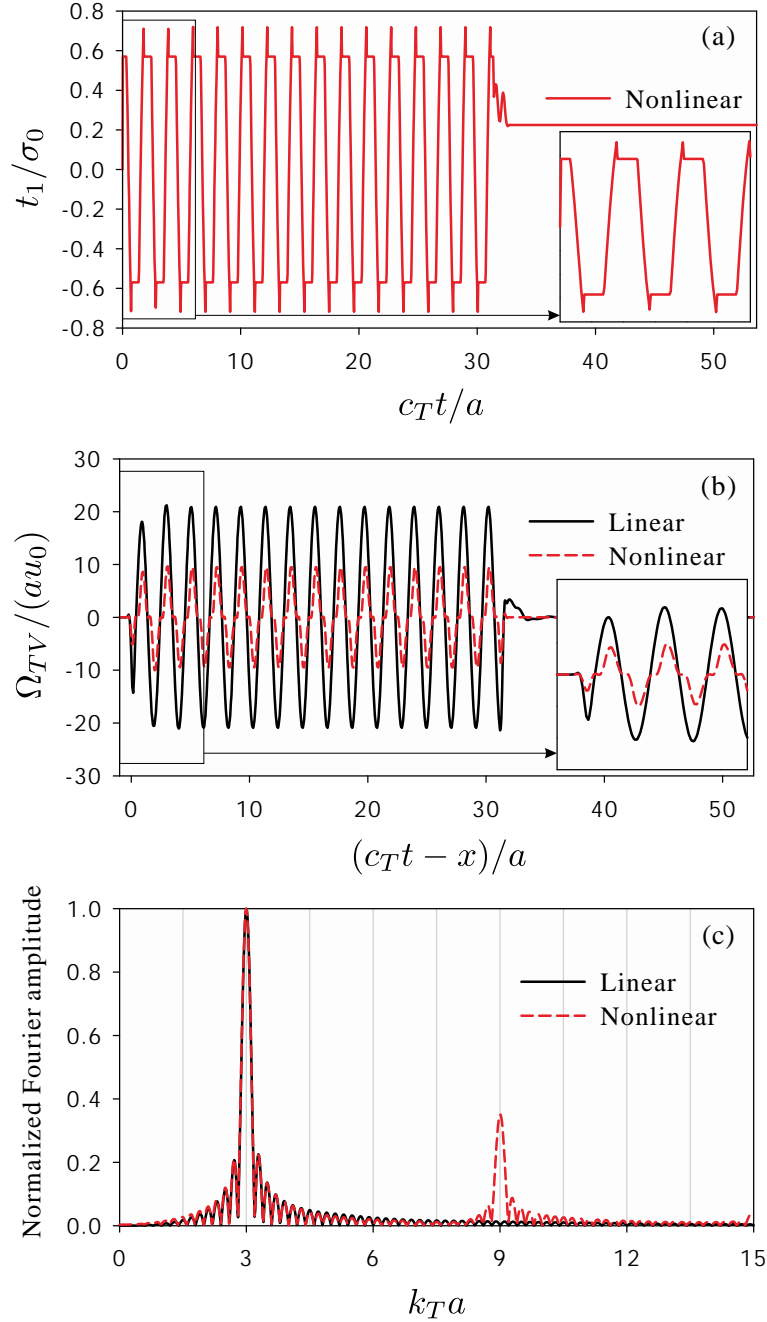


Figure 6.11.: Time variations of (a) tangential traction at the center point of a crack and (b) far-field amplitude of backscattered SV wave when a penny-shaped crack is subjected to an incident plane SV wave, and $\sigma^{\text{st}}/\sigma_0 = 1.0$. (c) is normalized frequency spectrum of far-field amplitude.

in the nonlinear case cannot take negative values due to contact conditions. From Fig. 6.10 (b), the waveform of $\Omega_L/(au_0)$ is distorted by the clapping motion. Therefore, the frequency spectrum of $\Omega_L/(au_0)$ in the nonlinear case contains higher-harmonic components as shown in Fig. 6.10 (c).

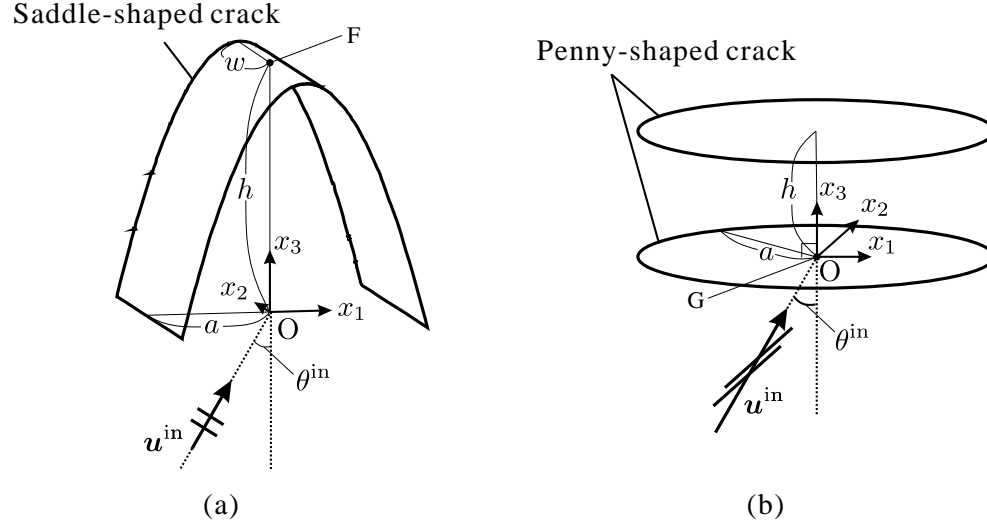


Figure 6.12.: Elastic wave scattering by (a) a saddle-shaped crack and (b) two penny-shaped cracks arranged in parallel.

Also in the 3-D case, it is confirmed that all (2nd, 3rd, 4th, etc.) orders of higher-harmonic waves are generated.

Second, numerical results of SV wave incidence are presented when $\theta^{\text{in}} = 0^\circ$, $k_T a = 3.0$, and $u_g/u_0 = 0.0$. In this case, the static compressive stress σ^{st} has a positive value over a crack uniformly in order to generate the dynamic friction force. σ^{st} is given by $\sigma^{\text{st}}/\sigma_0 = 1.0$ here. Time histories of tangential traction at the center point of a crack are shown in Fig. 6.11 (a). Time histories and normalized frequency spectra of far-field amplitude of backscattered SV wave are also presented in Fig. 6.11 (b), and (c), respectively. As shown in Fig. 6.11 (a), the tangential traction becomes similar to square wave due to dynamic friction force, and its amplitude corresponds to the dynamic friction coefficient μ_d . From Fig. 6.11 (b), the waveform of $\Omega_{TV}/(au_0)$ is distorted due to the friction force, and the amplitude is smaller than the linear one. Therefore, the 3rd higher-harmonic component is contained in the nonlinear case as shown in Fig. 6.11 (c). It is known that odd order of higher-harmonic waves are generated due to pure shear motion with contact [89], and that is also reproduced. From the above, we can confirm that the presented numerical method can accurately simulate the clapping motion and dynamic friction on crack faces.

6.7.3. Sub-harmonic simulation

In order to confirm that the sub-harmonic generation can be caused in the 3-D model, we present some numerical results in this section. The similar models to the ones in Section 5.5.3 is used for the 3-D sub-harmonic simulation. Therefore, a saddle-shaped crack and two penny-shaped cracks arranged in parallel in an infinite elastic solid depicted in Fig. 6.12 are considered as the analysis models. The time increment is taken as $f^{\text{in}} \Delta t = 0.05$, and the material constants are same as the higher-harmonic simulation in the previous section. The incident plane wave is assumed to be P

6. 3-D Simulation of Nonlinear Ultrasonic Waves Due to Interior Cracks

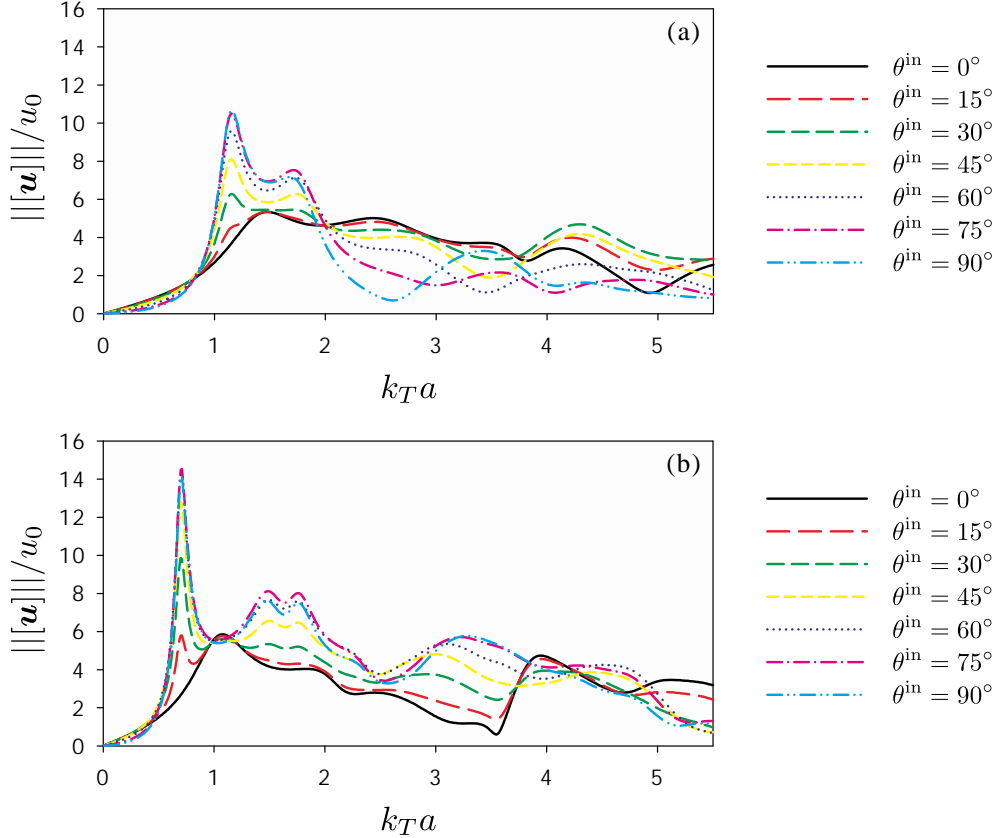


Figure 6.13.: Frequency responses for the model in Fig. 6.12 (a) using the frequency-domain BEM and assuming that crack faces are always separated. The norm $||[u]||/u_0$ at point F in Fig. 6.12 (a) for various θ^{in} and $k_T a$ is plotted when (a) $w/a = 1.0$ and (b) 2.0 .

wave, and $\varphi = L$ in Eq. (6.33).

Sub-harmonic generation by a saddle-shaped crack

First, we presented numerical results of wave scattering by a saddle-shaped crack in an infinite elastic solid as depicted in Fig. 6.12 (a). In the 2-D simulation, the nonlinear torsional vibration is caused at the inner part of a curved crack, and sub-harmonic waves are generated under certain conditions as presented in Section 5.5.3. Therefore, the similar model with finite width w in 3-D is considered. Only the cases that $h/a = 2.0$ and $\theta^{\text{in}} = 60^\circ$ are presented here because sub-harmonic waves are generated in a comparatively wide range of $k_T a$ and u_g/u_0 in the 2-D case as shown in Fig. 5.16.

In advance of the sub-harmonic simulation, the frequency response analysis varying w/a is conducted in order to predict the probability of sub-harmonic generation. The norm $||[u]||/u_0$ at point F in Fig. 6.12 (a) for various $k_T a$ and θ^{in} is plotted in Fig. 6.13. From Fig. 6.13 (a), the peak of $||[u]||/u_0$ is located at about $k_T a = 1.2$ in the case that $w/a = 1.0$. As shown in Fig. 6.13 (b), the results in the case that $w/a = 2.0$ are similar to the 2-D ones in Fig. 5.31 (e), and the peak

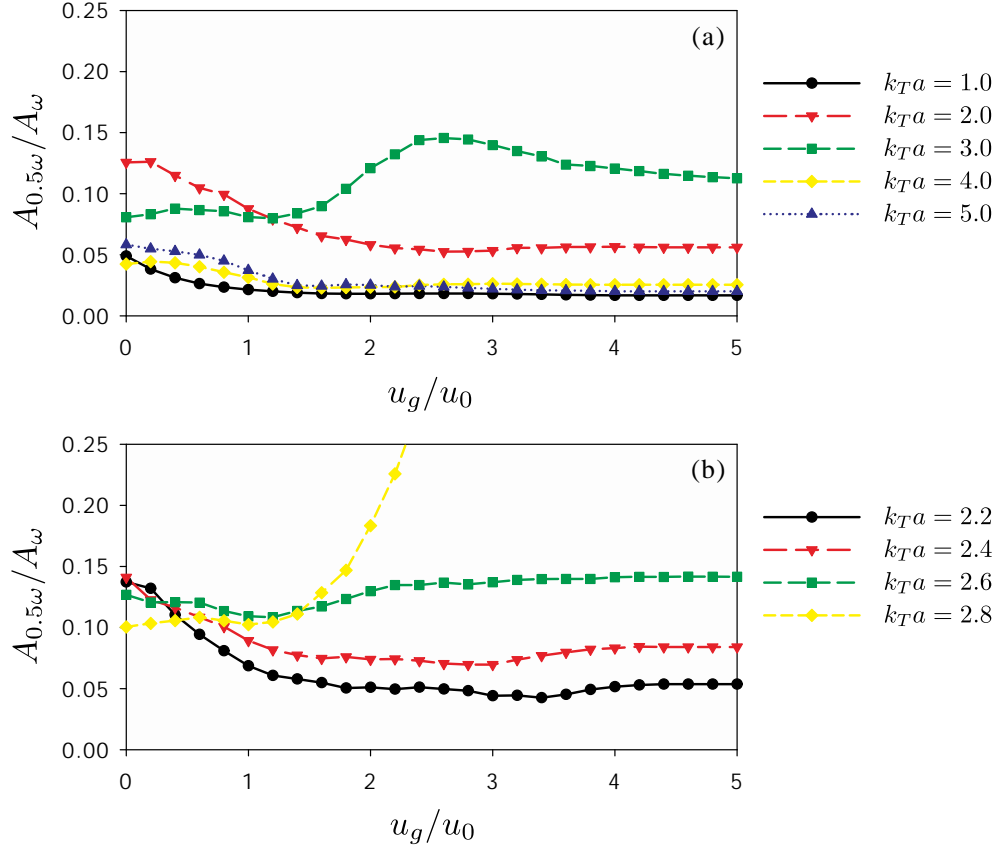


Figure 6.14.: Fourier amplitude ratio of sub-harmonic frequency to fundamental one for various pre-opening displacement u_g/u_0 when a saddle-shaped crack is subjected to an incident plane P wave ($w/a = 1.0$, $\theta^{\text{in}} = 60^\circ$, and $n^{\text{in}} = 15$).

of $||[\mathbf{u}]||/u_0$ is located at about $k_T a = 0.7$. Comparing Fig. 6.13 (a) and (b), $||[\mathbf{u}]||/u_0$ is more gentle in the case that $w/a = 1.0$ than $w/a = 2.0$. Therefore, it is expected that the sub-harmonic generation occurs in the case that $w/a = 2.0$ similarly to the 2-D case although that may be not caused in the case that $w/a = 1.0$.

It is difficult to conduct the same number of numerical simulations as the 2-D case because of the computational cost for the 3-D simulation. Therefore, we present numerical results varying the pre-opening displacement u_g/u_0 for several center wavenumbers of the incident wave $k_T a$. $A_{0.5\omega}/A_\omega$ for various u_g/u_0 in the case that $w/a = 1.0$ is presented in Fig. 6.14. $k_T a$ is changed from 1.0 to 5.0 with increments of 1.0 in Fig. 6.14 (a), and we could not confirm the sub-harmonic generation. According to the tendency of the 2-D results in Section 5.5.3, the sub-harmonic generation occurs at $k_T a$ which is a little larger than the double of the first peak of frequency response. In this case, the first peak of frequency response is located at about $k_T a = 1.2$, so that $k_T a$ is changed from 2.2 to 2.8 with fine increments in Fig. 6.14 (b). Although we could not find the sub-harmonic generation here, $A_{0.5\omega}/A_\omega$ in the case that $k_T a = 2.8$ becomes very large as shown in Fig. 6.14 (b). Therefore, $A_{0.5\omega}/A_\omega$ only in this case is plotted in Fig. 6.15 with a different vertical axis. The maximum value

6. 3-D Simulation of Nonlinear Ultrasonic Waves Due to Interior Cracks

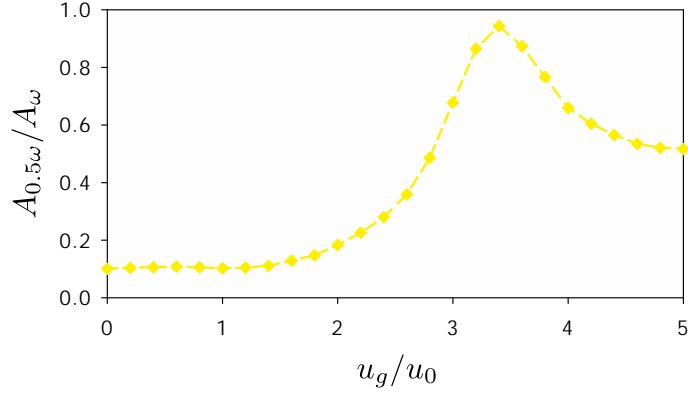


Figure 6.15.: Fourier amplitude ratio of sub-harmonic frequency to fundamental one for various pre-opening displacement u_g/u_0 when a saddle-shaped crack is subjected to an incident plane P wave ($k_T a = 2.8$, $w/a = 1.0$, $\theta^{\text{in}} = 60^\circ$, and $n^{\text{in}} = 15$).

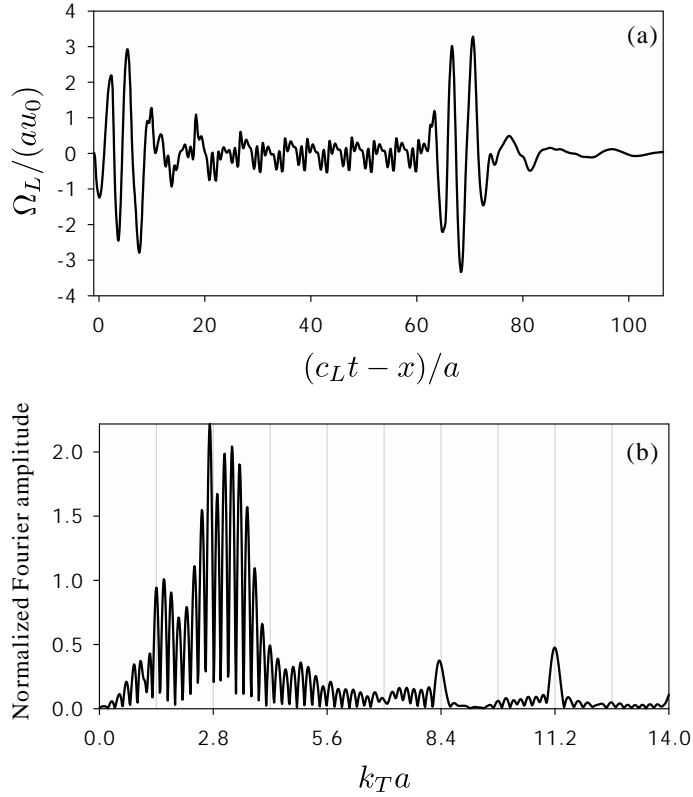


Figure 6.16.: (a) Time variation and (b) normalized frequency spectrum of far-field amplitude of backscattered P wave when a saddle-shaped crack is subjected to an incident plane P wave ($k_T a = 2.8$, $u_g/u_0 = 3.4$, $w/a = 1.0$, $\theta^{\text{in}} = 60^\circ$, and $n^{\text{in}} = 15$).

of $A_{0.5\omega}/A_{\omega}$ is about 0.95 as we can see from Fig. 6.15. In order to investigate what happened here, the time history and frequency spectrum of far-field amplitude of backscattered P wave are shown

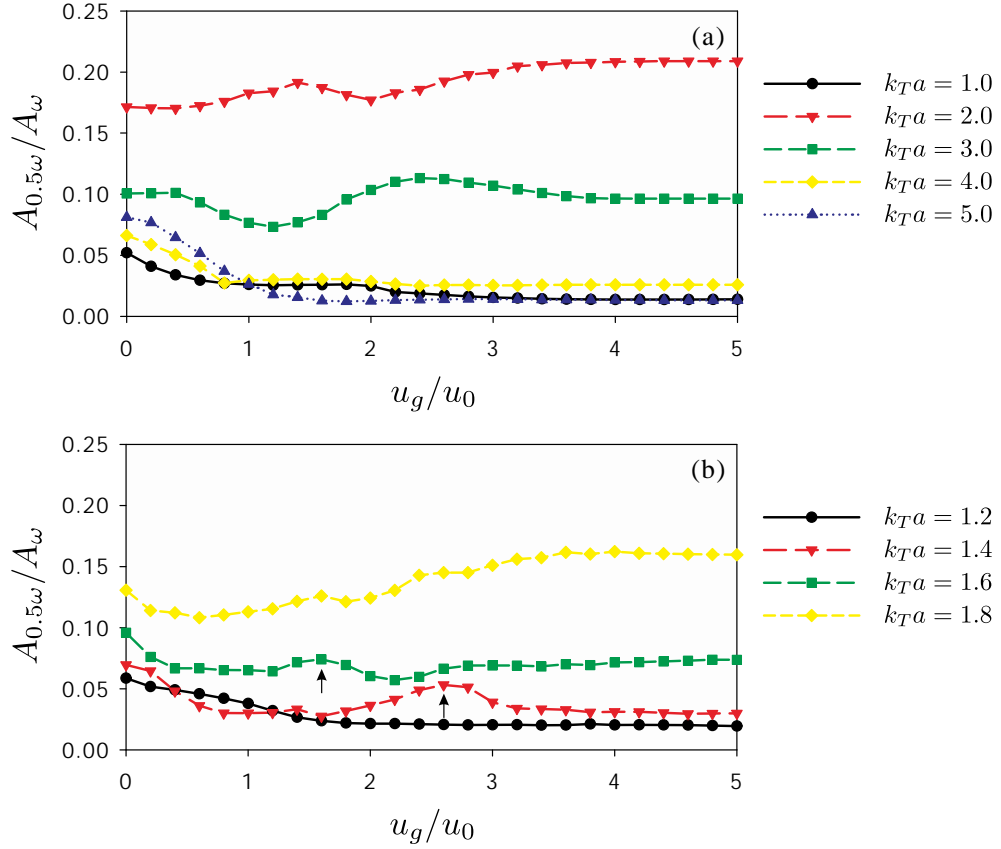


Figure 6.17.: Fourier amplitude ratio of sub-harmonic frequency to fundamental one for various pre-opening displacement u_g/u_0 when a saddle-shaped crack is subjected to an incident plane P wave ($w/a = 2.0$, $\theta^{\text{in}} = 60^\circ$, and $n^{\text{in}} = 15$).

in Fig. 6.16 when $k_T a = 2.8$, $u_g/u_0 = 3.4$. The frequency spectrum is normalized by A_{ω} . From Fig. 6.16 (a), the waveform of $\Omega_L/(au_0)$ is strongly distorted, and the amplitude is very small in the middle. The frequency spectrum is also distorted, and the peak is unstable and shifted as shown in Fig. 6.16 (b). As a result, A_{ω} is small, and $A_{0.5\omega}/A_{\omega}$ becomes large.

Next, $A_{0.5\omega}/A_{\omega}$ for various u_g/u_0 in the case that $w/a = 2.0$ is presented in Fig. 6.17. In Fig. 6.17 (a), $k_T a$ is changed from 1.0 to 5.0 with increments of 1.0, and we could not confirm the sub-harmonic generation from these cases. The first peak of frequency response is located at about $k_T a = 0.7$, and therefore, $k_T a$ is changed from 1.2 to 1.8 with fine increments in Fig. 6.17 (b). There are two slight peaks at around $k_T a = 1.2$ and $u_g/u_0 = 2.6$, and $k_T a = 1.4$ and $u_g/u_0 = 1.6$ as indicated by arrows, and we can confirm the sub-harmonic generation under these conditions. For instance of the sub-harmonic generation, the time history and normalized frequency spectrum of far-field amplitude of backscattered P wave are shown in Fig. 6.18 when $k_T a = 1.4$ and $u_g/u_0 = 2.6$. As shown in Fig. 6.18, the large and small amplitude is periodically repeated, and the slight peak of $A_{0.5\omega}/A_{\omega}$ is confirmed. However, they are not clear because $n^{\text{in}} = 15$. In order to show more clear sub-harmonic generation, the waveform and frequency spectrum in the case that $n^{\text{in}} = 30$ are

6. 3-D Simulation of Nonlinear Ultrasonic Waves Due to Interior Cracks

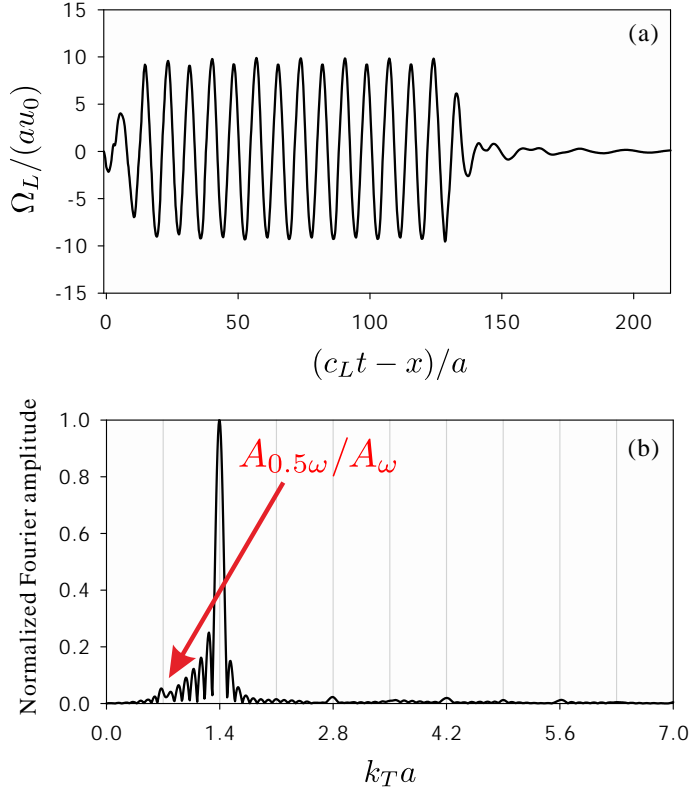


Figure 6.18.: (a) Time variation and (b) normalized frequency spectrum of far-field amplitude of backscattered P wave when a saddle-shaped crack is subjected to an incident plane P wave ($k_T a = 1.4$, $u_g/u_0 = 2.6$, $w/a = 2.0$, $\theta^{\text{in}} = 60^\circ$, and $n^{\text{in}} = 15$).

presented in Fig. 6.19. It can be confirmed from Fig. 6.19 (a) that the waveform becomes stable in the state that large and small amplitude is repeated periodically. The more clear peak of $A_{0.5\omega}/A_\omega$ can be seen in Fig. 6.19 (b) than in Fig. 6.18 (b). $A_{0.5\omega}/A_\omega$ in this case is much smaller than that in the 2-D case. However, it is expected that $A_{0.5\omega}/A_\omega$ becomes large as w/a increases because the case that $w/a \rightarrow \infty$ is equivalent to the 2-D one. The sub-harmonic generation can be caused for the model in Fig. 6.12 (a) with sufficiently large w/a .

Sub-harmonic generation by two penny-shaped cracks arranged in parallel

Second, we present numerical results of the wave scattering by two penny-shaped cracks arranged in parallel in an infinite elastic solid as depicted in Fig. 6.12 (b). In the 2-D simulation, the nonlinear bending vibration is caused at the part between two straight-line cracks, and sub-harmonic waves are generated under certain conditions as presented in Section 5.5.3. Therefore, it is expected that similar bending vibrations are generated in the 3-D case for the model in Fig. 6.12 (b). Only the normal incidence is considered here because the sub-harmonic waves can be observed in the 2-D case except $\theta^{\text{in}} = 90^\circ$.

In advance of the sub-harmonic simulation, the frequency response analysis varying h/a is con-

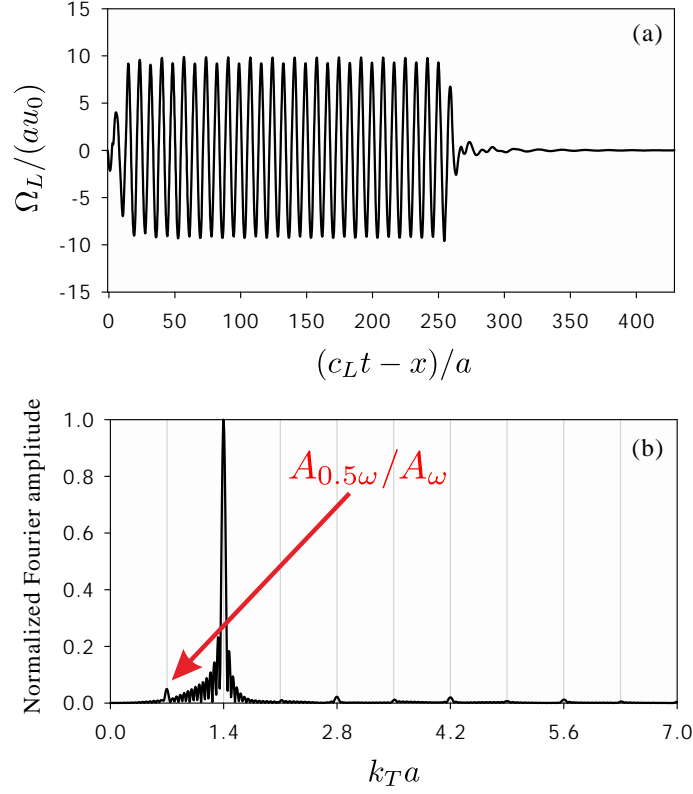


Figure 6.19.: (a) Time variation and (b) normalized frequency spectrum of far-field amplitude of backscattered P wave when a saddle-shaped crack is subjected to an incident plane P wave ($k_T a = 1.4$, $u_g/u_0 = 2.6$, $w/a = 2.0$, $\theta^{\text{in}} = 60^\circ$, and $n^{\text{in}} = 30$).

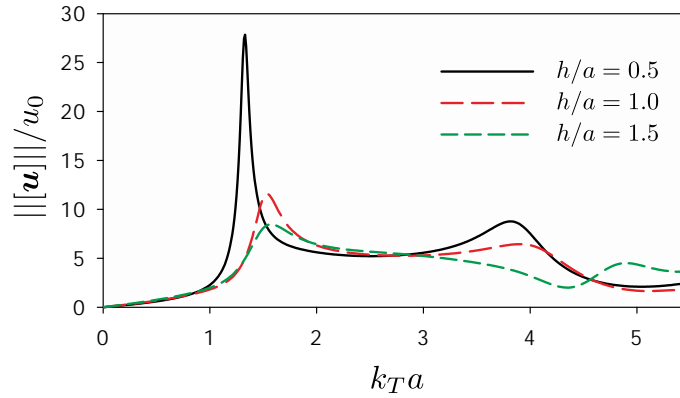


Figure 6.20.: Frequency responses for the model in Fig. 6.12 (b) using the frequency-domain BEM and assuming that crack faces are always separated. The norm $||[\mathbf{u}]||/u_0$ at point G in Fig. 6.12 (b) for various h/a and $k_T a$ is plotted when $\theta^{\text{in}} = 0^\circ$.

ducted in order to predict the probability of sub-harmonic generation. The norm $||[\mathbf{u}]||/u_0$ at point G in Fig. 6.12 (b) for various $k_T a$ is plotted in Fig. 6.20. From Fig. 6.20, the results are very similar

6. 3-D Simulation of Nonlinear Ultrasonic Waves Due to Interior Cracks

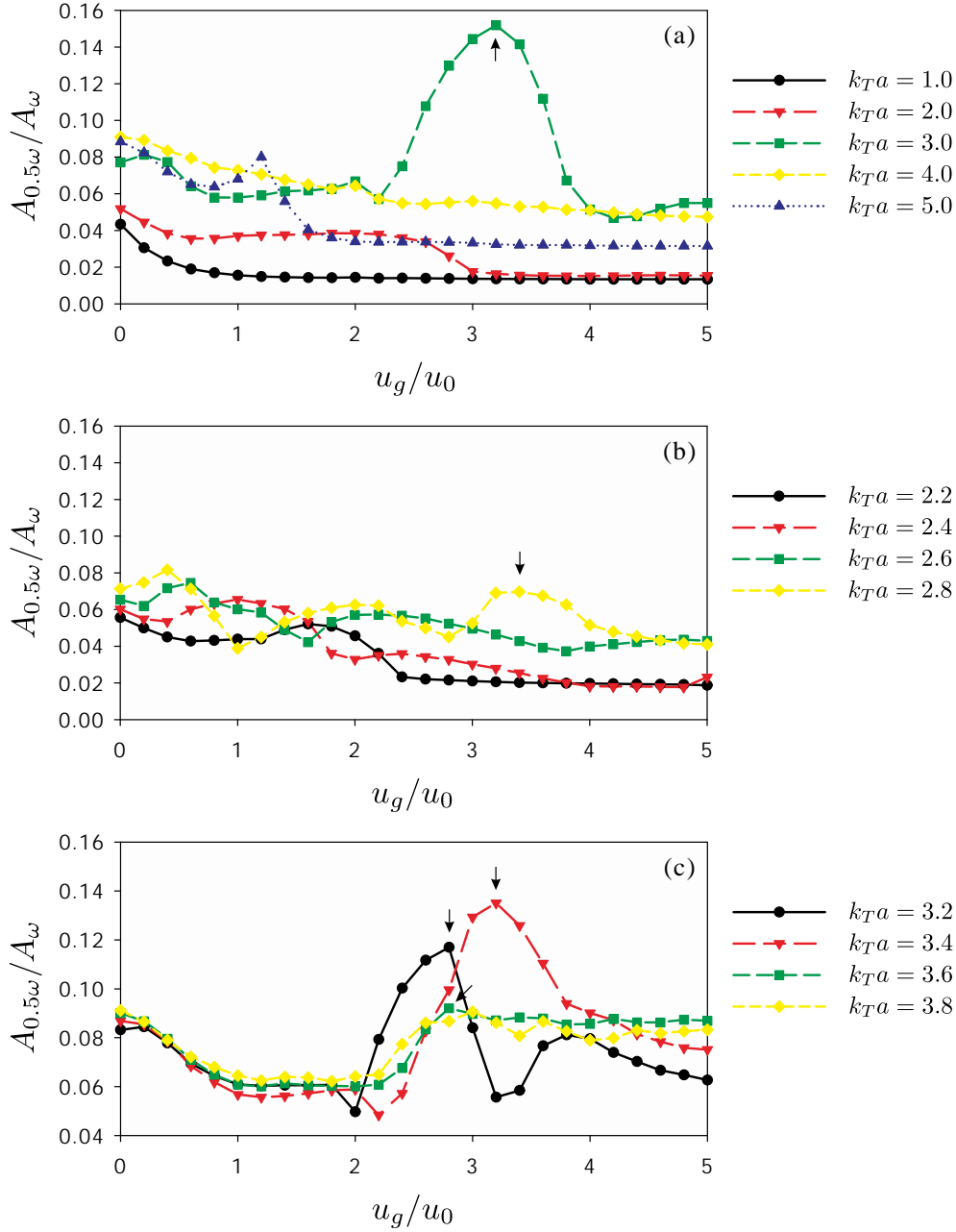


Figure 6.21.: Fourier amplitude ratio of sub-harmonic frequency to fundamental one for various pre-opening displacement u_g/u_0 when two penny-shaped cracks arranged in parallel are subjected to an incident plane P wave ($h/a = 0.5$, $\theta^{\text{in}} = 0^\circ$, and $n^{\text{in}} = 15$).

to the 2-D ones in Fig. 5.32. Therefore, it is expected that sub-harmonic waves are generated in the cases that $h/a = 0.5$ and 1.0.

$A_{0.5\omega}/A_{\omega}$ for various u_g/u_0 in the case that $h/a = 0.5$ is presented in Fig. 6.21. In Fig. 6.21 (a), $k_T a$ is changed from 1.0 to 5.0 with increments of 1.0, and a peak of $A_{0.5\omega}/A_{\omega}$ is observed around $k_T a = 3.0$ and $u_g/u_0 = 3.2$. In order to investigate the transition of $A_{0.5\omega}/A_{\omega}$ varying

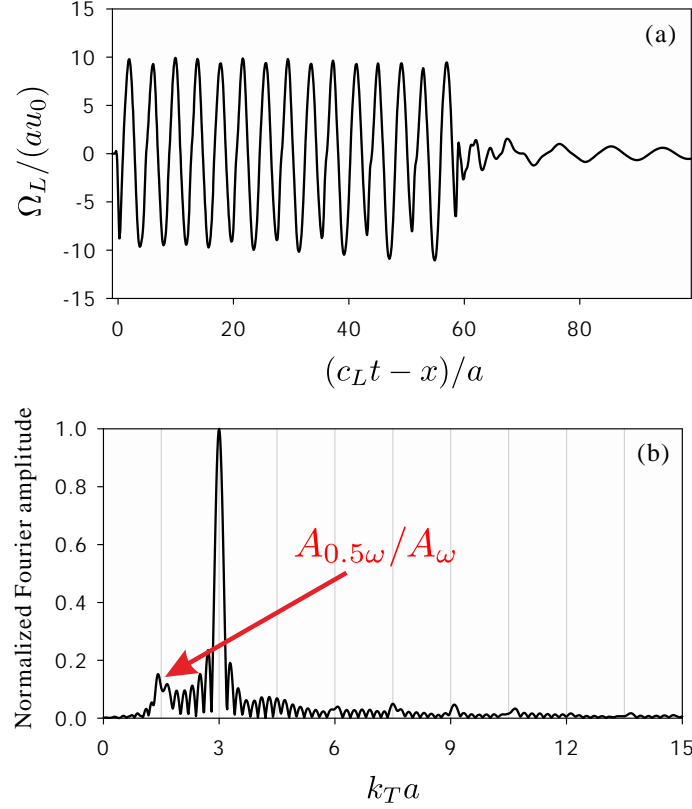


Figure 6.22.: (a) Time variation and (b) normalized frequency spectrum of far-field amplitude of backscattered P wave when two penny-shaped cracks arranged in parallel are subjected to an incident plane P wave ($k_T a = 3.0$, $u_g/u_0 = 3.2$, $h/a = 0.5$, $\theta^{\text{in}} = 0^\circ$, and $n^{\text{in}} = 15$).

$k_T a$, $A_{0.5\omega}/A_\omega$ for $k_T a = 2.2$ to 2.8 and 3.2 to 3.8 with fine increments are shown in Fig. 6.17 (b) and (c), respectively. There are several peaks of $A_{0.5\omega}/A_\omega$ in Fig. 6.17 (b) and (c), specifically around $k_T a = 2.8$ and $u_g/u_0 = 3.4$, $k_T a = 3.2$ and $u_g/u_0 = 2.8$, $k_T a = 3.4$ and $u_g/u_0 = 3.2$, and $k_T a = 3.6$ and $u_g/u_0 = 2.8$ as indicated by arrows. Under these conditions, the sub-harmonic generation can be confirmed. For instance of the sub-harmonic generation, the time history and normalized frequency spectrum of far-field amplitude of backscattered P wave are shown in Fig. 6.22 when $k_T a = 3.0$, $u_g/u_0 = 3.2$. As shown in Fig. 6.22, the large and small amplitude is periodically repeated around the last part, and the peak of $A_{0.5\omega}/A_\omega$ is confirmed. However, they are not clear because $n^{\text{in}} = 15$. In order to show more clear sub-harmonic generation, the waveform and frequency spectrum in the case that $n^{\text{in}} = 30$ are presented in Fig. 6.23. From Fig. 6.23 (a), it is confirmed that the waveform becomes stable in the state that large and small amplitude is repeated periodically. The more clear peak of $A_{0.5\omega}/A_\omega$ can be seen in Fig. 6.23 (b) than in Fig. 6.22 (b).

Next, $A_{0.5\omega}/A_\omega$ for various u_g/u_0 in the case that $h/a = 1.0$ is presented in Fig. 6.24. In Fig. 6.24 (a), $k_T a$ is changed from 1.0 to 5.0 with increments of 1.0 , and we could not confirm the sub-harmonic generation in these cases. The first peak of the frequency response is located at about

6. 3-D Simulation of Nonlinear Ultrasonic Waves Due to Interior Cracks

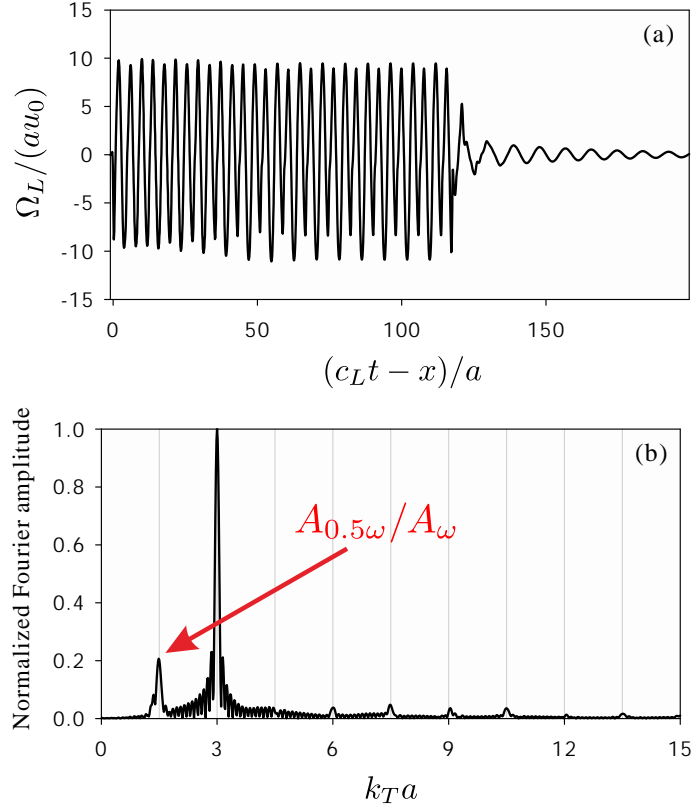


Figure 6.23.: (a) Time variation and (b) normalized frequency spectrum of far-field amplitude of backscattered P wave when two penny-shaped cracks arranged in parallel are subjected to an incident plane P wave ($k_T a = 3.0$, $u_g/u_0 = 3.2$, $h/a = 0.5$, $\theta^{\text{in}} = 0^\circ$, and $n^{\text{in}} = 30$).

$k_T a = 1.6$, and therefore, $k_T a$ is changed from 3.2 to 3.8 with fine increments in Fig. 6.24 (b). However, We could not find the sub-harmonic generation in these cases. As a result, it seems to be harder for the 3-D model in Fig. 6.12 (b) than the 2-D model in Fig. 5.11 (b) that the sub-harmonic generation is caused. This may be because the width of cracks is finite, and the effect of multiple reflection is weaker in the 3-D case than the 2-D case.

6.8. Concluding remarks

- In Chapter 6, we have successfully applied the new CQ-FMBEM to the 3-D nonlinear ultrasonic simulation for cracks in an infinite elastic solid. The validity of our proposed method was confirmed through numerical results of normal incidence of P and S waves to a penny-shaped crack. We have also succeeded in the simulation of sub-harmonic generation due to interior cracks with contact boundary conditions in 3-D.
- From numerical results for the linear problem, the accuracy and efficiency of the CQ-FMBEM for crack problems were confirmed. The computational complexity of the CQ-FMBEM is

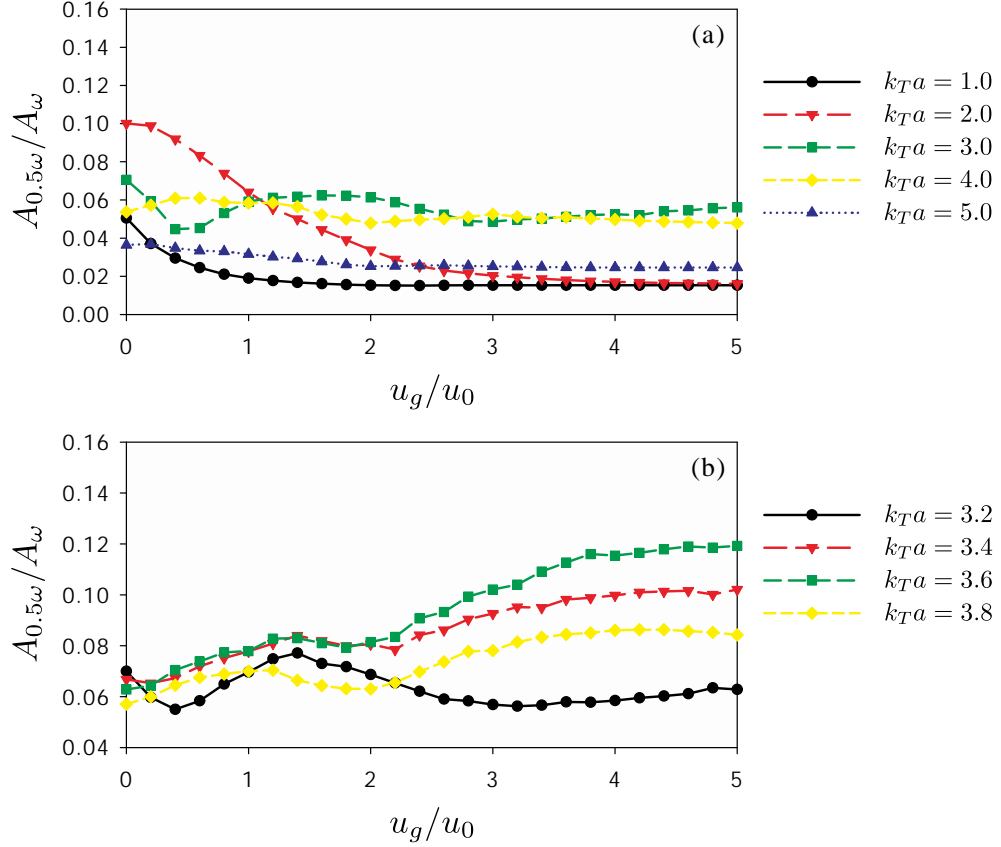


Figure 6.24.: Fourier amplitude ratio of sub-harmonic frequency to fundamental one for various pre-opening displacement u_g/u_0 when two penny-shaped cracks arranged in parallel are subjected to an incident plane P wave ($h/a = 1.0$, $\theta^{\text{in}} = 0^\circ$, and $n^{\text{in}} = 15$).

$O(NM_e \log N \log M_e)$. The far-field contributions can be rapidly calculated for the Galerkin formulation because double integrals with respect to source and field points are separated in the multipole expansion.

- For the case that a saddle-shaped crack is subjected to an incident plane P wave, we conducted the numerical simulation with two kinds of finite width w . We could observe the sub-harmonic generation in the case that $w/a = 2.0$ from numerical results but not for $w/a = 1.0$. As a result, it has been confirmed that the sub-harmonic generation occurs if w is sufficiently large.
- For the case that two penny-shaped cracks arranged in parallel are subjected to an incident plane P wave, we conducted the simulation with two kinds of interval h . It could also be found that the sub-harmonic generation is caused if sufficiently small h similarly to the 2-D case. However, we could not see the sub-harmonic generation in the case that $h/a = 1.0$. Therefore, the finite width may also be significant in this case.

Chapter 7

Final Remarks

In this dissertation, we have investigated the acceleration of CQ-BEM for 3-D acoustic and elastic wave problems. The proposed fast CQ-BEM is accurate and efficient for the large-scale wave problems especially dealing with the (semi-) infinite domain. The application of the fast CQ-BEM to the nonlinear ultrasonic simulation has also been performed, and the behavior of nonlinear ultrasonic waves has been investigated through numerical results. The results obtained by this study are summarized as follows:

Chapter 1 We have explained the background of this study about the NLUT based on CAN and the TD-BEM. To investigate the behavior of higher-harmonic generation and the mechanism of sub-harmonic one, we focused numerical simulation as the theoretical approach. In the previous researches, the behavior of higher-harmonic generation due to an interface crack has not been investigated in full 3-D, and there are a few reports of sub-harmonic simulation. Therefore, it is necessary to carry out these simulations and to quantitatively analyze them. For this type of problems, the TD-BEM is considered as an appropriate numerical method because of its accuracy and efficiency. However, the conventional TD-BEM has some problems such as instability in time-marching process and large computational complexity. Therefore, we mentioned the importance of the stabilization and acceleration of the TD-BEM in this chapter.

Chapter 2 The IRK-based CQ-BEM formulation and its important aspects are presented in this chapter. This numerical method produces more accurate numerical solutions than the linear multistep-based one although the required memory and computational time increase in the same N and M_e . However, it is sometimes difficult to satisfy accuracy requirements using the linear multistep-based CQ-BEM. Therefore, we strongly recommend to use the IRK-based CQ-BEM because of its high performance in accuracy.

Chapter 3 We have successfully accelerated the IRK-based CQ-BEM in this chapter. The original computational complexity and required memory of the IRK-based CQ-BEM are $O(m^2 N^2 M_e^2)$ even if we use an iterative solver. As the result of the acceleration based on the FMM and the rapid convolution algorithm, the computational complexity and required memory can be

7. Final Remarks

reduced to $O(mNM_e \log N \log M_e)$ and $O(mNM_e)$, respectively. We have also presented its applicability to the elastic wave and coupled acoustic-elastic wave problems.

Chapter 4 The 3-D simulation of nonlinear ultrasonic waves due to an interface crack with contact boundary conditions between two semi-infinite elastic solids, has been performed in this chapter. The appropriate boundary element formulation for this problem has been proposed in order to accurately compute the tangential velocity of displacement. We have been carried out some numerical simulations of the higher-harmonic generation and validated the numerical model of interface crack through obtained numerical results. For normal incidence of P and S waves, the reflection and transmission coefficients between two materials significantly effect in the static compressive stress. For oblique incidence of P wave, the amplitude of scattered wave rapidly fluctuates due to the behavior of reflection and transmission coefficients near the critical angle.

Chapter 5 The long-time analyses of the nonlinear ultrasonic generation by interior and surface breaking cracks in 2-D have been implemented by the non-accelerated CQ-BEM. Verification and validation of the proposed CQ-BEM have been conducted by solving the fundamental problems. From the simulation of higher-harmonic waves due to a straight-line crack, it was found that there is optimal static compressive stress for the 2nd higher-harmonic generation related with the normalized wavenumber of the incident wave. On the other hand, we have successfully conducted the numerical simulation of the sub-harmonic generation under certain conditions. From numerical results, we have investigated the relation between the characteristic of frequency response and the probability of sub-harmonic generation. As a result, the sub-harmonic generation is caused due to interior cracks with some pre-opening displacements when the frequency of the incident wave is a little larger than the first mode quasi-eigenfrequency of the linear system. However, the behavior of sub-harmonic generation due to a surface breaking crack is different, and that occurs when the frequency of the incident wave is about triple of the first mode quasi-eigenfrequency of the linear system.

Chapter 6 The 3-D simulation of nonlinear ultrasonic waves due to cracks in an infinite elastic solid has been conducted by the fast CQ-BEM presented in Chapter 3. Therefore, the fast CQ-BEM has been extended to the 3-D crack problem and verified by solving linear problems. We also presented the computational complexity through some numerical results. The crack model has also been validated by solving the fundamental nonlinear problems such as a penny-shaped crack subjected to normal incidence of P and S waves. From the numerical results of the nonlinear ultrasonic simulation, it was confirmed that the sub-harmonic generation is caused under the similar conditions to the 2-D cases.

In this study, we succeeded in reproducing the sub-harmonic waves due to the CAN in the 2-D and 3-D numerical simulations as presented in Chapters 5 and 6. As a result, the sub-harmonic generation greatly depends on the *situation* such as size, shape, and arrangement of cracks and existence of free-surface. Therefore, it is difficult to use these phenomena for the NDE if there is

no information of flaws in advance of measurement, and the applicability is limited. However, it is important to completely reveal the mechanism and to make the range of applicability clear. Also, it may be expected that the sub-harmonic generation phenomenon is used for other engineering fields.

In the future, we are going to extend the proposed 3-D numerical method of nonlinear ultrasonic simulation to the scattering problems by a surface breaking crack similarly to the 2-D case. However, for performing many numerical simulations, the proposed CQ-BEM is not sufficiently fast. Therefore, we are going to continue the acceleration of the CQ-BEM. Also, we should compare obtained numerical results with experimental data and consider the consistency between numerical and experimental approaches.

The FDM and FEM are usually used for the time-dependent (nonlinear) problems because of their robustness, computational efficiency, and ease of formulation. On the other hand, the stability of TD-BEM has been improved and accelerated by some special techniques recently as shown in this dissertation. The author hopes that the TD-BEM is more widely used in the engineering fields.

Appendix A

Translation Operators and Recursions

The translation operators for the fundamental solution of the modified Helmholtz equation $(E|F)_{n,l}^{m,j}$ are obtained using the analogous manner as the Helmholtz equation [23].

$$(M|M)_{a,c}^{b,d}(\mathbf{y}_0 \rightarrow \mathbf{y}_1) = \sum_{e=|a-c|}^{a+c} (-1)^d \mathcal{A}_{c,e} W_{-b,d,b-d}^{a,c,e} F_{e,d-b}(\mathbf{y}_0 - \mathbf{y}_1), \quad (\text{A.1})$$

$$(M|L)_{a,c}^{b,d}(\mathbf{y}_1 \rightarrow \mathbf{x}_1) = \sum_{e=|a-c|}^{a+c} (-1)^{a+d} \mathcal{A}_{c,e} W_{-b,d,b-d}^{a,c,e} O_{e,d-b}(\mathbf{x}_1 - \mathbf{y}_1), \quad (\text{A.2})$$

$$(L|L)_{a,c}^{b,d}(\mathbf{x}_1 \rightarrow \mathbf{x}_0) = \sum_{e=|a-c|}^{a+c} (-1)^d \mathcal{A}_{c,e} W_{-b,d,b-d}^{a,c,e} F_{e,d-b}(\mathbf{x}_1 - \mathbf{x}_0), \quad (\text{A.3})$$

where $\mathcal{A}_{a,b} = (2a+1)(2b+1)$ and $W_{b,d,f}^{a,c,e}$ is expressed using Wigner-3j symbol $(\begin{smallmatrix} a & c & e \\ b & d & f \end{smallmatrix})$ [57] as follows:

$$W_{b,d,f}^{a,c,e} = \begin{pmatrix} a & c & e \\ 0 & 0 & 0 \end{pmatrix} \begin{pmatrix} a & c & e \\ b & d & f \end{pmatrix}. \quad (\text{A.4})$$

The recursions of $(E|F)_{a,c}^b$ are following [28]:

$$a_{ab}^+(E|E)_{a+1,c}^b = -a_{ab}^-(E|E)_{a-1,c}^b + a_{c-1,b}^+(E|E)_{a,c-1}^b + a_{c+1,b}^-(E|E)_{a,c+1}^b, \quad (\text{A.5})$$

$$b_{a,-b}^+(E|E)_{a+1,c}^{b+1} = b_{a,-b}^-(E|E)_{a-1,c}^{b+1} + b_{c-1,-b}^+(E|E)_{a,c-1}^b - b_{c+1,-b}^-(E|E)_{a,c+1}^b, \quad (\text{A.6})$$

$$a_{ab}^+(M|L)_{a+1,c}^b = -a_{ab}^-(M|L)_{a-1,c}^b - a_{c-1,b}^+(M|L)_{a,c-1}^b - a_{c+1,b}^-(M|L)_{a,c+1}^b, \quad (\text{A.7})$$

$$b_{a,-b}^+(M|L)_{a+1,c}^{b+1} = b_{a,-b}^-(M|L)_{a-1,c}^{b+1} - b_{c-1,-b}^+(M|L)_{a,c-1}^b + b_{c+1,-b}^-(M|L)_{a,c+1}^b, \quad (\text{A.8})$$

where coefficients a_{ab}^+ , a_{ab}^- , b_{ab}^+ , and b_{ab}^- are defined as follows:

$$a_{ab}^+ = \frac{\sqrt{(a+b+1)(a-b+1)}}{2a+1}, \quad a_{ab}^- = \frac{\sqrt{(a+b)(a-b)}}{2a+1}, \quad (\text{A.9})$$

$$b_{ab}^+ = \frac{\sqrt{(a-b+1)(a-b+2)}}{2a+1}, \quad b_{ab}^- = \frac{\sqrt{(a+b)(a+b-1)}}{2a+1}. \quad (\text{A.10})$$

A. Translation Operators and Recursions

The initial values for the recursion $(E|F)_{0,c}^0$ are given as follows:

$$(M|M)_{0,c}^0 = (2c+1)i_c(s_\varphi|\mathbf{y}_0 - \mathbf{y}_1|), \quad (\text{A.11})$$

$$(M|L)_{0,c}^0 = (2c+1)k_c(s_\varphi|\mathbf{y}_1 - \mathbf{x}_1|), \quad (\text{A.12})$$

$$(L|L)_{0,c}^0 = (2c+1)i_c(s_\varphi|\mathbf{x}_1 - \mathbf{x}_0|). \quad (\text{A.13})$$

Using the relations $(E|F)_{a,c}^b = (E|F)_{a,c}^{-b}$,

$$(E|E)_{a,c}^b = \frac{2c+1}{2a+1}(E|E)_{c,a}^b, \quad (M|L)_{a,c}^b = \frac{2c+1}{2a+1}(-1)^{a+c}(M|L)_{c,a}^b, \quad (\text{A.14})$$

and recursions (A.5)-(A.8) with appropriate computational procedure, the translation operators $(E|F)_{a,c}^b$ can be calculated in $O(N_t^3)$ computational time. Then, the scaling of the translation operators $(\mathcal{E}|\mathcal{F})_{a,c}^b$ can be calculated to replace $i_c(z)$ and $k_c(z)$ in Eqs. (A.11)-(A.13) with $\check{i}_c(z)$ and $\check{k}_c(z)$, respectively. Notice that the plus or minus signs in these recursions are different from the ones [28] for the Helmholtz equation.

Appendix B

Far-field Approximation of Scattered Waves

We explain the calculation method of far-field approximation of scattered waves.

B.1. Inclusions and cracks in 2-D and 3-D

Replacing the fundamental solutions in the integral representation of the scattered wave with the far-field approximated ones, the far-field scattered waves can be evaluated. Therefore, the far-field scattered wave $\mathbf{u}^{\text{sc};\text{far}}$ from inclusions with surface S and cracks with one side of crack faces S^+ in an infinite elastic solid can be described as follows:

$$\mathbf{u}^{\text{sc};\text{far}}(\mathbf{x}, t) = \int_0^t \int_S \mathbf{U}^{\text{far}}(\mathbf{x}, \mathbf{y}, t - \tau) \cdot \mathbf{t}(\mathbf{y}, \tau) dS_y d\tau - \int_0^t \int_S \mathbf{T}^{\text{far}}(\mathbf{x}, \mathbf{y}, t - \tau) \cdot \mathbf{u}(\mathbf{y}, \tau) dS_y d\tau, \quad (\text{B.1})$$

$$\mathbf{u}^{\text{sc};\text{far}}(\mathbf{x}, t) = - \int_0^t \int_{S^+} \mathbf{T}^{+;\text{far}}(\mathbf{x}, \mathbf{y}, t - \tau) \cdot [\mathbf{u}](\mathbf{y}, \tau) dS_y d\tau, \quad (\text{B.2})$$

where the superscript "far" indicates the far-field approximated function. Defining that $x = |\mathbf{x}|$ and $\hat{\mathbf{x}} = \mathbf{x}/x$ and considering $x \gg |\mathbf{y}|$ as the far-field condition, we can approximate as $r \simeq x - \hat{\mathbf{x}} \cdot \mathbf{y}$ and $\partial r / \partial x_i \simeq \hat{x}_i$. Consequently, the far-field approximated fundamental solutions corresponding to displacement and traction for 2-D elastodynamic problems in time-domain can be respectively obtained as follows:

$$U_{ij}^{\text{far}}(\mathbf{x}, \mathbf{y}, t) = \frac{1}{\mu \sqrt{8\pi x}} \sqrt{\frac{2}{\pi}} \left\{ \frac{c_T^2}{c_L^2} \hat{x}_i \hat{x}_j \frac{H\left(t - \frac{x - \hat{\mathbf{x}} \cdot \mathbf{y}}{c_L}\right)}{\sqrt{\left(\frac{t}{x} + \frac{1}{c_L}\right) \left(t - \frac{x - \hat{\mathbf{x}} \cdot \mathbf{y}}{c_L}\right)}} + (\delta_{ij} - \hat{x}_i \hat{x}_j) \frac{H\left(t - \frac{x - \hat{\mathbf{x}} \cdot \mathbf{y}}{c_T}\right)}{\sqrt{\left(\frac{t}{x} + \frac{1}{c_T}\right) \left(t - \frac{x - \hat{\mathbf{x}} \cdot \mathbf{y}}{c_T}\right)}} \right\}, \quad (\text{B.3})$$

B. Far-field Approximation of Scattered Waves

$$T_{ij}^{\text{far}}(\mathbf{x}, \mathbf{y}, t) = -\frac{1}{\sqrt{8\pi x}} \sqrt{\frac{2}{\pi}} \left\{ \frac{(c_L^2 - 2c_T^2) \delta_{ik} \hat{x}_j + 2c_T^2 \hat{x}_i \hat{x}_j \hat{x}_k}{c_L^3 \sqrt{\left(\frac{t}{x} + \frac{1}{c_L}\right) \left(t - \frac{x - \hat{\mathbf{x}} \cdot \mathbf{y}}{c_L}\right)}} n_k(\mathbf{y}) \delta\left(t - \frac{x - \hat{\mathbf{x}} \cdot \mathbf{y}}{c_L}\right) \right. \\ \left. + \frac{\delta_{jk} \hat{x}_i + \delta_{ij} \hat{x}_k - 2\hat{x}_i \hat{x}_j \hat{x}_k}{c_T \sqrt{\left(\frac{t}{x} + \frac{1}{c_T}\right) \left(t - \frac{x - \hat{\mathbf{x}} \cdot \mathbf{y}}{c_T}\right)}} n_k(\mathbf{y}) \delta\left(t - \frac{x - \hat{\mathbf{x}} \cdot \mathbf{y}}{c_T}\right) \right\}. \quad (\text{B.4})$$

Similarly, the counterparts for 3-D problems are given by

$$U_{ij}^{\text{far}}(\mathbf{x}, \mathbf{y}, t) = \frac{1}{4\pi x \mu} \left[\frac{c_T^2}{c_L^2} \hat{x}_i \hat{x}_j \delta\left(t - \frac{x - \hat{\mathbf{x}} \cdot \mathbf{y}}{c_L}\right) + (\delta_{ij} - \hat{x}_i \hat{x}_j) \delta\left(t - \frac{x - \hat{\mathbf{x}} \cdot \mathbf{y}}{c_T}\right) \right], \quad (\text{B.5})$$

$$T_{ij}^{\text{far}}(\mathbf{x}, \mathbf{y}, t) = -\frac{1}{4\pi x} \left\{ \left[\frac{c_T^2}{c_L^3} \hat{x}_i \left(\frac{c_L^2}{c_T^2} - 2 \right) \delta_{jk} + 2\hat{x}_i \hat{x}_j \hat{x}_k \right] n_k(\mathbf{y}) \delta\left(t - \frac{x - \hat{\mathbf{x}} \cdot \mathbf{y}}{c_L}\right) \right. \\ \left. + \frac{1}{c_T} \left[\delta_{ik} \hat{x}_j + \delta_{ij} \hat{x}_k - 2\hat{x}_i \hat{x}_j \hat{x}_k \right] n_k(\mathbf{y}) \delta\left(t - \frac{x - \hat{\mathbf{x}} \cdot \mathbf{y}}{c_T}\right) \right\}. \quad (\text{B.6})$$

Substituting Eqs. (B.3)–(B.6) into Eqs. (B.1) and (B.2) yields the following forms because the far-field scattered wave can be completely separated into P, SV, SH wave components in 3-D and P and SV (S) ones in 2-D.

$$\mathbf{u}^{\text{sc;far}}(\mathbf{x}, t) = \begin{cases} \frac{1}{4\pi x} \left[\hat{\mathbf{x}} \Omega_L \left(\hat{\mathbf{x}}, t - \frac{x}{c_L} \right) + \hat{\mathbf{v}} \Omega_{TV} \left(\hat{\mathbf{x}}, t - \frac{x}{c_T} \right) + \hat{\mathbf{h}} \Omega_{TH} \left(\hat{\mathbf{x}}, t - \frac{x}{c_T} \right) \right] & \text{for 3-D,} \\ \frac{1}{\sqrt{8\pi x}} \left[\hat{\mathbf{x}} \Omega_L \left(\hat{\mathbf{x}}, t - \frac{x}{c_L} \right) + \hat{\mathbf{v}} \Omega_T \left(\hat{\mathbf{x}}, t - \frac{x}{c_T} \right) \right] & \text{for 2-D,} \end{cases} \quad (\text{B.7})$$

where $\hat{\mathbf{v}}$ and $\hat{\mathbf{h}}$ are the displacement vectors of SV and SH waves, respectively. Ω_φ ($\varphi = L, TV$, or TH) is the far-field amplitude and indicates the invariable waveform of the scattered wave at far-field. The scattered waves at far-field are attenuated by distance in order of $O(1/\sqrt{x})$ and $O(1/x)$ for 2-D and 3-D cases, respectively, as shown in Eq. (B.7).

If we use the CQM formulation for evaluation of the far-field scattered waves, the equivalent scattered far-field can be obtained by using the far-field approximated Laplace-domain fundamental solutions. The approximated 2-D Laplace-domain fundamental solutions are obtained by using the asymptotic behavior of the modified Bessel function K_0 as follows:

$$K_0(s_\varphi r) \sim \sqrt{\frac{\pi}{2is_\varphi x}} \exp\left[-s_\varphi x + \frac{\pi}{4}i\right] \exp[s_\varphi \hat{\mathbf{x}} \cdot \mathbf{y}]. \quad (\text{B.8})$$

On the other hand, the 3-D counterparts are obtained by using the approximations $r \simeq x - \hat{\mathbf{x}} \cdot \mathbf{y}$ and $\partial r / \partial x_i \simeq \hat{x}_i$.

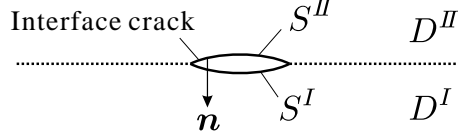


Figure B.1.: Interface crack of two-layered elastic solid.

B.2. Interface cracks between two semi-infinite elastic solids in 3-D

The far-field scattered waves by an interface crack are evaluated in Chapter 4. Therefore, the corresponding far-field approximated Green's function is shown. The far-field scattered waves can be evaluated by replacing \mathbf{T}^+ in Eq. (B.2) with Green's function for the two-layered semi-infinite elastic solid. The far-field approximated Green's functions can be obtained from the integral representation of the fundamental solutions using the ray theory [2] and the stationary phase method [80]. The ray theory has been applied to the BEM in order to improve the accuracy and efficiency by Kimoto and Hirose [41].

Let S^I and S^{II} be each side of crack faces as depicted in Fig. B.1. The integral form of far-field scattered wave from interface cracks is given by

$$\mathbf{u}^{\text{sc;far};I(II)}(\mathbf{x}, t) = - \int_0^t \int_{S^{I(II)}} \mathbf{H}^{\text{far};II(I) \rightarrow I(II)}(\mathbf{x}, \mathbf{y}, t - \tau) \cdot [\mathbf{u}](\mathbf{y}, \tau) dS_y d\tau, \quad (\text{B.9})$$

where $\mathbf{H}^{\text{far};I \rightarrow II}$ indicates the far-field approximation of traction Green's function for the two-layered elastic solid when the source and field points are located in D^I and D^{II} , respectively. Considering that inhomogeneous waves are generated over the critical angles, the scattered waves should be evaluated in frequency-domain. Therefore, the approximations of frequency-domain Green's function are shown here. The far-field approximation of frequency-domain traction Green's function for the two-layered elastic solid can be written as follows:

$$\begin{aligned} \tilde{H}_{ip}^{I(II) \rightarrow II(I); \text{far}}(\mathbf{x}, \mathbf{y}, \omega) = & - \sum_{\alpha=L,TV} \sum_{\beta=L,TV} \frac{n_j(\mathbf{y}) C_{pj kq}^{I(II)} \zeta_q^\pm}{4\pi x \mu^{I(II)} c_\alpha^{I(II)}} \\ & \times A_k^{\pm\alpha,\beta} d_i^{\pm\alpha,\beta} i\omega \exp \left[i\omega \left\{ \frac{x}{c_\beta^{II(I)}} - \frac{\zeta^\pm \cdot \mathbf{y}}{c_\alpha^{I(II)}} \right\} \right] \bigg|_{\zeta_1 = \frac{c_\alpha^{I(II)}}{c_\beta^{II(I)}} \hat{x}_1, \zeta_2 = \frac{c_\alpha^{I(II)}}{c_\beta^{II(I)}} \hat{x}_2} \\ & - \frac{n_j(\mathbf{y}) C_{pj kq}^{I(II)} \zeta_q^\pm}{4\pi x \mu^{I(II)} c_T^{I(II)}} A_k^{\pm TH, TH} d_i^{\pm TH, TH} i\omega \exp \left[i\omega \left\{ \frac{x}{c_T^{II(I)}} - \frac{\zeta^\pm \cdot \mathbf{y}}{c_T^{I(II)}} \right\} \right] \bigg|_{\zeta_1 = \frac{c_T^{I(II)}}{c_T^{II(I)}} \hat{x}_1, \zeta_2 = \frac{c_T^{I(II)}}{c_T^{II(I)}} \hat{x}_2}, \end{aligned} \quad (\text{B.10})$$

B. Far-field Approximation of Scattered Waves

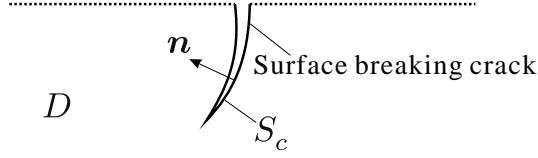


Figure B.2.: Surface breaking crack in elastic half-space.

where

$$A_k^{\pm\alpha,\beta} = T_{I(II) \rightarrow II(I)}^{\alpha,\beta}(\zeta^\pm) \frac{(c_T^{I(II)})^2}{c_\alpha^{I(II)} c_\beta^{II(I)}} \frac{|\hat{x}_3|}{\nu} d_k^{\pm\alpha}. \quad (\text{B.11})$$

The superscripts on the material constants such as C_{ijkl} and μ indicate each domain. In Eq. (B.11), $T_{I(II) \rightarrow II(I)}^{\alpha,\beta}(\zeta^\pm)$ is the transmission coefficient with propagation vector of the incident wave ζ^\pm when the wave mode is changed from α to β , and the wave is propagating from $D^{I(II)}$ to $D^{II(I)}$. The propagation vector ζ^\pm is defined by

$$\zeta^\pm = (\zeta_1, \zeta_2, \pm\nu), \quad \nu = \sqrt{1 - (\zeta_1)^2 - (\zeta_2)^2}, \quad (\text{B.12})$$

and $d^{\pm\alpha}$ and $d^{\pm\alpha,\beta}$ are the displacement vector before and after the transmission, respectively. The sign \pm has to be select to converge $\exp[\cdot]$ in Eq. (B.10). The Laplace-domain counterpart of Eq. (B.10) can be obtained by replacing ω with is . Only for $y_3 = 0$, the closed form of time-domain counterpart of Eq. (B.10) is available. Therefore, the time-domain expression can be used for the case in Chapter 4.

B.3. Surface breaking cracks in 2-D elastic half-space

The far-field scattered waves by surface breaking cracks in an elastic half-space are evaluated in Chapter 5. Therefore, the corresponding far-field approximated Green's function is shown. Let S_c be one side of crack faces as depicted in Fig. B.2. The integral form of far-field scattered wave from surface breaking cracks in an elastic half-space is given by

$$\mathbf{u}^{\text{sc;far}}(\mathbf{x}, t) = - \int_0^t \int_{S_c} \mathbf{H}^{\text{far}}(\mathbf{x}, \mathbf{y}, t - \tau) \cdot [\mathbf{u}](\mathbf{y}, \tau) dS_y d\tau, \quad (\text{B.13})$$

where \mathbf{H}^{far} indicates the far-field approximation of traction Green's function for the elastic half-space. The far-field approximation of frequency-domain traction Green's function for the elastic

half-space can be written as follows:

$$\begin{aligned} \tilde{H}_{ip}^{\text{far}}(\mathbf{x}, \mathbf{y}, \omega) = \tilde{T}_{ip}^{\text{far}}(\mathbf{x}, \mathbf{y}, \omega) - \sum_{\alpha=L,TV} \sum_{\beta=L,TV} \frac{n_j(\mathbf{y}) C_{pj k q} \zeta_q^{\pm}}{\mu c_{\alpha} \sqrt{8\pi k_{\beta} x}} \\ \times B_k^{\pm\alpha, \beta} d_i^{\mp\alpha, \beta} i\omega \exp \left[i\omega \left\{ \frac{x}{c_{\beta}} - \frac{\boldsymbol{\zeta}^{\pm} \cdot \mathbf{y}}{c_{\alpha}} \right\} + \frac{i\pi}{4} \right] \Big|_{\zeta_1 = \frac{c_{\alpha}}{c_{\beta}} \hat{x}_1}, \end{aligned} \quad (\text{B.14})$$

$$B_k^{\pm\alpha, \beta} = R^{\alpha, \beta}(\boldsymbol{\zeta}^{\pm}) \frac{(c_T)^2}{c_{\alpha} c_{\beta}} \frac{|\hat{x}_3|}{\nu} d_k^{\pm\alpha}, \quad (\text{B.15})$$

where \tilde{T}^{far} is the far-field approximation of the full-space traction fundamental solution. $\boldsymbol{\zeta}^{\pm}$ and ν for 2-D are different from the previous 3-D ones and they are defined by

$$\boldsymbol{\zeta}^{\pm} = (\zeta_1, \pm\nu), \quad \nu = \sqrt{1 - (\zeta_1)^2}. \quad (\text{B.16})$$

Appendix C

Free-field for two-layered elastic solid

We explain the calculation method of the free-field for a two-layered semi-infinite elastic solid subjected to the incident plane wave as depicted in Fig. C.1. In this study, the n^{in} cycles sinusoidal burst plane wave with amplitude u_0 such as Eq. (4.19), is utilized for the incident wave in the nonlinear ultrasonic simulations. If the incident wave \mathbf{u}^{in} is emitted from D^I , it can be written using the center circular frequency ω^{in} as follows:

$$\begin{cases} \mathbf{u}^{\text{in}}(\mathbf{x}, t) = u_0 \mathbf{d}_{\varphi}^{\text{in}} \sin(\Lambda_{\varphi}^I) H(\Lambda_{\varphi}^I) H(2\pi n^{\text{in}} - \Lambda_{\varphi}^I), \\ \Lambda_{\varphi}^I = \omega^{\text{in}} \left(t - \frac{\mathbf{p}^{\text{in}} \cdot (\mathbf{x} - \boldsymbol{\chi})}{c_{\varphi}^I} \right). \end{cases} \quad (\text{C.1a})$$

$$\quad (\text{C.1b})$$

If the incident angle is smaller than the critical one, it is easy to evaluate the propagation vectors after reflection and transmission using Snell's law. In this case, the reflection and transmission coefficients can be calculated easily from the given interface conditions and must be real values [73]. Consequently, the free-field can be calculated in time-domain directly. However, it is difficult to evaluate the free-field in time-domain if the incident angle is over the critical one. Therefore, we numerically construct the time-domain free-field using the inverse Fourier transform of the frequency-domain one.

Taking into account that n^{in} is integer, the Fourier transform of the Eq. (C.1) is given by

$$\begin{aligned} \mathcal{F}[\mathbf{u}^{\text{in}}(\mathbf{x}, t)](\mathbf{x}, \omega) &= \int_{-\infty}^{\infty} \mathbf{u}^{\text{in}}(\mathbf{x}, t) e^{i\omega t} dt \\ &= \frac{u_0 \mathbf{d}_{\varphi}^{\text{in}} \omega^{\text{in}}}{(\omega^{\text{in}})^2 - \omega^2} \left\{ \left(1 - \exp\left[\frac{2n^{\text{in}} i \pi \omega}{\omega^{\text{in}}}\right] \right) \exp\left[\frac{i\omega}{c_{\alpha}^I} \mathbf{p}^{\text{in}} \cdot (\mathbf{x} - \boldsymbol{\chi})\right] \right\}, \end{aligned} \quad (\text{C.2})$$

where ω is the circular frequency, and \mathcal{F} indicates the Fourier transform. Assuming continuity of displacement and traction on the interface, the following displacement fields of the reflected and transmitted waves in frequency-domain can be obtained by solving the reflection and transmission problem of an incident plane wave for a two-layered elastic solid.

C. Free-field for two-layered elastic solid

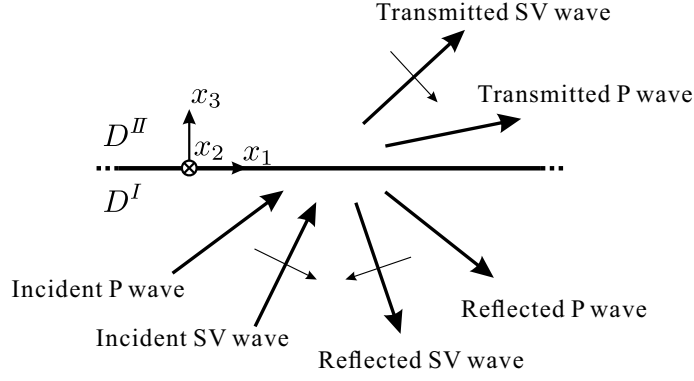


Figure C.1.: Reflection and transmission of the incident plane wave on the interface between two elastic solids.

$$\mathcal{F} [\mathbf{u}^{\text{ref};I}(\mathbf{x}, t)](\mathbf{x}, \omega) = \sum_{\beta=L,TV} \frac{u_0 \mathbf{d}_{\beta}^{\text{ref}} \omega^{\text{in}}}{(\omega^{\text{in}})^2 - \omega^2} R^{\varphi,\beta}(\mathbf{p}^{\text{in}}) \times \left\{ \left(1 - \exp \left[\frac{2n^{\text{in}} i \pi \omega}{\omega^{\text{in}}} \right] \right) \exp \left[\frac{i\omega}{c_{\beta}^I} \mathbf{p}_{\beta}^{\text{ref}} \cdot (\mathbf{x} - \boldsymbol{\chi}) \right] \right\}, \quad (\text{C.3})$$

$$\mathcal{F} [\mathbf{u}^{\text{trans};II}(\mathbf{x}, t)](\mathbf{x}, \omega) = \sum_{\beta=L,TV} \frac{u_0 \mathbf{d}_{\beta}^{\text{trans}} \omega^{\text{in}}}{(\omega^{\text{in}})^2 - \omega^2} T^{\alpha,\beta}(\mathbf{p}^{\text{in}}) \times \left\{ \left(1 - \exp \left[\frac{2n^{\text{in}} i \pi \omega}{\omega^{\text{in}}} \right] \right) \exp \left[\frac{i\omega}{c_{\beta}^{II}} \mathbf{p}_{\beta}^{\text{trans}} \cdot (\mathbf{x} - \boldsymbol{\chi}) \right] \right\}, \quad (\text{C.4})$$

where $R^{\varphi,\beta}(\mathbf{p}^{\text{in}})$ and $T^{\varphi,\beta}(\mathbf{p}^{\text{in}})$ are the reflection and transmission coefficients, respectively, when the incident plane wave is propagating to the \mathbf{p}^{in} direction and its mode is changed from φ to β . The time-domain free-field can be evaluated by means of the inverse Fourier transform after the calculation of Eqs. (C.3) and (C.4). For elastic half-space, the free-field can be evaluated in a similar way.

We show the reflection and transmission coefficients for the steel-aluminum interface which is used in Chapter 4. Therefore, the material constants in Table 4.1 are used. The positive directions of propagation and vibration are shown as the big and small arrows in Fig. C.1, respectively. The detailed calculation method of the reflection and transmission coefficients can be found in e.g. [3, 80, 73].

The real and imaginary parts of reflection and transmission coefficients for P wave incidence are shown in Fig. C.2. As shown in Fig. C.2, there is a critical angle which corresponds to the transmitted P wave when $\theta^{\text{in}} \simeq 65^\circ$. The similar graphs corresponding to SV wave incidence are shown in Fig. C.3. There are two critical angles which correspond to the transmitted and reflected P waves when $\theta^{\text{in}} \simeq 29^\circ$ and 32° , respectively. If the reflection and transmission coefficients are complex values, the corresponding phase shift is caused.

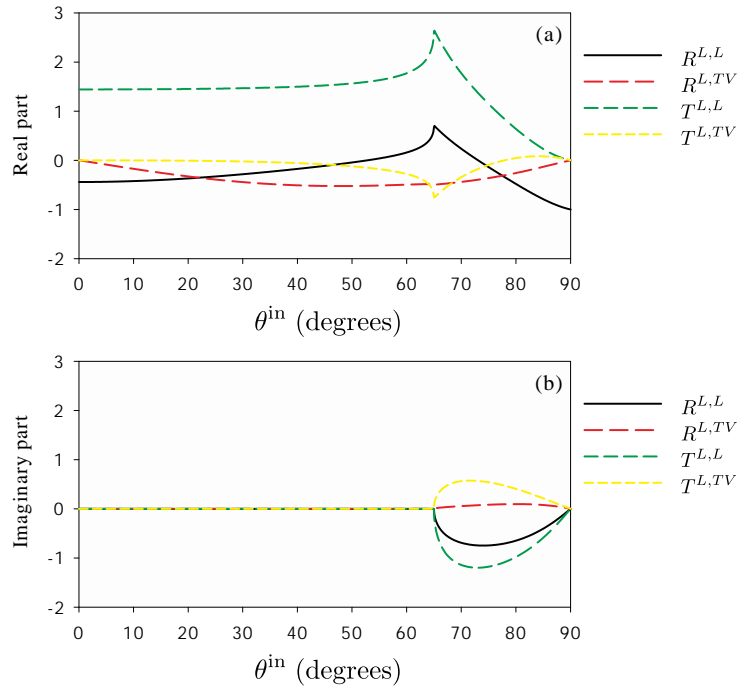


Figure C.2.: (a) Real parts and (b) imaginary parts of reflection and transmission coefficients of P wave incidence for various incident angles θ^{in} .

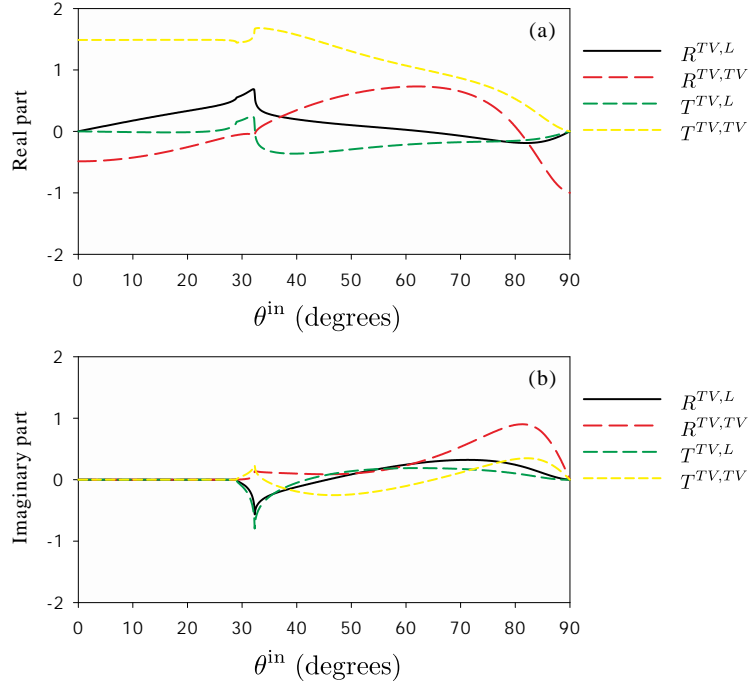


Figure C.3.: (a) Real parts and (b) imaginary parts of reflection and transmission coefficients of SV wave incidence for various incident angles θ^{in} .

Bibliography

- [1] Achenbach, J. D.: Wave propagation in elastic solids, North-Holland (1973).
- [2] Achenbach, J. D., Gautesen, A. K., and McMaken, H.: Ray methods for waves in elastic solids, Pitman (1982).
- [3] Aki, K. and Richards, P. G.: Quantitative seismology theory and methods Vol.1, W.H. Freeman (1980).
- [4] Banjai, L.: Multistep and multistage convolution quadrature for the wave equation: algorithms and experiments, *SIAM Journal on Scientific Computing*, **32**–5, pp.2964–2994 (2010).
- [5] Banjai, L. and Lubich, C.: An error analysis of Runge-Kutta convolution quadrature, *BIT Numer. Math.*, **51**, pp.483–496 (2011).
- [6] Banjai, L., Lubich, C., and Melenk, J. M.: Runge-Kutta convolution quadrature for nonsectorial operators arising in wave propagation, *Numer. Math.*, **119**, pp.1–20 (2011).
- [7] Banjai, L., Messner, M., and Schanz, M.: Runge-Kutta convolution quadrature for the boundary element method, *Comput. Meth. Appl. Mech. Engng.*, **245–246**, pp.90–101 (2012).
- [8] Banjai, L. and Kachanovska, M.: Fast convolution quadrature for the wave equation in three dimensions, *J. Comput. Phys.*, **279**, pp.103–126 (2014).
- [9] Bebendorf, M.: Approximation of boundary element matrices, *Numer. Math.*, **86** pp.565–589 (2000).
- [10] Bebendorf, M.: Hierarchical matrices, Springer (2008).
- [11] Becache, E., Nédélec, J. C., and Nishimura, N.: Regularization in 3D for anisotropic elastodynamic crack and obstacle problems, *J. Elasticity*, **31**, pp.25–46 (1993).
- [12] Bonnet, M.: Regularized direct and indirect symmetric variational BIE formulations for three-dimensional elasticity, *Eng. Anal. Bound. Elem.*, **15**, pp.93–102 (1995).
- [13] Bonnet, M.: Boundary integral equation methods for solids and fluids, John Wiley & Sons (1999).
- [14] Brebbia, C. A., Telles, J. C. F., and Wrobel, L. C.: Boundary element techniques, Theory and applications in engineering, Springer (1984).

Bibliography

- [15] Buck, O., Morris, W.L. and Richardson, J.M.: Acoustic harmonic generation at unbonded interfaces and fatigue cracks, *Appl. Phys. Lett.*, **33**–5, pp.371–373 (1978).
- [16] Calvo, M. P., Cuesta, E., and Palencia, C.: Runge-Kutta convolution quadrature methods for well-posed equations with memory, *Numer. Math.*, **107**, pp.589–614 (2007).
- [17] Chaillat, S., Bonnet, M., and Semblat, J. -F.: A Fast Multipole Method formulation for 3D elastodynamics in the frequency domain, *Comptes Rendus Mecanique*, **335**, pp.714–719 (2007).
- [18] Chaillat, S. and Bonnet, M.: Recent advances on the fast multipole accelerated boundary element method for 3D time-harmonic elastodynamics, *Wave Motion*, **50**, pp.1090–1104 (2013).
- [19] Choi, C. H., Ivanic, J., Gordon, M. S., and Ruedenbeg, K.: Rapid and stable determination of rotation matrices between spherical harmonics by direct recursion, *J. Chem. Phys.*, **111**–19, pp.8825–8831 (1999).
- [20] Delrue, S. and Abeele, K. V. D.: Three-dimensional finite element simulation of closed delaminations in composite materials, *Ultrasonics*, **52**, pp.315–324 (2012).
- [21] Marrero, M. and Domínguez, J.: Time-domain BEM for three-dimensional fracture mechanics, *Eng. Fract. Mech.*, **71**, pp.1557–1575 (2004).
- [22] Douglas, C. G.: Physics for scientists and engineers, 4th Edition, Addison-Wesley (2000).
- [23] Epton, M. A. and Dembart, B.: Multipole translation theory for the three dimensional Laplace and Helmholtz equations, *SIAM J. Sci. Comput.*, **16**, pp.865–897 (1995).
- [24] Ergin, A. A., Shanker, B., and Michielssen, E.: Fast evaluation of three-dimensional transient wave fields using diagonal translation operators, *J. Comput. Phys.*, **146**, pp.157–180 (1998).
- [25] Gaul, L., Kögl, M., and Wagner, M.: Boundary element methods for engineers and scientists, An introductory course with advanced topics, Springer (2003).
- [26] Greengard, L. and Rokhlin, V.: A fast algorithm for particle simulations, *J. Comput. Phys.*, **73**, pp.325–348 (1987).
- [27] Guiggiani, M., Krishnasamy, G., Rudolphi, T. J., and Rizzo, F. J.: A general algorithm for the numerical solution of hypersingular boundary integral equations, *J. Appl. Mech.*, **59**, pp.604–614 (1992).
- [28] Gumerov, N. and Duraiswami, R.: Fast multipole methods for the Helmholtz equation in three dimensions, Elsevier (2004).
- [29] Guoyou, Y., Mansur, W. J., Carrer, J. A. M., and Gong, L.: Stability of Galerkin and collocation time domain boundary element methods as applied to the scalar wave equation, *Comput. Struct.*, **74**, pp.495–506 (2000).

- [30] Ha-Duong, T., Ludwig, B., and Terrasse, I.: A Galerkin BEM for transient acoustic scattering by an absorbing obstacle, *Int. J. Numer. Meth. Eng.*, **57**, pp.1845-1882 (2003).
- [31] Hairer, E., Lubich, C., and Schlichte M.: Fast numerical solution of nonlinear Volterra convolution equations, *SIAM J. Sci. Stat. Comput.*, **6**, pp.532–541 (1985).
- [32] Hairer, E., Wanner, G., and Nørsett, S. P.: Solving ordinary differential equations I: nonstiff problems, Springer series in computational mathematics, Springer (1987).
- [33] Hairer, E. and Wanner, G.: Solving ordinary differential equations II: stiff and differential-algebraic problems, Springer series in computational mathematics, Springer (1991).
- [34] Hayashi, T. and Biwa, S.: Subharmonic wave generation at interface of a thin layer between metal blocks, *Jpn. J. Appl. Phys.*, **52**, 07HC02 (2013).
- [35] Hirose, S. and Achenbach, J. D.: Time-domain boundary element analysis of elastic wave interaction with a crack, *Int. J. Numer. Meth. Engng.*, **28**, pp.629–644 (1989).
- [36] Hirose, S.: Boundary integral equation method for transient analysis of 3-D cavities and inclusions, *Eng. Anal. Bound. Elem.*, **8–3**, pp.146–153 (1991).
- [37] Hirose, S. and Kitahara, M.: Calculation of scattered far-fields in layered materials, *JAS-COME*, **9**, pp.31–34 (1992) (in Japanese).
- [38] Hirose, S. and Achenbach, J. D.: Higher harmonics in the far-field due to dynamic crack-face contacting, *J. Acoust. Soc. Am.*, **93**, pp.142–147 (1993).
- [39] Hirose, S.: 2-D scattering by a crack with contact-boundary conditions, *Wave Motion*, **19**, pp.37–49 (1994).
- [40] Hsiao, G. C. and Wendland, W. L.: Boundary integral equations, Springer (2010).
- [41] Kimoto, K. and Hirose, S.: A coupling method of boundary element method and generalized ray theory for elastic wave scattering in a thick plate *Review of Quantitative Nondestructive Evaluation*, **22**, pp.41–48 (2003).
- [42] Kimoto, K. and Ichikawa, Y.: A finite difference method for elastic wave scattering by a planar crack with contacting faces, *Wave Motion*, **52**, pp.120–137 (2015).
- [43] Lachat, J. C. and Watson, J. O.: Effective numerical treatment of boundary integral equation: A formulation for three-dimensional elastostatics, *Int. J. Num. Meth. Eng.*, **10**, pp.991–1005 (1976).
- [44] Liu, Y. and Rizzo, F. J.: A weakly singular form of the hypersingular boundary integral equation applied to 3-D acoustic wave problems, *Comput. Meth. Appl. Mech. Engng.*, **96**, pp.271–287 (1992).

Bibliography

- [45] Liu, Y. and Rizzo, F. J.: Hypersingular boundary integral equations for radiation and scattering of elastic waves in three dimensions, *Comput. Meth. Appl. Mech. Engng.*, **107**, pp.131–144 (1993).
- [46] Lubich, C.: Convolution quadrature and discretized operational calculus I, *Numer. Math.*, **52**, pp.129–145 (1988).
- [47] Lubich, C.: Convolution quadrature and discretized operational calculus II, *Numer. Math.*, **52**, pp.413–425 (1988).
- [48] Lubich, C. and Ostermann, A.: Runge-Kutta methods for parabolic equations and convolution quadrature, *Math. Comput.*, **60**, pp.105–131 (1993).
- [49] Manolis, G. D.: Elastic wave scattering around cavities in inhomogeneous continua by the BEM, *J. Sound Vib.*, **266**, pp.281–305 (2003).
- [50] Martin, P. A. and Rizzo, F. J.: On boundary integral equations for crack problems, *Proc. R. Soc. Lond.*, A **421**, pp.341–355 (1989).
- [51] Maruyama, T., Saitoh, T., and Hirose, S.: Implicit Runge-Kutta based convolution quadrature boundary element method and its application to 3-D scalar wave propagation problems, *JASCOME*, **12**, pp.91–96 (2012) (in Japanese).
- [52] Maruyama, T., Saitoh, T., and Hirose, S.: Implicit Runge-Kutta based convolution quadrature time-domain fast multipole boundary element method for 3-D scalar wave problems, *Journal of JSCE*, Ser.A2 (Applied Mechanics), **69**–2, pp.I.175–I.185 (2013) (in Japanese).
- [53] Maruyama, T., Saitoh, T., and Hirose, S.: Implicit Runge-Kutta based CQ-FMBEM for coupled acoustic-elastic wave problems, *JASCOME*, **14**, pp.55–60 (2014) (in Japanese).
- [54] Maruyama, T., Saitoh, T., and Hirose, S.: 3-D numerical simulation of nonlinear ultrasonic testing using CQ-BEM, *Journal of JSCE*, Ser.A2 (Applied Mechanics), **70**–2, pp.I.235–I.246 (2014) (in Japanese).
- [55] Maruyama, T., Saitoh, T., Bui, T. Q., and Hirose, S.: Transient elastic wave analysis of 3-D large-scale cavities by fast multipole BEM using implicit Runge-Kutta convolution quadrature, *Comput. Meth. Appl. Mech. Engng.* (accepted).
- [56] Mendelsohn, D.A. and Doong, J.M.: Transient dynamic elastic frictional contact: a general 2D boundary element formulation with examples of SH motion, *Wave Motion*, **11**, pp.1–21 (1989).
- [57] Messiah, A.: Quantum Mechanics, John Wiley & Sons (1967).
- [58] Messner, M. and Schanz, M.: An accelerated symmetric time-domain boundary element formulation for elasticity, *Eng. Anal. Bound. Elem.*, **34**, pp.944–955 (2010).

- [59] Meziane, A., Norris, A. N. and Shuvalov, A. L.: Nonlinear shear wave interaction at a frictional interface: Energy dissipation and generation of harmonics, *J. Acoust. Soc. Am.*, **130**–4, pp.1820–1828 (2011).
- [60] Monegato, G., Scuderi, L., and Stanić, M. P.: Lubich convolution quadratures and their application to problems described by space-time BIEs, *Numer. Algorithms*, **56**, pp.405–436 (2011).
- [61] Nishimura, N. and Kobayashi, S.: A regularized boundary integral equation method for elastodynamic crack problems, *Comput. Mech.*, **4**, pp.319–328 (1989).
- [62] Nishimura, N.: Fast multipole accelerated boundary integral equation methods, *Appl. Mech. Rev.*, **55**–4, pp.299–324 (2002).
- [63] Niwa, Y., Hirose, S., and Kitahara, M.: Application of the boundary integral equation (BIE) method to transient response analysis of inclusions in a half space, *Wave Motion*, **8**, pp.77–91 (1986).
- [64] Odashima, A., Nakahata, K., and Kitahara, M.: Calculation of backscattered waveforms from defects with emphasis on phase, *JASCOME*, **18**, pp.23–28 (2001) (in Japanese).
- [65] Ohara, Y., Horinouchi, S., Hashimoto, M., Shintaku, Y., and Yamanaka, K.: Nonlinear ultrasonic imaging method for closed cracks using subtraction of responses at different external loads, *Ultrasonics*, **51**, pp.661–666 (2011).
- [66] Patter, J. N., Croxford, A. J., and Wilcox, P. D.: Nonlinear ultrasonic phased array imaging, *Phys. Rev. Lett.*, **113**, No.144301 (2014).
- [67] Pao, Y. -H. and Mow, C. -C.: Diffraction of elastic waves and dynamic stress concentrations, Crane and Russak (1973).
- [68] Rahman, M.: Time-harmonic body force loading of a mode-I penny-shaped crack, *Int. J. Solids Struct.*, **32**, pp.3191–3216 (1995).
- [69] Rice, J. R.: Elastic fracture mechanics concepts for interfacial cracks, *J. Appl. Mech.*, **55**, pp.98–103 (1988).
- [70] Richardson, J.M.: Harmonic generation at an unbounded interface-I. planar interface between semi-infinite elastic media, *Int. Engng. Sci.*, **17**, pp.73–85 (1979).
- [71] Ricker, N.: The computation of output disturbances from amplifiers for true wavelet inputs, *Geophysics*, **10**, pp.207–220 (1945).
- [72] Rokhlin, V.: Rapid solution of integral equations of classical potential theory, *J. Comput. Phys.*, **60**, pp.187–207 (1985).
- [73] Rose, J. L.: Ultrasonic waves in solid media, Cambridge University Press (1999).

Bibliography

- [74] Saad, Y. and Schultz, M. H.: GMRES: A generalized minimal residual algorithm for solving nonsymmetric linear systems, *SIAM J. Sci. Statist. Comput.*, **7**, pp.856–869 (1986).
- [75] Saitoh, T., Hirose, S., and Fukui, T.: Convolution quadrature boundary element method and acceleration by fast multipole method in 2-D viscoelastic wave propagation, *Theor. Appl. Mech. Jap.*, **57**, pp.385–393 (2009).
- [76] Saitoh, T. and Hirose, S.: Parallelized fast multipole BEM based on the convolution quadrature method for 3-D wave propagation problems in time-domain, *IOP Conference Series: Materials Science and Engineering*, **10** No.012242 (2010).
- [77] Saitoh, T., Furuta, Y., Hirose, S., and Nakahata, K.: Simulation of higher harmonics on non-linear ultrasonic testing using convolution quadrature time-domain boundary element method in 2-D elastodynamics, *J. JSCE Appl. Mech.*, **67**, pp.I_161–I_169 (2011) (in Japanese).
- [78] Saitoh, T., Chikazawa, F., and Hirose, S.: Convolution quadrature time-domain boundary element method for 2-D fluid-saturated porous Media, *Appl. Math. Model.*, **38**, pp.3724–3740 (2014).
- [79] Sarens, B., Verstraeten, B., Glorieux, C., Kalogiannakis, G., and Hemelrijck, D. V.: Investigation of contact acoustic nonlinearity in delaminations by shearographic imaging, laser doppler vibrometric scanning and finite difference modeling, *IEEE Trans. Ultrason. Ferr.*, **57**–6, pp.1383–1395 (2010).
- [80] Schmerr, L. W.: Fundamentals of Ultrasonic Nondestructive Evaluation, Plenum Press (1998).
- [81] Severin, F. M. and Solodov, I. Yu.: Experimental observation of acoustic demodulation in reflection from a solid-solid interface, *Sov. Phys. Acoust.*, **35**–4, pp.447–448 (1989).
- [82] Schanz, M. and Antes, H.: Application of 'operational quadrature methods' in time domain boundary element methods, *Meccanica*, **32**, pp.176–186 (1997).
- [83] Schanz, M., Antes, H., and Rüberg, T.: Convolution quadrature boundary element method for quasi-static visco- and poroelastic continua, *Comput. Struct.*, **83**, pp.673–684 (2005).
- [84] Sládek, J. and Sládek, V.: Dynamic stress intensity factors studied by boundary integro-differential equations, *Int. J. Num. Meth. Eng.*, **23**, pp.919–928 (1986).
- [85] Solodov, I. Yu., Asainov, A. F., and Len, K. S.: Non-linear SAW reflection: experimental evidence and NDE applications, *Ultrasonics*, **31**–2, pp.91–96 (1992).
- [86] Solodov, I. Yu. and Vu, C. A.: Popping nonlinearity and chaos in vibrations of a contact interface between solids, *Acoust. Phys.*, **39**, pp.476–479 (1993).

- [87] Solodov, I. Yu.: Nonlinear NDE using contact acoustic nonlinearity (CAN), *Ultrasonic Symposium 1994 Proceedings*, pp.1279–1283 (1994).
- [88] Solodov, I. Yu., Krohn, N., and Busse, G.: CAN: an example of nonclassical acoustic nonlinearity in solids, *Ultrasonics*, **40**, pp.621–625 (2002).
- [89] Solodov, I. Yu., Doring, D., and Busse, G.: New opportunities for NDT using non-linear interaction of elastic waves with defects, *J. Mech. Eng.*, **57**–3, pp.169–182 (2011).
- [90] Suo, Z.: Singularities, interfaces and cracks in dissimilar anisotropic media, *Proc. R. Soc. Lond.*, **A 427**, pp.331–358 (1990).
- [91] Takahashi, T., Nishimura, N., and Kobayashi, S.: A fast BIEM for three-dimensional elastodynamics in time domain, *Eng. Anal. Bound. Elem.*, **27**, pp.491–506 (2003).
- [92] Takahashi, T.: An interpolation-based fast-multipole accelerated boundary integral equation method for the three-dimensional wave equation, *J. Comput. Phys.*, **258**, pp.809–832 (2014).
- [93] Tanaka, M., Sládek, V. and Sládek, J.: Regularization techniques applied to boundary element methods, *Appl. Mech. Rev.*, **47**, pp.457–499 (1994).
- [94] Thau, S. A. and Lu, T. -H.: Transient stress intensity factors for a finite crack in an elastic solid caused by a dilatational wave, *Int. J. Solids Struct.*, **7**, pp.731–750 (1971).
- [95] Vorst, H. A.: Iterative Krylov methods for large linear systems: Cambridge monographs on applied and computational mathematics, Cambridge University Press (2003).
- [96] Williams, M. L.: The stresses around fault or crack in dissimilar media, *Bull. Seismol. Soc. America*, **49**–2, pp.199–204 (1959).
- [97] Wünsche, M., Zhang, Ch., Sladek, J., Sladek, V., Hirose, S., and Kuna, M.: Transient dynamic analysis of interface cracks in layered anisotropic solids under impact loading, *Int. J. Fract.*, **157**, pp.131–147 (2009).
- [98] Yamanaka, K., Mihara, T., and Tsuji, T.: Evaluation of closed cracks by model analysis of subharmonic ultrasound, *Jpn. J. Appl. Phys.*, **43**, pp.3082–3087 (2004).
- [99] Yoshida, K., Nishimura, N., and Kobayashi, S.: Analysis of three dimensional scattering of elastic waves by a crack with fast multipole boundary integral equation method, *J. Appl. Mech. JSCE*, **3**, pp.143–150 (2000) (in Japanese).
- [100] Yoshida, K., Nishimura, N., and Kobayashi, S.: Application of fast multipole Galerkin boundary integral equation method to elastostatic crack problems in 3D, *Int. J. Numer. Meth. Engng.*, **50**, pp.525–547 (2001).
- [101] Yoshida, K.: Applications of fast multipole method to boundary integral equation method, Ph.D. thesis, Kyoto University, Japan, (2001).

Bibliography

- [102] Zhang, C. and Achenbach, J. D.: Scattering of body waves by an inclined surface-breaking crack, *Ultrasonics*, **26**, pp.132–138 (1988).
- [103] Zhang, C. and Achenbach, J. D.: Numerical analysis of surface-wave scattering by the boundary element method, *Wave Motion*, **10**, pp.365–374 (1988).